

**UNSTEADY FLOW  
ORGANIZATION OF A SHOCK  
WAVE/BOUNDARY LAYER  
INTERACTION**

**RAYMOND A HUMBLE**

Copyright © 2008 R. A. Humble

Unsteady Flow Organization of a Shock Wave/Boundary Layer Interaction.

All rights reserved. No part of this publication may be reproduced, stored in a retrieval system, or transmitted, in any form, or by any means, electronic, mechanical, photo-copying, recording, or otherwise, without prior written permission of the publisher.

ISBN 978-90-597-2295-8

Front cover: created using the fractal generator Sterling-Ware v1.7 © 1998-1999 Stephen C Ferguson. Used with permission.



Printed in The Netherlands.



**UNSTEADY FLOW  
ORGANIZATION OF A SHOCK  
WAVE/BOUNDARY LAYER  
INTERACTION**

**RAYMOND A HUMBLE**

PROEFSCHRIFT

ter verkrijging van de graad van doctor  
aan de Technische Universiteit Delft,  
op gezag van de Rector Magnificus prof. dr. ir. J. T. Fokkema,  
voorzitter van het College voor Promoties,  
in het openbaar te verdedigen op woensdag 18 februari 2009 om 12.30 uur,  
door Raymond Anthony HUMBLE  
Master of Aeronautical Engineering,  
geboren te Gateshead, United Kingdom.

Dit proefschrift is goedgekeurd door de promotor(en):

Prof. dr. F. Scarano

Copromotor:

Dr. ir. B. W. van Oudheusden

Samenstelling promotiecommissie:

Rector Magnificus	voorzitter
Prof. dr. F. Scarano	Technische Universiteit Delft, promotor
Dr. ir. B. W. van Oudheusden	Technische Universiteit Delft, copromotor
Prof. dr. ir. P. G. Bakker	Technische Universiteit Delft
Prof. dr. ir. B. J. Boersma	Technische Universiteit Delft
Prof. dr. ir. B. J. Geurts	Universiteit Twente
Prof. dr. A. J. Smits	Princeton University, USA
Dr. H. Babinsky	Cambridge University, UK

This research was supported by the Dutch Technology Foundation STW under the VIDI—*Innovation Impulse* program, grant DLR.6198.

Keywords: boundary layer, shock wave, interaction, unsteady, turbulence, particle image velocimetry, tomography, high-speed, proper orthogonal decomposition, chaos theory, dynamical systems.

# SUMMARY

---

**O**NE of the most engaging yet perplexing phenomena in modern high-speed fluid dynamics is the interaction between a shock wave and a turbulent boundary layer (SWTBLI). In recent decades, there has been an evolving quest for a deeper understanding of the large-scale unsteadiness of SWTBLIs, primarily motivated by the desire to mitigate the intense wall-pressure fluctuations and heat transfer that can accompany shock oscillation, as well as the deficiencies of some of the most promising turbulence models, which seem to indicate the necessity of incorporating large-scale unsteady effects in order to accurately predict mean flow properties. Yet to date, there has been a failure of the SWTBLI community to reach a general consensus as to the underlying cause(s) of the large-scale unsteadiness, and its status remains an enigma.

In this thesis, a fundamental experimental study is carried out to investigate the unsteady flow organization of an incident SWTBLI at Mach 2.1. Planar and tomographic particle image velocimetry (PIV) are used in combination with data processing using the proper orthogonal decomposition (POD), complemented with hot-wire anemometry (HWA) and nonlinear time series analyses.

It is found that the global structure of the interaction region varies considerably in time. Although significant reversed-flow is measured instantaneously, on average, no reversed-flow is observed. The interaction instantaneously exhibits a multilayered structure, consisting of a high-velocity outer region, and a low-velocity inner region, separated by an interface containing vortical structures. The mean flow-field is therefore a simplified representation of a more complex instantaneous structure.

An inter-relationship appears to exist between the incoming boundary layer, separated flow region, and reflected shock wave. Specifically, when the boundary layer velocity profile is less-full than on the mean, then the streamwise extent of the separated flow region

is more likely to be larger than its median size, and the reflected shock wave appears upstream of its mean position, and vice versa. The POD provides a complementary analysis, and the returned eigenmodes may be viewed as a family of modes, each containing subspace representations of the phenomenology observed in the instantaneous realizations.

Extending the representation to include the spanwise dimension reveals a complex three-dimensional instantaneous flow organization. The incoming boundary contains large-scale coherent motions, in the form of three-dimensional streamwise-elongated regions of relatively low- and high-speed fluid. The reflected shock wave region conforms to these regions as they enter the interaction, and may be viewed as a superposition of a streamwise translation and a spanwise rippling. Farther from the wall, the streamwise motion of the reflected shock wave region decreases, and the region appears more uniform in the spanwise direction.

The HWA results reveal that the reflected shock wave region contains energetic frequencies an order of magnitude lower than those found within the undisturbed boundary layer at the same distance from the wall. The time series is shown to be represented as a chaotic attractor in a limited dimensional state-space. This attractor has a rich, underlying structure, which contains the signatures of the low- and high-speed regions as they enter the interaction. When considered in greater detail, attractor segments at earlier times resemble segments at later times, which affords itself to the application of a forecasting strategy. The signal is shown to be predicted over a length-scale that is several times greater than the most energetic wave-lengths found within the undisturbed boundary layer.

Thus, while at first glance the dynamics of the interaction appear hopelessly complex, it seems that there are some underlying features of its unsteady organization, involving large-scale motions within the incoming boundary layer, the separation bubble, and the reflected shock wave pattern, that suggest this may not be the case.

# SAMENVATTING

---

**D**E interactie tussen een schokgolf en een turbulente grenslaag (SWBTLI) vormt een van de meest aansprekende doch verbluffende verschijnselen in de moderne hogesnelheids stromingsleer. In de laatste decennia heeft een voortschrijdende zoektocht plaatsgevonden naar een dieper begrip van het grootschalige instationaire karakter van SWBTLIs. Hetgeen voornamelijk wordt gedreven door zowel het verlangen de intense drukfluctuaties and warmteoverdracht te verzachten, welke samengaan met de oscillaties van de schok, als de tekortkomingen van enkele van de meest veelbelovende turbulentiemodellen, welke lijken aan te geven dat het noodzakelijk is om de grootschalige fluctuaties mee te nemen voor een accurate voorspelling van de gemiddelde stromingseigenschappen. Tot de dag van vandaag heeft de SWBTLI-gemeenschap gefaald om tot een algemene overeenstemming te komen over de onderliggende oorzaak (oorzaken) van de grootschalige stromingsvariaties, waardoor zijn status een enigma blijft.

In dit proefschrift wordt een fundamentele experimentele studie beschreven, waarin de instationaire stromingsorganisatie van een invallende SWBTLI bij een Mach getal van 2.1 wordt onderzocht. Vlaksgewijze and tomografische particle image velocimetry (PIV) worden gebruikt in combinatie met dataverwerking gebruikmakend van de hoofdcomponentenanalyse (POD), aangevuld met gloeidraadmetingen (HWA) en niet-lineaire tijdsignaalanalyses.

Het blijkt dat de globale structuur van de interactie aanzienlijk in de tijd varieert. Hoewel de metingen laten zien dat instantaan significante terugstroming kan optreden, wordt in de tijdsgemiddelde stroming geen terugstroming waargenomen. Instantaan vertoont de interactie een gelaagde structuur, bestaande uit een buitenlaag met hoge snelheid en een onderlaag met lage snelheid, die gescheiden worden door een interface met wervelstructuren. Het gemiddelde snelheidsveld is daarom slechts een gesimplificeerde weergave van de meer complexe instantane structuur van de interactie.

Er lijkt een relatie te bestaan tussen de inkomende grenslaag, de loslaatblaas en de gereflecteerde schokgolf. Meer specifiek, wanneer de grenslaag relatief minder vol, zal het loslaatgebied in stromingsrichting waarschijnlijk een groter dan gemiddelde omvang hebben en lijkt de gereflecteerde schok meer stroomopwaarts te bewegen, en vice versa, overeenkomstig met wat is waargenomen in andere soorten interacties. Als complementaire analyse geeft de POD de eigenmodes, welke gezien kunnen worden als een familie van modes, die elk een subspace representatie geven van de verschijnselen die in de instantane realisaties worden waargenomen.

Uitbreiding van de beschrijving van de interactie in spanwijdterichting onthult een complexe driedimensionale stromingsorganisatie. De inkomende grenslaag bevat grootschalige coherente bewegingen, in de vorm van driedimensionale, in stromingsrichting verlengde gebieden van relatief hoge en lage snelheid. Het gereflecteerde schokgolfgebied past zich aan deze gebieden wanneer deze de interactie binnengaan en vertoont als gevolg daarvan een combinatie van translatie in stromingsrichting en een rimpeling in spanwijdterichting. Verder van de wand neemt de beweging van het gereflecteerde schokgolfgebied af en het gebied lijkt meer uniform in spanwijdterichting.

De HWA resultaten tonen dat het gereflecteerde schokgolfgebied lage energetische frequenties bevat, die een ordegrootte kleiner zijn dan die in de inkomende grenslaag op dezelfde afstand van de wand. Het tijdssignaal van de snelheid in het gereflecteerde schokgolfgebied kan worden gerepresenteerd als een chaotische attractor in een faseruimte met relatief lage dimensie. Deze attractor heeft een rijke, terugkerende structuur, waarin de kenmerken van de wisselwerking met de hoge en lage snelheidsstructuren zijn terug te vinden. Nader bekeken vertonen attractorsegmenten uit het verleden overeenkomst met die in de toekomst, wat gebruikt kan worden bij een voorspellingen. Het blijkt dat het signaalgedrag kan worden voorspeld over een lengteschaal die enkele malen groter is dan de meest energetische golflengtes in de ongestoorde grenslaag.

Hoewel de dynamica van de interactie op het eerste gezicht hopeloos complex lijkt, ziet er naar uit dat er onderliggende kenmerken in de instationaire stromingorganisatie optreden, welke beïnvloed worden door de grootschalige structuren in de inkomende grenslaag, de loslaatblaas en de gereflecteerde schokgolf, wat suggereert dat dit niet het geval is.

# CONTENTS

---

<b>Summary</b>	<b>v</b>
<b>Samenvatting</b>	<b>vii</b>
<b>Contents</b>	<b>ix</b>
<b>Acknowledgments</b>	<b>xiii</b>
<b>Nomenclature</b>	<b>xix</b>
<b>1 INTRODUCTION</b>	<b>1</b>
1.1 A Brief Historical Sketch	1
1.2 SWTBLI Background	3
1.3 Types of SWTBLI	7
1.4 Anatomy of the Present Interaction	12
1.4.1 Unseparated Case	13
1.4.2 Separated Case	15
1.5 SWTBLI Unsteadiness	19
1.6 Cause(s) of SWTBLI Unsteadiness	26
1.7 Thesis Aim and Objectives	34
1.8 Thesis Outline	35
<b>2 FUNDAMENTAL CONCEPTS</b>	<b>37</b>
2.1 Introductory Remarks	37
2.2 Terminology	38
2.3 Theoretical Foundations	39
2.4 Aspects of the Compressible Turbulent Boundary Layer	42
2.5 Van Driest Effective Velocity Concept	45
<b>3 EXPERIMENTAL TECHNIQUES &amp; ARRANGEMENTS</b>	<b>47</b>
3.1 Introductory Remarks	47
3.2 Flow Facility	48
3.3 Hot-Wire Anemometry	49
3.4 Planar PIV	52
3.4.1 Working Principles	52
3.4.2 Tracer Particles	53
3.4.3 Particle Imaging	54
3.4.4 Image Analysis	56

3.5	Planar PIV Experimental Arrangement	58
3.5.1	Incoming Boundary Layer	58
3.5.2	Shock Generator	60
3.5.3	Flow Seeding	61
3.5.4	Illumination	66
3.5.5	Image Recording	67
3.6	Tomographic PIV	69
3.6.1	Working Principles	69
3.6.2	Calibration	72
3.7	Tomographic PIV Experimental Arrangement	73
3.7.1	Incoming Boundary Layer	73
3.7.2	Shock Generator	74
3.7.3	Flow Seeding	76
3.7.4	Illumination	77
3.7.5	Image Recording	77
3.7.6	Reconstruction	81
3.8	Uncertainty Analysis	83
3.8.1	Analysis Outline	84
3.8.2	Summary of Measurement Uncertainties	90
<b>4</b>	<b>DATA ANALYSIS METHODS</b>	<b>93</b>
4.1	Introductory Remarks	93
4.2	Proper Orthogonal Decomposition	94
4.3	Mathematical Outline of POD	96
4.3.1	Direct Method	96
4.3.2	Snapshot Method	99
4.4	Nonlinear Time Series Analysis	104
4.4.1	Attractor Reconstruction	106
4.4.2	Correlation Dimension	115
4.4.3	Recurrence Plot	117
4.4.4	Lyapunov Exponent	118
4.4.5	Outline of a Forecasting Strategy	119
<b>5</b>	<b>BOUNDARY LAYER STUDY</b>	<b>125</b>
5.1	Introductory Remarks	125
5.2	Undisturbed Boundary Layer	126
5.2.1	Mean Velocity Profile	128
5.2.2	RMS Velocity Distributions	131
5.2.3	Reynolds-Averaged Shear Stress Distribution	132
5.2.4	Space-Time Organization	136
<b>6</b>	<b>2D FLOW ORGANIZATION</b>	<b>143</b>



6.1	Introductory Remarks	143
6.2	Assessment of Spanwise Uniformity	144
6.2.1	Surface Flow Visualization	144
6.2.2	PIV Spanwise Survey	145
6.3	Basic Flow Properties of the Interaction	147
6.3.1	Qualitative Features	147
6.3.2	Mean Velocity Pattern	150
6.3.3	Integral Parameters	153
6.4	Unsteady Flow Properties	155
6.4.1	Instantaneous Velocity Patterns	155
6.4.2	Instantaneous Vorticity Patterns	159
6.4.3	Intermittency	166
6.4.4	Behaviour of Separation & Reattachment	168
6.4.5	Role of the Incoming Boundary Layer	173
6.5	Turbulence Properties	178
6.5.1	RMS Velocity Distributions	178
6.5.2	Reynolds-Averaged Shear Stress Distribution	182
6.5.3	Equilibrium Phase Portraits	184
6.5.4	Structural Parameters	189
6.6	POD Analysis	192
<b>7</b>	<b>3D FLOW ORGANIZATION</b>	<b>203</b>
7.1	Introductory Remarks	203
7.2	Cross-Sectional Representations	204
7.3	3D Instantaneous Flow Organization: Lower Region	209
7.4	Vorticity Characterization	214
7.5	3D Instantaneous Flow Organization: Upper Region	223
7.6	Statistical Analysis	229
7.7	POD Analysis	234
<b>8</b>	<b>TEMPORAL ORGANIZATION</b>	<b>237</b>
8.1	Introductory Remarks	237
8.2	Time Series History	238
8.3	PSD Distributions	239
8.4	Nonlinear Time Series Analysis	243
8.4.1	Attractor Reconstruction	243
8.4.2	Correlation Dimension	253
8.4.3	Recurrence Plot	256
8.4.4	Lyapunov Exponent	258
8.4.5	Short-Term Forecasting	260
<b>9</b>	<b>TOWARD A CONCEPTUAL MODEL</b>	<b>265</b>

9.1	Introductory Remarks	265
9.2	Outline of a Physical Model	266
9.2.1	Two-Dimensional Characterization	266
9.2.2	Three-Dimensional Characterization	270
9.2.3	Temporal Characterization	272
9.3	Final Remarks	275
<b>10</b>	<b>CONCLUSIONS &amp; OUTLOOK</b>	<b>277</b>
10.1	Conclusions	277
10.2	Outlook	279
	<b>REFERENCES</b>	<b>283</b>
	<b>LIST OF PUBLICATIONS</b>	<b>309</b>

# ACKNOWLEDGMENTS

---

**I**N writing these acknowledgments, I know now that my PhD research finally comes to an end. Although only my name is on the front of this book, there are numerous exceptional individuals that I have had the privilege to meet over these last four years, and that I am in one way or another indebted to. It is difficult to find the right words to express my appreciation, but I want to take this opportunity to try and express my deepest gratitude to you all.

I would first like to thank my supervisors Prof. Fulvio Scarano and Dr. Bas van Oudheusden for their continual support throughout my PhD. We have had many lively discussions and debates on numerous topics, many outside the realm of my research, and I learned much from you both as a professional, as well as an individual. I want to thank you for the trust, freedom, and responsibility that you gave me from the very beginning, and for enabling me to always conduct my research in my own idiosyncratic manner. Since my Dutch has not improved at all since my first six months in Holland, I would like to thank Bas and Roeland de Kat for providing the Dutch summary.

I would like to thank Prof. Peter Bakker for his insightful comments on many of my papers and enthusiastic discussions on other aspects of my work, as well as Dr. Robbert Fokkink for his insights into chaos theory. I would also like to extend a special thank you to Dr. Marc Gerritsma, who without his initial interest in me before I came to Holland, I probably would have never had the opportunity to come to Delft and carry out my PhD. It is strange the way in which events sometimes transpire in life to help you achieve your goals.

I would like to extend a thank you to all the technical staff within the High-Speed Aerodynamics Laboratory at Delft. I thank Erik de Keizer for his patience in my endless requests to make wind-tunnel runs, Frits Donker Duyvis for his skill in the careful design of many of the important experimental components, as well as for the provision of many of the technical schematics presented in this thesis, Peter Duyndam for his craftsmanship and for our Dutch

conversations, and Nico van Beek for his support in solving the endless complexities of computer software.

I would like to thank Dr. Gerrit Elsinga for his expertise and collaboration on several of the experiments reported in this thesis, Ferry Schrijer for his expertise throughout my PhD, and Raf Theunissen for his humour and antics abroad. You are all model researchers. I would like to thank Roeland de Kat and Daniele Ragni for all our esoteric coffee conversations together this past year, for their sharp, challenging, and sometimes controversial views on topics ranging from philosophy, turbulence, gravity, politics, uncertainty analysis, string theory, girls, and emergence; just some of our usual Monday morning conversations.

I would also like to thank the original basement guys: Erik Nennie, Steven Bosscher, and the late Patricia, for those times in the very beginning. Patricia I still think about you and miss you very much. I want to also thank the newer, now ex-basement guys: Peter Lucas, Alex Loeven, Bart Horsten, Frank Bos, and Mohamed Elsayed for their company and for those of you who dared to come to Leiden and try the infamous *Fandango Special*. I thank Sander van Zuijlen, Jeroen Witteveen, and Aukje de Boer, for never complaining about the noise from all my experiments.

I also want to thank the Masters students that have suffered under my supervision over the years, but whose assistance has enabled me to complete my research: Marthijn Tuinstra, Stefano Antonetti, Alan Anelli, and Paul Blinde. I have enjoyed our collaborations together, and I learned as much from you all as I tried to instruct. I also thank Dirk Jan Kuik for his collaborations during the tomographic experiments.

Of course my work experience before my PhD was crucial for my professional development, and I would also like to extend my thanks to Dr. Keith Warburton and Mr. Steve Daley of the Defence Science & Technology Laboratories in the United Kingdom, who have been instrumental in my subsequent development as a PhD researcher, and who inspired me to pursue a career in fluid dynamics.

My time in Holland has been a remarkable and unforgettable experience, and that experience would not have been nearly as fulfilling without the many friends that I have made here. I would first like to thank Abel Ponger for everything that we have shared

together over these last years. I thank him for all our trips to countries sensible people never dare go, for still putting up with me after all this time, and for helping me in ways that he will never know. You are a true friend.

I would like to thank Danny Taylor for all our unforgettable times living in England together, and for first convincing me to move to Holland. I thank Aren Lee for all those crazy times in Noordwijk and for always letting me crash at his place at the weekends, as well as Jessy Groenewoud, Dave Lemmers, and Joost Wilson, who made the times there always memorable.

I want to thank Simon Laird for allowing his apartment to be my second home, for his unique Scottish humour, and for all those excellent barbecues. I thank Xiomara Sanchez Garcia for what we have shared together, Andres Fernando and Sandra Maas for all the talks, David Frew and Helen Frew for the times and drinks in Leiden, Shamone for simply being Shamone, Agnes de Wolf for being a friendly neighbour who always dropped by, as well as Adrian Bell and Matthijs Jansen who always managed to take my money at poker.

I would also like to thank my friends in Amsterdam and Volendam: Niek Dijkman, Daan Ponger, Mostafa Bouhout, Kosta Karathanasis, Daniel Hoogstraat, and Mark Weber, for showing and teaching me about Dutch life; it is truly one of the best. I thank them for all our trips, parties, and memories together; that if you can remember, then you did not have enough to drink.

I want to thank Crystal Stanley and Stephanie Gardner for all their talks of encouragement and unforgettable support when completing my PhD was nothing more than an elusive ideal, Gerie Veerman for all the coffees, fashion tips, and shopping together in Amsterdam, Else Jonk, Anne Jonk, and Marlies den Elzen, for all the great dinners and parties together in Leiden, and Nina Pockett for being a friendly Brit who I could talk to.

I would also like to thank Laura Gomez, Ana Cristina Puerta, Ana Maria Acosta Fajardo, Ekaterina Kostochkina, Daria Silkina, and Anastasia Silkina, for all the unforgettable memories that they have given me over these last years, for showing and teaching me about the wonderful places of Colombia and Russia, for coming over to visit from so far, and for everything else that they have done for me.

I would also like to thank my good friends back in England: Paul Williams, Paul Robinson, Mark Dobison, Grant Miller, and Kevin Dobison. I thank them for being there from the very beginning, for always coming out when I returned home, and for always accepting me for what I am. I also thank Vikki Hewison and Claire Young for visiting and still staying in touch with me over all these years.

I would like to extend a very special thank you to Alfred and Joanne Humble, for the invaluable help and support that they gave me in the very beginning, in those difficult months when I first came to Holland. I want you both to know that without your help, none of this would have ever been possible. Thank you so much more than you know.

I want to also give a very special thank you to Viviana Guerrero, for so many things that I cannot write here, nor would I be able to express properly. And so all I will say is thank you for giving me one of the most precious gifts that I could ever hope for, and for being one of the few people to understand me; not with your eyes, but with your hands; for not seeing what I appear to be, but touching upon what I am. I will never forget our chapter together my mariposita.

And last, but of course not least, I would like to extend the deepest thanks to my family back in England: Richard, Janice, and Michelle. I want to thank them for their unconditional love, support, and encouragement throughout my life. I know that I have not been around as much as I should have, but I hope that the pages in this book are at least a partial justification for this. I would like to think that Ronald would have been proud. But in all this time, I always knew that you were only ever a phone call, or a flight away, and that means more to me than you will ever know.

Raymond Humble  
Delft 2008

*We make a living out of what we get;  
we make a life out of what we give.*

*Sir Winston Churchill (1874–1965)*





# NOMENCLATURE

---

Latin:

$a$	constant
$a_k$	POD temporal coefficient
$A$	anisotropy parameter
$b$	constant
$B$	constant
$c_p$	specific heat capacity at constant pressure
$c_w$	hot-wire thermal capacity
$C$	correlation value, correlation matrix
$C(\varepsilon)$	correlation integral
$C_D$	drag coefficient
$C_f$	skin friction coefficient
$C_\tau$	shear stress coefficient
$d$	embedding dimension
$d_{diff}$	Airy disk diameter
$d_p$	particle diameter
$d_\tau$	particle image diameter
$D$	displacement, kernel function
$D_a$	aperture diameter
$e$	internal energy
$E$	light intensity, voltage
$f$	frequency, focal length, smooth map
$f_\#$	f-number
$f^\tau$	smooth map
$\Delta f$	frequency resolution
$F$	force
$F^\tau$	smooth map
$G$	equilibrium constant
$h$	specific enthalpy, smooth observation function
$H$	total enthalpy, shape factor
$I$	triple point, particle image intensity, mutual information, current intensity, impulse

$k$	thermal conductivity, wave-number
$K$	kernel
Kn	Knudsen number
$l$	Prandtl mixing-length
$l_c$	calibration dot physical distance
$l_w$	length of hot-wire
$L$	length of interaction zone, hot-wire constant
$L_x, L_y$	length and width of field-of-view, respectively
$M$	Mach number, magnification factor, size of interrogation area, ensemble size, manifold, hot-wire constant
$n$	number of dimensions
$n_c$	calibration dot pixel distance
$n_x, n_y$	length and width of field-of-view (pixels), respectively
$n_x, n_y, n_z$	number of grid points in $x, y, z$ directions, respectively
$N$	size of interrogation area, total number voxels in line-of-sight, number of data points
Nu	Nusselt number
OF	overlap factor
$p$	static pressure, probability
$P_0$	stagnation pressure
Pr	Prandtl number
$q$	general variable in the momentum equations
$Q$	constant, second invariant of velocity gradient tensor
$r$	recovery factor, constant
$R$	reattachment point, universal gas constant, averaged space-correlation tensor
Re	Reynolds number
$\mathbf{R}_{i,j}$	recurrence plot matrix
$R_s$	pressure ratio
$R_{uv}$	correlation coefficient
$R_{VP}$	correlation coefficient
$R_{VR}$	correlation coefficient
$R_w$	hot-wire resistance
$s$	state-space variable, distance
$\Delta s$	maximum particle displacement
$\mathbf{s}$	state vector

$S$	separation point, shock-normal abscissa
$S_L$	Strouhal number based on $L$
$St$	Stokes number
$t$	time
$t_{lyap}$	Lyapunov time
$\Delta t$	laser pulse time separation
$T$	time, static temperature
$T_0$	stagnation temperature
$u, v, w$	streamwise, spanwise, wall-normal instantaneous velocity components
$u_{eq}$	van Driest effective velocity
$u_n$	shock normal velocity
$u_\tau$	friction velocity
$\Delta u$	maximum particle slip velocity
$U_\infty$	free-stream velocity
$\nu$	correlation dimension
$\mathbf{v}$	velocity vector
$\nabla \mathbf{v}$	velocity gradient tensor
$V$	velocity
$V_s$	shock velocity
$\mathbf{V}$	velocity vector
$w_{i,j}$	weighting coefficient
$W_s$	interrogation window size
$x(t)$	hot-wire anemometry mass-flux time signal
$x, y, z$	streamwise, spanwise, wall-normal spatial coordinates
$x_r$	reattachment location
$x_s$	separation location
$\Delta x$	vector spacing
$\mathbf{x}$	state vector
$X$	particle trajectory, hot-wire constant
$X, Y, Z$	streamwise, spanwise, wall-normal spatial coordinates; Lorenz attractor phase variables
$Y$	hot-wire constant
$z_0$	distance between image plane and lens
$Z_0$	distance between lens and object plane

Greek:

$\alpha$	compression ramp angle, polynomial coefficient
$\gamma$	intermittency, ratio of specific heats
$\delta$	boundary layer thickness
$\delta(0)$	initial trajectory separation distance
$\delta(x)$	trajectory separation distance
$\delta_{ij}$	Kronecker delta
$\delta_v$	viscous length-scale
$\delta_z$	focal depth
$\delta^*$	displacement thickness
$\varepsilon$	RMS uncertainty, threshold value
$\eta$	recovery factor
$\theta$	momentum thickness
$\Theta$	Heavyside function
$\Theta_w$	hot-wire temperature
$\kappa$	von Kármán constant, digital resolution
$\lambda$	wave-length, POD eigenvalue, Lyapunov exponent
$\Lambda$	mapping function
$\mu$	fluid viscosity, scalar relaxation parameter
$\mu_I$	mean of image intensity $I$
$\mu^v$	volume or bulk viscosity
$\xi$	particle trajectory
$\Pi$	Coles wake parameter
$\rho$	fluid density
$\sigma$	RMS quantity, constant
$\tau$	shear stress, time-delay
$\tau_{corr}$	correlation time
$\tau_f$	characteristic flow time-scale
$\tau_p$	particle response time
$\tau_{shock}$	shock wave time-scale
$\nu$	kinematic viscosity
$\phi$	POD eigensubspace parameter
$\Phi$	POD eigenvector, convective heat-loss rate to flow, generic smooth map, squared modulus of Fourier transform
$\psi$	POD eigenmode

$\omega$	frequency $2\pi f$ , vorticity
$\Omega$	flow domain

Subscripts:

0	initial condition, stagnation condition
1	upstream condition
2	downstream condition
$aw$	adiabatic wall condition
$c$	convective velocity condition, cut-off condition
$e$	boundary layer edge condition
$f$	fluid condition
$i$	incompressible condition
$max$	maximum condition
$min$	minimum condition
$n$	shock-normal condition
$opt$	optimum condition
$p$	particle condition
$pi$	initial particle condition
$RMS$	root-mean-square value
$t$	turbulent condition
$w$	wall condition, wire condition
$wo$	undisturbed wall condition
$\infty$	free-stream condition

Superscripts:

$\bar{\cdot}$	time-averaged quantity
'	fluctuating quantity
+	log-law scale
*	complex conjugation

Abbreviations:

CCD	charge couple device
CTA	constant temperature anemometer
D	detachment
DNS	direct numerical simulation
HWA	hot-wire anemometry
$inv$	inviscid limit

ID	incipient detachment
ITD	incipient transitory detachment
TD	transitory detachment
LDA	laser Doppler anemometry
LDV	laser Doppler velocimetry
LES	large-eddy simulation
MART	multiplicative algebraic reconstruction technique
PDF	probability density function
PIV	particle image velocimetry
POD	proper orthogonal decomposition
ppp	particles per pixel
PSD	power spectral density
RANS	Reynolds-averaged Navier-Stokes
RMS	root-mean-square
SWBLI	shock wave/boundary layer interaction
SWTBLI	shock wave/turbulent boundary layer interaction
TiO <sub>2</sub>	titanium dioxide
TST	transonic-supersonic wind-tunnel
<i>UI</i>	upstream influence line

# CHAPTER 1 INTRODUCTION

---

## 1.1 A Brief Historical Sketch

**I**NTEREST in compressible flows has perhaps existed ever since Galileo (1564–1642) first expressed his curiosity about the difference between the speeds of sound and light. Shortly afterwards, Newton (1643–1727) became attracted to the problem, and guided by artillery tests carried out a mathematical analysis of the speed of sound, which would lead to his famously incorrect\* formulation for the speed of sound in air (see also Anderson 1990; Bar-Meir 2008). Much of the work that followed focused on the theoretical nature of shock waves, with major contributions by Poisson in 1808 and Challis in 1848, culminating in

---

\* Newton incorrectly assumed the flow to be isothermal instead of adiabatic. His formulation was therefore missing a factor  $\gamma(=1.4)$ , the ratio of specific heats.

the seminal work of Rankine (1870*a*, 1870*b*) and Hugoniot (1887, 1889), who succeeded in independently deriving the fundamental equations for flow properties across a normal shock wave.

The existence of shock waves themselves, however, had remained a controversial issue, and it was not until 1887 that Mach presented the first visualization of shock waves around a bullet in supersonic flight using the shadowgraph technique (see figure 1.1, from Anderson 1990). This helped provide impetus to the emerging practical interest in compressible flows, which was taking place in part due to the technological improvements of firearms, which led to guns capable of shooting bullets approaching the speed of sound, and in part due to the development of steam turbines, which necessitated compressible flow analyses.

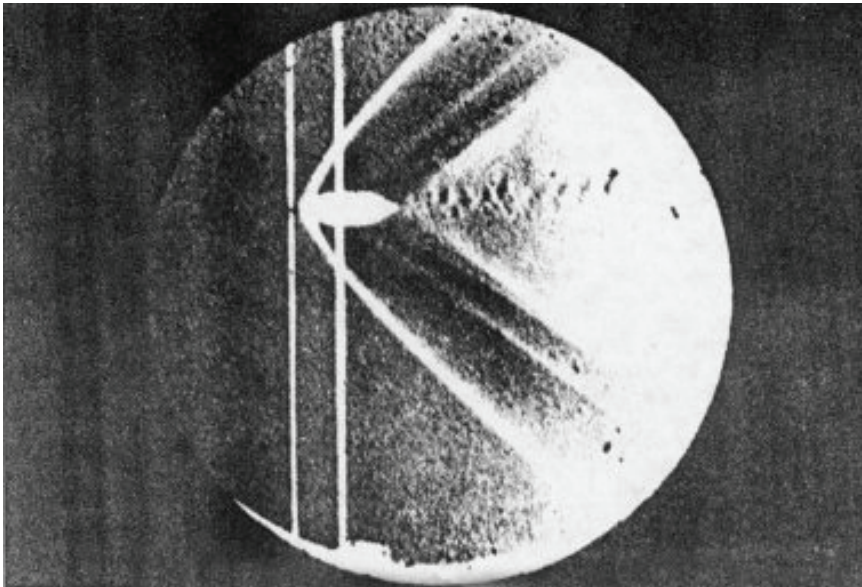


FIGURE 1.1: One of the first photographs visualizing shock waves around a bullet in supersonic flight by Ernst Mach 1887 using the shadowgraph technique. The bullet is travelling from right to left. From Anderson (1990).

At the beginning of the twentieth century, Prandtl (1904) proposed the concept of the boundary layer, which represented a watershed moment in the history of fluid mechanics. The theory of the boundary layer stated that no matter how high the Reynolds number,



there must always exist a small layer at the surface of a body immersed in a real fluid where the effects of viscosity cannot be neglected. This concept was used to explain many perplexing phenomena of the time, such as flow separation from a surface in particular, and finally bridged the gap between the seemingly irreconcilable fields of classical hydrodynamics and hydraulics, to serve as a scientific basis for understanding the physics of real fluids (see Young 1989).

The development of an effective boundary layer theory took place at a time when the field of aviation was emerging, and somewhat surprisingly, engineering scientists became quickly motivated to focus on the practical problems of compressibility. Although the forward speed of the aircraft of the time was much slower than the speed of sound, their propeller tips often approached this speed, resulting in a dramatic loss of propeller efficiency, which was later ascribed to the presence of shock waves (see Anderson 1990). Together with the development of boundary layer theory, important ideas could be advanced in the physics of fluids around bodies under compressible flow conditions (see Stack 1934).

Such knowledge would prove to be crucial by World War II, as combat pilots were beginning to experience first-hand the dangers of compressibility. When diving from high altitudes, they would report an alarming loss of control of their aircraft, which would often lead to fatal consequences (see Stack 1934). Engineering scientists began to suspect that such observations were related to an intimate relationship between shock waves and the boundary layer, and they would soon encounter the shock wave/turbulent boundary layer interaction (SWTBLI) phenomenon.

## 1.2 SWTBLI Background

Perhaps the first experimental observation of a SWTBLI published in open source literature was by Ferri (1939), when a deflection of a trailing edge flap in transonic flow caused a weak oblique shock wave ahead of the hinge-line (see Dolling 2001). This led to premature boundary layer separation, which was a rather puzzling observation at the time, since separation occurred in a region of expected favourable pressure gradient (see figure 1.2 for a dramatic example of such an interaction).

Shortly afterwards, Donaldson (1944) found when investigating nozzle characteristics, that the nozzle performance differed widely from what was expected when the nozzle became over-expanded and shock waves became present. The flow-field appeared significantly more complicated than the simple shock wave reflection model, proposed by neglecting the presence of the boundary layer, and such disagreements between theory and experiment raised questions concerning the flow physics present.

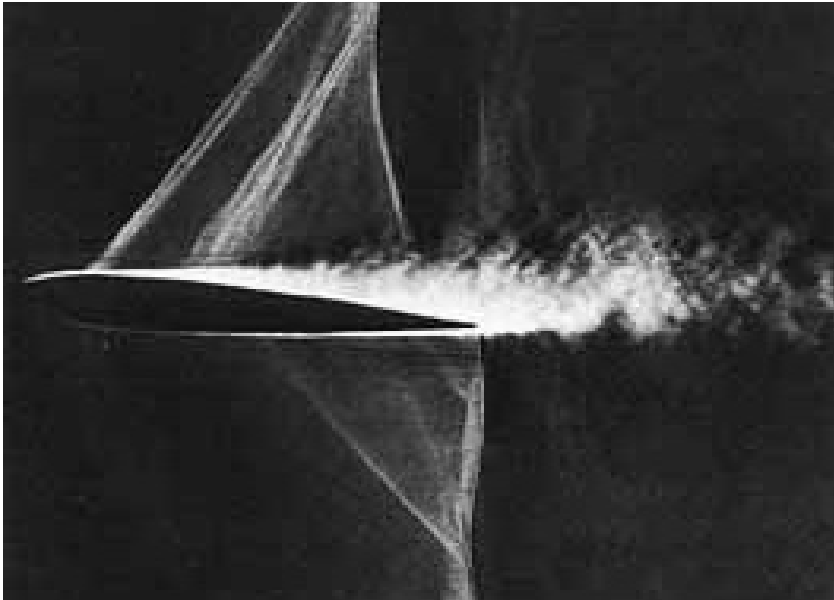


FIGURE 1.2: Schlieren visualization of a SWTBLI on a NACA 0012 aerofoil. The flow direction is from left to right. From Baals & Corliss (1981).

By the post-war years, the problems and potential dangers of SWTBLIs were clear, and the first systematic experimental studies had begun. Pioneering studies were carried out independently by Ackeret *et al.* (1946), Fage & Sargent (1947) and Allen *et al.* (1947) among others, which demonstrated the importance of the phenomenon at transonic speeds. These experiments simulated the embedded supersonic region that occurs on an aerofoil at high-subsonic speeds and showed that the presence of the boundary layer significantly affects the overall flow-field.

At around the same time, theoretical solutions were also being sought. One of the first attempts was made by Howarth (1948), who considered an incident wave impinging the interface between two semi-infinite uniform streams of sub- and supersonic flow. He demonstrated qualitatively the upstream propagation of the disturbance, and showed that a compression wave is generated upstream of the incident wave. This model was later modified by Tsien & Finston (1949) who incorporated a boundary layer into the analysis. Fundamental ideas concerning supersonic boundary layer separation were later advanced by Lighthill (1953), who showed the importance of the upstream influence effect in SWTBLIs.

Detailed theoretical analyses were carried out by Ritter & Kuo (1953) and Kuo (1953), who considered the problem of both laminar and turbulent boundary layers by dividing the flow into a viscous layer near the wall and an outer supersonic potential flow. Restricting themselves to infinitesimal incident compression waves, which allowed the application of linearized theory, appreciable differences in the upstream influence of the laminar and turbulent interactions were demonstrated; namely, that the upstream influence in turbulent interactions was significantly less.

By the late 1940s and early 1950s, a series of experiments were being carried out in a purely supersonic boundary layer (Dolling 2001). Moeckel (1951) for instance, investigated flow separation ahead of obstacles on a flat plate, and on the basis of experimental and analytical results he delineated the various flow patterns observed as body thickness increases. Systematic studies were conducted by Liepmann *et al.* (1952) to investigate the reflection characteristics of the shock wave. The differences between laminar and turbulent interactions, first found in transonic flow, were confirmed, and investigated in detail.

Experiments by Donaldson & Lange (1952) determined the important conditions under which laminar and turbulent boundary layers would separate due to the pressure rise across the shock wave, demonstrating that the critical pressure rise across a shock wave which just causes boundary layer separation is proportional to the skin friction coefficient. Shortly afterwards, systematic studies were carried out by Holder *et al.* (1955), who designed a series of experiments aimed at providing fundamental information on the

phenomenon. Considering interactions between a plane incident shock wave and flat plate boundary layer, as well as transonic interactions on aerofoils, the Mach number and Reynolds number dependency, as well as the state of the incoming boundary layer (laminar or turbulent) was extensively documented.

These results were later emphasized in the seminal paper by Chapman *et al.* (1957), who considered laminar, transitional, and turbulent boundary layer separation caused by a ramp, a step, as well as an oblique shock wave. It was found that certain characteristics of separated flows did not depend on the way in which flow separation occurred. In particular, the pressure distribution prior to flow separation was found to be almost independent of the downstream geometry. This was a remarkable discovery, because it meant that any phenomenon near separation would depend only on the simultaneous solution of the boundary layer and external flow equations, and not on the geometric boundary conditions determining the flow downstream. This experimental observation led to the development of *free interaction theory*, from which a simplified order-of-magnitude analysis deduced certain information about the effects of Reynolds number on the pressure rise characteristics prior to flow separation.

Another powerful concept developed for self-induced separation in supersonic flow was the subdivision of the boundary layer into several regions with distinctly different properties, leading to the asymptotic theory of viscous-inviscid interaction, now known as *triple-deck theory*. This was simultaneously formulated by Neiland (1969) and by Stewartson & Williams (1969), based on an asymptotic analysis of the Navier-Stokes equations. Such theoretical analyses were indispensable in the late 1960s and mid-70s, before the proliferation of numerical methods in particular, and as noted by Settles (1993), the publication record shows spurts of activity during this time, which he speculates was due to the cold-war 'space-race' and the Space Shuttle development efforts.

Research efforts in SWTBLI have continued apace to the present day, ascribed in part due to the sustained fundamental importance of SWTBLIs in high-speed internal and external aerodynamics flow problems of practical interest, and in part due to the need for experimental benchmarks for computation fluid dynamics (CFD)

prediction efforts. For reviews on much of the early work on SWTBLIs, of which we have only touched upon here, the interested reader is referred to Green (1970), Stanewsky (1973), Hankey & Holden (1975), Adamson & Messiter (1980), and Détery (1985), who discuss interactions that are two-dimensional on the mean. For more recent reviews, see Settles & Dolling (1990), Dolling (1993), Dolling (2001), and Smits & Dussauge (2006) for detailed discussions, including three-dimensional interactions.

### 1.3 Types of SWTBLI

At this point, it is instructive to introduce some different types of SWTBLI that are typically investigated in order to provide the context for the present type of interaction considered. Research spanning several decades has focused on a variety of simplified generic geometries, which denote representative parts of high-speed aerospace applications. Figure 1.3 schematically illustrates some typical examples of SWTBLIs, which may occur on a hypersonic vehicle for example.

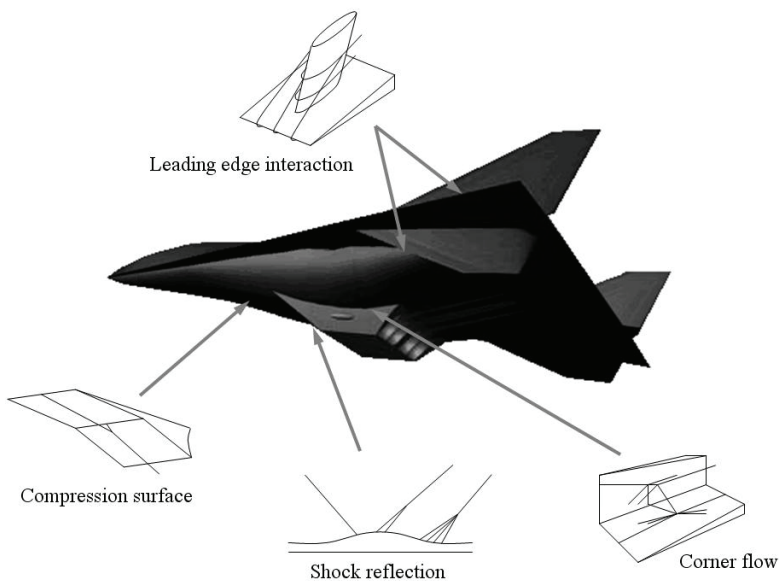


FIGURE 1.3: Some typical examples of SWTBLIs on a hypersonic vehicle. Hypersonic vehicle from Adrian Mann © 2002.

Some of these basic SWTBLI configurations, among others, are briefly summarized below, although it should be stressed that there are many variants of these geometries:

**External Interaction:** The flow over an aerofoil at transonic speeds (typically  $M_\infty > 0.7$ , where  $M_\infty$  is the free-stream Mach number), often leads to the formation of shock waves and an attendant external SWTBLI, as shown in figure 1.4, from Déleury & Bur (2000). This type of interaction can lead to sudden loss of lift, increase in drag, as well as a rapid movement in the centre of pressure. In addition, shock-induced separation may occur, leading to large amplitude shock wave oscillations. Since these phenomena often take place within the general operating conditions of modern transport aircraft, they remain the subject of intensive scientific research.

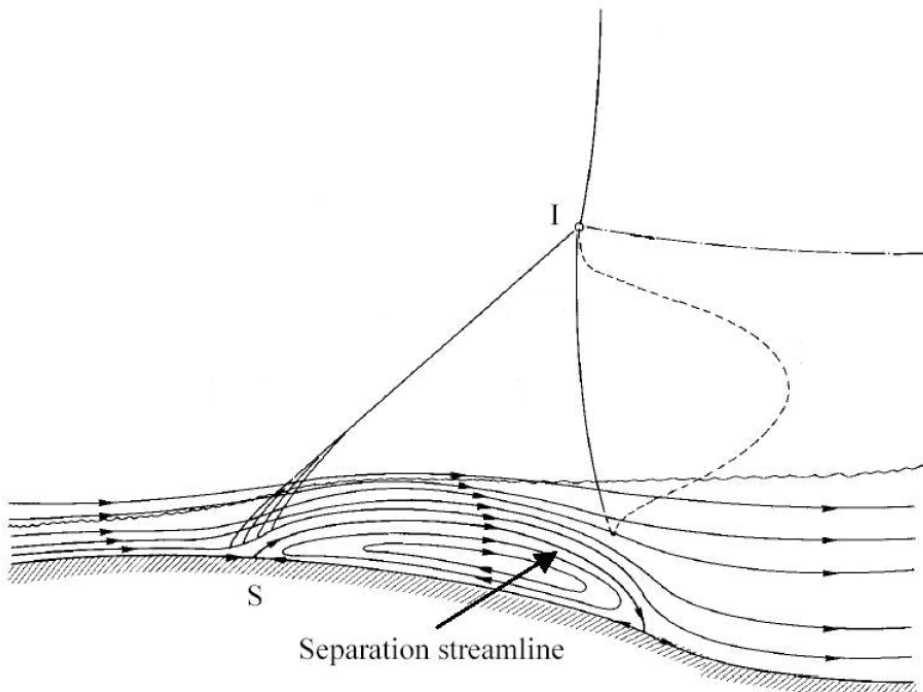


FIGURE 1.4: Schematic of the physical features of an external interaction. From Déleury & Bur (2000).

In the case shown, flow separation is provoked by a normal shock wave in the outer flow. The incoming flow separates at S and gives rise to a separation shock wave. The flow behind this shock wave, however, is still typically supersonic. The separation shock wave intersects with the normal shock wave at point I leading to the formation of a slip-line farther downstream. A third shock wave emanates from point I towards the wall, and a supersonic 'tongue' (in this case) is present, indicated by the dashed line. The overall flow structure depicted is commonly called a *lambda pattern* (see Détery & Bur 2000 for further details).

**Ramp Flow:** A significant fraction of published papers on SWTBLIs have considered compression ramp interactions, which represent the type of flow-field encountered due to discontinuous changes in body geometry and deflected flap configurations (see e.g., Dolling & Murphy 1983; Ardonneau 1984; Dolling 1993). An unswept ramp is shown in figure 1.5, from Détery & Bur (2000). Here, the pressure gradient is provided by a discontinuous change in wall inclination, which is the origin of a shock wave system through which the incoming boundary layer is deflected. A separation bubble may form, which is bounded by the walls of the ramp and a separated shear layer. A second shock wave is generated near the reattachment of the shear layer on the inclined ramp, as the flow is turned parallel with the wall. These two waves intersect each other at I leading to a slip-line and a transmitted shock wave that proceeds towards the inclined wall. The compression ramp interaction therefore shares many similarities with the external interaction; the boundary layer responding to an attendant pressure gradient, with the main difference being the overall shock wave pattern (Détery & Bur 2000).

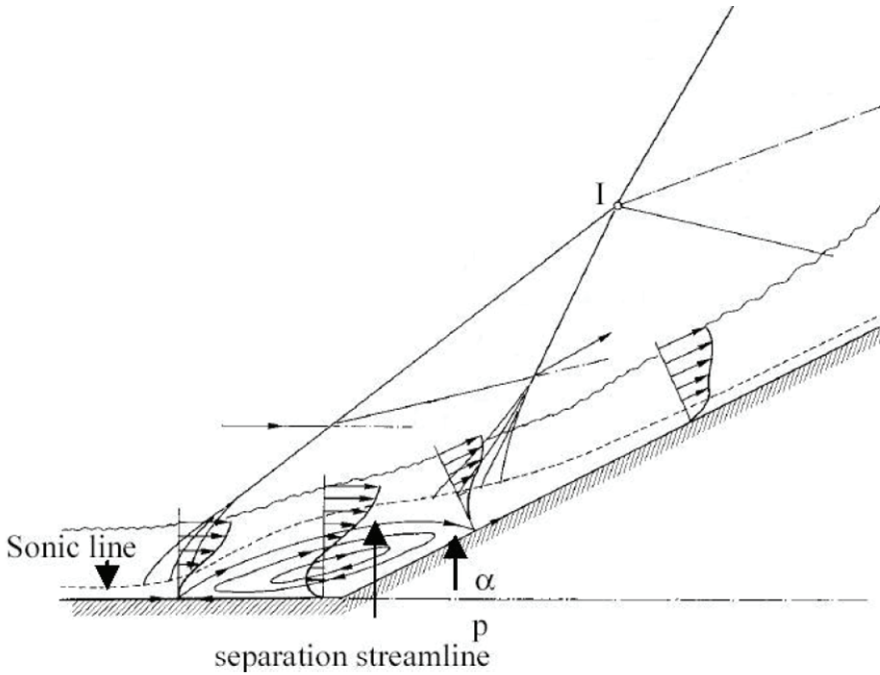


FIGURE 1.5: Schematic of the physical features of a compression ramp interaction. From Détery & Bur (2000).

**Reattachment Downstream of a Step:** The case of flow reattachment downstream of a step is shown in figure 1.6, adapted from Wisse (2005). Such an interaction has often been used as a benchmark to validate compressible flow solvers, and is closely related to the planar compressible base flow problem (see e.g., Humble *et al.* 2007c). It also shares similarities with step-induced separation. In the schematic shown, the approaching boundary layer expands rapidly at the shoulder towards the lower base pressure farther downstream. The boundary layer separates at the corner, and subsequently develops into a free shear layer. This shear layer together with the base wall bounds a region of slowly recirculating fluid. The shear layer grows continuously as it proceeds downstream, creating a momentum exchange with the recirculation region. The shear layer is then gradually turned back towards the free-stream direction, until it reattaches back onto the wall. A further compression takes place within the shear layer, leading to the formation of a reattachment or trailing shock wave. The flow begins to recover farther downstream.



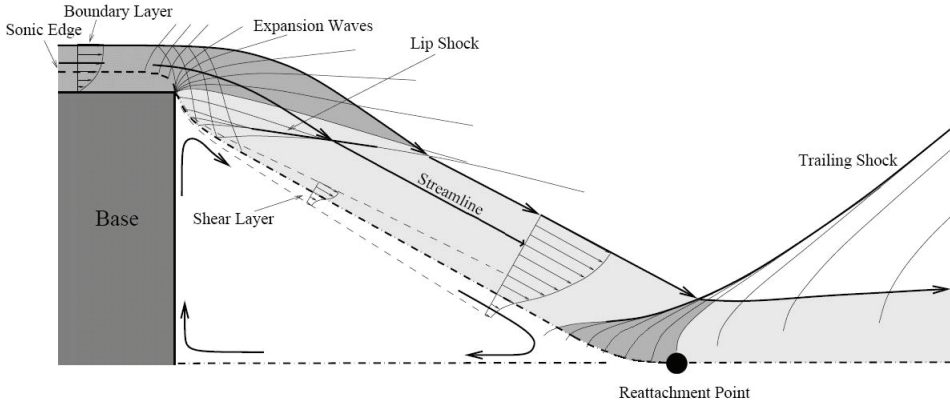


FIGURE 1.6: Schematic of the physical features of a backward-facing step interaction. Adapted from Wisse (2005).

**Fin Interactions:** Interactions involving sharp or blunt upright fins mounted on a flat plate have received considerable attention due to their applications for missile stabilization and control surfaces, as well as their relevance for supersonic and hypersonic inlet design. For an illuminating review of several decades of experimental swept SWTBLI research, using upright fins mounted on a flat plate as the archetype, the reader is referred to work of Settles (1993). A blunt fin interaction is shown schematically in figure 1.7, from Houwing *et al.* (2001), as reported by Bueno (2006). A complex three-dimensional flow-field is generated due to the boundary layers both on the fin and the flat plate. In the schematic shown, flow separation is provoked upstream of the fin, leading to the formation of a bow shock wave and lambda pattern near the fin juncture. This lambda pattern sweeps around the fin, leading to the formation of (in this case) a large horseshoe vortex and a smaller secondary vortex system.

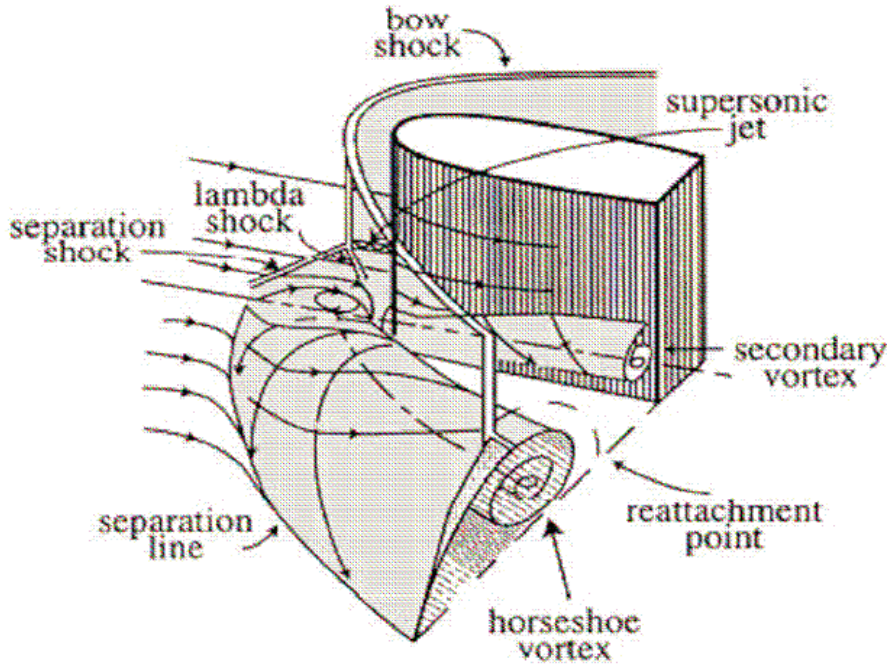


FIGURE 1.7: Schematic of the physical features of a blunt fin interaction. From Houwing *et al.* (2001), as reported by Bueno (2006).

## 1.4 Anatomy of the Present Interaction

The type of interaction considered in this thesis is the incident or shock reflection interaction. For high-speed aeronautical applications, this interaction represents the process that typically takes place within high-speed air intakes. Here, the incoming flow is typically decelerated through a succession of oblique shock waves, and this process must be carefully managed in order to minimize the losses that occur where the shock wave intersects the boundary layer. Although not as well-documented in literature compared to several of the interactions outlined above, reviews of much of the early work on incident SWTBLIs, concerning two-dimensional interactions, may be found in Green (1970), Hankey & Holden (1975), and Adamson & Messiter (1980). More recent reviews, with emphasis on the unsteadiness properties, may be found in Délerly & Marvin (1986) and Smits & Dussauge (2006).

In what follows, we provide a detailed discussion of the mean phenomenology of this type of interaction, which will help us develop a descriptive language to interpret the unsteady results later on. We draw on much of the physical description provided by Détery & Marvin (1986) and Détery & Bur (2000), and the reader is referred to these works for further details. Consider a turbulent boundary layer developing in an initially zero-pressure-gradient flow. A steady incident shock wave is generated in the free-stream that impinges the boundary layer. Consider the following cases:

### 1.4.1 Unseparated Case

In this first case, the pressure gradient initially imposed by the incident shock wave is considered insufficient to cause mean boundary layer separation. The resulting flow-field is shown in figure 1.8, based on the schematic from Détery & Bur (2000). We arbitrarily subdivide the interaction into the following regions:

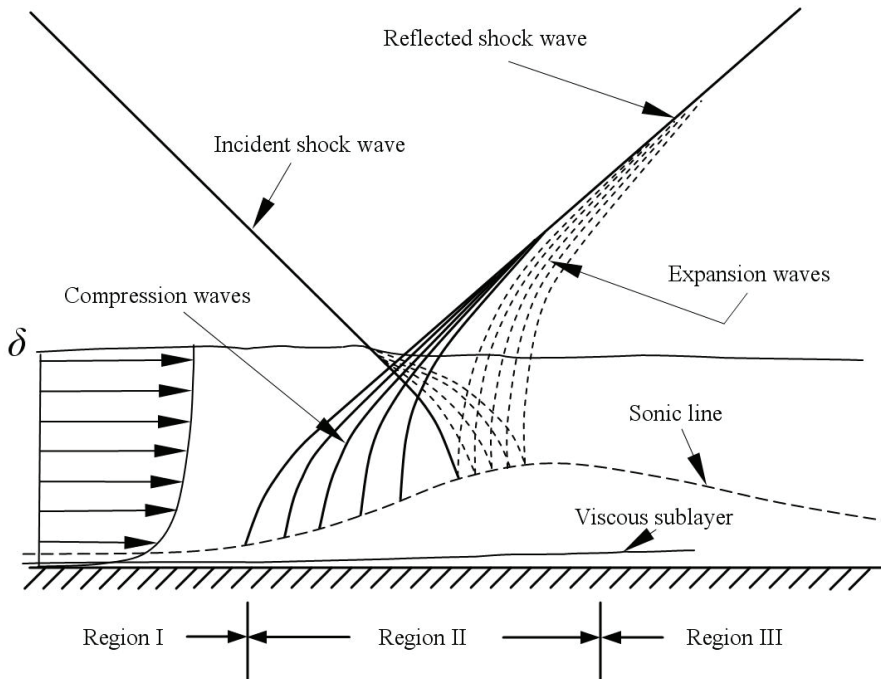


FIGURE 1.8: Schematic of the unseparated incident SWTBLI. Based on the schematic from Détery & Bur (2000).

**Region I:** In this region, the undisturbed boundary layer of thickness  $\delta$  first encounters the interaction. As the shock wave penetrates into the boundary layer, its influence is necessarily transmitted upstream through the subsonic part of the boundary layer very close to the wall, as indicated by the dashed line. The pressure rise associated with the incident shock wave is therefore felt upstream of the point where the shock wave would meet the surface in the absence of the boundary layer. The initial thickness and subsequent development of the subsonic layer depends critically on the incoming boundary layer velocity distribution. In a turbulent boundary layer, a greater momentum transfer typically occurs between adjacent layers of fluid normal to the wall than in a laminar boundary layer. This generally results in a smaller subsonic channel and a shorter upstream influence effect. In addition, a turbulent boundary layer typically has a lower velocity deficit compared to a laminar boundary layer, and hence a greater resistance to the retardation.

**Region II:** In response to the increasing pressure, the streamline directions within the subsonic layer begin to diverge, and the layer increases in thickness. The neighbouring streamlines in the supersonic flow are also turned away from the wall, leading to the very first compression waves, which emanate from the sonic line. Because in turbulent boundary layers the subsonic layer is relatively thin with respect to the boundary layer thickness, the compression waves almost coalesce as the outgoing reflected shock wave before they reach the edge of the boundary layer. As the incident shock wave penetrates through the boundary layer, it experiences a progressive decrease in local Mach number. The incident shock wave therefore begins to curve, becoming vanishingly weak when it reaches the sonic line. In addition, as it passes through the boundary layer, it also encounters the compression waves generated by the dilatation of the subsonic layer. This serves to weaken the incident shock wave, making it spread out into compression waves. On reaching the sonic line, these compression waves are reflected as a series of expansion waves. The refraction of these waves and of the reflected shock wave, as they both propagate through the boundary layer, is replaced by a continuous process (D elery & Bur 2000).

**Region III:** In this region, the boundary layer undergoes a recovery process. The subsonic portion of the boundary layer now begins to contract, and the inner part of the boundary layer accelerates. Generally, the entire interaction region is of the order of a few boundary layer thicknesses, and the important flow phenomena remain embedded within the boundary layer. The general flow pattern does not therefore differ significantly from the inviscid solution (D elery & Bur 2000).

### 1.4.2 Separated Case

In this case, the pressure gradient imposed by the incident shock wave is now sufficient to cause mean boundary layer separation. The resulting flow-field is more complicated than its unseparated counterpart, and is shown in figure 1.9, based on the schematic from D elery & Bur (2000). We again arbitrarily subdivide the interaction into the following regions:

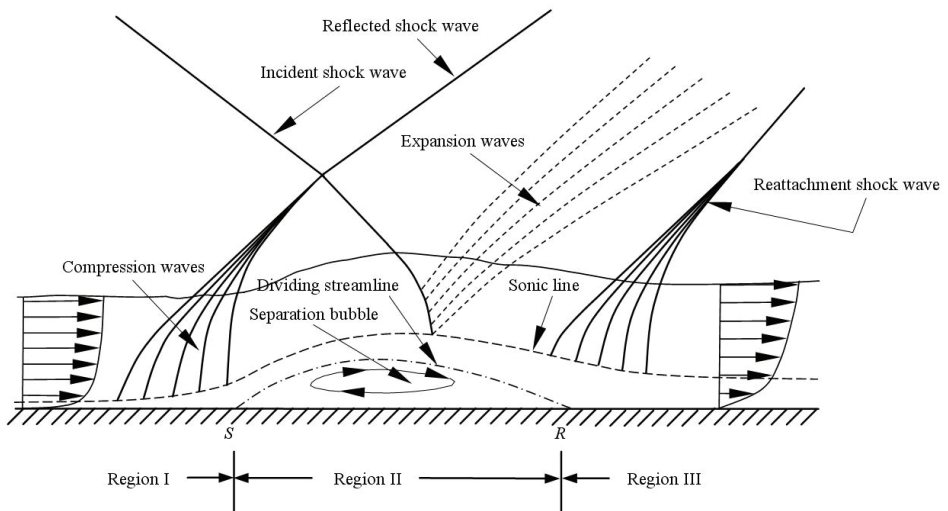


FIGURE 1.9: Schematic of the separated incident SWTBLI. Based on the schematic from D elery & Bur (2000).

**Region I:** In this region, the incoming boundary layer again encounters the interaction. The pressure gradient is now sufficient to cause the low-momentum fluid near to the wall to return upstream, and the boundary layer separates from the surface. Since the static pressure is initially transmitted essentially without change wall-normal through the boundary layer, the separation process can be initially considered a *free interaction process*, resulting from a local self-induced interaction between the boundary layer and outer inviscid flow. That is, the pressure rise to separation is generally regarded as being independent of the downstream flow geometry. In addition, the compression waves that coalesce to form the reflected shock wave generally leave the boundary layer farther upstream than in the unseparated case. This creates an additional flow phenomenon not generally observed in the unseparated case; namely, that the reflected shock wave intersects with the incident shock wave outside of the boundary layer, leading to the formation of a slip-line (not shown in the schematic). The incident shock wave is refracted and continues towards the wall, where it penetrates into the separated shear layer.

**Region II:** Fluid begins to be redirected upstream, as part of the separation process. The point where the skin friction coefficient becomes zero is classically defined as the separation point  $S$ , although this can only be interpreted as such under steady and two-dimensional flow conditions (see Simpson 1989 for a further discussion). The boundary layer detaches to form a separated shear layer. Downstream of this point, there exists a bubble of recirculating fluid, bounded by the wall and a dividing streamline. This dividing streamline emanates from  $S$  and terminates at the reattachment point  $R$ . Once separated, the shear layer encounters the incident shock wave. This shock wave begins to curve as it enters the shear layer in response to the decreasing Mach number, and reflects from the sonic line as an expansion wave. Unlike in the unseparated flow case, however, the subtle spreading of the incident shock wave into compression waves is not generally observed, since the incident shock wave does not encounter the compression waves generated by the dilatation of the subsonic layer. The separated shear layer passes through the expansion fan and is turned back towards the wall where it reattaches.

The extent of the separated flow region depends critically on the ability of the shear layer to overcome the adverse pressure gradient at reattachment. Generally speaking, the pressure rise across the interaction is divided between the pressure rise at separation and the pressure rise at reattachment (Délery & Bur 2000). Between the separated shear layer and reversed-flow region a mixing occurs, with a transfer between the outer higher-momentum fluid and inner reversed-flow region. As a result, the local velocity along the dividing streamline increases with streamwise development. This fluid eventually gains enough momentum to overcome the pressure gradient and reattach to the surface.

It is generally accepted that the pressure rise at separation does not depend on the downstream conditions (see Chapman *et al.* 1957). Therefore, a greater pressure rise imparted to the boundary layer, as a result of an increase in incident shock wave strength, would necessarily lead to a greater pressure rise at reattachment. The velocity required by fluid particles along the dividing streamline in order to reattach therefore increases, and this necessitates a longer distance for the sufficient mixing with the higher momentum shear layer to take place. This explains why an increase in incident shock wave strength leads to a longer separated flow region (Délery & Bur 2000).

**Region III:** At reattachment, the separation bubble vanishes. The necessary turning of the flow back parallel to the wall is accompanied by a series of recompression waves, which coalesce to form a reattachment shock wave in the free-stream flow. The flow has now passed through a series of complicated flow patterns both inside and outside of the boundary layer, and undergoes a recovery process farther downstream. However, unlike in the unseparated case, the flow phenomena discussed above are generally no longer confined to within the boundary layer, and the interaction no longer resembles the inviscid solution. The effect of the interaction on the recovering boundary layer is therefore more pronounced, and the mean properties of the boundary layer may take  $O(10)$  undisturbed boundary layer thicknesses to fully recover (see e.g., Wu & Martin 2007).

Finally, it should be noted that the Reynolds number is an important parameter to consider when discussing unseparated and separated SWTBLIs. One of the key results to arise from free interaction theory was that an *increase* in pressure rise and interaction extent should occur with *increasing* Reynolds number. This result had been well-verified for laminar flows, but it was in contradiction with observations in high Reynolds number turbulent flows, where it was found that the opposite trend occurred (see e.g., Délerly 1985). This subject was the source of much controversy in the 1970s and prompted major research efforts to resolve this issue.

As reported by Délerly (1985), the answer lay in the competition between viscous and pressure forces within the boundary layer. Viscous forces tend to keep the boundary layer from separating, by transferring momentum to the lower part of the boundary layer at the expense of the outer higher momentum fluid. In contrast, pressure forces decelerate the fluid until flow separation occurs. The separation characteristics are intrinsically associated with the shear stress behaviour close to the wall. Specifically, any action that increases the skin friction coefficient  $C_f$  generally increases the resistance of the boundary layer to an adverse pressure gradient. An increase in  $C_f$  can be readily accomplished by lowering the Reynolds number. Therefore, a laminar boundary layer becomes more difficult to separate as the Reynolds number decreases. However, the shape parameter  $H$ , used to characterize the fullness of the boundary layer profile, does not vary independently with  $C_f$  as the Reynolds number changes, and it happens that in turbulent flows the filling of the boundary layer profile tends to outweigh the decrease in  $C_f$  with increasing Reynolds number.

As a result of these competing influences, the extent of the interaction domain therefore *increases* with *increasing* Reynolds number for low to moderate Reynolds number interactions ( $Re_\delta < 10^5$ , where  $\delta$  is the undisturbed boundary layer thickness and other parameters are based on the free-stream conditions), whereas the interaction domain *decreases* with *increasing* Reynolds number at high Reynolds number interactions ( $Re_\delta > 10^5$ ). Since free interaction theory favours the viscous forces, it was more suited to low Reynolds number flows and did not appreciate this trend reversal at higher Reynolds numbers.



This is important in the present interaction, where it will be shown that there is little or no separated flow on average, given the relatively high Reynolds number of the present experiments ( $Re_\delta \sim 7 \times 10^5$ ). The reader may compare this with other incident interactions at significantly lower Reynolds numbers (see e.g., Dupont *et al.* 2006, where  $Re_\delta \sim 6 \times 10^4$ ) where flow separation *is* observed on the mean.

## 1.5 SWTBLI Unsteadiness

While the above time-averaged descriptions are quite clear, in reality SWTBLIs are inherently unsteady phenomena, and the resulting picture is considerably more complex and less well-understood. Yet the extant literature on SWTBLI unsteadiness is too large and diverse to be surveyed meaningfully within the confines of this book, and so we instead take a stroll through some of the major contributions in the field, within the context of a brief historical sketch, without pretending to be exhaustive.

It had already been known since the 1950s that shock-induced turbulent boundary layer separation was an inherently unsteady phenomenon, where shock wave unsteadiness was noted in early flow visualizations (e.g., Chapman *et al.* 1957). Yet at the time, the only practical experimental techniques widely available to investigators were typically short-exposure Schlieren or shadow photography, in combination with some limited high-speed cinematography capability. Without quantitative information, a further assessment of the unsteadiness could not be made.

With the proliferation of fluctuating surface pressure measurements in the mid-60s, that could be used in conjunction with fast-response pitot-probes and hot-wire anemometry (HWA), a quantitative description of the unsteadiness became possible (see Dolling 2001). Perhaps the first study of the problem was by Kistler (1964), who observed an intermittent pressure signal when measuring the wall-pressure fluctuations ahead of a forward-facing step. It was found that this was due to the turbulent fluctuations within the incoming boundary layer and separated flow, which were being modulated by the large pressure jumps associated with the motion of the separation shock wave. Similar observations would later be made in a variety of other SWTBLIs experiments.

Figure 1.10 shows for example, a sample time history of the separation shock wave motion in a compression ramp interaction, inferred from Dolling (1993), as reported by Beresh *et al.* (1997). It can be seen that the inferred shock wave motion consists of both small-scale and large-scale components. Such an observation has been made in both two- and three-dimensional interactions, and major research efforts to try and better understand the physical mechanism(s) responsible for this behaviour have been undertaken. The interested reader is referred to Dolling (2001) and Smits & Dussauge (2006) and the references cited therein for a further discussion.

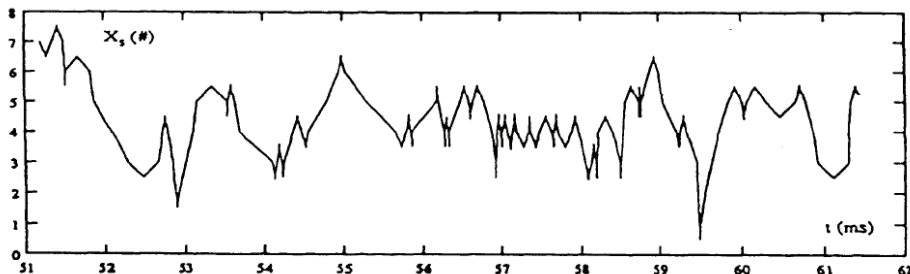


FIGURE 1.10: Sample time history of the streamwise position of the separation shock wave in a  $28^\circ$  compression ramp interaction at Mach 5. Vertical axis represents the streamwise positions of the pressure transducers in the shock foot region. From Dolling (1993), as reported by Beresh *et al.* (1997).

With the advent of laser Doppler velocimetry (LDV) in the 1970s, it became possible to obtain flow properties nonintrusively and at a high spatial resolution. As a result, LDV demonstrated to be one of the most suitable flow diagnostic techniques to describe turbulence properties (see Scarano 2006), and was used extensively to characterize the turbulence within SWTBLIs. For example, two-colour laser velocimetry was applied to various interactions in a transonic channel by Déleroy (1983). The importance of turbulence anisotropy was demonstrated, which led to important statements being made regarding the suitability of computational models (in particular, Reynolds-averaged Navier-Stokes (RANS) computations), to solve this type of flow problem.

Ardonceanu (1983) used LDV with HWA to investigate a compression ramp interaction, and deduced qualitative aspects of the turbulence using spectral analysis and short-time exposure Schlieren photography. He found that a large amount of turbulence energy was contained in large-scale structures, which persisted downstream of the interaction. Kuntz *et al.* (1987) considered a series of interactions using LDV, and made two-component coincident velocity measurements to investigate turbulent boundary layer properties downstream of the interaction. They found that the velocity profiles were wake-like in nature, and were beginning to return to equilibrium conditions. Significant increases in Reynolds stresses were observed, and indications of the presence of large-scale turbulent structures were found in the redeveloping boundary layer. Shortly afterwards, Selig *et al.* (1989) investigated the turbulence structure, and showed that the maximum mass-flux intensity was amplified through the interaction, with probability density functions (PDFs) showing a bimodal distribution downstream of the interaction, which they attributed to the presence of large-scale motions associated with the instability of the inflectional velocity profiles.

Yet while LDV was instrumental in providing detailed information on the statistical nature of turbulence, it suffered from shortcomings that restricted its use. For example, as a point-wise measurement technique, it was incapable of making large-scale instantaneous quantitative measurements. This was especially problematic by the mid-80s and early 1990s, because there was a growing interest in the role of large-scale structures in the mixing processes of SWTBLIs (see e.g., Smits & Dussauge 2006). Hence there was a need for the visualization of such large-scale turbulent structures; a role in which planar visualization techniques excel.

For example, Beresh *et al.* (1997) used double-pulsed planar laser scattering (PLS)<sup>†</sup> imaging in a Mach 5 compression ramp interaction, and acquired image pairs that showed the evolution of large-scale boundary layer structures, as they passed through the shock wave. Such an image is shown in figure 1.11, from N. T. Clemens and D. S.

---

<sup>†</sup> It should be noted that planar laser scattering, also known as light-screen, light-sheet, or vapour-screen imagining, originated much earlier than is perhaps suggested here, in the early 1960s (see Settles 1993).

Dolling, as reported by Andreopoulos *et al.* (2000). The image clearly shows an intermittent incoming turbulent boundary layer, which interacts with the separation wave, leading to a significant distortion of the latter.

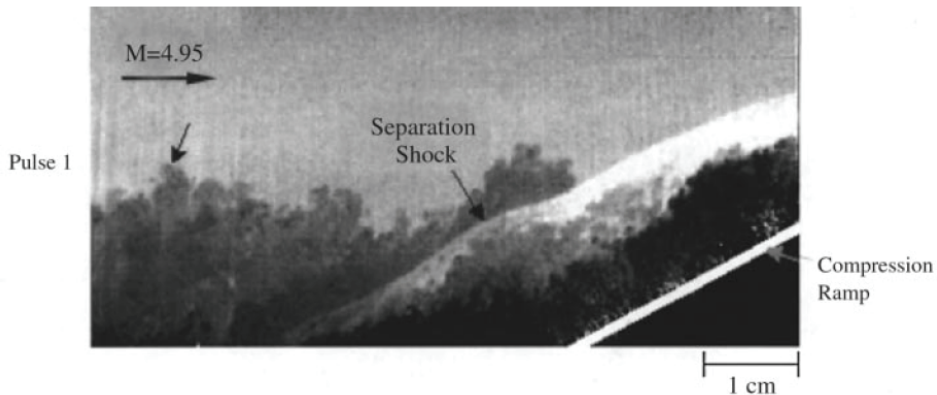


FIGURE 1.11: A single-pulse planar laser scattering image of a hypersonic compression ramp interaction using a condensed alcohol fog. From N. T. Clemens and D. S. Dolling, as reported by Andreopoulos *et al.* (2000). In this image the free-stream appears *grey* and the boundary layer appears *dark grey*. The flow direction is from left to right. Observe the intermittent nature of the incoming turbulent boundary layer edge and the distortion of the separation shock wave.

Smith & Smits (1995) have also conducted a particularly edifying study using Schlieren and Rayleigh scattering to visualize the outer layer structure of supersonic boundary layers. They characterized the outer layer as consisting of an array of regularly-spaced uniform low-density bulges, separated from a uniform higher-density free-stream by a sharp, instantaneously ragged interface, reminiscent of the classical work decades earlier by Kovasznay *et al.* (1970), who had investigated incompressible outer layer boundary layer structure. Although such planar techniques were successful in the visualization of turbulent structures, many of the flow features were felt to be still lacking due to the inability of these techniques to make direct instantaneous velocity/vorticity flow-field measurements. A need remained for techniques that permitted multipoint or whole-field quantitative flow measurements to be made.

With developments in nonintrusive, laser-based illumination systems, in combination with digital imaging technology in the past few decades, much attention has become focused on flow diagnostic techniques that can make quantitative large-scale instantaneous measurements, such as particle image velocimetry (PIV) in particular (see e.g., Adrian 1991; Raffel *et al.* 2007). Together with the ability to acquire and process large amounts of data, this technique offers the opportunity to quantitatively investigate the unsteady flow phenomena associated with SWTBLIs (Dolling 2001). Although the initial applications of PIV have been primarily in low-speed incompressible flows, it has been gaining confidence as a robust time-effective flow diagnostic tool in high-speed flows for several years now (see Scarano 2006). As a result, PIV has been successfully applied to the SWTBLI problem.

For example, Hou *et al.* (2003) have employed PIV at Mach 2 to investigate shock system unsteadiness in compression corner flows. The global structure of the interaction regime was characterized, where it was found based on ensemble-averages, that the scale of the separated region, velocity fluctuations, and domain of the perturbed flow, were all influenced significantly by the position of the shock foot. Beresh *et al.* (1997) carried out time-sequenced PLS simultaneously with PIV, as well as surface pressure measurements to determine the shock foot position, and made statements regarding the underlying cause(s) of the large-scale unsteadiness, as will be discussed later on. Dupont *et al.* (2008) have recently used PIV to investigate the length-scales of the turbulent structures in an incident SWTBLI at Mach 2.23, and a processing of the velocity vector fields enabled a characterization of the mixing layer of separation.

Recently, PIV studies have also focused on SWTBLI control. For example, Bueno (2006) conducted a wide-field PIV study at Mach 2 to investigate the influence of a pulsed-jet on a compression ramp interaction. These novel experiments were conducted to explore the possibilities of controlling the shock wave unsteadiness. It was found that the pulsed-jet had a significant effect on the interaction structure and it was speculated that the injectors used were acting as vortex generators, which were inhibiting boundary layer separation.

Yet to date, most of the quantitative experimental studies on SWTBLIs have relied on single-point measurement techniques, such as HWA and LDV, or planar techniques, such as planar PIV (Dolling 2001). The inability to make instantaneous volumetric measurements often leads to ambiguities in the interpretation of the data, which necessitates various assumptions being made to link these reduced-dimensional representations to the three-dimensional structure of the SWTBLI flow organization.

On the other hand, the spectacular progress made in numerical methods and computer technology in the last few decades has meant that CFD, utilizing large-eddy simulations (LES) and direct numerical simulation (DNS) in particular, has elucidated many of the three-dimensional features of wall-bounded turbulence (see e.g., Zhou *et al.* 1999; Jeong *et al.* 1997; Ringuette *et al.* 2008), and have shown that the SWTBLI problem can be successfully treated by numerical simulations in rather spectacular detail (see e.g., Pirozzoli & Grasso 2006 see also figure 1.12; Wu & Martin 2007; Wu & Martin 2008; Touber & Sandham 2008).

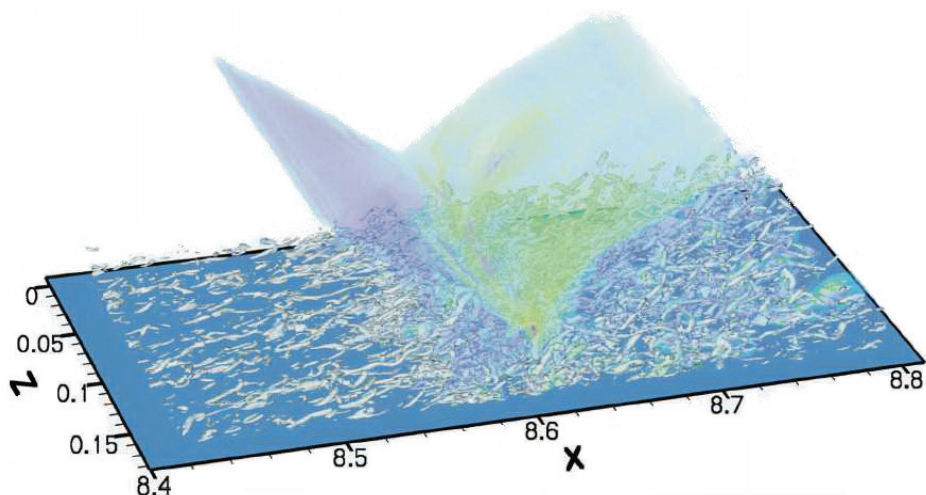


FIGURE 1.12: Rendering of the instantaneous three-dimensional structure of an incident SWTBLI by DNS at Mach 2.25 and  $Re_\theta=3725$ . Vortical structures are visualized in *grey* and coloured isosurfaces represent pressure gradient modulus. From Pirozzoli & Grasso (2006).

It has become clear, however, at least for DNS, that a direct quantitative comparison with high Reynolds number experiments is not possible in the foreseeable future, due to the significant Reynolds number limitation, as well as the limited size of the computational domain. As noted by Wu & Martin (2008), this is particularly important in the study of SWTBLIs, since the Reynolds number influences the size of the interaction, as well as the shock waves within the boundary layer due to the location of the sonic line. This Reynolds number limitation therefore leaves the three-dimensional instantaneous SWTBLI phenomenology at high Reynolds numbers very much an open question.

Experimentalists have therefore long been motivated, in the quantitative visualization of turbulent fluid flows, to move towards volumetric methods. Current techniques based on the PIV method include the scanning light sheet method (Brucker 1996), holographic PIV (Hinsch 2002), and defocusing digital PIV (Pereira & Gharib 2002). Yet drawbacks of these techniques include the requirement of the scanning rate to be greater than the flow time-scales of interest, complicated optical arrangements, as well as a limited seeding particle concentration, respectively.

One of the most recent volumetric extensions of the PIV technique, which arguably minimizes these limitations, as well as being suitable for application to high-speed flows, is tomographic PIV (Elsinga *et al.* 2006). This technique determines the particle velocity field within a three-dimensional measurement volume based on the simultaneous view of illuminated particles by digital cameras placed along several different viewing directions.

While the initial applications of tomographic PIV have been performed in low-speed, low Reynolds number flows (see Schröder *et al.* 2007; Elsinga *et al.* 2007b), its extension to the supersonic flow regime has been recently achieved by Humble *et al.* (2007a) and Elsinga *et al.* (2007). Figure 1.13 shows for example, a recent result within a Mach 2 boundary layer from Elsinga (2008). The instantaneous three-dimensional vortex distribution is visualized in green, along with meandering zones of relatively low-speed fluid in dark blue. The application of tomographic PIV to the SWTBLI problem is therefore considered to be well-posed.

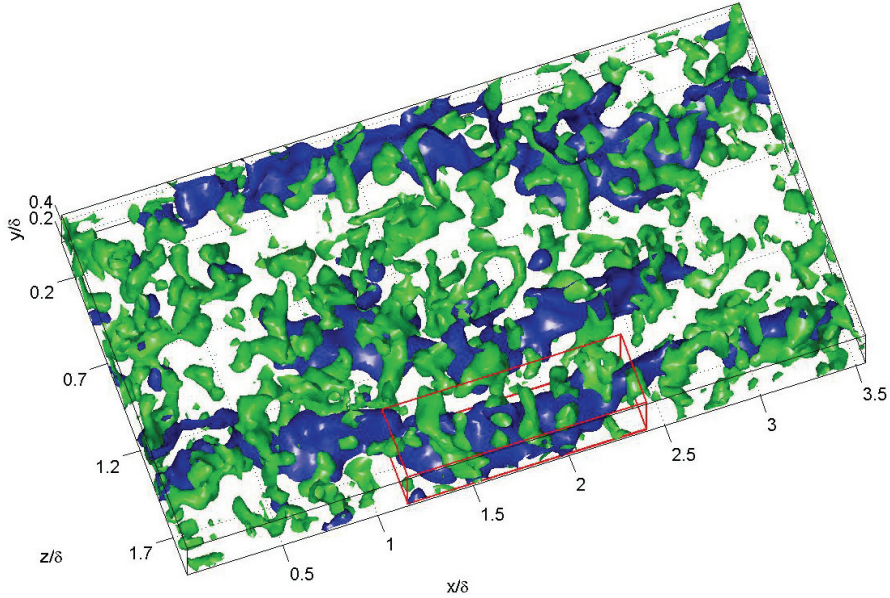


FIGURE 1.13: Instantaneous three-dimensional vortex distribution within a supersonic turbulent boundary layer at Mach 2 using the  $Q$ -criterion (green) and relatively low-speed zones ( $u/U_\infty < 0.89$ , shown in blue) for  $0.34 < y/\delta < 0.67$ . Flow is from left to right. Observe the elongated meandering zones of relatively low-speed fluid (in blue), characteristic of turbulent boundary layers. From Elsinga (2008).

## 1.6 Cause(s) of SWTBLI Unsteadiness

One of the most surprising aspects to arise from the investigations of SWTBLI unsteadiness is the apparent discrepancy between the characteristic frequencies within the incoming turbulent boundary layer and those across the shock wave system and separated flow region, whose dominant frequencies have been observed to be orders of magnitude lower. As noted by Wu & Martin (2008) for instance, numerous experiments have reported that the time-scale of the low-frequency shock wave motion is of the order  $10\delta/U_\infty$ – $100\delta/U_\infty$  (see e.g., Dolling 2001; Dussauge *et al.* 2006 and the references cited therein), in contrast to the characteristic time-scale of the eddies within the incoming boundary layer being  $\delta/U_\infty$ , where  $\delta$  is the boundary layer thickness and  $U_\infty$  is the free-stream velocity.



This discrepancy is exemplified in figure 1.14, which shows the mean and root-mean-square (RMS) pressure distributions (left) and power spectral density (PSD) distributions (right), in a  $28^\circ$  compression ramp interaction at Mach 5, from Erengil & Dolling (1991), as reported by Hou (2003). Subscripts  $w$  and  $w_0$  refer to wall and undisturbed wall conditions, respectively, and  $inv$  refers to the inviscid limit.  $UI$  refers to the upstream influence line, where the mean static pressure first begins to rise.  $S$  and  $R$  refer to mean separation and reattachment locations, respectively. Observe the local peak in the RMS pressure upstream of  $S$ , followed by a rapid decrease and then increase farther downstream. The PSD distributions within the region of shock motion (at locations 2 and 3) show two peaks: a relatively high-frequency peak (20–40 kHz) due to the boundary layer turbulence, and a relatively low-frequency peak (0.3–1 kHz) due to the shock foot motion.

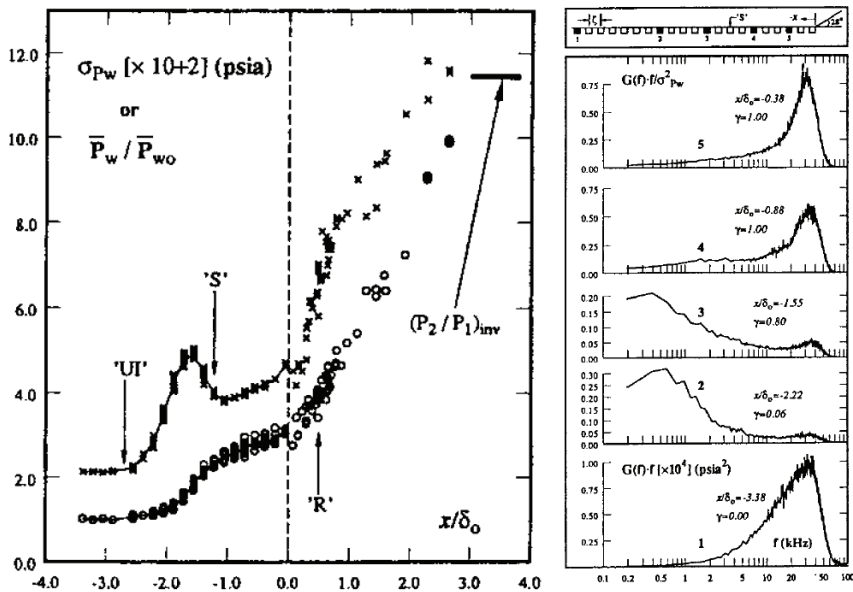


FIGURE 1.14: Fluctuating pressure data of a  $28^\circ$  compression ramp interaction at Mach 5 using flush-mounted pressure transducers. Mean and RMS pressure distributions (left), and PSDs measured at several locations (right). Subscripts  $w$  and  $w_0$  refer to wall and undisturbed wall conditions, respectively, and  $inv$  refers to the inviscid limit.  $S$  and  $R$  refer to mean separation and reattachment locations, respectively. From Erengil & Dolling (1991), as reported by Hou (2003).

A better understanding of the low-frequency unsteadiness is important to mitigate the premature structural fatigue caused by the intense fluctuating wall-pressures and heat transfer that occupy shock oscillation (Dolling 2001), as well as the recognized deficiencies of some of the most promising turbulence closure models, which seem to indicate the necessity of incorporating large-scale unsteady effects in order to accurately predict mean flow quantities (see Knight & Degrez 1998). This importance has prompted major research efforts to try and determine the precise cause(s) of this unsteadiness, yet explanations have diverged to include a number of debated and sometimes contradictory conclusions.

For example, Plotkin (1975) developed a mathematical model based on the perturbation of a shock by random fluctuations within the incoming boundary layer that was able to represent the manner in which broad-band perturbations lead to low-frequency motion of the separation bubble and shock system. This model was later substantiated by the experimental work of Poggie & Smits (2001), who used it in their investigation of the origins of shock unsteadiness in a reattaching shear layer. In an influential paper, Andreopoulos & Muck (1987) suggested that the frequency of the shock wave system unsteadiness scaled on the bursting frequency of the incoming boundary layer, concluding that the turbulence of the incoming boundary layer was largely responsible for the shock wave motion.

Such fluctuations within the incoming boundary layer were further investigated by Erenkil & Dolling (1991), who developed conditional sampling algorithms for wall-pressure measurements to determine correlations between the pressure fluctuations within the incoming boundary layer and shock wave motion (see also Hou 2003). They found that there was a distinct correlation between pressure fluctuations within the incoming boundary layer and changes in the direction of the separation shock wave. They concluded that the high-frequency jitter component of the shock wave motion was due to the turbulence structures that were convected into the interaction. Interestingly, only weak evidence of a correlation for the large-scale shock wave motion was observed, and the authors speculated that such motion could be associated with a mechanism within the incoming boundary layer with a much larger length-scale.

This work was elaborated on by Erengil & Dolling (1993), who used fast-response wall-pressure measurements to study Mach 5 compression ramp and blunt-fin interactions. Strong correlations were found between the shock foot velocity and instantaneous pressure ratio across the shock wave, as shown in figure 1.15, from Erengil & Dolling (1993). Observe in this figure the negative time-delays, suggesting that the shock velocity is preceded by the pressure ratio. As noted by Hou (2003), this provides evidence of a cause-and-effect relationship between wall-pressure fluctuations and the separation shock wave unsteadiness.

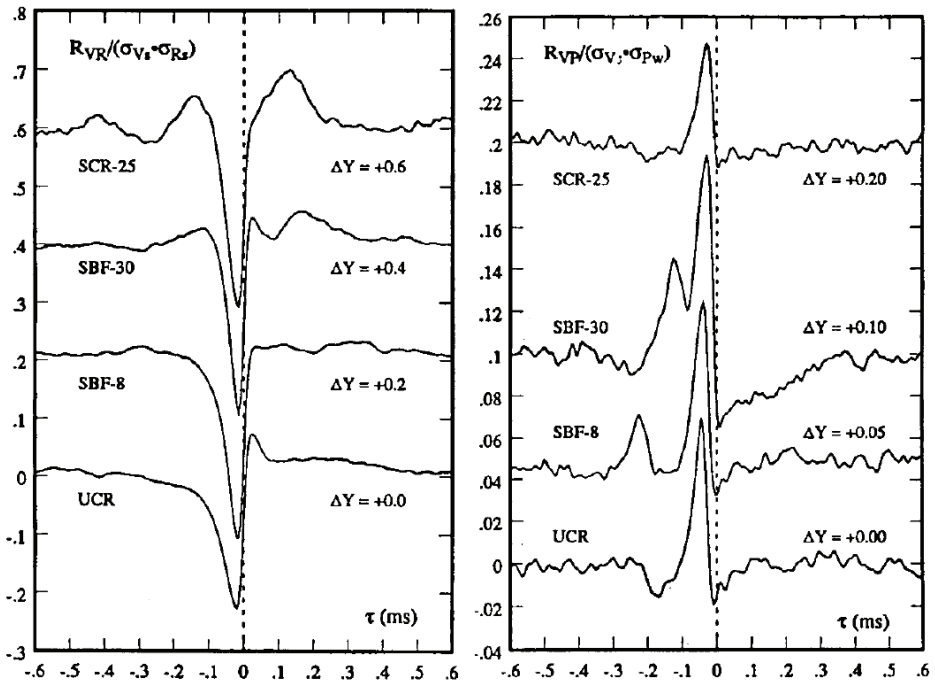


FIGURE 1.15: Distribution of normalized cross-correlation coefficient  $R_{VR}$  between the shock velocity  $V_s(t)$  and pressure ratio  $R_s(t)$  (left), and cross-correlation coefficient  $R_{VP}$  between shock velocity  $V_s(t)$  and upstream pressure ratio  $p_w(t)$  (right). Results are shown for  $28^\circ$  unswept ramp (UCR),  $28^\circ$  ramp with  $25^\circ$  sweep (SCR-25); blunt-fin with  $30^\circ$  sweep (SBF-30); and blunt-fin with  $8^\circ$  sweep (SBF-8). From Erengil & Dolling (1993).

As a result, Erengil & Dolling (1993) concluded that the small-scale motion of the shock wave was caused by its response to the convection of turbulent fluctuations through the interaction. Furthermore, they proposed that the large-scale motion was the result of an expansion and contraction of the separation bubble. A simple physical model was developed, whereby the expansion and contraction of the separated flow region displaces the separation shock upstream and downstream, respectively, whereas the small-scale motion is due to the turbulent fluctuations.

This physical model was consistent with the observation of a small-scale motion superimposed on a large-scale motion (c.f. figure 1.10), but raised important questions as to why the separation bubble underwent such a motion. This was addressed by McClure (1992), who carried out further investigations, and made the interesting observation that mean pitot pressure measurements made at a given height within the upstream boundary layer were lower for upstream shock wave locations than for downstream locations. This suggested that the boundary layer thickness was perhaps associated with the large-scale shock wave motion, and prompted further investigations to resolve the issue.

Beresh *et al.* (1997) elaborated on this work, by carrying out time-sequenced PLS simultaneously with PIV and surface pressure measurements. The PLS images were obtained upstream within the incoming boundary layer simultaneously with the surface pressure measurements to determine the shock foot position. The results suggested that there was no significant relationship between the incoming boundary layer thickness and the shock foot position.

The PIV results, however, were more revealing. Conditionally-averaged velocity fields based on the shock foot location, providing mean velocity profiles through the boundary layer, showed that while there was no significant difference in shock wave location with incoming boundary layer thickness, there was a noticeable difference in the incoming velocity profile with shock wave location. One particularly edifying numerical study conducted a few years earlier by Hunt & Nixon (1995) using LES had shown an approximate one-to-one relationship between shock velocity and fluctuations within the boundary layer. While the experimental results were insightful, however, no such numerical trend was found.

Perhaps the most compelling study in this respect is by Beresh *et al.* (2002). Improving on their previous experimental dataset, it was shown that positive streamwise velocity fluctuations corresponded to a downstream shock position, whereas negative velocity fluctuations corresponded to an upstream shock position. Changes in velocity fluctuations lead to changes in the fullness of the velocity profile, and this led to the construction of a simple inferred model, whereby a fuller velocity profile entering the interaction provides an increased resistance to flow separation and hence a downstream displacement of the shock wave, and vice versa. This model is schematically illustrated in figure 1.16, from Beresh *et al.* (2002).

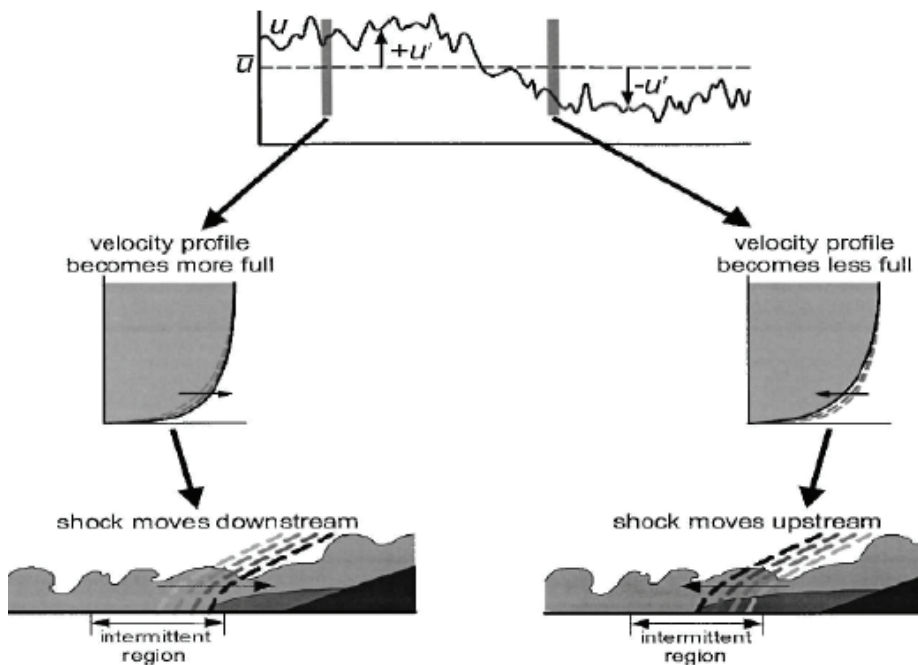


FIGURE 1.16: Conceptual model of the effect of the incoming boundary layer profile on the shock foot motion. A fuller velocity profile entering the interaction provides an increased resistance to flow separation and hence a downstream displacement of the shock wave, and vice versa. From Beresh *et al.* (2002).

The preponderance of large-scale motions within turbulent flows (see e.g., Cantwell 1981; Robinson 1991; Adrian *et al.* 2000), has also motivated workers to investigate these motions within the context of SWTBLI large-scale unsteadiness. For instance, Ganapathisubramani *et al.* (2007) have applied PIV in the streamwise–spanwise plane of their compression ramp interaction, and observed alternating large-scale regions of low- and high-speed fluid within the logarithmic region of the incoming boundary layer. They have proposed that these regions are associated with the low-frequency motion of the separated flow region and shock wave, as will be discussed in further detail later on. Such features have also been observed experimentally in supersonic boundary layers by Samimy *et al.* (1994), Ganapathisubramani *et al.* (2006), Elsinga *et al.* (2007), as well as computationally using DNS by Ringuette *et al.* (2008).

At this point, it is important to emphasize that most of the work cited above has been carried out on compression ramp interactions, and generalizations of these models to the incident SWTBLI is still an open question (Dupont *et al.* 2006). Although less well-documented compared with the compression ramp interaction, similar behaviour has been found in the shock reflection case, such as the low-frequency motion of the reflected shock wave when boundary layer separation is involved.

For example, Pirozzoli & Grasso (2006) carried out a DNS at Mach 2.25 and characterized the mean and fluctuating properties, as well as the three-dimensional instantaneous flow organization. They proposed that the large-scale unsteadiness in their shock reflection interaction is associated with an acoustic feedback mechanism; similar to what is involved in the generation of tones in cavities and screeching jets. Coherent structures were shown to interact with the incident shock wave leading to the production of acoustic waves that propagate upstream, inducing an oscillatory motion of the separation bubble and subsequent flapping motion of the reflected shock wave. This has since been substantiated by the recent LES work of Toubert & Sandham (2008).

In comparison, Dussauge *et al.* (2006) have recently reviewed and analyzed evidence of the large-scale unsteadiness observed in incident SWTBLIs, and concluded from the experimental results that the three-dimensional structure of the separated bubble may be at the

origin of such unsteadiness. In particular, Dupont *et al.* (2006) obtained characteristic time- and length-scales in their incident SWTBLI, and found strong statistical evidence of a link between low-frequency shock movements and the downstream interaction.

Finally, it is also worth mentioning that given the absence of a clear correlation between the large-scale low-frequency motion and either the upstream or downstream flow structure, speculation has also arisen that the shock motion may be driven, at least in part, by some type of facility-dependent forcing mechanism (see Dolling 2001). In response to this, Weiss & Chokani (2007) conducted the first experimental investigation of a SWTBLI in a quiet wind-tunnel (i.e., a lower free-stream turbulence level, obtained using bleed-valves upstream of the wind-tunnel throat) to determine whether or not the unsteady characteristics of the separation shock wave in a compression ramp interaction were influenced by the level of free-stream noise. In short, they found that there was no difference in the power spectra between the conventional and quiet operating configurations (the latter having an acoustic energy in free-stream disturbances that is half the former in the dominant frequency band), and they concluded that the unsteady characteristics of the separation shock wave are not affected by free-stream noise.

Thus, to date it has been difficult to unambiguously associate the large-scale unsteadiness of the shock system with another length-scale or turbulent mechanism. It would appear that a mechanism with a length-scale much larger than the incoming boundary layer thickness would be required in order to reconcile the large-scale unsteadiness. Yet no comprehensive framework has so far been formulated in which all the results to date can be satisfactorily explained, and the failure of the SWTBLI community to gain a general consensus has only reinforced the status of the interaction as an enigma.

## 1.7 Thesis Aim and Objectives

The aim of this thesis is to experimentally investigate the interaction between an incident shock wave and a turbulent boundary layer in order to gain a better understanding of its physical nature, in particular, its unsteady flow organization. To this end, a series of objectives can be set out with varying degrees of ambition and confidence:

At a low level of ambition, but with a high degree of confidence, the first objective is to outline the mean and statistical properties of the interaction. This will be in terms of its surface flow pattern, mean velocity pattern, and its turbulence properties.

At a higher level of ambition, but with perhaps a lower degree of confidence, it hopes to better explicate the unsteady two- and three-dimensional organization of the interaction, and to establish the role of the incoming boundary layer, separated flow region, and reflected shock wave, as constituent elements in the large-scale unsteadiness.

The next objective is to distil from the experimental evidence a reduced-order description of the unsteadiness. This can be accomplished by applying the proper orthogonal decomposition (POD) to both the planar and tomographic PIV data, to obtain global eigenmodes that can be used to further characterize the unsteady flow organization. HWA in combination with nonlinear time series analyses can be used in order to make statements regarding the temporal organization of the interaction.

The final objective is to consolidate the major observations of the research and formulate a physical model summarizing the interaction's unsteady flow organization.



## 1.8 Thesis Outline

Chapter 2 outlines the fundamental concepts that will be used. An outline of the working terminology and definitions is first given. The relevant flow equations are then described, followed by the basic properties of the compressible turbulent boundary layer.

Chapter 3 is devoted to a description of the measurement techniques and experimental arrangements. The flow facility is first described. This is followed by an outline of HWA, the working principles and methodology of planar and tomographic PIV, as well as their respective experimental arrangements. An uncertainty analysis of the measured properties is then presented.

Chapter 4 gives an outline of the data analysis methods used, which consists of the POD and nonlinear time series analyses. Their description, application, and relevance to the present work are provided.

Chapter 5 establishes the boundary conditions of the experiment by describing the undisturbed boundary layer in detail, characterized in terms of its mean, turbulence, and spatiotemporal properties.

Chapter 6 presents a description of the two-dimensional flow organization of the interaction. The mean flow properties are first described, followed by the instantaneous velocity/vorticity organization. Statistical flow properties are then presented, followed by the POD analysis.

Chapter 7 presents the three-dimensional flow organization of the interaction. Cross-sectional results in the wall-parallel plane are first presented, followed by the volumetric representations showing the three-dimensional instantaneous velocity/vorticity organization. Statistical flow properties are then presented, followed by the POD analysis.

Chapter 8 complements the study with a temporal characterization of the interaction using HWA. A dynamical systems approach is taken using nonlinear time series analyses.

Chapter 9 consolidates the major observations made in the thesis and formulates a physical model of the interaction's unsteady flow organization.

Finally, chapter 10 presents the major conclusions drawn and an outlook toward future work is given.



# CHAPTER 2 FUNDAMENTAL CONCEPTS

---

## 2.1 Introductory Remarks

**B**EFORE embarking on a detailed description of the work carried out, it is instructive to first outline some terminology, working definitions, relevant flow equations, and other fundamental concepts, because they will be essential to the interpretation and judgment of the results later on. We first begin by defining the terminology that will be used. An outline of the relevant flow equations then follows, to provide the context for some of their simplifications and analysis later on. A description of the basic properties of the compressible turbulent boundary layer is then given.

## 2.2 Terminology

All names and symbols mentioned herein refer to a Cartesian coordinate system. In the planar PIV study, the streamwise (longitudinal) and wall-normal (vertical) directions are denoted by the spatial coordinates  $x$  and  $y$ , respectively, and correspond to the instantaneous local velocities  $u$  and  $v$ , respectively. In the tomographic PIV study, the streamwise, spanwise, and wall-normal, directions are denoted by the spatial coordinates  $x$ ,  $y$ ,  $z$ , respectively. The wall is therefore in the  $x$ - $y$  plane. These spatial coordinates correspond to the instantaneous local velocities  $u$ ,  $v$ ,  $w$ , respectively.

All dimensions are presented in outer-scaling, since this is the most appropriate scaling for the region of the interaction considered. That is, the spatial coordinates are normalized by the undisturbed boundary layer thickness  $\delta$ , which corresponds to the wall-normal location where  $0.99U_\infty$ , where  $U_\infty$  is the free-stream, or undisturbed velocity. Variables will, however, be quoted in inner variables when it is considered appropriate. These inner, wall, or ‘plus’ units  $x^+$ ,  $y^+$ ,  $z^+$  and  $u^+$ ,  $v^+$ ,  $w^+$  refer to the normalization by the viscous length and velocity scales,  $\nu/u_\tau$  and  $u_\tau$ , respectively (where  $\nu$  and  $u_\tau$  are the kinematic viscosity and friction velocity, respectively).

The term *interaction* will be used synonymously with *interaction region*. The terms *coherent motion*, or *coherent structure*, will be used interchangeably. Despite their intuitive appeal as concepts, they have proven notoriously difficult to formally define. Following the definition of Robinson (1991), the above terms will be considered as being: “a three-dimensional region of the flow over which at least one fundamental flow variable (velocity component, density, temperature etc.) exhibits significant correlation with itself or with another variable over a range of space and/or time that is significantly larger than the smallest scales of the flow.” Thus, vortices will be considered a coherent motion, as well as spatially extended regions of relatively low- and high-speed fluid. The terms *low-speed* and *high-speed* themselves will be used as relative terms, often relative to the local spatial region in which they occur.

The term *vortex* also has no universally accepted definition, but following the definition of Robinson (1991) we consider that: “a vortex exists when instantaneous streamlines mapped onto a plane normal to the vortex core exhibit a roughly circular, or spiral pattern, when viewed from a reference frame moving with the center of the vortex core.” The terms

*quasistreamwise* or *streamwise-elongated* will be applied to any entity with a predominantly streamwise orientation, recognizing that it may be significantly curved, rotated, or tilted with respect to the streamwise axis (Robinson 1991).

## 2.3 Theoretical Foundations

The independent variables of instantaneous velocity are considered functions of three spatial coordinates  $x, y, z$  and time  $t$ , such that

$$\left. \begin{aligned} u &= u(x, y, z, t) \\ v &= v(x, y, z, t) \\ w &= w(x, y, z, t) \end{aligned} \right\} \quad (2.1)$$

Under the continuum hypothesis, and assuming a linear relation between the stress tensor and the rate-of-strain tensor for a Newtonian fluid, the fundamental equations of the conservation of mass and momentum describing the instantaneous motion of a compressible turbulent viscous fluid in the absence of body forces may be written as (see e.g., Anderson 1991; White 1991)

Continuity:

$$\frac{\partial \rho}{\partial t} + \nabla \cdot (\rho \mathbf{v}) = 0 \quad (2.2)$$

Momentum:

$$\rho \left( \frac{\partial \mathbf{v}}{\partial t} + \mathbf{v} \cdot \nabla \mathbf{v} \right) = -\nabla p + \mu \nabla^2 \mathbf{v} + (4\mu/3 + \mu^v) \nabla (\nabla \cdot \mathbf{v}) \quad (2.3)$$

where the bold face denotes a vector quantity,  $\rho$  is the fluid density,  $p$  is the pressure,  $\mu$  is the fluid viscosity, and  $\mu^v$  is the volume or bulk viscosity. In turbulent flows, for the purposes of both theoretical and numerical treatment, the instantaneous flow is typically divided into a mean component and a fluctuation component using Reynolds decomposition (see White 1991). The mean component is defined as

$$\bar{\cdot} \equiv \lim_{T \rightarrow \infty} \frac{1}{T} \int_{t_0}^{t_0+T} \cdot(x, y, z, t) dt \quad (2.4)$$

where  $t_0$  and  $T$  are times and the dot stands for the variable of interest. Using Reynolds decomposition, instantaneous quantities are defined as

$$\left. \begin{aligned} u &= \bar{u} + u' & \rho &= \bar{\rho} + \rho' \\ v &= \bar{v} + v' & p &= \bar{p} + p' \\ w &= \bar{w} + w' & T &= \bar{T} + T' \end{aligned} \right\} \quad (2.5)$$

The time-average of the fluctuating quantities is zero, since for example

$$\frac{1}{T} \int_{t_0}^{t_0+T} u' dt = \frac{1}{T} \int_{t_0}^{t_0+T} u dt - \frac{\bar{u}}{T} \int_{t_0}^{t_0+T} dt = \bar{u} - \bar{u} = 0 \quad (2.6)$$

and it follows that

$$\bar{u}' = \bar{v}' = \bar{w}' = 0 \quad (2.7)$$

The (two-dimensional) compressible boundary layer equations may be derived from the momentum equations above, with  $x$  and  $y$  parallel and normal to the wall, respectively, by making the approximations that  $v \ll u$  and  $\partial/\partial x \ll \partial/\partial y$ . Also, since we are interested in a compressible boundary layer, not all of the fluctuating quantities are important. Specifically, for nonextreme Mach numbers (typically  $M_\infty < 5$ ), then the fluctuation quantities of the variables  $\rho'$ ,  $p'$ ,  $T'$  (and hence transport properties such as  $\mu'$  etc.) play only a minor role (see e.g., Spina *et al.* 1991; White 1991) and may consequently be neglected. Using the additional assumptions that

$$\bar{v} \ll \bar{u} \quad q' \ll \bar{q} \quad \forall q \quad (2.8)$$

where  $q$  stands for a variable in the momentum equations, we may write the two-dimensional compressible boundary layer equations, including the energy equation as (see White 1991)

Continuity:

$$\frac{\partial}{\partial x}(\overline{\rho u}) + \frac{\partial}{\partial y}(\overline{\rho v}) = 0 \quad (2.9)$$

Momentum:

$$\begin{aligned} \overline{\rho u} \frac{\partial \bar{u}}{\partial x} + \overline{\rho v} \frac{\partial \bar{u}}{\partial y} &= \rho_e U_e \frac{dU_e}{dx} + \frac{\partial}{\partial y} \left( \bar{\mu} \frac{\partial \bar{u}}{\partial y} - \overline{\rho u' v'} \right) \\ \frac{\partial \bar{p}}{\partial y} &= - \frac{\partial}{\partial y} (\overline{\rho v' v'}) \ll \left| \frac{\partial \bar{p}}{\partial x} \right| \end{aligned} \quad (2.10)$$

Energy:

$$\overline{\rho u} \frac{\partial \bar{h}}{\partial x} + \overline{\rho v} \frac{\partial \bar{h}}{\partial y} = \bar{u} \frac{\partial \bar{p}}{\partial x} + \frac{\partial}{\partial y} \left( \bar{k} \frac{\partial \bar{T}}{\partial y} - \overline{\rho v' h'} \right) + \left( \bar{\mu} \frac{\partial \bar{u}}{\partial y} - \overline{\rho u' v'} \right) \frac{\partial \bar{u}}{\partial y} \quad (2.11)$$

where the subscript  $e$  refers to the boundary layer edge conditions. The quantity  $h$  is the specific enthalpy, given by  $h=e+p/\rho$ , where  $e$  is the internal energy, and  $k$  is the thermal conductivity. Notice that, unlike in a laminar boundary layer, there is a slight (mean) pressure gradient normal to the wall due the variable mean density and wall-normal velocity fluctuations. This variation is generally ignored, however, and hence the pressure gradient is essentially determined by the free-stream conditions (i.e.,  $d\bar{p}/dx \approx -\rho_e U_e dU_e/dx$ ).

The integration of the boundary layer momentum equation across the boundary layer height  $\delta$  leads to the (compressible) von Kármán integral momentum equation

$$\frac{\partial}{\partial x} (\rho_e U_e^2 \theta) + \delta^* \rho_e U_e \frac{dU_e}{dx} = \tau_w \quad (2.12)$$

where  $\tau_w$  is the shear stress at the wall given by

$$\tau_w = \mu \left. \frac{\partial \bar{u}}{\partial y} \right|_{y=0} \quad (2.13)$$

The shear stress is closely related to the skin friction coefficient  $C_f$  defined as

$$C_f = \frac{\tau_w}{\frac{1}{2} \rho_e U_e^2} \quad (2.14)$$

Two useful parameters are introduced in the von Kármán integral momentum equation above; namely, the displacement thickness  $\delta^*$  and momentum thickness  $\theta$ , defined respectively by

$$\delta^* = \int_0^\delta \left( 1 - \frac{\rho \bar{u}}{\rho_e U_e} \right) dy, \quad \theta = \int_0^\delta \frac{\rho \bar{u}}{\rho_e U_e} \left( 1 - \frac{\bar{u}}{U_e} \right) dy \quad (2.15)$$

The ratio between these two quantities,  $H = \delta^* / \theta$ , is known as the *shape factor* or *shape parameter*, and this will be an important parameter in subsequent chapters, being a measure of the fullness of the boundary layer velocity profile.

## 2.4 Aspects of the Compressible Turbulent Boundary Layer

A significant problem in theoretical analyses of turbulent boundary layers is that they do not admit to similarity solutions. That is, the velocity profiles are not geometrically similar and do not collapse onto a single curve when  $u/U_e$  is plotted against an appropriate dimensionless wall-normal coordinate (see Cebeci & Cousteix 1999). This is because the viscous-dependent region of the boundary layer close to the wall, and the Reynolds-stress-dependent region away from the wall, both require different length-scales. This presents difficulties when attempting to specify the behaviour of the turbulent boundary layer, since one velocity-scale and one length-scale is insufficient. This has led theorists to develop different length-scales in



each region to deal with the composite nature of the turbulent boundary layer. It was Prandtl and von Kármán who first deduced, on dimensional grounds, that the profile for a turbulent boundary layer consists of three different layers (see White 1991). The velocity- and length-scales to be used are first nondimensionalized, such that

$$u^+ = \frac{u}{u_\tau}, \quad y^+ = \frac{u_\tau y}{\nu_w}, \quad u_\tau = \sqrt{\frac{\tau_w}{\rho_w}} \quad (2.16)$$

where  $\nu_w$  is the kinematic viscosity at the wall,  $\tau_w$  is the wall shear stress, and  $u_\tau$  is the friction velocity. We may then distinguish the three layers of the turbulent boundary layer as:

*Inner layer:*  $y^+ \leq 5$ . Within this inner layer, known as the *viscous sublayer*, the velocity profile depends on the wall shear stress, fluid properties, and distance from the wall, but not on free-stream parameters. Its thickness is very small, typically  $5\nu/u_\tau$ , where  $\nu/u_\tau$  is the *viscous length-scale*  $\delta_v$  of the boundary layer (i.e.,  $y^+ = y/\delta_v$ ). Within this region, the velocity profile is linear and can be written as

$$u^+ = y^+ \quad (2.17)$$

*Buffer layer:*  $5 \leq y^+ \leq 30$ . Within this region, the velocity profile is neither linear nor logarithmic (see below), but instead a smooth merging between the two.

*Logarithmic layer:*  $y^+ \geq 35$ ;  $y/\delta < 0.1-0.2$ . Within this region is the logarithmic overlap, which begins from the buffer layer and extends out to the wake-region, where the velocity profile begins to rise above the logarithmic curve. Within the logarithmic region, the velocity can be written in terms of inner variables from dimensional analysis as

$$u^+ = \frac{1}{\kappa} \ln y^+ + B \quad (2.18)$$

where the quantities  $\kappa$  and  $B$  are determined from experiment, although to first order, values that can be used to correlate supersonic and hypersonic boundary layers are typically taken to be  $\kappa=0.41$  and  $B=5.0$  (see White 1991), and these will be the values adopted in this thesis. As a matter of fact, Spalding (1961) has provided a single composite formula for the entire wall-related region given by

$$y^+ = u^+ + e^{-\kappa B} \left[ e^{\kappa u^+} - 1 - \kappa u^+ - \frac{1}{2}(\kappa u^+)^2 - \frac{1}{6}(\kappa u^+)^3 \right] \quad (2.19)$$

which includes all of the regions described above.

*Wake region:*  $y/\delta > 0.1-0.2$ . While the relations for the regions above have proven successful for describing smooth-wall turbulent boundary layers, specifying an outer law for the wake region is problematic because of the dependence on the pressure gradient. While there have been several approaches to specifying the velocity profile in this region, one of the most popular is Coles' law of the wake, first proposed by Coles (1956), who deduced an expression for the velocity profile by observing that the additional component appeared to have a wake-like structure. By adding his wake component to the log-law above, we have an expression for the velocity profile from the overlap to the wake region given by

$$u^+ = \frac{1}{\kappa} \ln y^+ + \frac{2\Pi}{\kappa} \sin^2 \left( \frac{\pi y}{2 \delta} \right) \quad (2.20)$$

where  $\Pi$  is the *Coles wake parameter*. Using these formulae, a complete description of the mean velocity profile of the turbulent boundary layer may be obtained. The last problem that remains is how to characterize the mean velocity profile for a compressible turbulent boundary layer in relation to its incompressible counterpart. A number of theories have been developed over the years to specify the velocity profile of compressible turbulent boundary layers. Despite varying degrees of success in these theories, the general consensus is that the van Driest compressibility transformation can be used to give a good description of the boundary layer velocity profile in the log-law region (White 1991), and this will be the approach adopted here.

## 2.5 Van Driest Effective Velocity Concept

The basic methodology of the van Driest compressibility transformation involves a compressible extension to the Prandtl mixing-length hypothesis, which is integrated to give an effective velocity relation. The temperature-density dependence is modelled using the Crocco-Busemann relation. Briefly, following the outline of White (1991), consider the eddy transport definitions

$$-\overline{\rho u'v'} = \mu_t \frac{\partial \bar{u}}{\partial y}, \quad -\overline{\rho u'h'} = k_t \frac{\partial \bar{T}}{\partial y} \quad (2.21)$$

where  $\mu_t$  and  $k_t$  are the turbulent viscosity and turbulent thermal conductivity, respectively. Rewriting the momentum equation for a compressible turbulent boundary layer in terms of  $\mu_t$ , and the energy equation in terms of the total enthalpy  $H = \bar{h} + \bar{u}^2/2$ , we have for the condition that  $\text{Pr} \approx \text{Pr}_t \approx 1$  (where  $\text{Pr}$  and  $\text{Pr}_t$  are the laminar and turbulent Prandtl numbers, respectively), a particular solution that  $H = \text{constant}$  throughout the boundary layer. Assuming that the specific heat capacity of air for a constant pressure process  $c_p$  is constant, such that  $\bar{h} = c_p \bar{T}$ , then the Crocco-Busemann relation can be written as a relation between temperature and velocity, viz.

$$\bar{T} = \bar{T}_w + (\bar{T}_{aw} - \bar{T}_w) \frac{\bar{u}}{U_e} - \frac{\bar{u}^2}{2c_p} \quad (2.22)$$

where  $\bar{T}_{aw}$  is the adiabatic wall temperature,  $\bar{T}_{aw} = \bar{T}_e + U_e^2/2 - \bar{T}_w$ . Making the boundary layer assumption that the wall-normal pressure gradient is negligible (i.e.,  $\partial \bar{p}/\partial y \approx 0$ ), then with the equation of state  $\bar{p} = \bar{\rho} R \bar{T}$ , the density ratio  $\bar{\rho}/\bar{\rho}_w$  can be written as the inverse of the temperature ratio  $\bar{T}/\bar{T}_w$ . To obtain the van Driest transformation, we make use of the eddy viscosity concept with the condition that  $\bar{\rho} = \bar{\rho}(y)$ . Van Driest (1951) adapted the mixing-length model to read

$$\tau \approx \tau_t = \bar{\rho} \kappa^2 y^2 \left( \frac{\partial \bar{u}}{\partial y} \right)^2 \quad (2.23)$$

Writing the Crocco-Busemann relation as a density ratio and substituting this into Prandtl's mixing-length hypothesis and integrating, gives the profile  $\bar{u}=\bar{u}(y)$  in closed form in terms of an effective velocity  $u_{eq}$

$$u_{eq} = \frac{U_e}{a} \left( \sin^{-1} \frac{2a^2 \bar{u} / U_e - b}{Q} + \sin^{-1} \frac{b}{Q} \right) = u_\tau \left( \frac{1}{\kappa} \ln y^+ + B \right) \quad (2.24)$$

where

$$a = \left( \frac{\gamma-1}{2} M_e^2 \frac{\bar{T}_e}{\bar{T}_w} \right)^{1/2} \quad b = \left( \frac{\bar{T}_{aw}}{\bar{T}_w} - 1 \right) \quad Q = (b^2 + 4a^2)^{1/2} \quad (2.25)$$

The right-hand-side is the incompressible law-of-the-wall, and the left-hand-side is the effective velocity  $u_{eq}$ . For an adiabatic boundary layer  $b=0$ ,  $Q=2a$ , and  $u_{eq}$  becomes

$$u_{eq} = \frac{U_e}{a} \left( \sin^{-1} \frac{a\bar{u}}{U_e} \right) \quad a^2 = 1 - \frac{\bar{T}_e}{\bar{T}_{aw}} \quad (2.26)$$

The skin friction coefficient  $C_f$  may then be obtained from

$$C_f = \frac{u_\tau^2 \rho_w}{\frac{1}{2} \rho_e U_e^2} \quad (2.27)$$

As noted by Spina *et al.* (1991), the success of the van Driest transformation has become so common that its limitations are often over-looked. Its limitations include the absence of strong pressure gradients, a Prandtl number of unity, the validity of the mixing-length model, high Reynolds number similarity, and independence of upstream history. Nevertheless, the van Driest transformation has been shown to give good agreement with incompressible results over a wide range of Mach numbers, various wall-heating conditions, and pressure gradients (see Spina *et al.* 1991), and its application in the present study is therefore considered to be justified.

# CHAPTER

# 3

# EXPERIMENTAL TECHNIQUES & ARRANGEMENTS

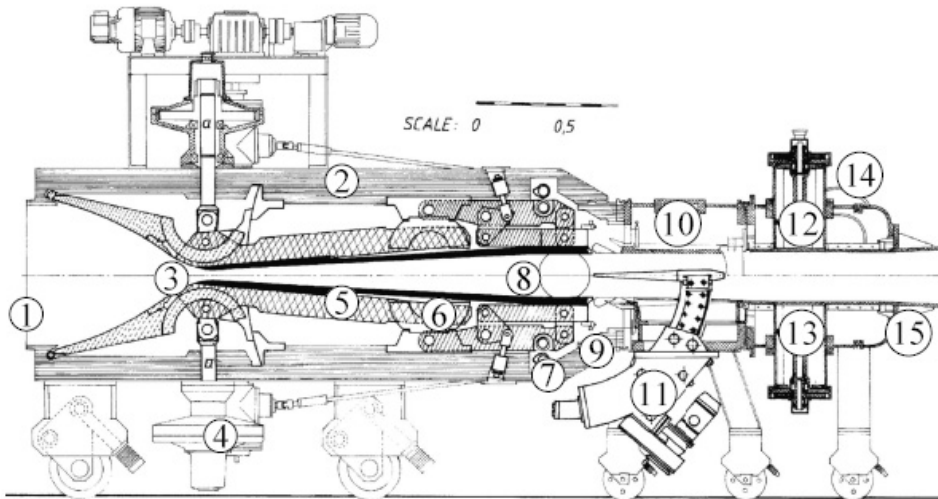
---

## 3.1 Introductory Remarks

**T**HE experimental techniques and arrangements used are described herein, beginning with a description of the experimental flow facility. A brief outline of the HWA system is then provided, followed by the working principles of planar and tomographic PIV, along with a description of their respective experimental arrangements. An uncertainty analysis of the measured properties is then given. This chapter draws on much of the material on the planar PIV technique provided by Raffel *et al.* (2007), tomographic PIV by Elsinga *et al.* (2006), and the theoretical foundations given by Westerweel (1997). For more extensive material on PIV in particular, the interested reader is referred to Adrian (1986, 1991) and Grant (1997).

### 3.2 Flow Facility

All experiments were performed in the blow-down transonic-supersonic wind-tunnel (TST-27) of the High-Speed Aerodynamics Laboratories at Delft University of Technology. A schematic of the experimental facility is shown in figure 3.1. The flow direction is from left to right. The facility generates flows in the Mach number range 0.5–4.2, in a test-section of maximum dimensions 280(W) mm×270(H) mm, and exhausts through the outlet diffuser to atmospheric pressure. The Mach number can be set by means of a continuous variation of the throat section and flexible nozzle walls. The tunnel operates at unit Reynolds numbers typically ranging from  $30 \times 10^6$  to  $130 \times 10^6 \text{ m}^{-1}$ .



- |                               |                             |                               |
|-------------------------------|-----------------------------|-------------------------------|
| 1. Settling chamber           | 6. Node bearing             | 11. Angle of attack mechanism |
| 2. Nozzle section             | 7. Boundary layer mechanism | 12. Choke section             |
| 3. Variable nozzle            | 8. Supersonic test-section  | 13. Choke body                |
| 4. Adjustable screw mechanism | 9. Rapid clamp coupling     | 14. Bleed-off device          |
| 5. Semi-flexible wall         | 10. Model support section   | 15. Outlet diffuser           |

FIGURE 3.1: Schematic of experimental facility TST-27. Flow direction is from left to right. Original figure used with permission by Frits Donker Duyvis. Adapted from Kuik (2007).

The stagnation or settling chamber is supplied with dry oil-free air that is stored within a separate 300 m<sup>3</sup> vessel at pressures within the range 20–40 bar. This air is delivered by a 230 kW computer-controlled compressor plant, and is dried with a high-pressure dryer, which lowers the water content to below 10 parts per million. In addition, between the vessel and settling chamber there is a 5 μm dust filter that removes small particles, which may contaminate the flow. A fully charged vessel contains approximately 14,300 kg of air, enabling a blow-down use of the wind-tunnel of approximately 300 seconds. The free-stream turbulence level within the test-section has been determined by HWA, and was found to be 1% $U_\infty$  within the Mach number range 1.9–2.3 (see also Scarano & van Oudheusden 2003). This turbulence level was obtained by the presence of damping screens in the settling chamber.

### 3.3 Hot-Wire Anemometry

The hot-wire anemometer probe consists of a very fine metallic wire supported by two conducting prongs (see e.g., Comte-Bellot 1976; Smits *et al.* 1983; Logan 1989 and the references cited therein). The wire is heated by an electric current passing through it (the Joule effect) and is cooled at the same time by the surrounding convecting fluid. By analyzing the fluctuating voltage across the wire, fluctuations in flow variables may be deduced. Assuming that the fluctuations are small compared with their time-averaged value, and that the wire is oriented normal to the mean flow so that the contribution of the transverse fluctuating component can be considered negligible, then the rate of change of energy stored in the wire filament may be written as (see Comte-Bellot 1976)

$$c_w \frac{d\Theta_w}{dt} = R_w I^2 - \Phi \quad (3.1)$$

where  $c_w$  is the thermal capacity of the wire,  $\Theta_w$  is the temperature of the wire,  $R_w$  is the wire resistance,  $I$  is the current intensity, and  $\Phi$  is the convection heat-loss rate to the flow. For a constant-temperature anemometer (CTA) with zero thermal lag, where the wire

temperature by Joule heating is in equilibrium with convection to the surrounding flow, then  $d\Theta_w/dt=0$  and

$$R_w I^2 = \Phi \quad (3.2)$$

Following Ko *et al.* (1978), the convection heat-loss rate to the flow can be expressed as

$$\Phi = \pi l k_0 (\Theta_w - \eta T_0) \text{Nu} \quad (3.3)$$

where  $l$  is the length of the wire,  $k_0$  is the thermal conductivity of the wire at stagnation conditions,  $\eta$  is the recovery factor and Nu is the Nusselt number; a dimensionless heat transfer coefficient. Following Smits *et al.* (1983), the heat transfer from the wire filament may be described by the semi-empirical relation

$$\text{Nu} = X + Y \text{Re}^n \quad (3.4)$$

where  $X$ ,  $Y$ , and  $n$  are constants. Using Ohm's law, then the left-hand-side of (3.1) can be written in terms of voltage as  $E^2/R$ . Combining equations (3.2) and (3.3), then (3.4) may be written for calibration purposes as

$$E^2 = L + M (\rho u)^n \quad (3.5)$$

where  $L$  and  $M$  are constants for a given wire at a particular overheat ratio and stagnation temperature. We find that  $n=0.55$  gives a suitable fit to the static calibration data, consistent with the work of Smits *et al.* (1983), thus establishing the link between measured voltage and mass flow. The wire was calibrated using the mean voltage at several heights within the boundary layer and the mean mass flow, determined from the measured PIV velocity profile, in combination with the adiabatic Crocco-Busemann relation, with a constant recovery factor equal to 0.89 (see White 1991).



In the present experiments, an electronic traversing hot-wire system consisted of a DISA (now Dantec) 55M10 CTA bridge in combination with a Dantec 55P11 single-wire probe (see also Elsinga 2008). The tungsten wire was 1.25 mm long with a diameter of  $5\ \mu\text{m}$ . The experimental arrangement for the hot-wire experiments is shown in figure 3.2. The overheat ratio was varied by changing the bridge resistance, and was set at 0.88 so that the probe was mainly sensitive to the momentum fluctuations  $(\rho u)'$  and not total temperature fluctuations  $T_0'$  (see Smits *et al.* 1983).

The frequency response of the probe/circuit combination was estimated by examining its response to a square-wave signal. The response was optimized by adjusting the anemometer gain and filter settings. Optimal adjustment produced a square-wave response that was nearly critically-damped. The frequency response was (conservatively) estimated to be about 20 kHz, which will be sufficient for our present purpose, which is to concentrate on the large time-scales developing within the interaction. Importantly, this frequency response is similar to the ones reported in other studies using the same equipment, such as Miller *et al.* (1987), who report a frequency response of 13–20 kHz for a  $5\ \mu\text{m}$  wire, as well as Ligrani *et al.* (1989), who used a  $0.6\ \mu\text{m}$  wire, and reported perturbation decay times from square-wave tests to be  $10\ \mu\text{s}$  to  $25\ \mu\text{s}$ , indicative of a frequency response over 40 kHz.

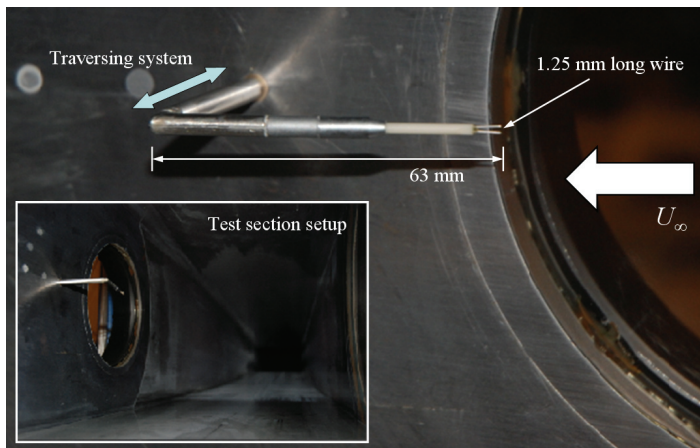


FIGURE 3.2: HWA experimental arrangement. Flow direction is from right to left. Inset shows test-section setup (looking upstream).

## 3.4 Planar PIV

### 3.4.1 Working Principles

PIV is a nonintrusive optical technique that measures the velocity simultaneously at numerous points within a fluid. The fluid is seeded with tracer particles that are considered to (1) not alter the motion of the fluid, and (2) exactly follow the motion of the fluid (see Westerweel 1997). The local fluid velocity at location  $X$  is obtained indirectly as a displacement  $D$  of the tracer particles within a finite time interval  $\Delta t = t_2 - t_1$ , viz.

$$D(X; t_1, t_2) = \int_{t_1}^{t_2} v[X(t), t] dt \quad (3.6)$$

where  $v[X(t)]$  is the velocity of the tracer particles along its trajectory  $X$  within the time interval  $\Delta t$ . For ideal tracer particles, the tracer particle velocity  $v$  is equal to the local fluid velocity  $u(X, t)$ . Note also that the displacement is obtained from the average velocity along the particle's trajectory over the time  $\Delta t$ . The tracer particle distribution is established by illuminating the measurement domain approximating a plane twice in short succession  $\Delta t$  by a pulsed laser. The light scattered by the particles at each illumination is captured in two separate frames of a charge couple device (CCD) sensor. A statistical analysis is then applied to the two particle image patterns in order to determine the most likely displacements of the particle ensemble and hence the instantaneous velocity vector field. A schematic of an experimental arrangement for a typical PIV experiment is shown in figure 3.3, from Raffel *et al.* (2007). The following subsections describe in further detail these essential components.

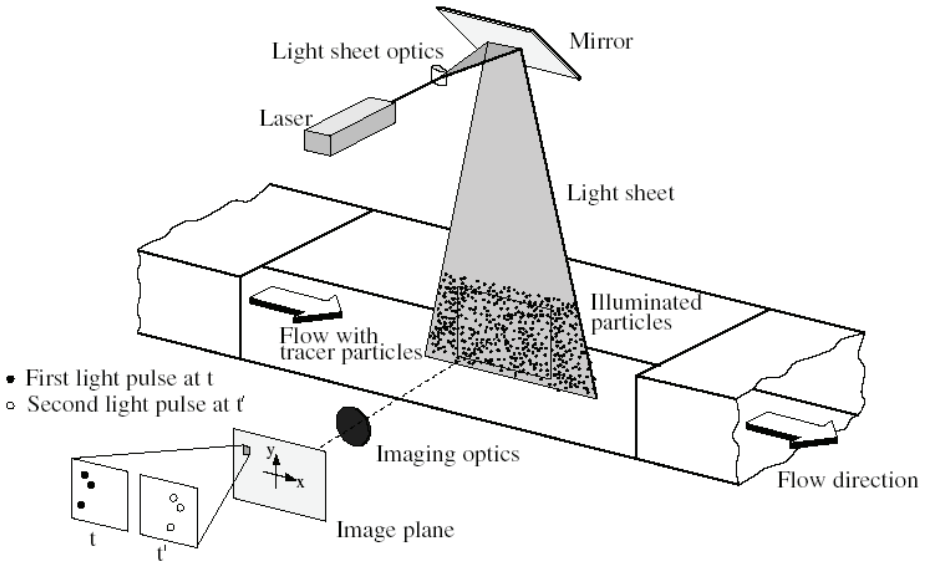


FIGURE 3.3. Experimental arrangement of a typical PIV experiment. From Raffel *et al.* (2007).

### 3.4.2 Tracer Particles

The condition that the particles must follow the flow with fidelity typically necessitates that the particle diameter be sufficiently small, but the particles must also be large enough so that they scatter enough light. Consider the motion of a particle in a continuous medium. If external forces, such as gravitational, and electrostatic forces etc. can be considered negligible, then the tracking capability of the particle is a function of its shape, particle diameter  $d_p$ , particle density  $\rho_p$ , fluid density  $\rho_f$ , and fluid dynamic viscosity  $\mu_f$  or kinematic viscosity  $\nu = \mu_f / \rho_f$ . For spherical particles, an expression relating the instantaneous relative velocity  $\mathbf{V} = \mathbf{U}_p - \mathbf{U}_f$  between the particle and the fluid, to the instantaneous velocities  $\mathbf{U}_p$  and  $\mathbf{U}_f$  of the particle and the fluid, respectively, is given by (see Melling 1997)

$$\begin{aligned} \frac{\pi d_p^3}{6} \rho_p \frac{d\mathbf{U}_p}{dt} = & -3\pi\mu_f d_p \mathbf{V} + \frac{\pi d_p^3}{6} \rho_f \frac{d\mathbf{U}_f}{dt} - \frac{1}{2} \frac{\pi d_p^3}{6} \rho_f \frac{d\mathbf{V}}{dt} \\ & - \frac{3}{2} d_p^2 (\pi\mu_f \rho_f)^{1/2} \int_{t_0}^t \frac{d\mathbf{V}}{d\xi} \frac{d\xi}{(t-\xi)^{1/2}} \end{aligned} \quad (3.7)$$

where the acceleration force and viscous resistance according to Stokes law are represented by the first two terms. The third term represents an additional force due to the pressure gradient acting on the particle, as a result of the acceleration of the surrounding fluid. The fourth term represents the resistance of an inviscid fluid to the acceleration of the sphere, whereas the fifth term is known as the *Basset history integral*, which is a resistance due to flow unsteadiness. For PIV in gases such as air, only the first two terms are important because of the large density ratio  $\rho_p/\rho_f$ , and the equation of motion becomes

$$\frac{d\mathbf{U}_p}{dt} = \frac{\mathbf{U}_p - \mathbf{U}_f}{\tau_p} \quad (3.8)$$

where  $\tau_p$  is the characteristic time lag of the particle, which may be obtained from (see e.g., Schrijer *et al.* 2006)

$$\tau_p = \frac{4}{3} \frac{\rho_p d_p^2}{C_D \text{Re}_d \mu_f} \quad (3.9)$$

where  $C_D$  is the drag coefficient and  $\text{Re}_d$  is the Reynolds number based on the particle diameter. As a compromise to the above considerations and what follows, titanium dioxide ( $\text{TiO}_2$ ) particles were adopted as tracers in the present experiments. Such particles are well-suited for application in supersonic flows due to their submicron size, high refractive index, thermodynamic and chemical inertness, high-melting point, and low-cost (Raffel *et al.* 2007). However, it is well-known that such solid particles can agglomerate, therefore introducing an uncertainty in the estimation of the effective particle diameter, as discussed by Schrijer *et al.* (2006). This necessitates a particle response assessment in order to establish the actual flow tracer performance, which will be dealt with in §3.5.3.

### 3.4.3 Particle Imaging

When the tracer particles are viewed through a finite aperture lens, their image as a distance point source does not appear as a point in

the image plane, but forms a Fraunhofer diffraction pattern, consisting of an Airy disk surrounded by Airy rings (see Raffel *et al.* 2007). The diameter of the Airy disk  $d_{diff}$  is important in PIV imaging, because it represents the smallest particle image that can be obtained for a given imaging configuration. The value of  $d_{diff}$  for a given aperture diameter  $D_a$  and wave-length  $\lambda$  may be estimated by approximating the normalized intensity distribution of the Airy pattern by a Gaussian bell curve and using the lens equation given by

$$\frac{1}{z_0} + \frac{1}{Z_0} = \frac{1}{f} \quad (3.10)$$

where  $z_0$  is the distance between the image plane and lens, and  $Z_0$  is the distance between the lens and object plane. Defining a magnification factor  $M$  as

$$M = \frac{z_0}{Z_0} \quad (3.11)$$

the diffraction limited minimum diameter  $d_{diff}$  can be expressed as

$$d_{diff} = 2.44 f_{\#} (M + 1) \lambda \quad (3.12)$$

where  $f_{\#}$  is the f-number, defined as the ratio between the focal length  $f$  and aperture diameter  $D_a$ . Expression (3.12) is valid when imaging small particles at small magnifications. For larger particles and/or magnifications, then the influence of geometric imaging becomes important. For an aberration-free lens, the minimum particle image diameter  $d_{\tau}$  may be estimated using (see Adrian *et al.* 1991)

$$d_{\tau} = \sqrt{(M d_p)^2 + d_{diff}^2} \quad (3.13)$$

where  $d_p$  is the particle diameter. In the present experiments, however, the small particle sizes mean that  $d_{\tau} \approx d_{diff}$ . Note that the value of  $d_{diff}$  must be sufficiently large (typically  $>2$  pixels) to avoid

phenomenon such as *peak-locking*, where improper subpixel estimation leads to a displacement bias error that has a periodic pattern on pixel intervals (see Westerweel 1997; Raffel *et al.* 2007). In addition, it is clear from the above that for a given magnification (which is dependent on the experimental arrangement), only  $f_{\#}$  can be typically increased to give a sufficient value of  $d_{diff}$ , resulting in less light being collected by the imager. This causes the particle image contrast to decrease. Furthermore,  $f_{\#}$  also determines the focal depth  $\delta_z$  given by

$$\delta_z = 4.88\lambda \left[ \frac{f_{\#}(M+1)}{M} \right]^2 \quad (3.14)$$

which must be carefully managed in order to maintain proper focus of the flow domain. It should therefore be at least equal to the laser sheet thickness. This will be especially important in the tomographic PIV experiments, as will be discussed later on.

### 3.4.4 Image Analysis

For the purposes of PIV image analysis, the tracer particle distribution is described in terms of a pattern. The resulting particle images show the instantaneous locations of the tracer particles as peaks in the light intensity. For a sufficiently small  $\Delta t$ , the two consecutive images have light intensity distributions with the second exposure approximately shifted with respect to the first. This shift may be determined using a correlation technique. Briefly, consider schematically two particle images at times  $t$  and  $t+\Delta t$ , as shown in figure 3.4, adapted from Raffel *et al.* (2007).

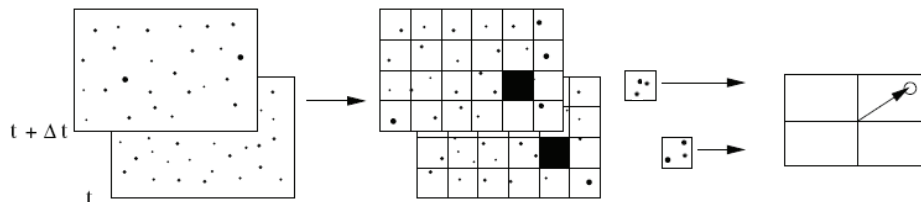


FIGURE 3.4. Illustration of digital PIV cross-correlation process. Adapted from Raffel *et al.* (2007).

The images are first divided into smaller subregions called *interrogation windows*, which contain local light intensity distributions. Let the distributions of light intensity within an interrogation area at times  $t$  and  $t+\Delta t$  be  $I_1(i, j)$  and  $I_2(i, j)$ , respectively, for the  $i$ th and  $j$ th pixels. The two intensity distributions are then cross-correlated by sliding the smaller template  $I_1$  around template  $I_2$  by a shift  $(dx, dy)$ . The sum of the products of all the overlapping pixel intensities at each spatial shift  $(dx, dy)$  returns the map of correlation value  $C(dx, dy)$ , which is essentially a measure of the degree of matching between the two samples for a given shift, and is given by

$$C(dx, dy) = \sum_{i=0}^M \sum_{j=0}^N \left[ I_1(i, j) - \mu_{I_1} \right] \left[ I_2(i + dx, j + dy) - \mu_{I_2} \right] \quad (3.15)$$

By applying this for a range of shifts, a correlation map is formed. Here,  $M \times N$  is the size of the interrogation area,  $\mu_{I_1}$  is the average of  $I_1$  computed once, whereas  $\mu_{I_2}$  is the average of  $I_2$ . The correlation function is normalized using the intensity standard deviation from each window (see Raffel *et al.* 2007)

$$c(dx, dy) = \frac{C(dx, dy)}{\sqrt{\sigma_1} \sqrt{\sigma_2}} \quad (3.16)$$

where

$$\sigma(x, y) = \sum_{i=0}^M \sum_{j=0}^N \left[ I(i, j) - \mu_I \right]^2 \quad (3.17)$$

The largest peak in the correlation map  $c(dx, dy)$  represents the most probable displacement within each interrogation window. With knowledge of the time separation  $\Delta t$ , the velocity vector field can then be determined. The *signal-to-noise ratio* is then defined as the ratio between the first and second largest correlation peaks.

It is clear from the above, that the cross-correlation of finite interrogation windows in PIV results in a spatial filtering of the velocity field. It has been shown by Scarano & Riethmuller (2000)

that the frequency response of the cross-correlation procedure is essentially similar to that of the moving-average filter, with a kernel size equal to the final interrogation window size, except of course with the addition of noise. Furthermore, the finite time separation between two recordings also leads to a low-pass time-filtered representation of the velocity field. Accordingly, velocity fluctuations with a time-scale shorter than the time separation  $\Delta t$  between two recordings (i.e., in our case  $\Delta t = O(10^{-6}$  s), or  $f = O(10^6$  Hz)) will be affected (see also Scarano 2003). However, as will be shown later, the spatial and temporal scales of interest to the present study remain, for the most part, unaffected.

Improvements to the data yield in the interrogation process may be achieved by implementing advanced adaptive evaluation algorithms. To meet the compromise between an adequate spatial resolution due to a sufficient interrogation area size, and an adequate signal-to-noise ratio due to a sufficient particle density, the images in the present study are interrogated several times within an iterative scheme. A window offset in a multi-pass interrogation is also utilized to maximize the number of matched particles, thereby increasing the signal-to-noise ratio (see Westerweel 1997). Schrijer & Scarano (2003) discuss the stability and resolution of iterative image PIV with spatial various filtering methods, and have shown that significantly less modulation occurs due to the implementation of the iterative interrogation process.

Furthermore, in situations where the flow exhibits motions other than translation, such as vortex flows, sheared flows, or shocked flows, then large velocity differences can occur within the interrogation window. An iterative window deformation is therefore used to compensate for the in-plane gradients within the interrogation window. For a more complete discussion on iterative deformation techniques, the reader is referred to Scarano (2002).

## 3.5 Planar PIV Experimental Arrangement

### 3.5.1 Incoming Boundary Layer

The boundary layer developing along the upper wall of the wind-tunnel was utilized in order to realize the advantages of a thick boundary layer; namely, an increase in the scales of the mean and



fluctuating flow-field, which aids the spatial resolution within the measurement domain. The boundary layer developed along a smooth surface under adiabatic flow conditions for a development length of approximately 2 m. The wind-tunnel was operated at a nominal free-stream Mach number  $M_\infty=2.1$  (measured free-stream velocity  $U_\infty=518$  m s<sup>-1</sup>), with a stagnation pressure of  $P_0=276 \pm 3$  kPa and stagnation temperature of  $T_0=286 \pm 3$  K. (These uncertainties were estimated from temperature and pressure read-outs during the wind-tunnel runs. See also §3.8 for a more complete uncertainty analysis.)

On entering the measurement domain, the boundary layer thickness (99% of  $U_\infty$ ) was  $\delta=20$  mm, with displacement thickness  $\delta^*=4.4$  mm, and momentum thickness  $\theta=1.4$  mm. The corresponding skin friction coefficient determined from  $C_f=2u_\tau^2\rho_w/\rho_eU_e^2$  gives  $C_f=1.52 \times 10^{-3}$ , corresponding to a friction velocity  $u_\tau=\sqrt{(\tau_w/\rho_w)}=19.4$  m s<sup>-1</sup>. The friction velocity (and thus the skin friction coefficient) was deduced using a least squares fit of the PIV data to the van Driest log-law. The Reynolds number based on the momentum thickness,  $Re_\theta=U_\infty\theta/\nu_\infty=4.92 \times 10^4$  (where  $\nu_\infty$  is the kinematic viscosity in the free-stream). The Reynolds number based on the friction velocity and boundary layer thickness,  $Re_\tau=u_\tau\delta/\nu_w=8600$  (where  $\nu_w$  is the kinematic viscosity at the wall). The experimental conditions are summarized in table 3.1.

Table 3.1. Experimental conditions for the planar PIV  
SWTBLI

Parameter	Quantity
$M_\infty$	2.07
$U_\infty$ , m s <sup>-1</sup>	518
$C_f$	$1.52 \times 10^{-3}$
$\delta_{99}$ , mm	20
$\delta^*$ , mm	4.4
$\theta$ , mm	1.4
$u_\tau$ , m s <sup>-1</sup>	19.4
$P_0$ , kPa	276
$T_0$ , K	286
$Re_\theta$	$4.92 \times 10^4$
$Re_\tau$	8600

### 3.5.2 Shock Generator

A shock generator was placed in the middle of the test-section to generate the incident shock wave. The generator consisted of a 100 mm chord single-sided wedge giving a free-stream deflection angle of  $8^\circ$ . The wind-tunnel did not start for larger deflections angles under the present flow conditions considered. Previous experiments that have considered incident SWTBLIs, such as Détery and Marvin (1986), and Dupont *et al.* (2006) for instance, have shown that the chosen angle is sufficient to produce (incipient) flow separation, which will be shown later on to appear to be the case in the present experiments. The shock generator was rigidly mounted on one side of the wind-tunnel and spanned 96% of the test-section. A technical drawing of the shock generator in side-view is shown in figure 3.5. In addition, for the distance chosen from the wall, the chord length of the shock generator was sufficient to avoid the expansion fan at its shoulder from influencing the interaction. The shock generator was machined out of aluminium and included a thickened root at the wall attachment.

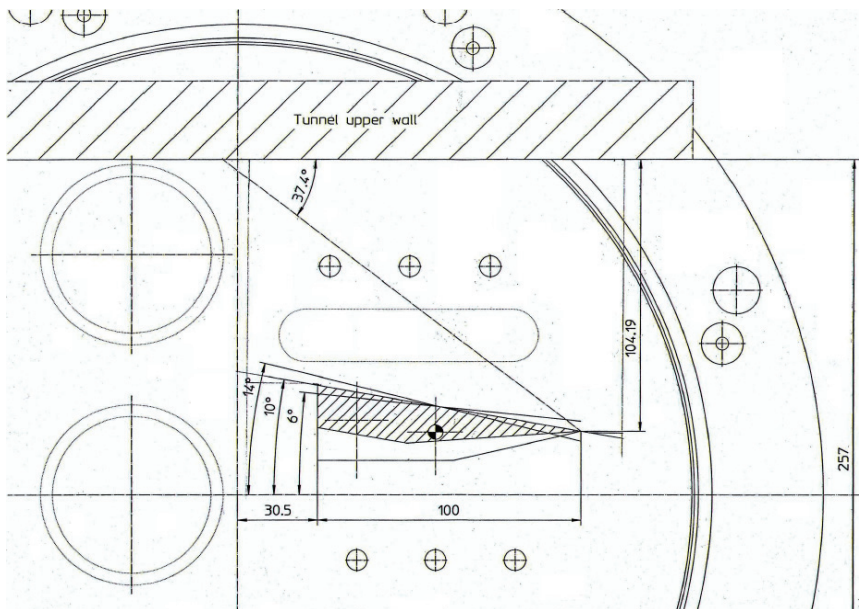


FIGURE 3.5: Technical drawing of the full-span shock generator in planar view. Flow direction is from right to left. Used with permission by Frits Donker Duyvis.

A schematic representation of the test-section configuration for the planar PIV system is shown in figure 3.6. All measurements made in the planar PIV SWTBLI experiments were conducted on the centre-line of the wind-tunnel unless otherwise stated.

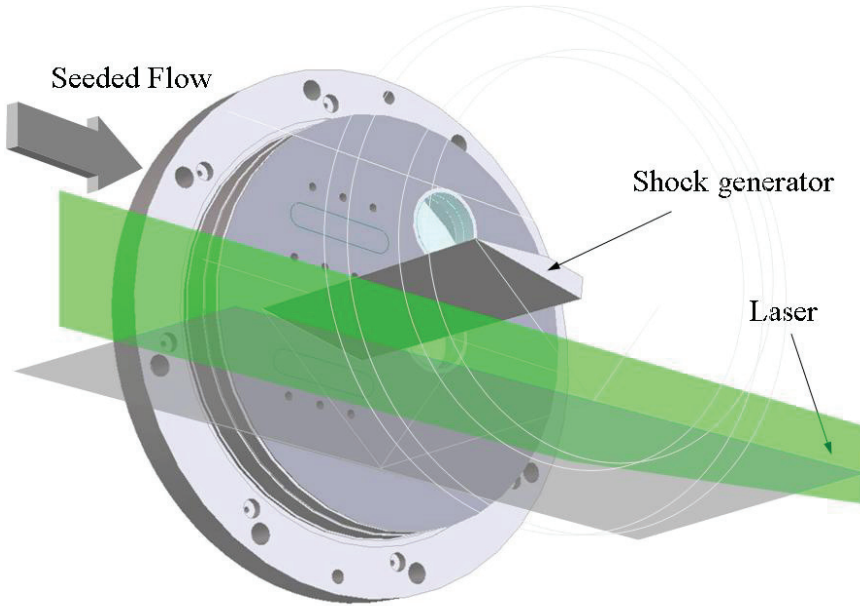


FIGURE 3.6: Schematic of the planar PIV SWTBLI experimental configuration. Illumination is along the centre-line from downstream of the test-section. Flow direction is from left to right. Adapted with permission by Frits Donker Duyvis.

### 3.5.3 Flow Seeding

UV-TITAN L830  $\text{TiO}_2$  particles were used as tracers, with a manufacturer-specified nominal diameter of 50 nm (effective or agglomerated diameter  $d_p \sim 400$  nm, see Schrijer *et al.* 2006) and a bulk density of  $200 \text{ kg m}^{-3}$ . As discussed earlier, such powders have a tendency for particle agglomeration, and a controlled dispersion of the particles into the wind-tunnel was therefore required.

A cyclone separator was employed to entrain the particles and seed the settling chamber, as shown in figure 3.7(right). The cyclone contained air pressurized at 10 bar, which was fed through primary

and secondary inlets. The primary inlet (A) was fed directly into the cyclone to entrain the particles in the air. The secondary inlet (B) was used to increase the air mass flow and therefore the velocity of the seeded air flow prior to injection into the settling chamber, although its effect was found to be minimal. Flow was injected into the settling chamber through the master valve (C). Once in the settling chamber, the seeded flow issued into the wind-tunnel nozzle through a two-dimensional seeding rake. A cross-sectional schematic view of the settling chamber showing the seeding rake and apparatus is shown in figure 3.7(left). The seeding rake spanned approximately  $26 \times 30 \text{ cm}^2$  and consisted of six vertical profile-shaped bars, each with six orifices. The rake was positioned approximately 2 m upstream of the test-section. As discussed by Scarano (2006), the interference of the seeding with the flow was assessed by HWA measurements in the free-stream. It was found that an increase in turbulence intensity of about  $0.2\% U_\infty$  occurred, which is considered acceptable for the present experiments. Furthermore, no evidence of inhomogeneous turbulence was found, except of course, for the wind-tunnel side-wall boundary layers.

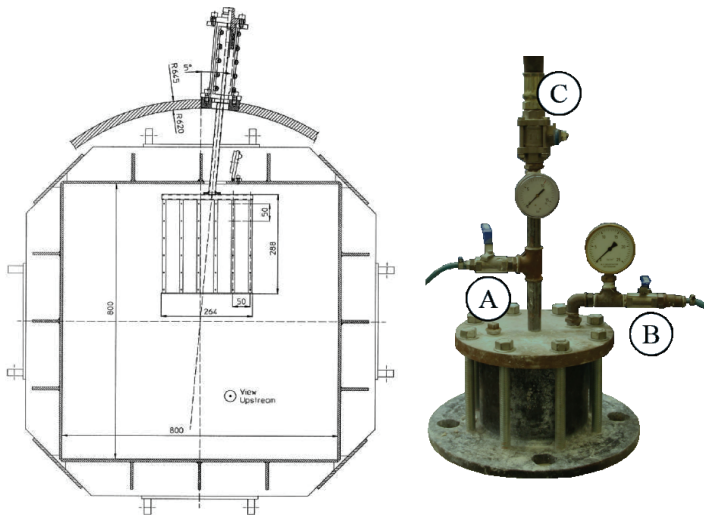


FIGURE 3.7: The planar PIV seeding system. Shown is a cross-sectional schematic of the settling chamber with seeding rake (left). Used with permission by Frits Donker Duyvis. Shown is the cyclone generator (right). Modified from Kuik (2007). Note that both apparatus are not shown to scale.

For PIV applications in supersonic flow, the particle's temporal response can be conveniently quantified by the time it takes the particle to respond to a step velocity variation, such as that imposed by a normal, or oblique shock wave. In this case, the relaxation time is simply  $\tau_p$ . If the initial particle velocity is  $\mathbf{U}_{pi}$ , then the solution for the instantaneous particle velocity  $\mathbf{U}_p = \mathbf{U}_p(t)$  is given by (see Raffel *et al.* 2007)

$$\mathbf{U}_p - \mathbf{U}_f = (\mathbf{U}_{pi} - \mathbf{U}_f) e^{-\frac{t}{\tau_p}} \quad (3.18)$$

To evaluate the particle's temporal response, the steady oblique shock wave (OSW) generated in the free-stream was used for such an assessment, following the procedure proposed by Scarano & van Oudheusden (2003). UV-TITAN L830 TiO<sub>2</sub> particles with a manufacturer-specified nominal diameter of 50 nm and a bulk density of 200 kg m<sup>-3</sup> were used (see also Schrijer *et al.* 2006). The planar PIV measurement returns the spatial distribution of the velocity, making it possible to extract a velocity profile across the OSW. The velocity component normal to the shock wave was considered for the analysis. Figure 3.8 shows the distribution of the mean normal velocity along with the shock-normal abscissa  $S$ .

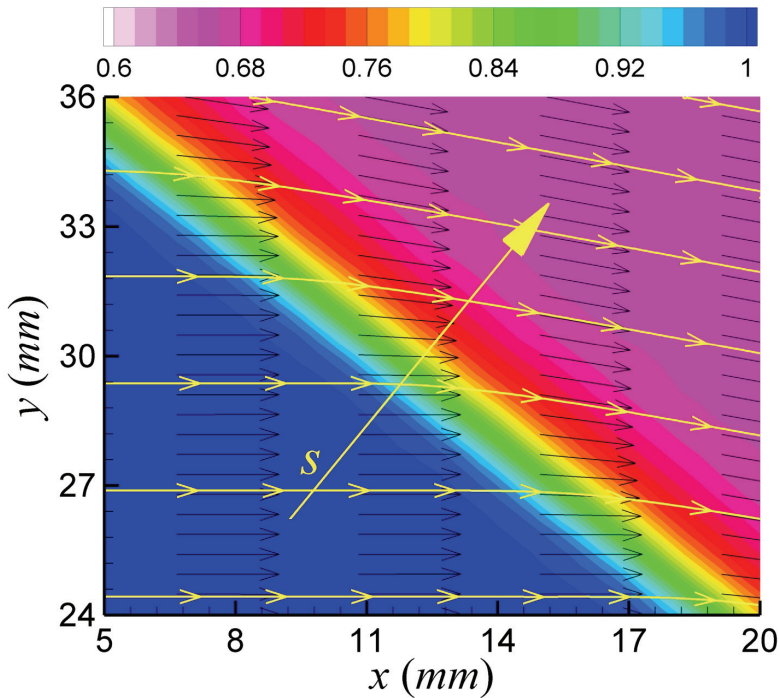


FIGURE 3.8. Distribution of  $\bar{u}_n/\bar{u}_{n1}$  across the OSW. Shock-normal abscissa  $S$  is shown in yellow. Streamlines are also shown in yellow for visualization. Final interrogation window size is  $1.9 \text{ mm} \times 1.6 \text{ mm}$  with a vector spacing of approximately  $0.5 \text{ mm}$ . From Humble *et al.* (2007b).

To assess the temporal response of the particles, the profile of the velocity is shown against  $S$  in figure 3.9, where  $S=0$  denotes the shock wave position. Here,  $\bar{u}_{n1}$  and  $\bar{u}_{n2}$  are the upstream and downstream mean velocity respectively, normal to the shock wave. Observe an appreciable distance before the particle velocity downstream of the shock wave reaches its reference value. The effects of a finite spatial resolution are also evident, where it can be seen that the velocity begins to decrease prematurely, approximately one quarter of a window size upstream of the shock wave (see table 3.2), as a result of the averaging effect intrinsic to the PIV interrogation method. The particle relaxation time  $\tau_p$  was obtained by an exponential curve fit of  $\bar{u}_n = \bar{u}_n(s)$  and returns  $\tau_p = 2.1 \mu\text{s}$ , corresponding to a frequency response  $f_p \sim 500 \text{ kHz}$ . This result was found to be relatively insensitive to small changes in interrogation settings (and even laser pulse time separation

depending on the signal-to-noise ratio), and is also within 5% of the  $\tau_p$  value reported by Schrijer & Scarano (2007) under similar experimental conditions.

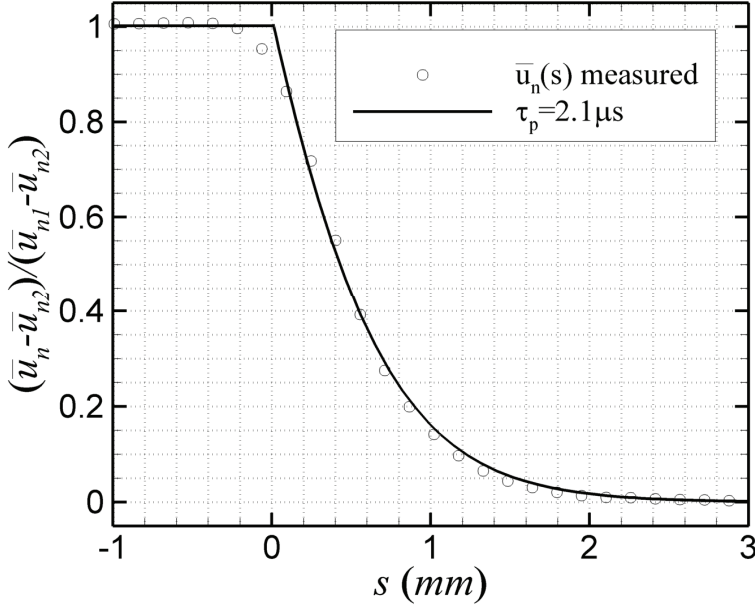


FIGURE 3.9. Velocity profile extracted along  $S$ .  $S=0$  denotes shock wave position. Final interrogation window size is  $1.9 \text{ mm} \times 1.6 \text{ mm}$  with a vector spacing of approximately  $0.5 \text{ mm}$ . From Humble *et al.* (2007b).

The present experimentally determined  $\tau_p$  may be compared with a theoretical value following the approach of Scarano & van Oudheusden (2003) using

$$\tau_p = d_p^2 \frac{\rho_b}{18\mu_f} (1 + 2.7\text{Kn}_d) \quad (3.19)$$

where  $\text{Kn}_d$  is the Knudsen number based on  $d_p$ . An expression for the Knudsen number in terms of the Mach number and Reynolds number is given by (see Schaaf and Chambre 1958)

$$\text{Kn}_d = 1.26\sqrt{\gamma} (M_{\Delta u} / \text{Re}_d) \quad (3.20)$$

where  $\gamma$  is the ratio of specific heats, taken as  $\gamma=1.4$  for air. The Mach number  $M_{\Delta u}$  and Reynolds number is based on  $\Delta u$ , which is taken to be the maximum particle slip velocity, which occurs immediately downstream of the shock wave. This was determined to be  $M_{\Delta u}=0.38$ . The downstream Reynolds number based upon the nominal  $d_p$  was determined to be  $Re_d \sim 1$ . Inserting these parameters into equation (3.19) returns a relaxation time  $\tau_p$  of less than  $1 \mu s$ . The discrepancy between this result and the measured result is ascribed to particle agglomeration, a phenomenon that introduces an uncertainty on the effective particle size and hence response characteristics. Inserting the experimentally determined  $\tau_p$  into equation (3.19) returns an effective particle agglomerate size of  $d_p \approx 900 \text{ nm}$ ; about twice as large as the (average)  $d_p=400 \text{ nm}$  size inferred from electron scans of the porous agglomerates, as reported by Schrijer *et al.* (2006).

As suggested by Samimy & Lele (1991), the particle dynamic effects can be further parameterized by the Stokes number  $St$ , defined as the ratio between  $\tau_p$  and a characteristic flow time-scale  $\tau_f$  ( $St=\tau_p/\tau_f$ ). For accurate flow tracking at the time-scale represented by  $\tau_f$  it is necessary to meet the criterion that  $St \ll 1$ . Taking  $\tau_f$  to be the outer flow time-scale  $\tau_f=\delta/U_\infty$  ( $\approx 20 \times 10^{-3}/520$ ) then this gives  $\tau_f \approx 40 \mu s$ . The corresponding Stokes number is therefore  $St \approx 0.05$ . The tracer particles therefore track the flow with fidelity at the time-scale of  $\tau_f$ . In addition, following the dynamic particle simulation results of Samimy & Lele (1991), this corresponds to a RMS slip velocity of about  $1\% U_\infty$ .

### 3.5.4 Illumination

Flow illumination was provided by a Big Sky CFR PIV-200 Nd:Yag laser with 200 mJ pulsed energy and a 7 ns pulse duration at wavelength 532 nm, as shown in figure 3.10 (left). Laser light access was provided by a probe inserted into the flow downstream of the model, as shown in figure 3.10 (right), along with a rendered impression of the laser light. The laser pulse time separation was  $\Delta t=2 \mu s$ , allowing a particle displacement of 1 mm in the free-stream flow. The light sheet was positioned in the middle of the test-section and was 1.5 mm thick.



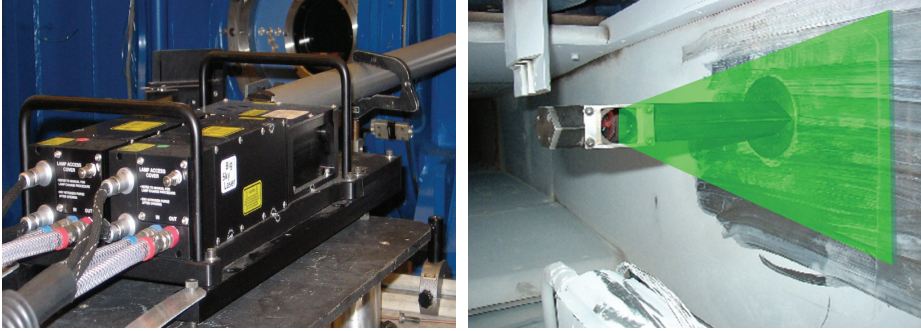


FIGURE 3.10: Photographs of the Big Sky CFR PIV-200 Nd: Yag laser (left), and the laser probe showing rendered impression of the laser light sheet formation (right). The probe is inserted downstream of test-section and is facing upstream, illuminating along the centre-line of the test-section.

### 3.5.5 Image Recording

Particle images were recorded by a PCO Sensicam QE, a 12-bit CCD camera with a  $1376 \times 1040$  pixel-sized sensor. Only 416 pixel rows were used given the large aspect ratio of the investigated flow region, and enabled an increased recording rate of 10 Hz. The camera was equipped with a Nikon 60 mm focal objective with  $f_{\#}=8$ , in combination with a narrow-bandpass 532 nm filter in order to minimize ambient light interference.

The flow was imaged in the streamwise ( $x$ ) and wall-normal ( $y$ ) directions over a field-of-view of  $129 \times 40$  mm<sup>2</sup> ( $6.5\delta \times 2\delta$ ), respectively, resulting in a digital resolution of approximately 11 pixels mm<sup>-1</sup>. A dataset of order 1000 image pairs was acquired (i.e., 1000 velocity fields). The recorded images were interrogated using a cross-correlation algorithm with iterative multi-grid window deformation (see Scarano & Riethmuller 2000). The images were interrogated using a final rectangular interrogation window size of  $21 \times 17$  pixels ( $1.9 \times 1.6$  mm<sup>2</sup>) ( $0.1\delta \times 0.08\delta$ ), with an overlap factor of 75%. This results in a vector spacing of about 0.5 mm ( $0.03\delta$ ). These parameters are summarized in table 3.2 and pertain exclusively to the PIV SWTBLI results presented in §6 2D Flow Organization.

Table 3.2. Summary of the planar PIV recording parameters

Parameter	Quantity
Field-of-view	129(L) $\times$ 40(H) mm <sup>2</sup>
Interrogation volume	1.9 $\times$ 1.6 $\times$ 1.5 mm <sup>3</sup>
Digital image resolution	$\approx$ 11 pixels mm <sup>-1</sup>
Objective focal length	$f=60$ mm
f-number	$f_{\#}=8$
Laser pulse separation	2 $\mu$ s
Seeding density	0.15 ppp

An example of a typical particle image recording of the interaction is depicted in figure 3.11. There is clearly a nonuniform seeding concentration throughout the interaction. In particular, the incident and reflected shock waves can be visualized, whereas the boundary layer is highlighted by a comparatively lower seeding level. Turbulent activity within the downstream boundary layer can also be observed, as well as the intermittent nature of the boundary layer edge. By visual inspection, the seeding density is estimated to be about 0.15 particles per pixel (ppp).

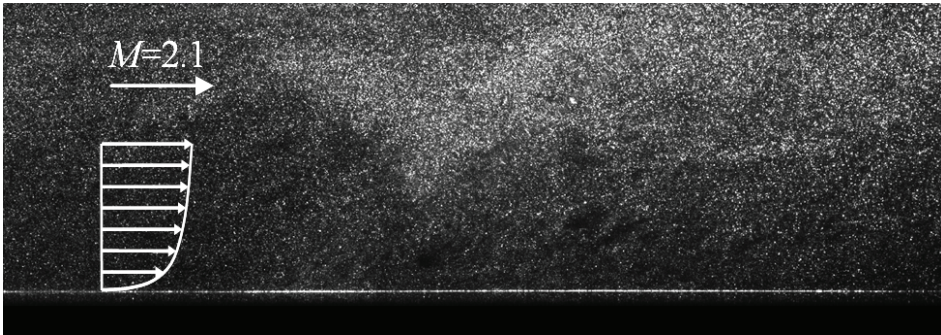


FIGURE 3.11: An example of a typical particle image recording from the planar PIV experiment. Field-of-view is 129 $\times$ 40 mm<sup>2</sup>. Note that the incoming boundary layer is 20 mm thick (based on  $0.99U_{\infty}$ ). From Humble *et al.* (2007b).

Post-processing involved identifying erroneous vectors using the universal median test (see Westerweel & Scarano 2005) with a maximum median deviation set at 2.5. The number of spurious vectors was less than 3% in the dataset. These were removed, and were replaced using a linear interpolation scheme.

## 3.6 Tomographic PIV

### 3.6.1 Working Principles

Tomographic PIV extends the PIV method to three-dimensional space, based on the principles of optical tomography, which essentially reconstructs a three-dimensional volume (the object) on the basis of a set of simultaneous images taken from different viewing directions. A detailed discussion of the principles and implementation of the tomographic PIV technique is given by Elsinga *et al.* (2006), and only its salient features are discussed here.

Briefly, tracer particles are illuminated within a measurement volume by a pulsed light source, as shown in the schematic in figure 3.12, based on Elsinga *et al.* (2006). The scattered light is captured simultaneously from several different viewing directions by a series of CCD cameras. The object is then reconstructed as a three-dimensional light intensity distribution using the multiplicative algebraic reconstruction technique (MART) (see Herman & Lent 1976).

In this approach, the object is represented in discretized form, as a three-dimensional array of cubic voxel elements, and the set of linear equations, which model the imaging system, is solved iteratively. The object is given by a series of three-dimensional voxels in physical space  $(X, Y, Z)$ , with the light intensity given by  $E(X, Y, Z)$ . The projection of the light intensity distribution onto each image pixel  $(x_i, y_i)$  gives the image intensity distribution  $I(x_i, y_i)$  for each viewing direction. The system of equations relating  $E$  and  $I$  is given by

$$\sum_{j \in N_i} w_{i,j} E(X_j, Y_j, Z_j) = I(x_i, y_i) \quad (3.21)$$

where  $w_{i,j}$  is the weighting coefficient that describes the contribution of the  $j$ th voxel intensity  $E(X_j, Y_j, Z_j)$  to the  $i$ th pixel intensity  $I(x_i, y_i)$ .  $N_i$  is the total number of voxels in the line-of-sight corresponding to the  $i$ th pixel  $(x_i, y_i)$ .

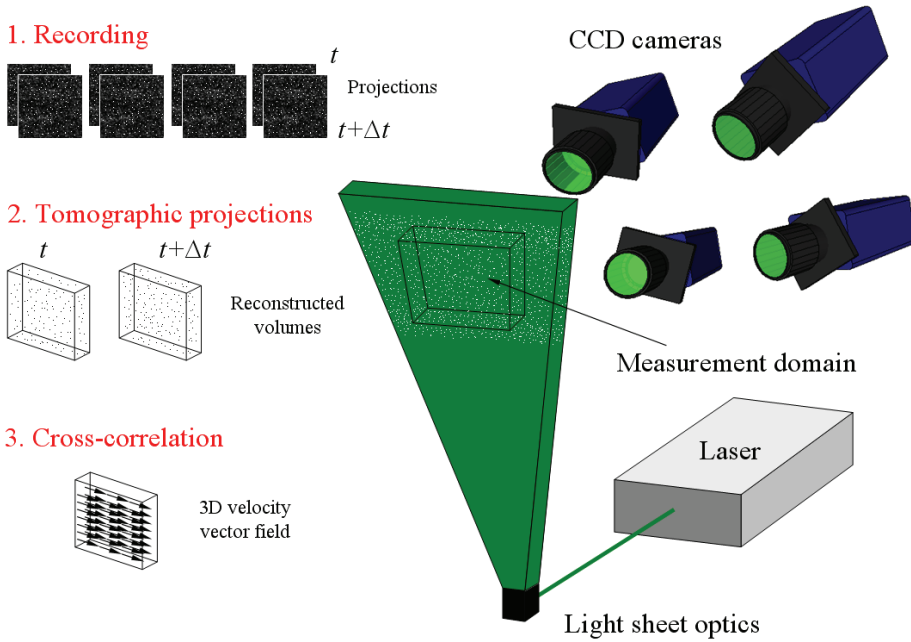


FIGURE 3.12. A schematic of the working principles of tomographic PIV. Procedure includes illuminating the flow with a laser and recording image projections by CCD cameras. The projections are then reconstructed as three-dimensional particle distributions, which are then cross-correlated to give a volumetric velocity vector field. Based on Elsinga *et al.* (2006).

A top-view representation of the imaging model used in the reconstruction is shown schematically in figure 3.13, from Elsinga *et al.* (2006). The grey levels shown indicate the value of  $w_{i,j}$  in each voxel with respect to the pixel  $I(x_1, y_1)$ .

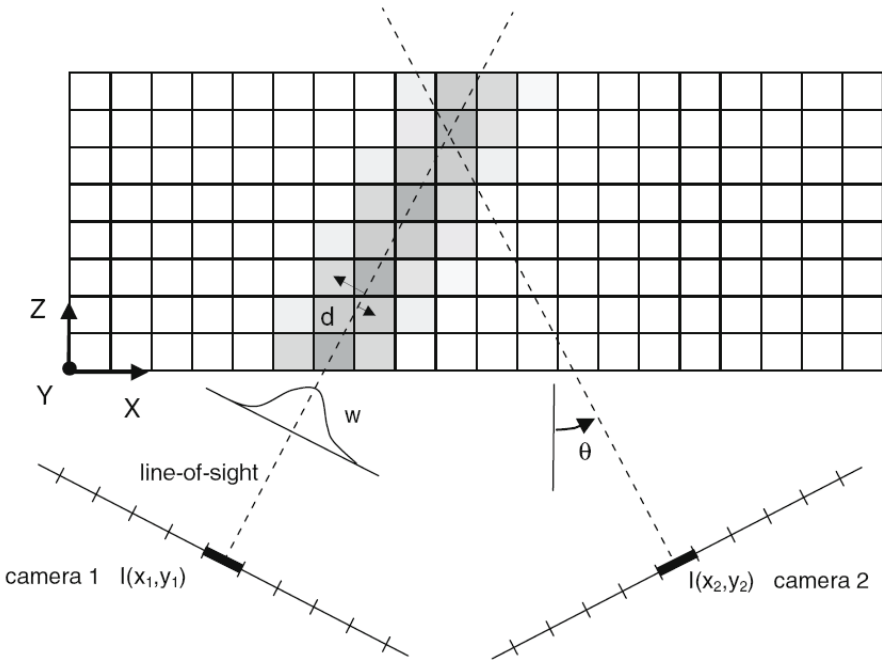


FIGURE 3.13. A top-view schematic representation of the imaging model used in the tomographic reconstruction. *Grey* levels indicate the value of weighting coefficient  $w_{ij}$  in each voxel with respect to the pixel  $I(x_i, y_i)$ . From Elsinga *et al.* (2006).

In practice, the MART is implemented as an iterative technique, with the update of the system of equations based on the ratio between the measured pixel intensity and the projection of the object, along with an appropriate scalar relaxation parameter. The iterative object update is

$$E^{k+1}(X_j, Y_j, Z_j) = E^k(X_j, Y_j, Z_j) \times \left[ I(x_i, y_i) / \sum_{j \in N_i} w_{i,j} E^k(X_j, Y_j, Z_j) \right]^{\mu w_{i,j}} \quad (3.22)$$

where  $\mu$  is the scalar relaxation parameter, with the property that  $\mu \in (0, 1)$ . The magnitude of the update is therefore determined by the ratio of the measured pixel intensity  $I(x_i, y_i)$  with the projection of the

current object  $E^k(X_j, Y_j, Z_j)$ . The MART scheme requires that both  $E$  and  $I$  are positive definite. Elsinga *et al.* (2006) have shown that the accuracy of the tomographic reconstruction depends on a number of parameters including (1) the number of viewing cameras, (2) the particle density present in the images, and (3) to a lesser extent the angles between the viewing directions. The most commonly adopted configuration is four cameras with a seeding density of 0.05 ppp, with viewing angles within the range 15 and 40 degrees (Elsinga *et al.* 2006).

### 3.6.2 Calibration

Since accurate reconstruction relies on accurate triangulation of the camera views, the image coordinates  $(x, y)$  are mapped to those within the reconstructed volume  $(x', y')$  through a calibration procedure, similar to that followed in stereoscopic PIV. A calibration target was recorded by each camera at several depth positions within the volume, providing the different viewing directions and fields-of-view. The physical coordinates were subsequently mapped onto pixel coordinates using

$$\begin{pmatrix} x \\ y \end{pmatrix} = \begin{bmatrix} x' + dx(x', y') \\ y' + dy(x', y') \end{bmatrix} \quad (3.23)$$

To establish the mapping function in a two-dimensional plane perpendicular to the viewing direction, the method of Soloff *et al.* (1997) was used. Alternative methods include the *pinhole model* for instance, but the method of Soloff *et al.* (1997) was found to be superior. In this approach, the offsets  $dx$  and  $dy$  are determined using the normalized coordinates  $s=2(x'-x_0)/n_x$  and  $t=2(y'-y_0)/n_y$ , where  $n_x$  and  $n_y$  are the image size in pixels and  $(x_0, y_0)$  is the origin, and are approximated by a third-order polynomial, as a function of  $s$  and  $t$

$$\begin{pmatrix} dx \\ dy \end{pmatrix} = \begin{pmatrix} a_0 + a_1s + a_2s^2 + a_3s^3 + a_4t + a_5t^2 + a_6t^3 + a_7st + a_8s^2t + a_9st^2 \\ b_0 + b_1s + b_2s^2 + b_3s^3 + b_4t + b_5t^2 + b_6t^3 + b_7st + b_8s^2t + b_9st^2 \end{pmatrix} \quad (3.24)$$

The coefficients of the polynomial were determined by placing a calibration plate containing  $10 \times 10$  markers of known size and position in the measurement plane  $(x', y')$  and recording them as a calibration image located in  $(x, y)$ . Multiple calibrations in planes parallel to the viewing direction were made in steps of 5 mm in depth, over a total range of 10 mm covering the light sheet (i.e., three calibration planes). Linear interpolation was used to find the corresponding image coordinates between depth positions. Calibrations made using additional planes did not significantly affect the results.

After the acquisition of the recorded images during the experiment, a self-calibration procedure was then carried out (see Wieneke 2007). This refines the manual calibration based on the particle images, and redefines the viewing plane such that it coincides with the laser. The three-dimensional mapping function is corrected accordingly. This allows the above-mentioned triangulation to be corrected to a residual disparity below 0.2 pixels (see Wieneke 2007). As also noted by Elsinga (2008), the self-calibration was found to slightly increase the returned vorticity levels, but does not affect the appearance of the flow structures to be discussed. The three-dimensional velocity fields were determined by a three-dimensional spatial cross-correlation of the reconstructed particle distributions.

## 3.7 Tomographic PIV Experimental Arrangement

### 3.7.1 Incoming Boundary Layer

The tomographic PIV experiments necessitated a different experimental arrangement to the planar PIV experiments. In particular, the boundary layer developing along the side-wall was chosen as the test boundary layer in order to improve the optical access through a viewing window. This configuration was also considered advantageous for the digital imaging of high-speed compressible boundary layers, since the density gradient  $(\bar{\rho}_w/\bar{\rho}_e \approx 0.6$  at  $M_e=2.1$ , where  $w$  and  $e$  denote the wall and boundary layer edge conditions, respectively) was now parallel with the viewing direction. This arrangement has been shown by Elsinga *et al.* (2005) to minimize aero-optical distortion effects associated with the PIV

technique. As a result of the above, no aero-optical distortion effects were observed in the tomographic PIV experiments.

The wind-tunnel was operated at a nominal free-stream Mach number  $M_\infty=2.1$  (measured free-stream velocity  $U_\infty=503 \text{ m s}^{-1}$ ), with a stagnation pressure of  $P_0=282 \pm 3 \text{ kPa}$  and stagnation temperature of  $T_0=273 \pm 3 \text{ K}$ . Although the boundary layer develops along the side-wall, it is anticipated that the boundary layer characteristics are the same as for the planar PIV interaction experiment. The interested reader may confirm this by looking ahead to figure 5.3, which shows a comparison of the planar and tomographic PIV undisturbed boundary layer turbulence properties.

### 3.7.2 Shock Generator

A 70 mm chord sting mounted shock generator imposing a deflection angle of  $10^\circ$  was placed in the free-stream flow to generate the incident shock wave and spanned 65% of the test-section height. Previous experiments have shown that this  $10^\circ$  shock generator provides a very similar flow-field along the centre-line as the full-span  $8^\circ$  shock generator used in the planar PIV SWTBLI experiments, i.e., the two interactions are both close to incipient separation, and they share very similar mean velocity and turbulence properties (see Tuinstra 2005).

Unfortunately, there is no surface flow visualization available for the full-span shock generator interaction. And so it must be conceded that a quasisymmetric region alone is insufficient to claim that the two flows are the same; the separation behaviour could of course be different. Given the qualitative nature of the tomographic PIV discussion later on, this is not considered to be a major concern. However, the use of a limited-span shock generator did raise concerns regarding the spanwise uniformity of the interaction region investigated, which are addressed in §5.2. An 80 cm long sting held the shock generator at both ends and was attached to the floor of the wind-tunnel downstream of the test-section. A technical drawing of the complete sting apparatus is shown in figure 3.14.



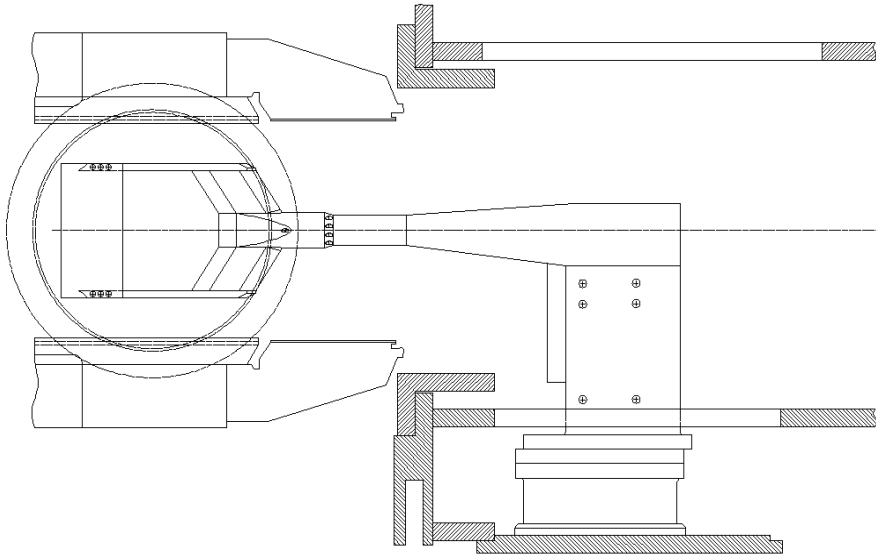


FIGURE 3.14. Technical drawing of the sting apparatus used in the tomographic PIV SWTBLI experiments. Flow direction is from left to right. Drawing is not to scale.

A schematic representation of the experimental arrangement is shown in figure 3.15. Note that the sting has been omitted for clarity. The origin of the reference coordinate system is located at the extrapolated wall impingement point of the incident shock wave, with  $x$  measured in the downstream flow direction,  $y$  in the spanwise direction measured from the centre of the test-section, and  $z$  normal to the wall.

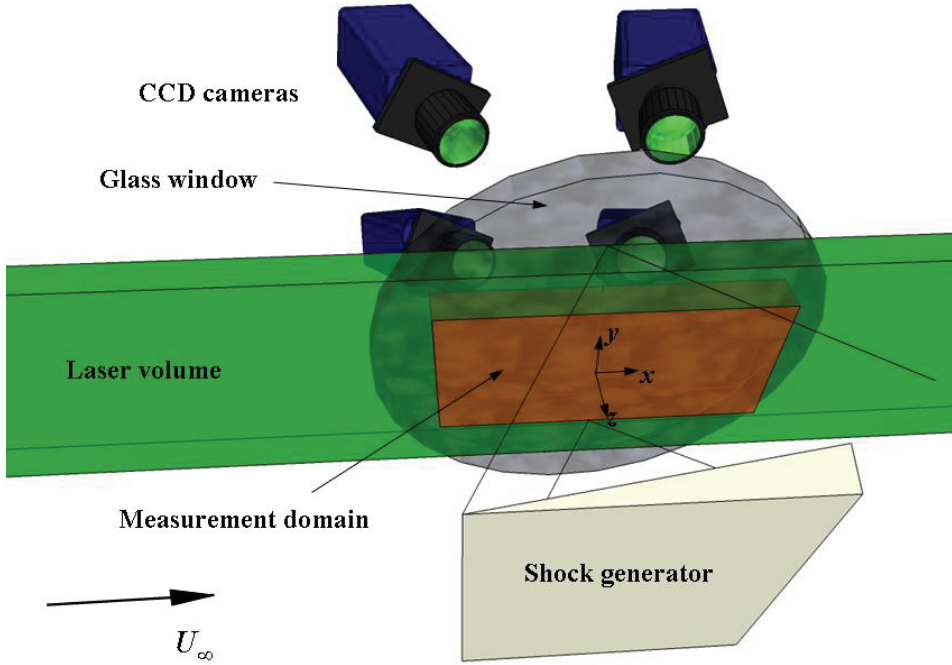


FIGURE 3.15: Schematic representation of the tomographic PIV SWTBLI experimental arrangement. Note that the sting has been omitted for clarity. From Humble *et al.* (2008).

### 3.7.3 Flow Seeding

The boundary layer developing on the side-wall also necessitated a different flow seeding distribution system to the one used in the planar PIV SWTBLI experiments. In particular, a pipe of 10 mm diameter was inserted into the side of the settling chamber to seed the upstream boundary layer. Kemira-300  $\text{TiO}_2$  particles with a manufacturer-specified nominal diameter of 170 nm and a bulk density of  $200 \text{ kg m}^{-3}$  were adopted as tracers (see also Schrijer *et al.* 2006) due to a shortage of the UV-TITAN L830 50 nm particles. The flow was seeded to an average particle concentration of  $2 \text{ particles mm}^{-1}$  (16 particles per interrogation box). The average particle image density was approximately 0.05 ppp. The particle relaxation time of the 170 nm particles across an incident shock wave has been previously measured to be  $\tau_p = 2.3 \mu\text{s}$ , corresponding to a frequency response  $f_p \sim 450 \text{ kHz}$  (Schrijer & Scarano 2007).

The corresponding Stokes number (based on  $\delta/U_\infty \approx 40 \mu\text{s}$ ) was about 0.06, indicating again that the particles track the flow with fidelity at the time-scale of  $\tau_f$ . This also corresponds to a RMS slip velocity of about  $1\%U_\infty$ . Interestingly, this suggests that despite the difference in nominal diameters between the 50 nm and 170 nm particles, they actually agglomerate to similar sizes, and therefore have similar temporal response characteristics.

### 3.7.4 Illumination

The seeded flow was illuminated by a Spectra-Physics Quanta Ray double-pulsed Nd:Yag laser, with 400 mJ pulsed energy and a 6 ns pulse duration at wave-length 532 nm. Laser light access into the test-section was provided by the laser probe used in the planar PIV SWTBLI experiments, but with the light shaped into a volume using light optics. Because of the illumination very close to the wall, a knife-edge slit filter was used before light entered the probe in order to remove the low-energy fringes present, and to give a better approximation of a top-hat light intensity distribution. This confinement of the illuminated region also facilitated the tomographic reconstruction phase. To minimize reflections, illumination was almost tangent to the wall. The laser pulse separation was set at  $2 \mu\text{s}$ , which allowed a particle displacement in the free-stream of approximately 1 mm ( $\approx 20$  voxels).

### 3.7.5 Image Recording

Particle images were recorded by four LaVision Imager Pro X CCD cameras with a  $2048 \times 2048$  14-bit pixel-sized sensor (acknowledgments to LaVision GmbH), as shown in figure 3.16. Only 1216 pixels were used in the spanwise direction of the interaction given the aspect ratio of the flow region investigated. At the same time, this enabled an increased recording rate of 10 Hz. The flow was imaged in the streamwise, spanwise, and wall-normal directions over a volume of approximately  $70 \times 40 \times 10 \text{ mm}^3$  ( $3.5\delta \times 2\delta \times 0.5\delta$ ), respectively, with a digital imaging resolution of approximately  $23 \text{ pixels mm}^{-1}$ . The solid angle enclosed between all four cameras was  $40^\circ \times 35^\circ$  in the streamwise–wall-normal and spanwise–wall-normal planes, respectively.

Each camera was equipped with a Nikon 60 mm focal objective, with Scheimpflug adapters to place the focal plane in the mid-section of the measurement volume and so maintain the entire measurement domain in focus. The objectives were equipped with a narrow-bandpass 532 nm filter to minimize ambient light interference. The two cameras in forward scatter had f-number  $f_{\#}=11$ , whereas the two cameras in back-scatter had f-number  $f_{\#}=8$ .

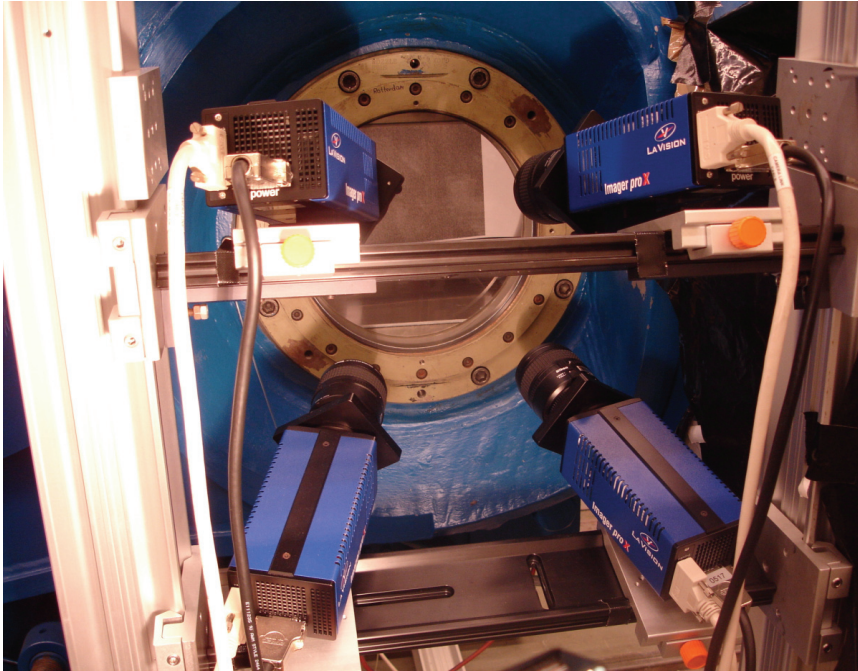


FIGURE 3.16: Photograph of the tomographic PIV SWTBLI experimental arrangement.

The tomographic PIV recording parameters are summarized in table 3.3 and pertain exclusively to the PIV SWTBLI results presented in §7 3D Flow Organization. Synchronization between the cameras, laser, and image acquisition was accomplished by a LaVision programmable timing unit controlled through DaVis 7.3 software, which was also used in the data recording, volume calibration, self-calibration, reconstruction, and the three-dimensional cross-correlation based interrogation that yielded the velocity vector fields.

Table 3.3. Summary of the tomographic PIV recording parameters

Parameter	Quantity
Field-of-view	70(L) $\times$ 40(H) $\times$ 10(W) mm <sup>3</sup>
Interrogation volume	2.1 $\times$ 2.1 $\times$ 2.1 mm <sup>3</sup>
Digital image resolution	$\approx$ 23 pixels mm <sup>-1</sup>
Objective focal length	$f=60$ mm
f-number	$2\times f_{\#}=11$ , $2\times f_{\#}=8$
Laser pulse separation	$2 \mu\text{s}$
Seeding density	0.05 ppp

In view of a boundary layer thickness of 20 mm, the tomographic PIV field-of-view extends over only half of the boundary layer thickness. Experiments were therefore performed in two regions, which are described in table 3.4, carried out by translating both the light probe and camera system. Reconstructed volumes were discretized at  $20^3$  voxels per mm<sup>3</sup>. The particle images were interrogated using windows of final size  $42\times 42\times 42$  voxels with an overlap factor of 75%, resulting in a vector spacing of about 0.5 mm ( $0.03\delta$ ) in each direction. These two regions characterize the lower and upper parts of the interaction, respectively. A dataset of order 200 velocity vector volumes was acquired in each region.

Table 3.4. Description of the tomographic PIV measurement regions

	$\Delta x$ , mm	$\Delta y$ , mm	$z$ -range, mm	Vector grid size ( $x, y, z$ )	Vector spacing (mm)
Lower region	75 ( $3.8\delta$ )	40 ( $2.0\delta$ )	2–12 ( $0.1$ – $0.6\delta$ )	141 $\times$ 74 $\times$ 22	0.54 ( $0.03\delta$ )
Upper region	69 ( $3.5\delta$ )	42 ( $2.1\delta$ )	12–20 ( $0.6$ – $1.0\delta$ )	130 $\times$ 79 $\times$ 20	0.53 ( $0.03\delta$ )

Particle images were preprocessed before volume reconstruction to eliminate background illumination and to reduce the effects of random noise. This involved subtracting the time-minimum background intensity, as well as a sliding spatial minimum using a kernel of 51 pixels. Gaussian smoothing using a kernel of  $3 \times 3$  points with a standard deviation of unity was then applied (see Elsinga 2008 for further details).

Figure 3.17 shows an example of an instantaneous raw image on the left, and the preprocessed image on the right. It should be remarked that the pre-processing discussed above does not affect the validity of the results (see for example figure 5.3), but was found by Elsinga (2008) to improve the reconstruction quality (defined as the correlation coefficient between the reconstructed and an exact light intensity distribution) by 7% for noise levels of 10% (where noise is expressed as a ratio of background light intensity with the peak intensity) for example. In the present data, the effect of pre-processing was mainly to increase the signal-to-noise ratio by about 10%, to an average value of about 2.5 within the measurement domain.

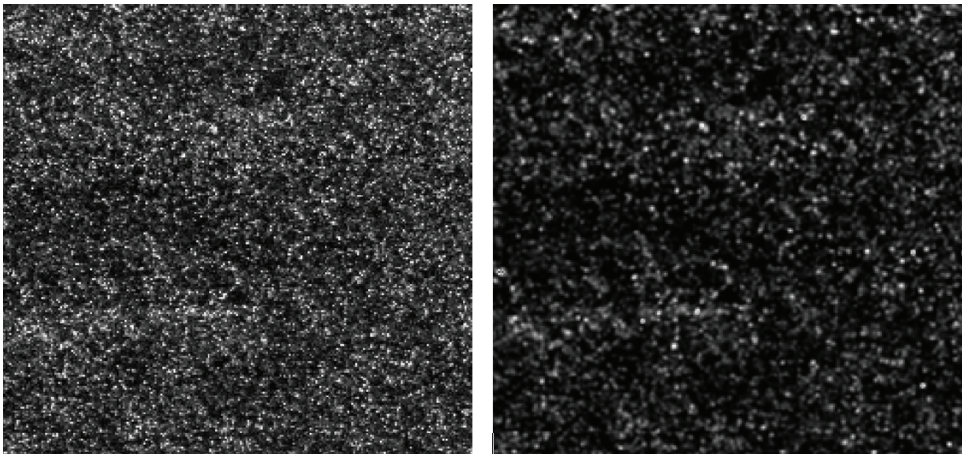


FIGURE 3.17: An example of an instantaneous raw image (left) and the preprocessed image (right).

Post-processing involved identifying erroneous vectors using the universal median test (see Westerweel & Scarano 2005) with a maximum median deviation set at 2.5. The number of spurious vectors was less than 5% in the dataset. (This number was slightly higher, typically at 7% using the original particle images.) These spurious vectors were removed, and replaced using a linear interpolation scheme. To ease visualization, the instantaneous velocity fields were filtered using a three-dimensional Gaussian filter based on a kernel of  $3 \times 3 \times 3$  points with a standard deviation of unity.

### 3.7.6 Reconstruction

As an illustrative example of the tomographic PIV reconstruction, a representation of the three-dimensional light intensity distribution from the experiment in the lower region is shown in figure 3.18 (see also Scarano *et al.* 2006 for a similar representation). The yellow and red spheres indicate light intensity maxima in the first and second exposures, respectively. The sphere radii are scaled proportional to the square root of the particle intensity. Using this figure as an indication of particle positions, it can be seen that the particle density increases somewhat within the compression region ( $x/\delta > -1.5$ ), although this is difficult to observe in this representation. Closer inspection reveals that in many cases paired particles can be distinguished, whereas in many other cases unpaired particles can be observed. The variation in light intensity is ascribed to particle agglomeration, a phenomenon which introduces an uncertainty on the effective particle size.



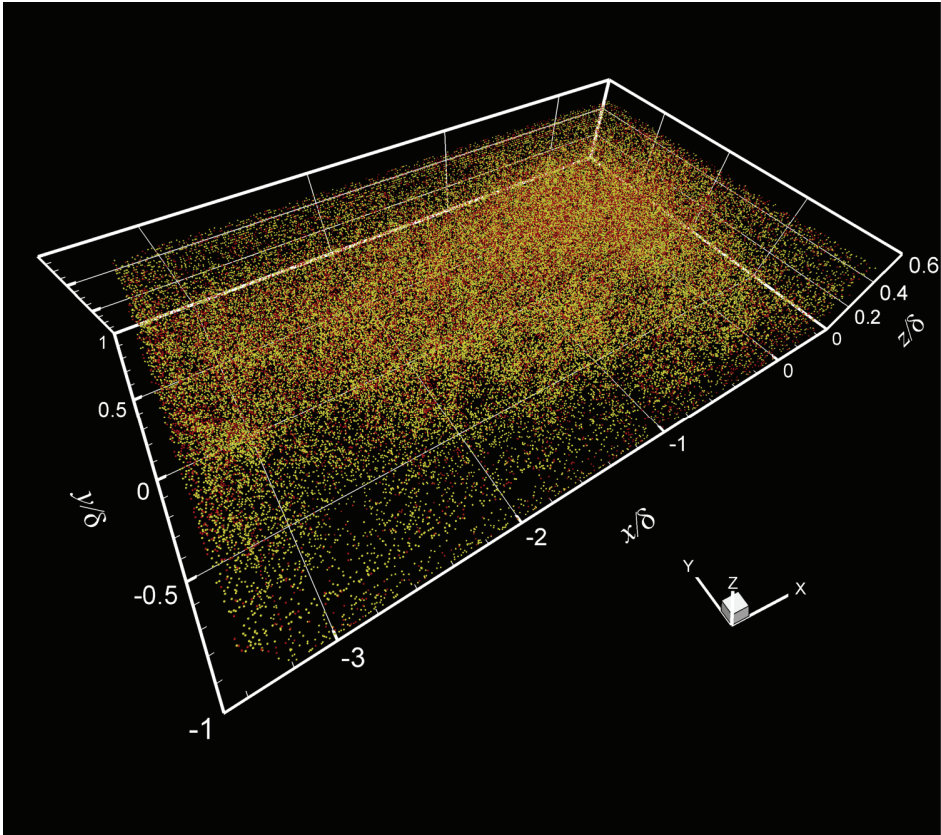


FIGURE 3.18: Representation of the three-dimensional light intensity distribution of the interaction: lower region ( $z/\delta=0.1-0.6$ ). Yellow and red spheres indicate light intensity maxima in the first and second exposures, respectively. The radii of the spheres are scaled proportional to the square root of the particle intensity following Scarano *et al.* (2006).

A three-dimensional cross-correlation of such a particle distribution yields a volumetric velocity vector field. An example of a typical velocity vector field for the lower region of the interaction is shown in figure 3.19. The vectors are shown in a convective frame of reference of  $0.8U_\infty$  and only vectors at the boundaries of the measurement domain are displayed for clarity.



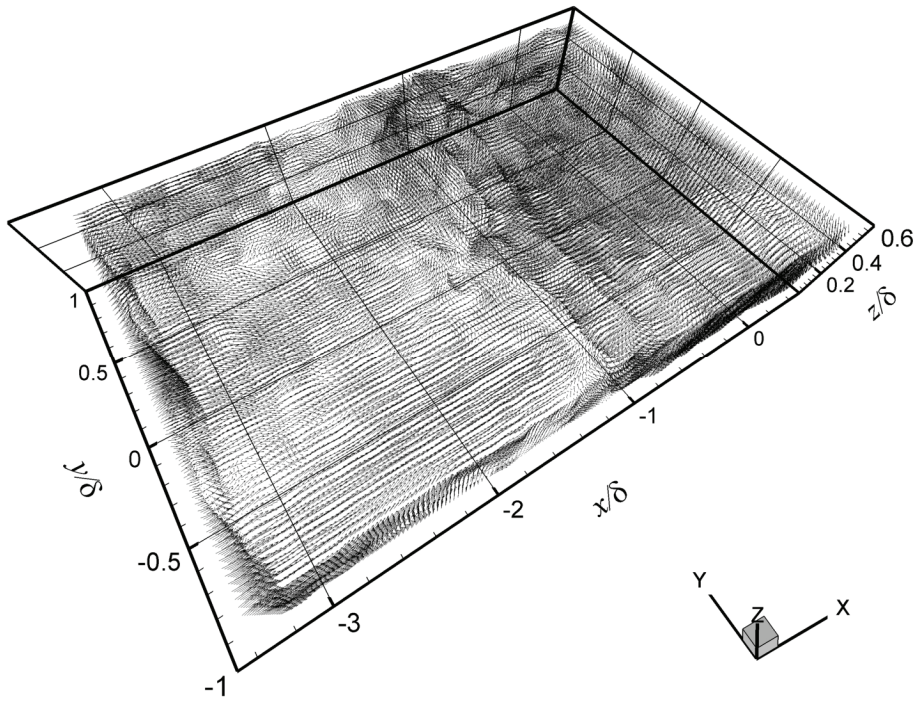


FIGURE 3.19: An example of the velocity vector distribution within the interaction: lower region ( $z/\delta=0.1-0.6$ ). Vectors are shown in a convective reference frame of  $0.8U_\infty$  and only vectors at the boundaries of the measurement domain are displayed for clarity. From Humble *et al.* (2008).

### 3.8 Uncertainty Analysis

If the results in this thesis are to be meaningful, then one should aim to communicate on the quality of the data obtained. Having outlined the principles of the measurement techniques and the experimental parameters used, we are now in a position to conduct an uncertainty analysis of the measured properties. Such an analysis is imperative in order to quantitatively assess the quality of the results to be discussed, to substantiate their validity, as well as to guide us on an appropriate discussion of their nature.

### 3.8.1 Analysis Outline

The accuracy of an experimental measurement indicates the closeness of agreement between an experimentally determined value of a quantity and its true value, and we define *error* as this difference (Stern *et al.* 1999). Now in reality, true values of measured quantities are rarely known, and we must estimate this error, and this estimate is our *uncertainty* (Stern *et al.* 1999). To quantify the measurement uncertainties in the present study, we consider a forward uncertainty propagation approach, using linear-error propagation equations. This involves propagating uncertainty using prior assumptions about the various contributing errors. This method was chosen because its mathematical background is well-documented, it requires only minimal calculations, and it is relatively quick and easy to implement. Other forward uncertainty propagation approaches include Monte Carlo propagation and reliability methods for example.

Before proceeding, it is worth mentioning that disadvantages of the forward uncertainty approach in general, include the assumptions of Gaussian and independent (uncorrelated) errors, (although the method can be extended to non-Gaussian distributions and correlated errors), and that the models (i.e., the various expressions relating the measured properties) are valid representations of the real physical system (i.e., the experiment). The approach will be shown to be well-suited to the present study, however, which seeks to provide a rough estimate of the measurement uncertainties associated with the measured properties.

The field of uncertainty quantification in experimental fluid dynamics is very large, and we therefore aim to communicate only some of the salient features here. We begin by following the approach originally outlined by Kline & McClintock (1953), although the reader is also referred to the detailed work of Stern *et al.* (1999), who provide an extensive summary of the AIAA Standard (1995) for experimental uncertainty assessment methodology. Since we are dealing with experimental data from PIV, we primarily concern ourselves with the measurement uncertainties associated with velocity. To begin with, the following expressions for determining the statistical properties are valid for the velocity components (the streamwise component for example):

The mean values:

$$\bar{u}(\mathbf{x}) = \frac{1}{M} \sum_{n=1}^M u(\mathbf{x}, t_n) \quad (3.25)$$

The normal stresses:

$$\overline{u'^2}(\mathbf{x}) = \frac{1}{M} \sum_{n=1}^M [u(\mathbf{x}, t_n) - \bar{u}(\mathbf{x})]^2 \quad (3.26)$$

The Reynolds-averaged shear stress:

$$\overline{u'v'}(\mathbf{x}) = \frac{1}{M} \sum_{n=1}^M [u(\mathbf{x}, t_n) - \bar{u}(\mathbf{x})][v(\mathbf{x}, t_n) - \bar{v}(\mathbf{x})] \quad (3.27)$$

where  $\mathbf{x} = \{x, y\}$  and  $\mathbf{x} = \{x, y, z\}$  in the planar and tomographic PIV experiments, respectively,  $M$  is the ensemble size (i.e., the total number of PIV velocity fields), and  $t_n$  is the  $n$ th time instant. The RMS measurement uncertainty  $\varepsilon$  associated with a finite number of samples  $M$  of velocity fields may be quantified using the following expressions (see Benedict & Gould 1996):

The mean velocity:

$$\varepsilon_{\bar{u}} = \frac{\sqrt{\overline{u'^2}}}{\sqrt{M}} \quad (3.28)$$

The RMS velocity:

$$\varepsilon_{\sqrt{\overline{u'^2}}} = \varepsilon_{\langle u' \rangle} = \frac{\sqrt{\overline{u'^2}}}{\sqrt{2M}} \quad (3.29)$$

The Reynolds-averaged shear stress:

$$\varepsilon_{u'v'} = \frac{\sqrt{1 + R_{uv}^2} \sqrt{u'^2} \sqrt{v'^2}}{\sqrt{M}} \quad (3.30)$$

where  $R_{uv}$  is the correlation coefficient given by

$$R_{uv} = \frac{\overline{u'v'}}{\sqrt{\overline{u'^2}} \sqrt{\overline{v'^2}}} \quad (3.31)$$

which has its own uncertainty given by

$$\varepsilon_{R_{uv}} = \frac{1 - R_{uv}^2}{\sqrt{M}} \quad (3.32)$$

In addition, each instantaneous velocity vector is affected by measurement error and therefore has an associated RMS measurement uncertainty  $\varepsilon_u$ . Similarly, each velocity gradient has an RMS uncertainty (e.g.,  $\varepsilon_{\partial u/\partial x}$ ). (Note that the uncertainties of the mean properties due to a limited ensemble size already include the uncertainties of the instantaneous values.) The magnitudes of these uncertainties in PIV are more difficult to estimate than for the mean properties. They depend on a wide range of parameters, such as final window interrogation size, particle image density, uncertainties on the particle displacements, the laser pulse time separation, calibration procedure, etc. (see Raffel *et al.* 2007). To attempt to quantify the measurement uncertainty associated with these contributions, let us first generalize this situation, and follow the outline given by Kline & McClintock (1953), by considering the measurement of a quantity  $y$  that depends on a series of  $n$  variables  $x$ , such that

$$y = f(x_1, x_2, \dots, x_n) \quad (3.33)$$

Each variable  $x$  is subject to a RMS measurement uncertainty  $\varepsilon_x$ , as well as a RMS measurement uncertainty on the quantity  $y$  itself  $\varepsilon_y$ .

Using a Taylor series expansion and neglecting terms of  $O(\Delta x)^2$  we may estimate the RMS measurement uncertainty of our quantity  $y$  as

$$\varepsilon_y = \sqrt{\left(\frac{\partial f}{\partial x_1} \varepsilon_{x_1}\right)^2 + \left(\frac{\partial f}{\partial x_2} \varepsilon_{x_2}\right)^2 + \dots + \left(\frac{\partial f}{\partial x_n} \varepsilon_{x_n}\right)^2} \quad (3.34)$$

where the partial derivatives are termed *sensitivity coefficients*. These sensitivity coefficients are a measure of the way errors in the individual measurements propagate as errors in the experimental result. In essence, if a small error in one of the measured variables  $x$  propagates into a small error in the result  $y$ , then the larger the sensitivity coefficient, the more sensitive  $y$  is to that small error in  $x$  (see also Stern *et al.* 1999).

Note that we assume that each  $\varepsilon_x$  is uncorrelated with one another. Although this is not strictly true, this assumption will be sufficient for our present purpose, which is to establish a rough estimate of the measurement uncertainties. In addition, the reader may also note that we have implicitly assumed a statistical dispersion that is one standard deviation of a Gaussian distribution (i.e., 68.3%). To be even more conservative, we could have considered  $n$  standard deviations, in which case each  $\varepsilon_x$  would be multiplied by  $n$ .

With this framework at hand, we can develop it within the context of the present experiments, to make estimates on the overall RMS uncertainty on the instantaneous velocity and velocity gradient, and other related quantities. Consider first the instantaneous velocity  $u$ . Adopting a linear error propagation procedure, we establish the sensitivity coefficients for the velocity as

$$u = \frac{\Delta s}{\Delta t}, \quad \left| \frac{\partial u}{\partial (\Delta s)} \right| = \frac{1}{\Delta t}, \quad \left| \frac{\partial u}{\partial (\Delta t)} \right| = \frac{\Delta s}{\Delta t^2} \quad (3.35)$$

where  $\Delta s$  is the (maximum) physical particle displacement between laser pulses, and  $\Delta t$  is the pulse time separation. Both  $\Delta s$  and  $\Delta t$  have their own RMS uncertainties  $\varepsilon_{\Delta s}$  and  $\varepsilon_{\Delta t}$ , respectively. To determine them, let  $\kappa$  be the (reciprocal) spatial resolution given by  $\kappa = l_c / n_c$ , where  $l_c$  is the distance between the calibration plate dots

corresponding to  $n_c$  pixels. (Alternatively,  $\kappa$  may also be defined as  $\kappa=L_x/n_x$ , where  $L_x$  is the length of the field-of-view corresponding to  $n_x$  pixels.) The sensitivity coefficients associated with  $\kappa$  are therefore

$$\left| \frac{\partial \kappa}{\partial l_c} \right| = \frac{1}{n_c}, \quad \left| \frac{\partial \kappa}{\partial n_c} \right| = \frac{l_c}{n_c^2} \quad (3.36)$$

Hence the RMS uncertainty of the resolution  $\varepsilon_\kappa$  is estimated by

$$\varepsilon_\kappa = \sqrt{\left( \frac{\partial \kappa}{\partial l_c} \varepsilon_{l_c} \right)^2 + \left( \frac{\partial \kappa}{\partial n_c} \varepsilon_{n_c} \right)^2} = \sqrt{\left( \frac{1}{n_c} \varepsilon_{l_c} \right)^2 + \left( \frac{l_c}{n_c^2} \varepsilon_{n_c} \right)^2} \quad (3.37)$$

where  $\varepsilon_{n_c}$  is the RMS uncertainty associated with  $n_c$ , and  $\varepsilon_{l_c}$  is the RMS uncertainty associated with  $l_c$ . In the planar PIV study, we consider  $\varepsilon_{l_c}^\ddagger$  to be the misalignment between the calibration plate and laser sheet, whereas for the tomographic PIV study  $\varepsilon_{l_c}=0$ , due to the self-calibration, where in both cases we assume that the distance between the physical calibration dots is known exactly. The RMS uncertainty on the particle displacement  $\varepsilon_{\Delta s}$  is therefore given by

$$\varepsilon_{\Delta s} = \sqrt{(\kappa \varepsilon_{cc})^2 + \left( \frac{\Delta s}{\kappa} \varepsilon_\kappa \right)^2} \quad (3.38)$$

where  $\varepsilon_{cc}$  is the RMS uncertainty in the digital cross-correlation, which is a measure of the error in determining the displacement based on the PIV cross-correlation. The RMS uncertainty on the velocity  $\varepsilon_u$  can now be estimated using

$$\varepsilon_u = \sqrt{\left( \frac{\partial u}{\partial (\Delta s)} \varepsilon_{\Delta s} \right)^2 + \left( \frac{\partial u}{\partial (\Delta t)} \varepsilon_{\Delta t} \right)^2} \quad (3.39)$$

---

<sup>‡</sup> Strictly speaking, this is in fact a maximum uncertainty not an RMS uncertainty, although for simplicity it will be considered as such in the present analysis.

which can be expressed in terms of the sensitivity coefficients as

$$\varepsilon_u = \sqrt{\left(\frac{1}{\Delta t} \varepsilon_{\Delta s}\right)^2 + \left(\frac{\Delta s}{\Delta t^2} \varepsilon_{\Delta t}\right)^2} \quad (3.40)$$

Since the velocity is sampled on an evenly-spaced Cartesian grid, finite differencing may be used to determine the velocity gradients, and we can estimate the associated RMS uncertainty. To proceed, we first assume that the measurement uncertainty in each neighbouring quantity is independent of their neighbours. Although this is again not strictly true because of the finite overlap and smoothing of the vectors, the resulting analysis will provide a rough estimate of the measurement uncertainty. Consider the central differencing scheme, which gives the local gradient (in this case  $\partial u/\partial x$ ) at the  $i$ th location

$$\left(\frac{\partial u}{\partial x}\right)_i \approx \frac{u_{i+1} - u_{i-1}}{2\Delta x} \quad (3.41)$$

where  $\Delta x$  is the vector spacing  $\Delta x = W_s(1-\text{OF})\kappa$ , where  $W_s$  is the window size (in pixels) and OF is the overlap factor, where  $\text{OF} \in (0, 1)$ . The RMS uncertainty  $\varepsilon_{\Delta x}$  is therefore  $\varepsilon_{\Delta x} = W_s(1-\text{OF})\varepsilon_\kappa$ . Adopting a similar procedure as above, we may establish sensitivity coefficients for the velocity gradient as

$$\left|\partial\left(\frac{\partial u}{\partial x}\right)/\partial u_{i+1}\right| = \left|\partial\left(\frac{\partial u}{\partial x}\right)/\partial u_{i-1}\right| = \frac{1}{2\Delta x}, \quad \left|\partial\left(\frac{\partial u}{\partial x}\right)/\partial \Delta x\right| = \frac{\partial u}{\partial x} \frac{1}{\Delta x} \quad (3.42)$$

The associated RMS measurement uncertainty  $\varepsilon_{(\partial u/\partial x)}$  (say) of the velocity gradient is then given by

$$\varepsilon_{(\partial u/\partial x)} = \sqrt{\left[\frac{\partial\left(\frac{\partial u}{\partial x}\right)}{\partial u_{i+1}} \varepsilon_u\right]^2 + \left[\frac{\partial\left(\frac{\partial u}{\partial x}\right)}{\partial u_{i-1}} \varepsilon_u\right]^2 + \left[\frac{\partial\left(\frac{\partial u}{\partial x}\right)}{\partial \Delta x} \varepsilon_{\Delta x}\right]^2} \quad (3.43)$$

where we base  $\varepsilon_u$  on the free-stream displacement in order to obtain the largest measurement uncertainty on  $\varepsilon_{(\partial u/\partial x)}$ . The RMS uncertainty of the velocity gradient can therefore be expressed in terms of the sensitivity coefficient values as

$$\varepsilon_{(\partial u/\partial x)} = \sqrt{2 \left( \frac{1}{2\Delta x} \varepsilon_u \right)^2 + \left( \frac{\partial u}{\partial x} \frac{\varepsilon_{\Delta x}}{\Delta x} \right)^2} \quad (3.44)$$

### 3.8.2 Summary of Measurement Uncertainties

Using the outline above, the RMS measurement uncertainties for the planar and tomographic PIV experiments are summarized in table 3.5 based on the parameters outlined above and taken from literature where appropriate. The reader should note that this analysis does not hold at all spatial scales within the flow, but only those relevant to the spatial resolution of the experiments; specifically those scales of the order of the final interrogation window size and above. Also, many of these uncertainties represent ‘worst case scenarios’, in the sense that maximum displacements, RMS values etc., have been used in order to provide conservative estimates of the RMS uncertainties. The reader will also observe that not all of the uncertainties reported here are relevant to our discussion, but they are included for completeness.

In general, it can be seen that the largest RMS uncertainties are associated with the instantaneous velocity gradients, instantaneous vorticity, and Reynolds-averaged shear stress, although the latter in the tomographic PIV experiments is attributed to the limited number of volumes obtained. These will become important points for discussion in forthcoming chapters. Overall, it can be concluded that most of the quantities to be discussed have a sufficiently low RMS uncertainty to warrant a quantitative discussion (i.e., < 5% say), and those quantities which do not, we will restrict ourselves to a more qualitative discussion, although this will not affect the overall conclusions to be drawn.



Table 3.5. Summary of RMS measurement uncertainties

Parameter	Planar PIV	Tomographic PIV
$U_\infty$	518 m s <sup>-1</sup>	503 m s <sup>-1</sup>
Ensemble size $M$	1000	200
$L_x$	129 mm	70 mm
$n_x$	1376 pixels	2048 pixels
$\kappa = L_x/n_x$	0.09 mm pixel <sup>-1</sup>	0.03 mm pixel <sup>-1</sup>
$1/\kappa$	11 pix. mm <sup>-1</sup>	29 pix. mm <sup>-1</sup>
$l_c$	10 mm	10 mm
$n_c$	110 pixels	290 pixels
$W_s$ (in $x$ direction)	21 pixels	42 pixels
OF	75%	75%
$\varepsilon_{cc}$	0.1 pixels <sup>a</sup>	0.1 pixels <sup>a</sup>
$\varepsilon_{lc}/l_c$	<0.1% <sup>b</sup>	0
$\varepsilon_{nc}$	0.1 pixels <sup>c</sup>	0.2 pixels <sup>d</sup>
$\varepsilon_\kappa/\kappa$	<0.1%	<0.1%
$\Delta s$	1 mm	1 mm
$\Delta t$	2 $\mu$ s	2 $\mu$ s
$\Delta x$	0.5 mm	0.5 mm
$\varepsilon_{\Delta s}/\Delta s$	0.9%	0.3%
$\varepsilon_{\Delta t}/\Delta t$	0.4% <sup>e</sup>	0.3% <sup>e</sup>
$\varepsilon_{\Delta x}/\Delta x$	<0.1%	<0.1%
$\varepsilon_{\bar{u}}/U_\infty$	<0.1% <sup>f</sup>	0.1% <sup>f</sup>
$\varepsilon_{\bar{v}}/U_\infty$	0.6% <sup>g</sup>	1.4% <sup>g</sup>
$\varepsilon_{\langle u \rangle}/U_\infty$	0.4% <sup>h</sup>	1% <sup>h</sup>
$\varepsilon_{\langle u \rangle}/\langle u \rangle_{\max}$	2.2% <sup>i</sup>	5% <sup>i</sup>
$\varepsilon_{\bar{u}\bar{v}}/(\bar{u}\bar{v})_{\max}$	25% <sup>j</sup>	55% <sup>j</sup>
$\varepsilon_{R_{uv}}/(R_{uv})_{\max}$	5% <sup>k</sup>	10% <sup>k</sup>
$\varepsilon_{u^2}/U_\infty$	1%	2%
$\varepsilon_{(\partial u/\partial x)}/(\partial u/\partial x)_{\text{RMS}}$	18% <sup>l</sup>	36% <sup>l</sup>
$\varepsilon_{ \omega }/(\partial u/\partial x)_{\text{RMS}}$	25% <sup>m</sup>	88%
$\varepsilon_{\text{slip}}/U_\infty$	1% <sup>n</sup>	1% <sup>n</sup>

<sup>a</sup> see Raffel *et al.* (2007).

<sup>b</sup> based on laser sheet thickness and calibration plate length.

<sup>c</sup> based on Soloff *et al.* (1997) polynomial fit RMS.

<sup>d</sup> based on the self-calibration disparity map (see Wieneke 2007).

- <sup>c</sup> based on the laser pulse width.
- <sup>f</sup> based on the free-stream RMS.
- <sup>g</sup> based on the maximum RMS.
- <sup>h</sup> based on the maximum RMS.
- <sup>i</sup> based on the maximum RMS.
- <sup>j</sup> based on the maximum  $R_{wv}$  and RMS values.
- <sup>k</sup> based on the maximum  $R_{wv}$ .
- <sup>l</sup> based on the maximum  $(\partial u / \partial x)_{\text{RMS}}$ .
- <sup>m</sup> for planar PIV absolute vorticity is taken to be the out-of-plane component.
- <sup>n</sup> RMS slip velocity based on the particle dynamics simulation of Samimy & Lele (1991) assuming a Stokes number  $St=0.05-0.06$ .

# CHAPTER

# 4

# DATA ANALYSIS

# METHODS

---

## 4.1 Introductory Remarks



THE complexity of the interaction will make it desirable to distil from the experimental evidence a simplified description of the overall dynamics that can be more readily understood. To achieve this, it is desirable to record accurate data that reveal the instantaneous structure of the flow-field, and then seek approaches for its analysis and synthesis that can lead to a reduced-order description, while at the same time ensuring that the most important features are retained. Two approaches that can be used in this role is the proper orthogonal decomposition (POD) (see Berkooz *et al.* 1993), and nonlinear time series analyses, the latter often used within the context of chaos theory (see Guckenheimer 1986). Both have been used in fluid dynamics and will be shown to be

particularly well-suited to the present SWTBLI problem. We devote this chapter to a description of these approaches and their implementation in the present study.

## 4.2 Proper Orthogonal Decomposition

The POD offers a rational procedure for decomposing a signal into a basis of nonspecified functions, chosen to represent the energy of that signal in the fewest number of modes. The attractiveness of the technique lies in its optimality, in the sense of an automatic generation of problem-optimized (modal) base functions, where a finite number of these modes represent more energy than any other set of orthogonal modes. In other disciplines, the POD technique goes by other names, such as Karhunen-Loève decomposition, principal component analysis, as well as the Hotelling transformation, and the POD has been used in a wide variety of applications, ranging from meteorology and oceanography (see e.g., Preisendorfer 1988) to artificial neural networks (see e.g., Krischer *et al.* 1993).

With the experimental discovery of coherent motions within turbulent fluid flows (see e.g., Townsend 1956), the first real evidence that a reduction in the complexity of turbulence might be possible was recognized, and approaches for the analysis and synthesis of the data were sought. One of the earliest applications of POD in fluid dynamics was by Lorenz (1956) in meteorology, where he used it as a method to identify large-scale features observed to be generated in the atmosphere. Somewhat later, the technique was introduced into turbulent flow research by Lumley (see Lumley 1967), to exploit the presence of coherent motions, and was used as a rational method to highlight them. Yet the method was rather demanding to implement in its original form, however, until Sirovich (1987) proposed the *method of snapshots* to dramatically reduce the memory resources associated with processing large amounts of data.

One of the most extensive uses of the technique has been by Aubry *et al.* (1988), who used it to construct a low-order description of the coherent structures in a turbulent boundary layer. In a pioneering work, Herzog (1986) performed a complete three-dimensional POD analysis of a wall-bounded flow using a full two-point correlation dataset. With the proliferation of DNS, POD analyses have received

a new impetus. For example, Moin & Moser (1989) used DNS data of channel flow and carried out a comprehensive POD analysis. Also, Liberzon *et al.* (2005) have recently used POD on three-dimensional vorticity fields also obtained from DNS of a turbulent boundary layer flow.

The use of PIV data in POD analyses is also becoming increasingly common. For instance, Patte-Rouland *et al.* (2001) have applied POD to PIV data of an annular jet, and were able to dissociate the oscillation of the recirculation region and velocity fluctuations due to the turbulence flow behaviour. Bernero & Fiedler (2000) also considered the application of POD to PIV data of a jet in counterflow, and made statements about the stability of the flow. PIV data are particularly suited for POD analyses, since the entire spatial velocity field is available, leading to the construction of global eigenmodes that can be used to further characterize the instantaneous spatial organization of the flow. This is one of the main motivations for adopting the technique in the present study, as well as the ease of its implementation, and well-documented mathematical background.

Work in the application of POD to compressible flows, however, is not as abundant. Notable work in this area includes the study of Rowley *et al.* (2003), who have developed a framework for applying POD and Galerkin projection to compressible fluids. Also, Moreno *et al.* (2004) applied POD to PIV data to investigate compressible jet flows, to produce a low-order description of the flow phenomena present. Humble *et al.* (2007c) have also applied POD to PIV data on the compressible planar base flow problem, to delineate the underlying flow organization of the near wake structure with increasing compressibility. The application of POD to the present flow problem is therefore considered to be well-posed.

In what follows, an outline of the mathematical formulation of the POD is given. The interested reader is referred to the excellent review by Berkooz *et al.* (1993) for a more complete mathematical outline of the technique and its application to turbulent flows, including a discussion of the technique within the context of dynamical systems modelling, as well as its relation to some other techniques typically used in turbulence studies, such as linear stochastic estimation (see e.g., Adrian & Moin 1988) and conditional sampling (see e.g., Antonia 1981) for example.

## 4.3 Mathematical Outline of POD

### 4.3.1 Direct Method

In the present study, the fluctuating velocity field with respect to the estimated mean pattern is decomposed into a limited number of modes using the POD. The data in the present study represent velocity obtained from the PIV study. The mean velocity at a point  $\bar{u}(\mathbf{x})$  is subtracted from the instantaneous velocity  $u(\mathbf{x}, t)$ , leaving only data containing fluctuations from the mean  $u'(\mathbf{x}, t)$ , where  $\mathbf{x}=\{x, y\}$  and  $\mathbf{x}=\{x, y, z\}$  in the planar and tomographic PIV cases, respectively. The POD extracts time-independent orthonormal basis functions, empirical eigenfunctions, or eigenmodes,  $\psi_k(\mathbf{x})$ , and time-dependent orthonormal amplitude coefficients,  $a_k(t)$ , such that the reconstruction

$$u'(\mathbf{x}, t) = \sum_{k=1}^{\infty} a_k(t) \psi_k(\mathbf{x}) \quad (4.1)$$

is optimal, in the sense that the functions  $\psi$  maximize the normalized averaged projection of  $\psi$  onto  $u'$ , viz.

$$\max_{\psi} \frac{\langle (\psi(\mathbf{x}), u'(\mathbf{x}, t))^2 \rangle}{(\psi(\mathbf{x}), \psi(\mathbf{x}))} \quad (4.2)$$

Here,  $(f, g)$  denotes the  $L^2$  inner product

$$\int_{\Omega} f g^* d\Omega \quad (4.3)$$

where  $\Omega$  is the flow domain,  $*$  denotes complex conjugation, and the time-average is defined as

$$\langle \cdot \rangle = \lim_{T \rightarrow \infty} \frac{1}{T} \int_0^T dT \quad (4.4)$$

Thus, if the flow-field is projected along  $\psi(\mathbf{x})$ , then the average energy content is larger than if the flow-field is projected along any other structure, e.g., a Fourier mode. In the space orthonormal to this  $\psi(\mathbf{x})$ , the process may be repeated, and the complete set of  $k$  eigenmodes  $\psi_k(\mathbf{x})$  may be determined. It can be shown by calculus of variation (see Berkooz *et al.* 1993) that the necessary condition to maximize expression (4.2) is to solve the Fredholm integral equation of the second type

$$\int_{\Omega} R(\mathbf{x}; \mathbf{x}') \psi(\mathbf{x}') d\mathbf{x}' = \lambda \psi(\mathbf{x}) \quad (4.5)$$

The kernel of equation (4.5) is the averaged space-correlation tensor and is given by

$$R(\mathbf{x}; \mathbf{x}') = \langle u'(\mathbf{x}, t) u'^T(\mathbf{x}', t) \rangle \quad (4.6)$$

This space-correlation tensor is symmetric and positive definite. The non-negative and self-adjoint properties of  $R(\mathbf{x}; \mathbf{x}')$  ensure that all eigenvalues are real and non-negative, and can therefore be ordered such that  $\lambda_k \geq \lambda_{k+1} \geq \dots \geq 0$ . There is in fact a denumerable set of orthonormal solutions  $\psi_k(\mathbf{x})$  with corresponding real and positive eigenvalues  $\lambda_k$ . The eigenvalue with the largest magnitude is the maximum achieved in the maximization problem. The second largest eigenvalue is the maximum of the maximization process restricted to the space orthonormal to the first eigenmode

$$\max_{\psi \in L^2} \frac{\langle (\psi, u' - (u', \psi) \psi)^2 \rangle}{(\psi, \psi)} \quad (4.7)$$

where the arguments have been temporarily dropped for simplicity. The third largest eigenvalue is the maximum achieved when restricted to the space orthonormal to the first two, and so on. The eigenmodes have the following orthogonality condition

$$(\psi_i(\mathbf{x}), \psi_j(\mathbf{x})) = \delta_{ij} \quad (4.8)$$

where  $\delta_{ij}$  is the Kronecker delta with the property that

$$\delta_{ij} = \begin{cases} 1, & \text{if } i = j \\ 0, & \text{if } i \neq j \end{cases} \quad (4.9)$$

The eigenmodes can therefore be used as a basis for the flow-field

$$u'(\mathbf{x}, t) = \sum_{k=1}^{\infty} a_k(t) \psi_k(\mathbf{x}) \quad (4.10)$$

The coefficients  $a_k(t)$  are determined by the projection of the flow-fields on the global modes

$$a_k(t) = (u'(\mathbf{x}, t), \psi_k(\mathbf{x})) \quad (4.11)$$

The amount of energy of  $u'(\mathbf{x}, t)$  in the direction of  $\psi_k(\mathbf{x})$  is  $a_k(t)^2$ . Thus, the total energy is the sum of  $a_k(t)^2$  in all the different directions

$$e(t) = (u'(\mathbf{x}, t), u'(\mathbf{x}, t)) = \sum_{k=1}^{\infty} a_k(t)^2 \quad (4.12)$$

and their mean values are the eigenvalues  $\lambda_k$

$$\langle a_i(t) a_j(t) \rangle = \lambda_k \delta_{ij} \quad (4.13)$$

The POD ensures that the eigenmodes are optimal with respect to this energy content. That is, any other set of modes contain less energy on time-average, than the set of POD eigenmodes. To determine the eigenmodes, however, we must solve the Fredholm integral equation. Since  $R(\mathbf{x}; \mathbf{x}')$  is a full symmetric matrix, solving the integral equation is generally computationally expensive.



### 4.3.2 Snapshot Method

Sirovich (1987) therefore proposed the *method of snapshots* to make use of the fact that  $u'(\mathbf{x}, t)$  and  $\psi_k(\mathbf{x})$  span the same linear space. This enables the POD eigenmodes to be written as a linear sum of the data vectors. Consider the present experiments where  $N$  data measurements are simultaneously taken at  $M$  time instants  $t_n$ , such that the samples are uncorrelated and linearly independent. For the snapshot method, we require a set of  $M$  snapshots  $u'(\mathbf{x}, t_n)$  such that

$$u'_n(\mathbf{x}, t) = u'(\mathbf{x}, t_n) \quad (4.14)$$

The maximization problem can thus be reformulated for the snapshot problem as

$$\max_{\psi} \frac{\frac{1}{M} \sum_{n=1}^M (\psi(\mathbf{x}), u'(\mathbf{x}, t_n))^2}{(\psi(\mathbf{x}), \psi(\mathbf{x}))} \quad (4.15)$$

where the kernel  $R(\mathbf{x}; \mathbf{x}')$  is now approximated using the ergodicity hypothesis to state that

$$R(\mathbf{x}; \mathbf{x}') = \lim_{n \rightarrow \infty} \sum_{n=1}^M u'(\mathbf{x}, t_n) u'^T(\mathbf{x}', t_n) \quad (4.16)$$

The time between the snapshots must be large enough so that they are uncorrelated. In the present experiments, the acquisition frequency between any two velocity fields is 10 Hz, and so they may be considered uncorrelated in time with respect to the frequencies of interest (i.e.,  $O(\text{kHz})$ ). We also require a large enough sample size  $M$ , such that we make a reasonable approximation of  $R(\mathbf{x}; \mathbf{x}')$ . An acceptable degree of statistical convergence in the planar POD eigenspectrum was found to be reached if the ensemble size contained typically more than 100 realizations, consistent with previous studies by Humble *et al.* (2007c), who have considered the application of POD to PIV data in compressible planar base flows. As will be seen

later, statistical convergence is not obtained in the tomographic POD analysis (see e.g., figures 4.2 and 7.14), although this does not affect the conclusions to be drawn. Substituting (4.16) into the Fredholm integral equation results in a degenerate integral equation, in which the solutions are linear combinations of the snapshots

$$\psi_k(\mathbf{x}) = \sum_{n=1}^M \Phi_n^k u'(\mathbf{x}, t_n), \quad k = 1, \dots, M \quad (4.17)$$

where  $\Phi_n^k$  is the  $n$ th component of the  $k$ th eigenvector. The eigenmodes can then be found by solving the following eigenvalue problem

$$C\Phi = \lambda\Phi \quad (4.18)$$

where  $C$  is the correlation matrix given by

$$C_{ij} = \frac{1}{M} (u'_i(\mathbf{x}), u'_j(\mathbf{x})) \quad (4.19)$$

In this way, the eigenvectors of the  $N \times N$  matrix  $R$  are found by computing the  $M \times M$  matrix  $C$ —an attractive method in the case when  $M \ll N$ , as applies in the present study. (i.e., for the planar POD analysis, the ensemble size  $M \sim 500$ , whereas each snapshot containing vector fields of size  $N = 271(n_x) \times 116(n_y) \approx 31\,000$ . For the tomographic POD analysis,  $M \sim 100$ , whereas each snapshot containing vector fields of size  $N = 141(n_x) \times 74(n_y) \times 22(n_z) \approx 230\,000$ . The ensemble values were dictated mainly by memory limitations.)

The reconstruction of a snapshot using a truncated subset of  $K$  modes can be performed with

$$u(\mathbf{x}, t_n) = \bar{u}(\mathbf{x}) + \sum_{k=1}^K a_k(t_n) \psi_k(\mathbf{x}) \quad (4.20)$$

The total energy is given by the sum of the eigenvalues  $\lambda_k$ . Each eigenmode may therefore be assigned an energy percentage  $E_k$  based on the eigenmode's eigenvalue, such that

$$E_k = \lambda_k / \sum_{i=1}^M \lambda_i \quad (4.21)$$

In compressible flows, the best choice of norm is not obvious: many of the (inter-related) variables, including thermodynamic quantities may be important (see Rowley *et al.* 2004). This poses potential difficulties when only velocimetry data in compressible flow is at hand. For the purposes of the present study, the mean square fluctuating value of the velocity is used as the norm, which represents the ‘kinetic energy’ of the flow. This is the most common choice in POD analyses, even in compressible flows (see Moreno *et al.* 2004), and will be shown to be sufficient for our present purpose, which is to use the POD eigenmodes to further characterize the unsteady flow organization of the interaction. It is worth mentioning, however, that other authors have explored other norms associated with PIV data, such as the study by Kostas *et al.* (2005), who considered enstrophy, as well as kinetic energy. The use of POD vorticity modes was also explored in the present study, but the results were found to be unsatisfactory, which is thought to be due to the inadequate spatial resolution of the data.

To demonstrate the potential of the POD technique within the context of the present study, figure 4.1 shows the modal energy and cumulative modal energy distributions of the two-dimensional POD eigenmodes obtained from the planar PIV SWTBLI results (see §3.5 and §6.6). The POD eigenspectrum reveals that the first eigenmode is by far the most dominant, capturing almost 20% of the total energy; almost four times greater than the next eigenmode. A mode that contributes a substantial proportion of the total energy of the flow is considered to play a more significant role in the flow dynamics, than a mode that contains less energy (Kostas *et al.* 2005). It therefore appears that the first eigenmode represents an important contribution to the interaction’s unsteadiness, and this will become a focal point of our discussion later on.

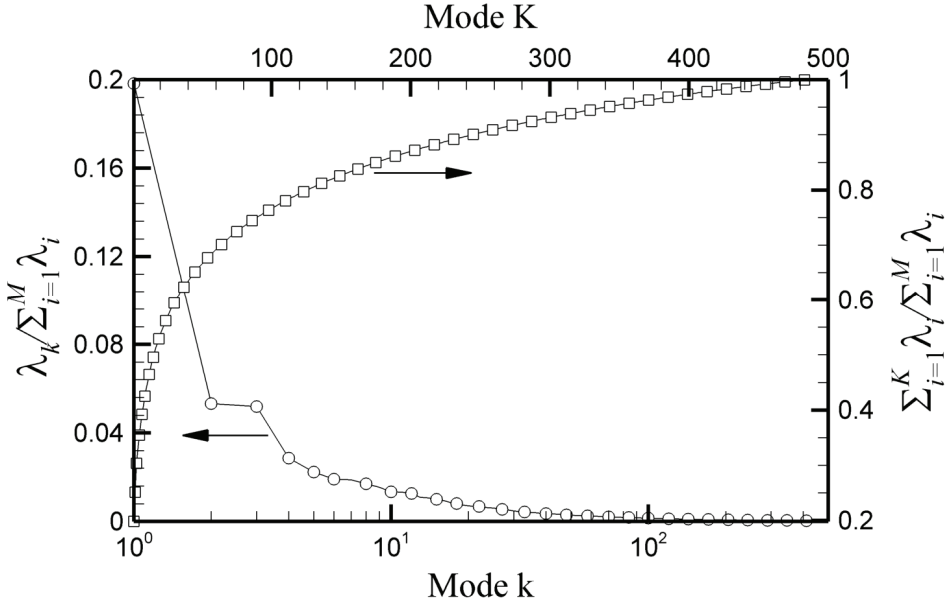


FIGURE 4.1. Eigenspectrum of the planar POD analysis. Modal energy content shown for the  $k$ th eigenmode and cumulative modal energy shown for the  $K$ th cumulative sum. Arrows assign data with appropriate axis.

In addition, Berkooz *et al.* (1993) has shown that if the eigenspectrum decays fast enough, then all the likely realizations of the flow can be found in a small set of subspace. The cumulative ratio  $\sum_{i=1}^K \lambda_i / \sum_{i=1}^M \lambda_i$  gives an indication of this energy convergence, by showing the amount of energy contained in the  $M$  element system, contained in the first  $K$  eigenmodes. To capture most of the energy, it is necessary that  $\sum_{i=1}^K \lambda_i \approx \sum_{i=1}^M \lambda_i$  and it is desirable that  $K \ll M$ .

The cumulative energy distribution shows that over 70 modes are required to capture 75% (say) of the total energy. In comparison, other POD studies that have used planar PIV data, such as the one by Bernero & Fielder (2000), report about 20 modes in their study of a jet in counter-flow, and Patte-Rouland *et al.* (2001), report about 60 modes in their study of an annular jet, for the same amount of energy. Only a limited number of modes (say  $< 10$ ) contain an appreciable fraction of the total energy (say  $> 2\%$ ), and we will therefore restrict our attention to discussing them later on.

Figure 4.2 shows the modal energy and cumulative modal energy distributions for the eigenmodes obtained from the tomographic PIV results.

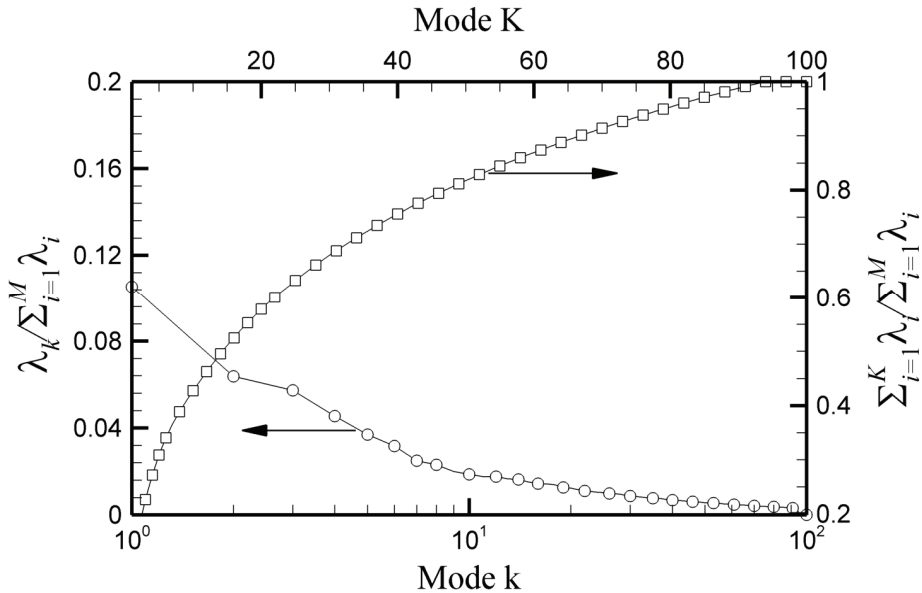


FIGURE 4.2. Eigenspectrum of the tomographic POD analysis. Modal energy content shown for the  $k$ th eigenmode and cumulative modal energy shown for the  $K$ th cumulative sum. Arrows assign data with appropriate axis. The vertical scale has been chosen to be same as for the planar POD eigenmodes for comparison.

The modal energy distribution shows again that the first eigenmode is by far the most dominant, containing over 10% of the total energy. Furthermore, only a limited number of eigenmodes (say  $< 10$ ) contain a significant fraction of the total energy. The cumulative energy distribution shows that over 40 modes are required to capture 75% of the total energy, which is comparable to the planar POD eigenmodes. It can therefore be concluded that an appreciable amount of total energy is captured within a subset of eigenmodes in both the planar and tomographic PIV data, but more importantly, these eigenmodes will be shown to provide a synthesis of the results later on. The application of the POD to the present SWTBLI problem is therefore considered to be well-posed.

## 4.4 Nonlinear Time Series Analysis

In the analysis and synthesis of our HWA time series data, we seek tools that can provide a powerful way to describe complicated observations with relatively simple mathematics. In the past few decades, scientists have become increasingly aware that relatively simple deterministic systems can behave in a complex, and seemingly unpredictable, or chaotic manner. Such systems have been found to arise in a large number of disciplines, ranging from mathematics and physics, to biology, chemistry, sociology, economics, and psychology to name a few (see e.g., Thompson & Stewart 1986).

In particular, the ability of seemingly simple nonlinear systems to produce complicated behaviour is very suggestive of turbulent fluid flows, and the application of nonlinear dynamical systems theory to fluid dynamics has consequently received much interest. When such systems have a limited number of degrees of freedom and exhibit complicated behaviour in time, which never repeats itself exactly, and which have a sensitive (exponential) dependence on deviations in the initial conditions, then the study of such systems falls within the domain of *chaos theory* (see e.g., Sprott 2003).

As noted by Aubry *et al.* (1988), the first explicit link between chaos theory and turbulence was made by Ruelle & Takens (1971), although Lorenz (1963) had already obtained a three-dimensional family of (chaotic) ordinary differential equations, as a minimal model for two-dimensional Rayleigh-Bénard convection. Several classical experiments have since then been conducted, which have demonstrated that chaos, or at least the route(s) to chaos, exists in fluid dynamical systems, the most extensive considering Taylor-Couette flow and Rayleigh-Bénard convection (see e.g., Guckenheimer 1986 for further details). Accounts of important works in this field can also be found in Lanford (1982) and Sreenivasan (1991) and the references cited therein.

However, as noted by Sommerer *et al.* (1997), chaos theory is no panacea for resolving the many problems of fluid dynamics. Like any theory applied to such a difficult field as fluid dynamics, there is always hope for a major breakthrough, followed by disappointment when none is forthcoming, followed by a more careful examination of the methods used (Sommerer *et al.* 1997). Chaos theory is arguably passing through the second to third phase now, and the reader must

be aware of this when formulating a view of the current state of the field within the context of fluid dynamics. As further noted by Sommerer *et al.* (1997), the applications of chaos theory are limited primarily to low-excitation flows, often those that are two-dimensional, and it also has a limited predictive capability. Despite all of this, however, it has made some important conceptual contributions in fluid dynamics, such as replacing Landau's classical picture of the onset of turbulence with Ruelle and Taken's strange attractor theory (although even the latter is considered incomplete, see Sommerer *et al.* 1997), and a nonlinear dynamics approach has proven fruitful in many cases relevant to the present study, such as elucidating the nature of coherent motions within boundary layers for example (see Aubry *et al.* 1988).

In light of the above, we therefore consider, along with many others, that chaos theory is not an all-encompassing theory of fluid dynamics, but rather a broad collection of tools that can provide a powerful way to describe complicated observations with relatively simple (albeit somewhat abstract) mathematics. In the present study, we wish to analyze a time series signal of the fluctuating mass-flux measured at an appropriate location within the interaction using HWA and apply a range of tools from nonlinear time series analysis (to be discussed below) to reveal hidden temporal structure that is not immediately obvious from the time series signal itself.

Now at the outset, it is worth stressing that there still remain active criticisms and suspicions on the existence of chaos in fluid dynamics. It is therefore necessary to address some of these concerns, in order to provide the reader with a clearer picture as to the purpose and limitations of what follows. As discussed at some length by Sivakumar (2000), the main reasons for these concerns are essentially the assumptions with which chaos identification methods have been developed: i.e., infinite and noise-free data, and the inability of the methods to provide irrefutable proof of the existence of chaos. These are at odds with the fact that experimental datasets are always noisy and finite. Sivakumar (2000) therefore concludes that the limitations of each specific method means that it may not be possible to provide a definite resolution of whether or not processes exhibit chaotic behaviour based on the application of a single method. To this, Cecen *et al.* (2004) also notes that applied research often fails to mention

these limitations explicitly, and the intricate details of the analysis often hide the statistical tests used. In the present study, this has motivated the use of a diverse range of characterization techniques, which will guide us on ascertaining whether or not the results from each of them are consistent, keeping in mind the interpretations and limitations of the methods used.

#### 4.4.1 Attractor Reconstruction

To begin with, consider a fluctuating mass-flux time signal within the interaction obtained by HWA. We denote this time sequence as  $x(t)$ ,  $t=1, \dots, N$ , where  $N$  is the number of data points. For the analyses that follow, it will be convenient to view  $x(t)$  in a state-space, which contains all of the possible states (see e.g., Thompson & Stewart 1986 for a rather qualitative introductory discussion on nonlinear dynamics and chaos theory). Each state is a value of fluctuating mass-flux (or as will be shown later, fluctuating velocity to first order), and corresponds to a unique point in state-space. The temporal evolution of  $x(t)$  may therefore be characterized as a moving particle travelling a trajectory in state-space. An *attractor* exists if there is a subset of state-space to which orbits tend to as time increases. The attractor will be considered *periodic* if  $x(t) = x(t+T)$  for some nonzero value  $T$ , and *nonperiodic* if  $x(t) \neq x(t+T)$  for  $t > T$ , although  $x(t)$  can come arbitrarily close to  $x(t+T)$  an arbitrary number of times.

Now, we would like to present a projection of this attractor onto a space of limited dimension that corresponds to the hot-wire signal. In other words, we would like to reconstruct a multidimensional state-space from a single observable only (i.e.,  $x(t)$ ). In a seminal paper, Packard *et al.* (1980) were the first to show that a dynamical system could be reconstructed based only on its output. As noted by Moore & Stenning (2001), they proposed that *any* time series of quantities measured from a dynamical system may be sufficient to construct a model that preserves its essential structure. This remarkable idea was later given a firm mathematical foundation by Takens (1981), who showed that if we measure the signal for a sufficient amount of time, then it is possible to reconstruct the attractor using delayed (or time-lagged) coordinates and an appropriate embedding procedure.



To be more precise, given its importance for what follows, we take some time to outline this embedding approach in a necessarily mathematical style. For  $t > 0$  consider that  $s(t)$ ,  $t=1, \dots, N$ , is a state of the dynamical system under consideration. Let  $\mathbf{s}(t)$  be the vector containing  $\{s(t)\}$  lying in an  $n$ -dimensional state-space denoted by  $M$ . Strictly speaking,  $M$  is a manifold, which is some subset of  $\mathbb{R}^n$ . Following Cambell *et al.* (2005), let the time evolution of  $\mathbf{s}(t)$  (i.e., the motion of the point through state-space) be given by some function

$$f^\tau : M \rightarrow M \quad (4.22)$$

such that

$$f^\tau [\mathbf{s}(t)] = \mathbf{s}(t + \tau) \quad (4.23)$$

where  $\mathbf{s}(t + \tau)$  is some future state, and  $\tau$  is called (somewhat inappropriately here) the *time-delay*. Now, we cannot observe  $\mathbf{s}(t)$ ; we only have our single time series  $x(t)$ . But consider a *generic* smooth map such that

$$\Phi : M \rightarrow \mathbb{R}^d \quad (4.24)$$

For  $d \geq 2n+1$ , Taken's (1981) embedding theorem tells us that  $\Phi$  is an *embedding*.<sup>§</sup> That is, the map  $\Phi$  can get us to every point in its image  $\Phi(\mathbf{s}(t))$ , and that it is differentiable in both directions. As noted by Cambell *et al.* (2005), the consequences of this are far-reaching. To illustrate this, we can define a map

$$F = \Phi \circ f \circ \Phi^{-1} \quad (4.25)$$

---

<sup>§</sup> It has since been shown, by several authors, that the condition  $d \geq 2n+1$  does not have to be necessarily satisfied (see e.g., Rosenstein *et al.* 1993).

which may be viewed as the same dynamical system as  $f$  under the coordinate transformation given by  $\Phi$ . This is important, because it means that coordinate-independent quantities of interest that we will consider later on, such as the correlation dimension and Lyapunov exponent etc., will be identical on  $f$  and  $F$ . Now, given a smooth observation function

$$h: M \rightarrow \mathbb{R} \quad (4.26)$$

and considering that  $\mathbf{x}(t)=h(\mathbf{s}(t))$ , then we can define an instance of  $\Phi$ , such that

$$\Phi(\mathbf{s}(t)) = \left\{ h(\mathbf{x}(t)), h(f^{-\tau}(\mathbf{x}(t))), \dots, h(f^{-(d-1)\tau}(\mathbf{x}(t))) \right\} \quad (4.27)$$

which can be written as

$$\Phi(\mathbf{s}(t)) = \left\{ x(t), x(t-\tau), x(t-2\tau), \dots, x(t-(d-1)\tau) \right\} \quad (4.28)$$

As further noted by Cambell *et al.* (2005), this provides a snapshot of the system  $\mathbf{x}(t)=\Phi(\mathbf{s}(t))$ , in our new space  $\mathbb{R}^d$ , the dynamics of which are given by  $F$ . The power of the approach lies in the fact that  $F$  is defined entirely in terms of the time-delay  $\tau$  in the observations, viz.

$$\begin{aligned} F^\tau \left\{ x(t), x(t-\tau), x(t-2\tau), \dots, x(t-(d-1)\tau) \right\} \\ = \left\{ x(t+\tau), x(t), \dots, x(t-(d-2)\tau) \right\} \end{aligned} \quad (4.29)$$

In essence then, we deduce the properties of  $F$  and hence  $f$  entirely in terms of the observed time series  $x(t)$ , despite not knowing any of the dynamics *a priori* (i.e., knowledge of  $\mathbf{s}(t)$ ). From a forecasting point of view, this is also extremely attractive, because the next state has only one unknown  $x(t+\tau)$ ; this will in fact be one of the main motivations for adopting the type of forecasting strategy that we do later on. It is worth mentioning that the term *generic* above, has a

strict meaning in dynamical systems theory; it means that Taken's theorem is true for 'almost all' positive and real values of time-delay. Only for a small subset does it not hold, but the probability of randomly selecting one of the elements from this subset is in fact zero. And so in essence, given a time series  $x(t)$ , we can construct in practically all cases (i.e., generically) a series of vectors diffeomorphically (i.e., topologically) equivalent to the original attractor. It is perhaps unsurprising then, that Taken's embedding theorem has been used ubiquitously in dynamical systems analyses over the last decades. The approach described above is schematically illustrated in figure 4.3, from Cambell *et al.* (2005).

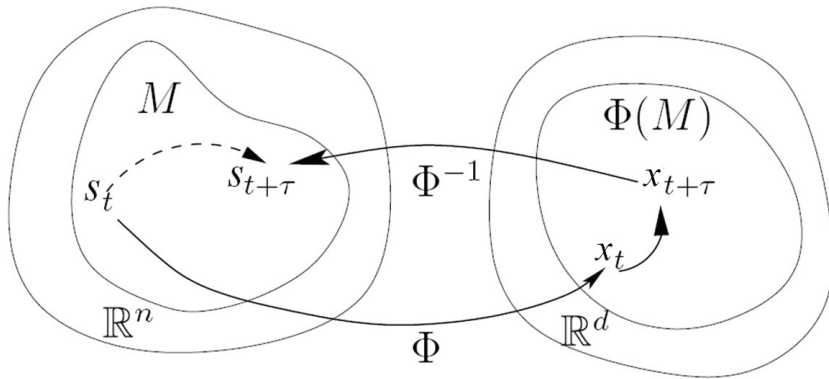


FIGURE 4.3. The coordinate transform  $\Phi$  illustrating Taken's embedding theorem. Note the slightly different notations used. Modified from Cambell *et al.* (2005).

With this mathematical background at hand, we can therefore investigate the topological properties of our attractor by observing the hot-wire scalar series  $x(t)$  in an embedding space given by the vector series

$$\mathbf{x}(t) = \{x(t), x(t+\tau), x(t+2\tau), \dots, x(t+(d-1)\tau)\} \quad (4.30)$$

where  $\tau$  is the time-delay and  $d$  is called the *embedding dimension* (to be determined and discussed later on).

While Taken's embedding theorem is a very powerful approach in dynamical systems theory, it in fact says nothing about how to specify

appropriate values for either  $\tau$  or  $d$  in general situations. Moreover, we do not know *a priori* the structure of the attractor we are trying to reconstruct, and so we must therefore decide on an appropriate value of delay  $\tau$  to deliver the best possible representation of its topological properties. On the one hand, if the time-delay chosen is too small, then consecutive measurements will give nearly the same results, and the reconstructed vectors will therefore be stretched along the diagonal in the embedding space. This will make it difficult to make statements regarding the structure of the attractor (as we will see later on). On the other hand, if the time-delay chosen is too large, then the vectors will become uncorrelated, and the reconstructed attractor will be obscured in embedding space. In view of these considerations, we must therefore select an ‘optimum’ time-delay. However, the best choice of  $\tau$  is not obvious, and various methods have been proposed in literature to determine it.

In the present study, we will use the average mutual information method proposed by Fraser & Swinney (1986), both because it is a popular choice in literature, and because its mathematical background is well-documented. Alternative approaches include using the autocorrelation function to estimate  $\tau$ , based on the  $1/e$  criterion for instance (see e.g., Sivakumar 2000), but mutual information is considered to be better suited for nonlinear time series analysis because it measures the *general* (nonlinear) dependence of two variables, whereas the autocorrelation measures only the *linear* dependence (see Fraser & Swinney 1986).

Following along the lines of Wang *et al.* (2004), let  $\mathbf{A}$  be the ensemble of values  $x(t)$  that are the first components of  $\mathbf{x}(t)$ , i.e.,  $\mathbf{A} = \{x(t) | t=1,2,\dots,N\}$ , and let  $\mathbf{B}$  be the second components of  $\mathbf{x}(t)$ , i.e.,  $\mathbf{B} = \{x(t+\tau) | t=1,2,\dots,N\}$ . Let  $a$  and  $b$  denote arbitrary elements of  $\mathbf{A}$  and  $\mathbf{B}$ , respectively.  $P_{\mathbf{A}}(a)$  is then the probability of observing  $a$  from the set  $\mathbf{A}$ , whereas  $P_{\mathbf{B}}(b)$  is the probability of observing  $b$  from the set  $\mathbf{B}$ . If  $P_{\mathbf{A},\mathbf{B}}(a, b)$  is the joint PDF, then the mutual information  $I(\tau)$  as a function of the time-delay  $\tau$  is given by

$$I(\tau) = \sum_{a \in \mathbf{A}, b \in \mathbf{B}} P_{\mathbf{A},\mathbf{B}}(a, b) \log_2 \left[ \frac{P_{\mathbf{A},\mathbf{B}}(a, b)}{P_{\mathbf{A}}(a) P_{\mathbf{B}}(b)} \right] \quad (4.31)$$

As noted by Martinerie *et al.* (1992), the mutual information  $I(\tau)$  is essentially the number of bits of  $x(t+\tau)$ , that can be predicted, on average, when  $x(t)$  is known. (Note that the mutual information concept shares superficial similarity with structure functions in turbulence research, which are functions that may be used to give an impression of the spread of energy across different eddy sizes, see e.g., Davidson 2004.) One wants to choose  $\tau$  so that the maximum amount of new information is obtained from each measurement. Therefore, it follows that  $x(t+\tau)$  should be as unpredictable as possible. Maximum unpredictability occurs at minimum predictability, and the optimum  $\tau$  is therefore considered to be the first minimum of the  $I(\tau)$  distribution (see also Fraser & Swinney 1986).

*Example:* As an illustrative example to show how the attractor reconstruction approach describe above is implemented in a well-known archetypal nonlinear dynamical system, consider the famous Lorenz system, first proposed by Lorenz (1963), as a minimal model for two-dimensional Rayleigh-Bérnard convection defined by

$$\begin{aligned}\dot{X} &= \sigma(Y - X) \\ \dot{Y} &= rX - Y - XZ \\ \dot{Z} &= XY - bZ\end{aligned}\tag{4.32}$$

where  $X$ ,  $Y$ ,  $Z$  are the unknown phase variables, and  $\sigma$ ,  $r$ ,  $b$  are parametric constants. The dot represents the ordinary derivative with respect to time. The system is a coupled set of ordinary differential equations that must be solved numerically. For the purposes of illustration, we arbitrarily choose  $\sigma=16$ ,  $r=45.92$ , and  $b=4$  to yield chaotic dynamics in the phase variables  $X$ ,  $Y$ ,  $Z$ , characterized by a strange attractor (see e.g., Wolf *et al.* 1985; Thompson & Stewart 1986). The equations are solved using a fourth-order Runge-Kutta scheme using a 50,000 point trajectory and integrated with a time-step of  $dt=0.005$ . Initial conditions are  $X(0)=1$ ,  $Y(0)=1$ ,  $Z(0)=1$ . The Lorenz attractor plotted in  $X$ ,  $Y$ ,  $Z$  state-space is shown in figure 4.4.

Following a trajectory spiralling out from one of the two symmetric fixed points (seen as the two ‘holes’ on either side within the attractor), Thompson & Stewart (1986) elegantly explain how the trajectory may be characterized as a nested sequence of shells, one inside another like Chinese boxes, or Russian dolls. The trajectory wanders chaotically back and forth, never repeating its previous path exactly, approaching arbitrarily close to its previous path an arbitrary number of times. The number of turns on each side before crossing over back over is not fixed, nor does the trajectory appear to settle into any pattern (Thompson & Stewart 1986). It is therefore both deterministic and unpredictable, and is arguably one of the most beautiful objects discovered in mathematics. Within the present context, this represents the attractor which we cannot observe.

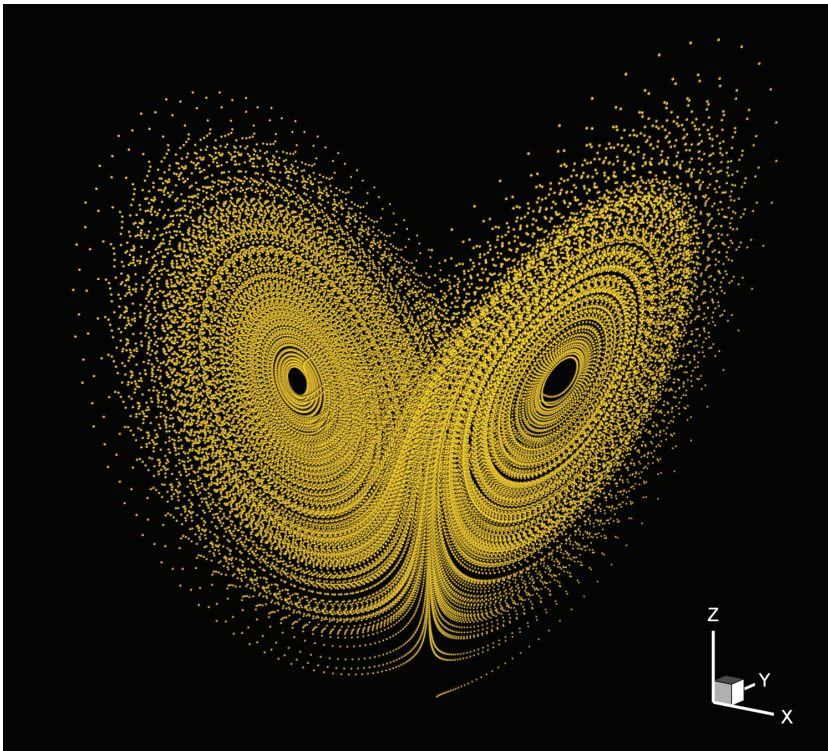


FIGURE 4.4: An example of the Lorenz attractor in  $(X, Y, Z)$  coordinates. Parameters chosen are  $\sigma=16$ ,  $r=45.92$ , and  $b=4$  using 50,000 data points with  $dt=0.005$ . Initial conditions are  $X(0)=1$ ,  $Y(0)=1$ ,  $Z(0)=1$ .

Consider now the time-evolution of only the  $X$  variable of the Lorenz attractor shown in figure 4.5. This represents our time series signal  $x(t)$ . (Alternatively, we could have also chosen the  $Y$  or  $Z$  variable.) Observe how after an initial transient, the signal can be seen to settle into an irregular oscillation that never repeats itself exactly. The signal is therefore nonperiodic, yet completely deterministic, and combined with a sensitivity to the initial conditions, leads to an effective long-term unpredictability, even if we know or can infer the rule; indeed one of the defining characteristics of deterministic chaos. The  $Y$  and  $Z$  components (not shown here for brevity) exhibit a similar qualitative behaviour.

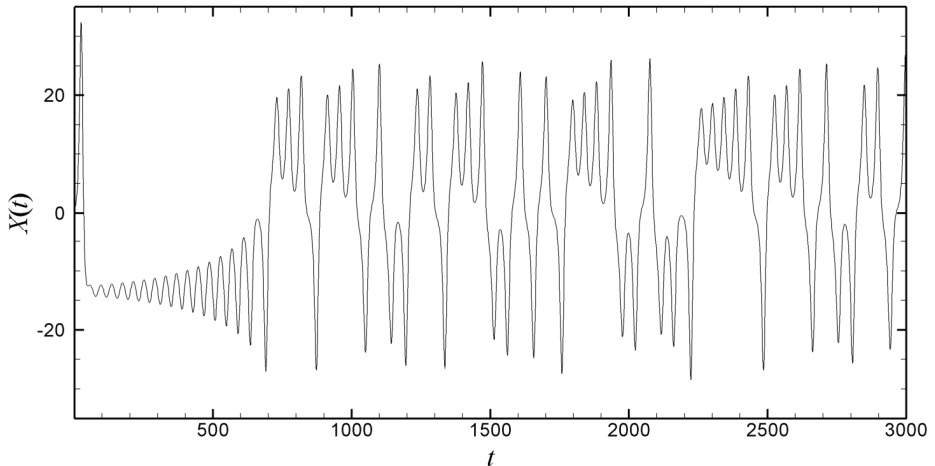


FIGURE 4.5: Time series of the  $X$  variable of the Lorenz attractor. Only first 3,000 points are shown for clarity. Parameters chosen are  $\sigma=16$ ,  $r=45.92$ , and  $b=4$  using 50,000 data points with  $dt=0.005$ . Initial conditions are  $X(0)=1$ ,  $Y(0)=1$ ,  $Z(0)=1$ .

The  $X$  time series (as well as the  $Y$  or  $Z$  time series) may be embedded to reconstruct the original Lorenz attractor. For the purposes of illustration, we use an embedding lag of  $\tau=4$  (see Rosenstein *et al.* 1993 for further details on how this number may be obtained by either the mutual information method or autocorrelation function; for many attractors, including the Lorenz attractor, the method chosen is not so important. The time-delay is also the same

value for  $Y$  and  $Z$ ). Using the embedding procedure, our reconstructed Lorenz attractor is plotted in three-dimensions using the delayed coordinates  $\{X(t), X(t+\tau), X(t+2\tau)\}$  and is shown in figure 4.6. As Taken's embedding theorem assures us, observe how the reconstructed attractor preserves the topological structure of the original Lorenz attractor, yet requires only a single time series. This is what we wish to reproduce in our case. Now, having laboured to outline a robust method to reconstruct our attractor, we now describe some typical methods used to quantitatively determine its properties.

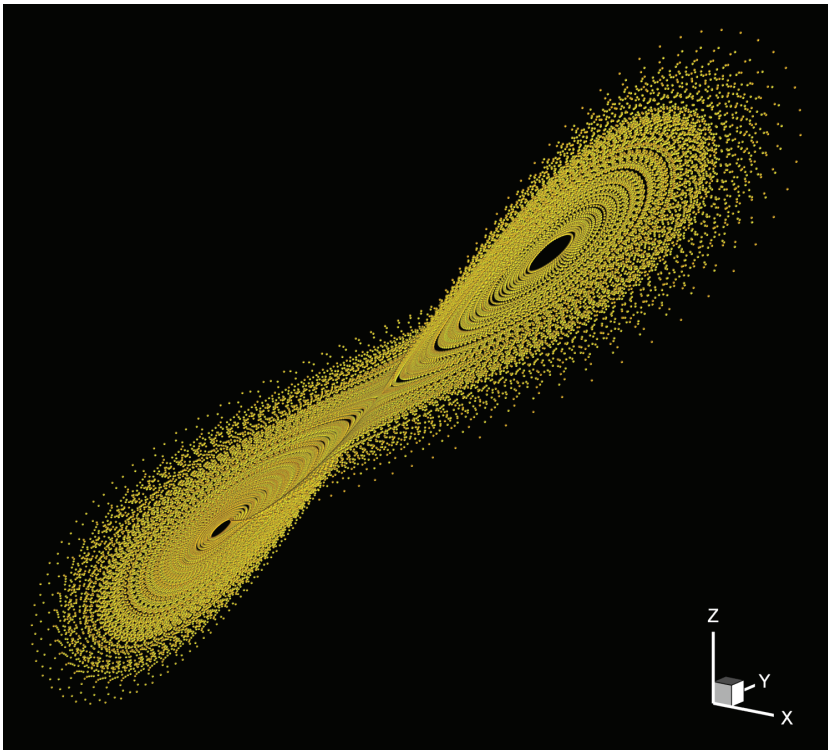


FIGURE 4.6: The reconstructed Lorenz attractor in time-lagged coordinates  $\{X(t), X(t+\tau), X(t+2\tau)\}$  using the  $X$ -coordinate of the original Lorenz attractor in figure 4.4. The reconstruction is a delay embedding in three-dimensions with an embedding lag of  $\tau=4$ .



### 4.4.2 Correlation Dimension

A simple quantification of the attractor's complexity may be provided by the correlation dimension  $\nu$ , first proposed by Grassberger & Procaccia (1983), which is a measure of the dimensionality of the space occupied by the set of points  $\mathbf{x}(t)$ . This will enable us to quantify the data for example, with respect to purely periodic data, which has a dimension of one, and noise, which has an infinite dimension. Several other definitions of fractal dimension also exist in literature, such as the Hausdorff dimension, information dimension, and box-counting dimension for example (see Mandelbrot 1982 for an illuminating discussion), but  $\nu$  has the advantage that it is quite easy to calculate and is a well-documented and very popular choice in literature. (In many cases,  $\nu$  can also be related to the other fractal dimensions.) Grassberger & Procaccia (1983) estimate this dimension by using the correlation integral  $C(\varepsilon)$ , defined as

$$C(\varepsilon) = \lim_{N \rightarrow \infty} \frac{1}{N^2} \sum_{\substack{i, j=1 \\ i \neq j}}^N \Theta(\varepsilon - \|\mathbf{x}_i - \mathbf{x}_j\|) \quad (4.33)$$

where  $N$  is the number of points and  $\Theta$  is the Heavyside function defined by

$$\Theta(x) = \begin{cases} 0 & \text{if } x < 0 \\ 1 & \text{if } x \geq 0 \end{cases} \quad (4.34)$$

In essence, the correlation integral  $C(\varepsilon)$  is the mean probability that two points chosen randomly at different times are within a certain distance  $\varepsilon$  of each other, and examines how this probability changes as this distance is increased. The norm is arbitrary because of the scaling of the correlation integral, but we will use the Euclidean metric given by

$$\|\mathbf{x}_i - \mathbf{x}_j\| = \sqrt{\sum_{k=1}^d (x_{i+(k-1)\tau} - x_{j-(k-1)\tau})^2} \quad (4.35)$$

for a given embedding dimension  $d$  (i.e., for a given number of  $d$  vectors). As  $N \rightarrow \infty$ , then the correlation integral for decreasing  $\varepsilon$  becomes

$$C(\varepsilon) \sim \varepsilon^\nu \quad (\varepsilon \rightarrow 0) \quad (4.36)$$

resulting in the correlation dimension  $\nu$  being defined as

$$\nu = \lim_{\varepsilon \rightarrow 0} \frac{\ln[C(\varepsilon)]}{\ln \varepsilon} \quad (4.37)$$

We can obtain  $\nu$  as the gradient of a log-log plot of  $C(\varepsilon)$  and  $\varepsilon$  (see Grassberger & Procaccia 1983), by seeking a scaling range of  $\varepsilon$  values for which  $\ln C(\varepsilon)/\ln \varepsilon$  is approximately constant for large  $N$  (for a given value of  $d$ ). The reader should be made aware that the literature on the correct and spurious estimation of  $\nu$  is especially large. Although it will not be repeated here, some caveats and misconceptions may be found in Grassberger *et al.* (1991) for example. Among some of the most important, as noted by Sprott & Rowlands (2001), is that the conditions  $\varepsilon \rightarrow 0$  and  $N \rightarrow \infty$  are inherently incompatible for finite datasets, and for many attractors  $\nu$  converges slowly necessitating long time series.

Eckmann & Ruelle (1992), among many others, have therefore quantified the minimum  $N$  to estimate  $\nu$ . They introduced the criterion that  $\nu < 2 \log_{10} N$ . Initial estimations of  $\nu$  in the present study revealed that it was going to be around 3 (the curious reader may look ahead to §8.4 to see the final value), thereby requiring  $N=100,000$  data points for  $2 \log_{10} N$  to be at least three times greater than the initial estimate of  $\nu$ . To be four times greater would require 1,000,000 data points, which was not computationally feasible in the present study. Other criteria for the minimum number of data points required are discussed at length by Sivakumar (2000), although in the present study, estimations of  $\nu$  were found to not change significantly (i.e., <10%) for data points greater than 10,000. The use of 100,000 points is therefore considered sufficient for our present purpose.

Considering the implications of  $\nu$  above, it is clear that white noise for example, would fill its space, since its components are

uncorrelated. The correlation dimension in this case would therefore be equal to whatever dimension it is placed in, and  $\nu$  would scale linearly with  $d$ . This is because an orbit of a random process is not expected to have any spatial structure. Contrastingly, the correlation dimension for a periodic orbit is one, for a two-dimensional surface is two, and for a strange (fractal) attractor it is a noninteger value. The correlation dimension has therefore often been used as a tool to distinguish noise from low-dimensional chaos (see Grassberger & Procaccia 1983).

### 4.4.3 Recurrence Plot

A comprehensive overview of the temporal structure of the attractor may be achieved by constructing a recurrence plot, first introduced by Eckmann *et al.* (1987), as a convenient way to characterize nonlinear dynamical systems (see also Marwan 2003 for an excellent discussion of recurrence plots). A recurrence plot is essentially a map depicting for any given moment in time, all the other times when a trajectory on the attractor visits roughly the same area of state-space. Consider forming an  $N \times N$  matrix  $\mathbf{R}_{i,j}$  of points using the optimally embedded vector  $\mathbf{x}(t)$  (Marwan 2003)

$$\mathbf{R}_{i,j} = \Theta\left(\varepsilon - \|\mathbf{x}_i - \mathbf{x}_j\|\right), \quad i, j = 1, \dots, N \quad (4.38)$$

where  $\varepsilon$  is a predefined threshold and  $\Theta$  is the Heavyside function. (Using the Euclidean norm again, the sharp reader will notice the close relationship between  $\mathbf{R}_{i,j}$  and  $C(\varepsilon)$ .) A point in state-space  $i, j$  appears in the recurrence plot when

$$\mathbf{x}_j \in U_i \cap \{\mathbf{x}_k \mid \varepsilon > \|\mathbf{x}_i - \mathbf{x}_k\|\} \quad (4.39)$$

where  $U_i$  is the set of nearest neighbours of  $\mathbf{x}_i$  using test points  $\mathbf{x}_k$  (i.e., if  $\mathbf{x}_j$  is one of the nearest neighbours of  $\mathbf{x}_i$  and it is within a sphere of radius  $\varepsilon$ ). Recurrence plots therefore give information on the temporal correlation of the points in state-space and will help us reveal recurrence in the data.

#### 4.4.4 Lyapunov Exponent

An indication of the long-term predictability of the time series signal may be provided by an estimate of the Lyapunov exponent of the reconstructed attractor (see Wolf *et al.* 1985). The Lyapunov exponent is a measure of the (average) exponential divergence of the time evolution of nearby trajectories in state-space. A positive exponent implies divergence of nearby trajectories, whereas a negative exponent implies convergence of nearby trajectories. The exponent is zero for regular trajectories. The more positive (negative) the exponent, the faster that nearby trajectories diverge (converge). It therefore shares a superficial similarity with the autocorrelation function (see below). It will also become a useful quantity in the formulation of the forecasting strategy that follows.

The simplest approximation to the Lyapunov exponent is obtained by numerically computing the time evolution of two trajectories that are initially close to each other. Briefly, suppose two trajectories are initially separated by a small distance  $\delta x(0)$ . If the attractor is chaotic, then orbits will, by definition, separate on average at an exponential rate, and one therefore finds that

$$|\delta x(t)| \approx |\delta x(0)| e^{\lambda_1 t} \quad (4.40)$$

where  $\lambda_1$  is the mean rate of separation—the (largest) Lyapunov exponent.\*\* The mean growth rate of the distance  $\delta x(t)$  is therefore given by

$$\lambda_1 = \lim_{t \rightarrow \infty} \frac{1}{t} \ln \frac{|\delta x(t)|}{|\delta x(0)|} \quad (4.41)$$

The determination of the Lyapunov exponent from an experimental data series (as opposed to a system of equations) is a nontrivial task, and has been treated rather extensively in literature

---

\*\* There is in fact a spectrum of  $n$  Lyapunov exponents for an  $n$ -dimensional system. However, restricting ourselves to determining only the largest exponent will be sufficient for our present purpose, which is to establish the average predictability of the data.

(see e.g., Rangarajan *et al.* 1998; Wolf *et al.* 1985; Caimi *et al.* 1997). In the present study, we use the method given Rosenstein *et al.* (1993), who have developed a robust algorithm for determining the (largest) Lyapunov exponent from experimental datasets that has been validated using (noisy) time series data from a variety of well-known chaotic attractors. Taking the logarithm of both sides of equation (4.40) we obtain

$$\ln|\delta x(t)| \approx \ln|\delta x(0)| + \lambda_1 t \quad (4.42)$$

and we seek a scaling range of  $t$  values for which  $\ln|\delta x(t)|/\ln|\delta x(0)|$  is approximately constant, with a slope proportional to  $\lambda_1$ .

It may be of interest to note, that the Lyapunov exponent is related to the autocorrelation function in the following way. If the value of  $\tau$  at which the autocorrelation falls to below  $1/e \approx 37\%$  is the *correlation time*  $\tau_{corr}$ , then with the correlation function symmetric about  $\tau=0$ , the full width is  $2\tau_{corr}$ . The reciprocal of this quantity,  $0.5/\tau_{corr}$ , is therefore an estimate of the average rate at which predictability is lost. This is sometimes called the *poor man's Lyapunov exponent* since it is similar to, although somewhat less sophisticated than, the largest Lyapunov exponent, in the sense that the correlation time is a convective time-scale, whereas the Lyapunov time is an evolution time-scale (see Sprott 2003).

#### 4.4.5 Outline of a Forecasting Strategy

One of the major goals of nonlinear time series analysis is prediction, i.e., forecasting the future development of the series from observations in the past (Dangelmayr *et al.* 1999). Within the present context, the characterization of the hot-wire signal as points travelling a trajectory in state-space, opens the possibility of formulating a forecasting strategy of its future behaviour. Moreover, as discussed by Farmer & Sidorowich (1987), among others, the ability to successfully forecast a seemingly random-looking time series may be the strongest test of whether or not low-dimensional chaos is really present.

The development of short-term forecasting techniques of chaotic time signals began with the seminal work of Takens (1981), and was initiated by Farmer & Sidorowich (1987), who were initially inspired by efforts to beat the game of roulette.<sup>††</sup> They proposed forecasting based on embedding the time series in a state-space and searching for nearby patterns to a given reconstructed state. In essence, segments of similar dynamical behaviour on the attractor are detected, and it is postulated that such segments of the past may resemble attractor segments in the future. Similar patterns of behaviour are located in the near vicinity of the point of interest, generally in the Euclidean sense, and their time evolution is utilized in order to provide an approximate prediction of the evolution of the point of interest.

Such nonlinear forecasting has attracted widespread interest due to the profound and obvious implications of being able to predict complex, seemingly chaotic processes, in fields ranging from the stock exchange (e.g., Bajo-Rubio *et al.* 2002), fluctuations in oil prices (e.g., Gori *et al.* 2006), solar sunspot activity (e.g., Sello 2001), to electroencephalography signals within the human brain (e.g., Blinowska & Malinowski 1991) to name a few. It is important to emphasize, that the forecasting philosophy behind what follows is distinctly different from other nonlinear archetypal forecasting methodologies, which are especially abundant in the literature. Some of the most prominent examples include neural network learning algorithms (see e.g., Rummelhart *et al.* 1986) and autoregressive conditionally heteroscedastic models (see e.g., Bollerslev *et al.* 1992) for instance, but we will use the *nearest neighbour* nonlinear forecasting approach proposed by Farmer & Sidorowich (1987), because it is especially well-suited to our dynamical systems analysis, as will be seen shortly, since it uses directly sets of points within the reconstructed state-space. Furthermore, its mathematical implementation and limitations are well-documented, and it is a popular choice in forecasting chaotic time series analyses.

As reported by Sello (2001), among many others, we first define a smooth map for the inverse nonlinear dynamical systems problem based on the behaviour of the related embedding vectors. To be more

---

<sup>††</sup> Given the proliferation of roulette within casinos in the world, it would appear that the authors were unsuccessful in this regard. (See also Gleick 1987.)

precise, the nonlinear deterministic behaviour of the embedding space implies the existence of a smooth map  $F^{\tau}$  that satisfies

$$F^{\tau}[\mathbf{x}(t)] = \mathbf{x}(t+1) \quad (4.43)$$

for a given embedding vector  $\mathbf{x}(t)$ , where we now use a slightly different notation than before in our outline of time-delay embedding for convenience. The inverse problem consists of constructing this smooth map given the scalar time series  $x(t)$ ,  $t=1, \dots, N$ , which is possible since we know that

$$\mathbf{x}(t) = \{x(t), x(t-\tau), x(t-2\tau), \dots, x(t-(d-1)\tau)\} \quad (4.44)$$

where for convenience we now consider negative lags instead of positive ones. The map  $F^{\tau}$  is the basis of the predictive model (Sello 2001). In order to proceed, we first divide the known time series  $x(t)$  into two parts: the first one is  $x(t)$ ,  $t=1, \dots, N'$ , (where  $N' < N$ ), which is used to set up the map  $F^{\tau}$ . This is the *training phase* of the model, which will be used to train the model to make predictions when  $t > N'$ . The second one is  $x(t)$ ,  $t= N'+1, \dots, N$ , which is the *prediction phase* of the model. This will be used to assess the accuracy of the model's prediction. To calculate the unknown function  $F^{\tau}$  and hence predict the future state, we first determine the last known state of the system, as represented by the embedded vector (see Bajor-Rubio *et al.* 2002)

$$\mathbf{x}_T(t) = \{x_T(t), x_T(t-\tau), x_T(t-2\tau), \dots, x_T(t-(d-1)\tau)\} \quad (4.45)$$

Given this last embedding vector, we then search for  $k$  similar states that have occurred in the past, by selecting the first  $k$  neighbouring vectors nearest to the reference vector  $\mathbf{x}_T(t)$  within the embedding space

$$\mathbf{x}_i(t) = \mathbf{x}_1(t), \mathbf{x}_2(t), \dots, \mathbf{x}_k(t) \quad i = 1, \dots, k \quad (4.46)$$

where we use the Euclidean metric and consider only one nearest neighbour from each nearby trajectory. We then postulate that the evolution of the selected vector is correlated with the evolution of the neighbouring vectors. The basic idea is that if the signal generates the map

$$F^\tau \{x_T(t), x_T(t-\tau), x_T(t-2\tau), \dots, x_T(t-(d-1)\tau)\} = \mathbf{x}_T(t+1) \quad (4.47)$$

where  $\mathbf{x}_T(t+1)$  is the future state vector, then this map  $F^\tau$  can be reconstructed from the data by looking in the neighbourhood of  $\mathbf{x}_T(t)$ . In other words, if  $F^\tau$  is smooth near  $\mathbf{x}_T(t)$ , then if a state

$$\mathbf{x}_i(t) = \{x_i(t), x_i(t-\tau), \dots, x_i(t-(d-1)\tau)\} \quad i = 1, \dots, k \quad (4.48)$$

in the neighbourhood of  $\mathbf{x}_T(t)$  resulted in the observation  $x_i(t+1)$  in the past, then the point  $x_T(t+1)$ , which we want to predict, must be somewhere near  $x_i(t+1)$ . We then repeat the process to predict the future states using a multi-step method, where the last known vector is composed from the previously predicted values. Mathematically, we approximate  $F^\tau$  through the solution of a least squares problem in embedding space by fitting a function that maps the first  $k$  neighbouring states onto their next immediate values. The predicted vector is given by a local regression for each component of the related  $k$  neighbouring vectors

$$x_T(t+1) = \alpha_0 x_T(t) + \alpha_1 x_T(t-\tau) + \dots + \alpha_{d-1} x_T(t-(d-1)\tau) + \alpha_d \quad (4.49)$$

where the coefficients are fitted using a linear regression of  $x_i(t+1)$  on

$$\mathbf{x}_i(t) = \{x_i(t), x_i(t-\tau), \dots, x_i(t-(d-1)\tau)\} \quad i = 1, \dots, k \quad (4.50)$$

The coefficients  $\alpha$  are therefore the coefficients  $\alpha'$  that minimize



$$\sum_{i=1}^k K_{h_\lambda}(\mathbf{x}_0, \mathbf{x}) \left[ x_i(t+1) - \alpha'_0 x_i(t) - \alpha'_1 x_i(t-\tau) \dots \right. \\ \left. - \alpha'_{d-1} x_i(t-(d-1)) - \alpha'_d \right]^2 \quad (4.51)$$

where  $K$  is the kernel given by

$$K_{h_\lambda}(\mathbf{x}_0, \mathbf{x}) = D \left( \frac{\|\mathbf{x} - \mathbf{x}_0\|}{h_\lambda(\mathbf{x}_0)} \right) \quad (4.52)$$

where  $h_\lambda$  is the kernel radius, which in our case is the distance from our chosen vector  $\mathbf{x}_7(t)$  to the farthest neighbour out of the  $k$  neighbours chosen. Now, we would like neighbours that are closer to our chosen point or predictee, to play a greater role in the forecasting than neighbours that are farther away. The neighbour distances are therefore weighted in terms of the neighbour-predictee proximity. In the present study, we use a tri-cube kernel given by

$$D(\|\mathbf{x} - \mathbf{x}_0\|/h_\lambda) = \begin{cases} \left(1 - \|\mathbf{x} - \mathbf{x}_0\|/h_\lambda\right)^3 & \text{if } \|\mathbf{x} - \mathbf{x}_0\|/h_\lambda \leq 1 \\ 0 & \text{if otherwise} \end{cases} \quad (4.53)$$

It should be remarked that the use of other kernels introduces different results, but a systematic exploration of the effects of kernel type is considered beyond the scope of the present study. It is worth mentioning, however, that several authors, such as Atkeson *et al.* (1996) and Yankov *et al.* (2006) for example, have argued that there is in general no clear evidence for the benefit of using a particular kernel function or norm within the context of the present approach. In the absence of rigorous criteria for the optimum performance of the model in generic situations, our purpose therefore, is to demonstrate the usefulness and applicability of such a nonlinear forecasting technique to the present SWTBLI problem, and to contextualize it within the framework of the present results. We will therefore attempt to distil some underlying aspects about the temporal nature of the interaction rather than conduct a systematic quantitative study.



# CHAPTER 5 BOUNDARY LAYER STUDY

---

## 5.1 Introductory Remarks

**H**AVING dispensed with the appropriate background, we now commence a discussion of the results. To begin with, a characterization of the undisturbed boundary layer is made in detail, because it is an essential prerequisite in any SWTBLI study, in order to establish the boundary conditions of the experiment, as well as to provide useful data for possible computational and/or analytical modelling purposes. It can also be used to substantiate the validity of the measurement techniques used. In this chapter, the undisturbed boundary layer is characterized in terms of its mean and turbulence properties using planar and tomographic PIV, complemented with a spatiotemporal characterization using HWA.

## 5.2 Undisturbed Boundary Layer

A separate high-resolution experiment using the planar PIV system was conducted in order to characterize the undisturbed boundary layer in detail. The experimental arrangement was the same as for the planar PIV SWTBLI experiments with the boundary layer developing along the wind-tunnel upper wall, but without the shock generator. The wind-tunnel was operated at a nominal free-stream Mach number  $M_\infty=2.1$  (measured free-stream velocity  $U_\infty=505 \text{ m s}^{-1}$ ), with a stagnation pressure of  $P_0=226 \pm 3 \text{ kPa}$  and stagnation temperature of  $T_0=278 \pm 3 \text{ K}$ . Note that the stagnation pressure (and hence Reynolds number) is appreciably lower than for the planar PIV SWTBLI experiments, although this does not significantly affect the results (see also Tuinstra 2005). On entering the test-section, the boundary layer thickness (99% of  $U_\infty$ ) was  $\delta=20 \text{ mm}$ , with displacement thickness  $\delta^*=3.9 \text{ mm}$ , and momentum thickness  $\theta=1.3 \text{ mm}$ . A log-law fit was again used in combination with the van Driest transformation to determine the skin friction coefficient,  $C_f=1.6 \times 10^{-3}$  corresponding to a friction velocity  $u_\tau=\sqrt{(\tau_w/\rho_w)}=19.4 \text{ m s}^{-1}$ . The Reynolds number based on the momentum thickness,  $\text{Re}_\theta=U_\infty\theta/\nu_\infty=3.96 \times 10^4$ . The Reynolds number based on the friction velocity and boundary layer thickness,  $\text{Re}_\tau=u_\tau\delta/\nu_w=7500$ . The experimental conditions are summarized in table 5.1.

Table 5.1. Experimental conditions of the boundary layer PIV study

Parameter	Quantity
$M_\infty$	2.05
$U_\infty, \text{ m s}^{-1}$	505
$C_f$	$1.6 \times 10^{-3}$
$\delta_{99}, \text{ mm}$	20
$\delta^*, \text{ mm}$	3.9
$\theta, \text{ mm}$	1.3
$u_\tau, \text{ m s}^{-1}$	19.4
$P_0, \text{ kPa}$	226
$T_0, \text{ K}$	278
$\text{Re}_\theta$	$3.96 \times 10^4$
$\text{Re}_\tau$	7500

The particle images were recorded at 10 Hz by a PCO Sensicam QE, a 12-bit CCD camera with a  $1376 \times 1040$  pixel-sized sensor. Only 432 pixel rows were used given the large aspect ratio of the flow region investigated. The camera was equipped with a Nikon 60 mm focal objective with  $f_{\#}=8$ , in combination with a narrow-bandpass 532 nm filter in order to minimize ambient light interference. The camera was rotated  $90^\circ$  relative to the other experimental setups in order to maximize the spatial resolution. The flow was imaged in the streamwise ( $x$ ) and wall-normal ( $y$ ) directions over a field-of-view of  $5 \times 16 \text{ mm}^2$  ( $0.25\delta \times 0.8\delta$ ), respectively, resulting in a digital resolution of  $86 \text{ pixels mm}^{-1}$ . Because of the limited field-of-view, note that the complete boundary layer is not resolved. Estimation of the integral parameters for this specific experiment should therefore be treated with caution. For further details of a complete undisturbed boundary layer characterization, but at a lower resolution, the reader is referred to Humble *et al.* (2007*b*). Alternatively, the reader may look back to table 3.1. The integral results are very similar.

In the present experiment, a dataset of order 500 image pairs was acquired. The recorded images were interrogated using the cross-correlation algorithm with iterative multi-grid window deformation (see Scarano & Riethmuller 2000). In order to suppress the effects of the wall, the images were interrogated using high aspect-ratio interrogation windows of final size  $61 \times 7$  pixels ( $0.7 \times 0.08 \text{ mm}^2$ ) ( $0.035\delta \times 0.004\delta$ ), with an overlap factor of 85%. These parameters are summarized in table 5.2 and pertain exclusively to the results presented in this chapter on the undisturbed boundary layer.

Table 5.2. Summary of the boundary layer PIV recording parameters

Parameter	Quantity
Field-of-view	$5(L) \times 16(H) \text{ mm}^2$
Interrogation volume	$0.7 \times 0.08 \times 1.5 \text{ mm}^3$
Digital image resolution	$\approx 86 \text{ pixels mm}^{-1}$
Objective focal length	$f=60 \text{ mm}$
f-number	$f_{\#}=8$
Laser pulse separation	$0.6 \mu\text{s}$
Seeding density	$0.15 \text{ ppp}$

### 5.2.1 Mean Velocity Profile

To begin with, profiles of the mean streamwise velocity ratio  $\bar{u}/U_e$ , mean static temperature ratio  $\bar{T}/T_e$ , and mean mass-flux ratio  $\bar{\rho}\bar{u}/\rho_e U_e$  within the undisturbed boundary layer are shown in figure 5.1. To ease visualization and aid statistical convergence, streamwise averaging has been used over a length of half a boundary layer thickness. Also, note that the data points are spaced a minimum distance of 4% of the figure size. The temperature and density were determined using the adiabatic Crocco-Busemann relation with a constant recovery factor  $r = \text{Pr}^{1/3} \approx 0.89$ , suitable for turbulent flow of gases (see White 1991). The sharp reader will notice that this is not strictly compatible with the derivation of the van Driest formulation earlier, which implicitly assumes that  $\text{Pr}=1$ , but it is done so because it is a commonly adopted practice in literature (see White 1991).

Typically, down to 10% of the boundary layer thickness, it can be seen that the local velocity is still nearly 80% of the free-stream value, so a large velocity variation occurs in a region very close to the wall, an observation that is indicative of turbulent boundary layers (see Smits & Dussauge 2006 for a further discussion). The static temperature increases rapidly as the wall is approached, indicating that the dissipation of kinetic energy is a source of heat. Assuming the boundary layer to be adiabatic, then the wall temperature is estimated to be  $T_w = T_{aw} \approx 260$  K. This may be compared with the total temperature  $T_0 = 278$  K. The discrepancy reflects the fact that the recovery factor is not taken to be unity (i.e.,  $\text{Pr} \neq 1$ ; there is not a perfect balance between dissipation and conduction, and so the wall temperature does not fully recover to the stagnation temperature). It should be mentioned that independent wall temperature measurements were not available in the present study. However, the total temperature in the stagnation chamber was measured, and was found to vary less than 5 K during the wind-tunnel runs.

The elevated temperature near the wall leads to a relatively low-density, high-viscosity region, with respect to the free-stream conditions, and much of the mass-flux is concentrated towards the outer part of the boundary layer. This temperature effect, however, is not so pronounced in this moderately supersonic turbulent boundary layer (see Spina *et al.* 1994), and is normally reserved for high-supersonic and hypersonic Mach numbers (typically  $M_\infty > 5$ ).

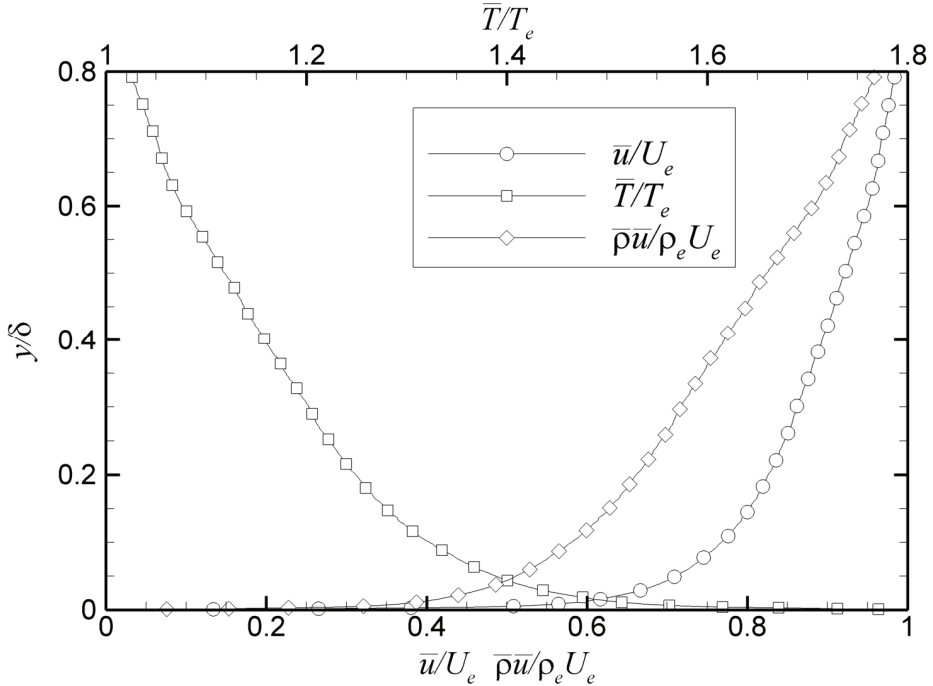


FIGURE 5.1: Profiles of the mean streamwise velocity ratio  $\bar{u}/U_e$ , mean static temperature ratio  $\bar{T}/T_e$ , and the mean mass-flux ratio  $\bar{\rho}\bar{u}/\rho_e U_e$  within the undisturbed boundary layer. Note that data points are spaced a minimum distance of 4% of the figure size.

To substantiate the validity of the PIV velocity data, the measured mean velocity profile  $\bar{u}=\bar{u}(y)$  is transformed into an effective velocity  $u_{eq}$  using the van Driest compressibility transformation. The corresponding law-of-the-wall fit is shown in figure 5.2. The experimental effective velocity profile coincides with the theoretical profile when the friction velocity,  $u_\tau=19.4 \text{ m s}^{-1}$ . The corresponding skin friction coefficient determined from  $C_f=2u_\tau^2\rho_w/\rho_e U_e^2$  returns  $C_f=1.6\times 10^{-3}$ , which agrees to within 10% of the van Driest II skin friction formula for a flat plate.

Within the logarithmic region, it can be seen that there is excellent agreement between the PIV data and the van Driest effective velocity. An appreciable departure of the experimental data from the single

composite formula of Spalding (1961) occurs for approximately  $y^+ < 30$ . This is due to a bias introduced into the data by a lack of spatial resolution (i.e., the final interrogation window size is effectively too large as the wall is approached). Points closer to the wall are therefore not shown. Similar behaviour has also been reported by Kostas *et al.* (2005) in their boundary layer experiment, as the buffer layer is approached. This bias was in fact the main motivation for using high-aspect ratio interrogation windows. It is worth mentioning that further improvements to the data yield may be achieved by the use of adaptive interrogation windows near the surface, and this is currently an active area of research. The interested reader is referred to Theunissen *et al.* (2007) for further details.

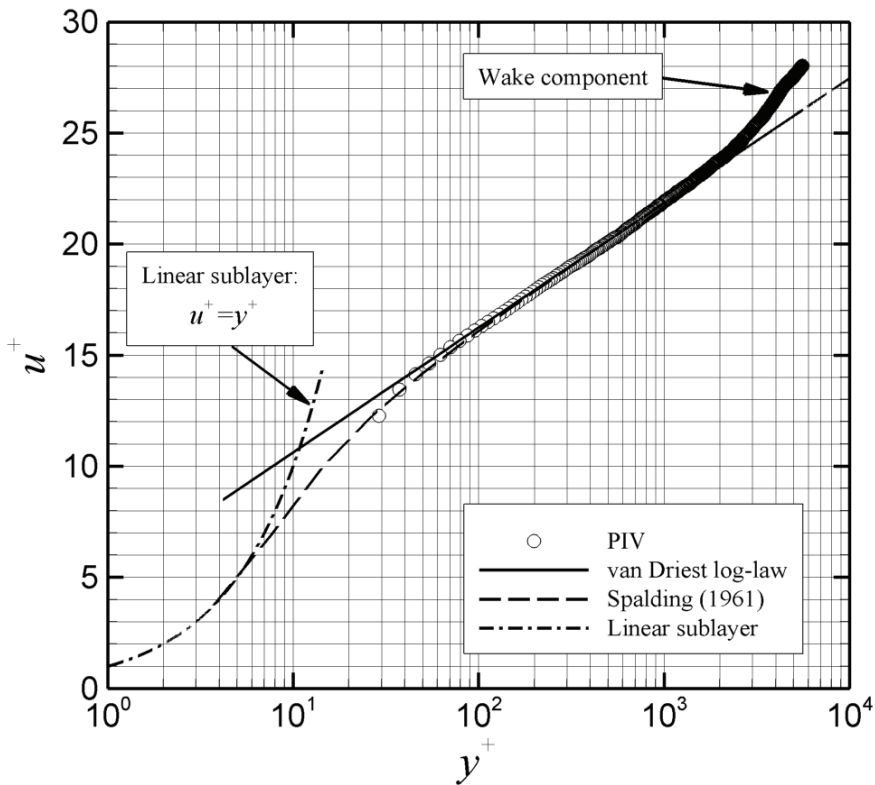


FIGURE 5.2: A comparison between the mean velocity measured by planar PIV and the van Driest law-of-the-wall. Spalding's composite formula is also shown for comparison. Modified from Humble *et al.* (2007b).



A (partially resolved) wake component, characteristic for turbulent boundary layers, can also be identified. The Coles wake parameter  $\Pi$ , which is used to help describe the deviation of the outer layer profile from the law-of-the-wall was determined to be  $\Pi = 0.45$ , which may be compared with the value of 0.55 commonly admitted for zero-pressure gradient incompressible boundary layers when  $Re_\theta > 5000$  (see Cebeci and Cousteix 1999). It should be remarked, however, that  $\Pi$  is considered to vary with boundary layer history and somewhat with Mach number (see White 1991), although the specific influences of these effects are not stated.

### 5.2.2 RMS Velocity Distributions

The turbulence properties are important to the further characterization of the undisturbed boundary layer, to provide useful data for computational and/or analytical modelling purposes, as well as to further substantiate the validity of the PIV data. The streamwise and wall-normal RMS velocity distributions within the boundary layer are compared to the results of Hou (2003), the HWA and laser Doppler anemometry (LDA) of Elena & Lacharme (1988), as well as the incompressible results of Klebanoff (1955) in figure 5.3. The results for the incoming boundary layer of the tomographic PIV experiment are also included for comparison (see also Elsinga 2008), and the axes are shown in the coordinates of these experiments. The data are normalized by the friction velocity. In addition, Morkovin's hypothesis (see Morkovin 1960) is used to take into account the density variation in the scaling by premultiplying the compressible data by the density ratio  $\sqrt{(\rho/\rho_w)}$ . This enables a comparison to be made with the incompressible data of Klebanoff (1955). The local mean density was deduced from the mean velocity distribution using the adiabatic Crocco-Busemann relation with a constant recovery factor  $r=0.89$ .

It is evident that both the planar and tomographic PIV results of the present boundary layer agree well with the other experimental results shown, and substantiate the validity of Morkovin's hypothesis. The sharp reader may recall the measurement uncertainty of the RMS velocity, which when scaled with  $u_\tau$  is about 20%; well within the results of Klebanoff (1955). This of course neglects the uncertainty on

the density, but the results are a further substantiation of our uncertainty analysis. The reader may also note how the wall-normal components of the compressible results all fall slightly below the incompressible data. This is because Morkovin's hypothesis is only strictly valid for the streamwise component (see Spina *et al.* 1991).

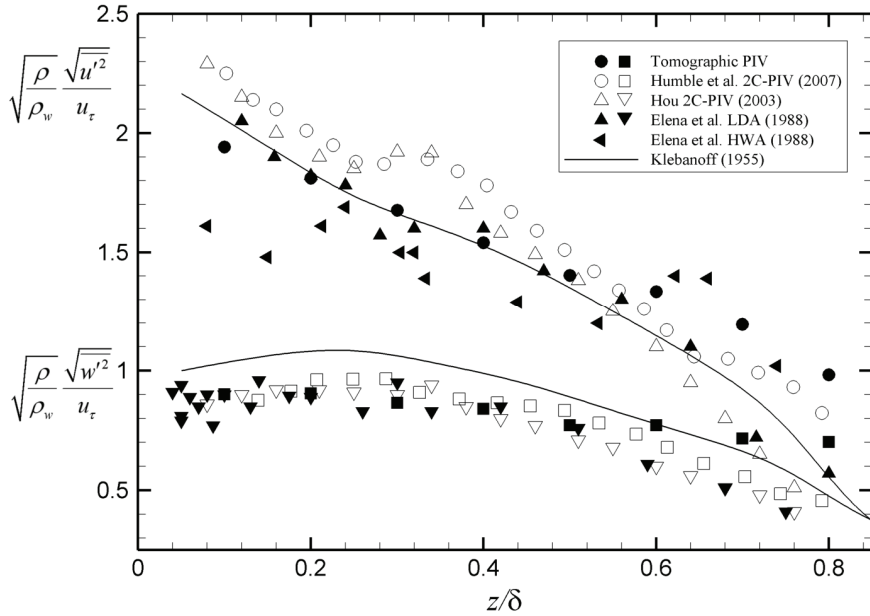


FIGURE 5.3: Comparison of velocity fluctuations within the compressible turbulent boundary layer using Morkovin's scaling. The present planar and tomographic PIV results are compared with the experimental data Hou (2003), Elena & Lacharme (1988), and Klebanoff (1955). From Humble *et al.* (2008).

### 5.2.3 Reynolds-Averaged Shear Stress Distribution

According to Morkovin (1960), subsonic-supersonic similarity for the Reynolds-averaged shear stress distribution in a zero-pressure-gradient turbulent boundary layer at high Reynolds number ( $>O(10^5)$  say) takes the form

$$\tau_t/\tau_w = -\overline{\rho u'v'}/\overline{\rho_w u_\tau^2} = -\overline{\rho u'v'}/\tau_w = f(\eta) \quad (5.1)$$

where  $f(\eta)$  represents a universal function, typically taken as Klebanoff's (1955) incompressible data (see Fernholz & Finley 1981). Scaling the shear stress distribution with this density ratio and friction velocity therefore enables a direct comparison to be made with the incompressible data of Klebanoff (1955). The results are shown in figure 5.4. Several interesting observations can be made.

The PIV results can be observed to systematically fall below the data of Klebanoff. This is thought to be associated with the low-pass filtering effect of the PIV interrogation method, as discussed earlier, which biases the results towards lower values. Although the attenuation of  $u'$  and  $v'$  due to PIV filtering is not immediately obvious (see figure 5.3), it is thought to be significantly exacerbated during the computation of the Reynolds shear stress. This was partially substantiated by the somewhat naïve but instructive exercise of corrupting two sinusoids with noise, representing  $u'$  and  $v'$ , and computing  $\overline{u'v'}$ , ensuring that the correlation coefficient between the data  $R_{uv}$  (see §6.5.4) was about  $-0.45$ . It was found that for moderate attenuations of  $u'$  and  $v'$  of the order of a few percent, dramatic attenuation of  $\overline{u'v'}$  of the order 50% could be achieved. Such biasing appears to increase as the wall is approached, most likely due to the presence of smaller eddies, although why there is not an increased attenuation of the streamwise and wall-normal RMS velocities (the wall-normal component in particular) is presently unknown. Further work is obviously required in this area.

By approximately  $y/\delta=0.15$ , the PIV Reynolds-averaged shear stress distribution exhibits a different behaviour; it begins to decrease rapidly, resulting in a departure from the incompressible data. This behaviour could not be attributed to reflections from the wall, nor from spatial resolution, and interrogation window effects. The sharp reader will recognize that beyond  $y/\delta=0.15$ , the discrepancy becomes greater than our 25% measurement uncertainty estimated earlier (see §3.8.2 table 3.5), which is still valid for this boundary layer (see eqn. 3.30). The discrepancy, however, cannot be explained due to the spatial scale limitation of the uncertainty analysis, because the final interrogation window size here is now much smaller than the 2 mm ( $0.1\delta$ ) in the planar PIV SWTBLI experiment (i.e., it is now  $0.7 \times 0.08 \text{ mm}^2$ ) (or  $0.035\delta \times 0.004\delta$ ). This discrepancy close to the wall is therefore unexpected.

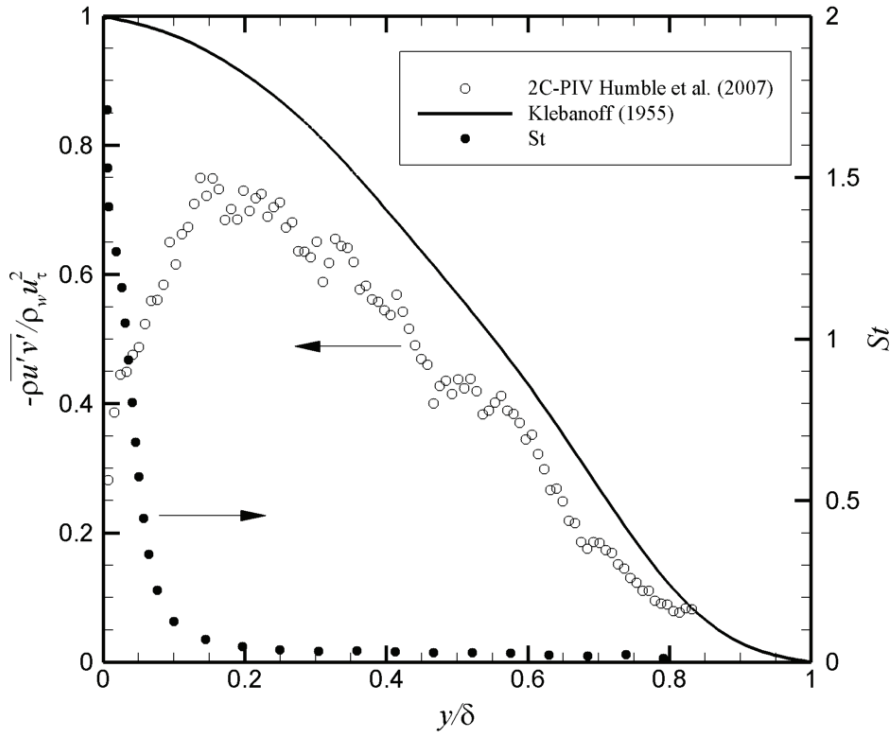


FIGURE 5.4: Reynolds-averaged shear stress distribution within the incoming boundary layer. Planar PIV results compared with the experimental data of Klebanoff (1955). The variation of the local Stokes number  $St$  is also shown (see text below for details). Arrows assign data with appropriate axis.

To offer an alternative possible reason for this discrepancy, we turn to a simple mixing-length model of the boundary layer. Mixing-length models are particularly useful because they provide a physical picture of the eddy sizes that are important in the mixing processes and will enable the shear stress to be associated with a time-scale. Consider Boussinesq's first-order turbulence closure hypothesis that the turbulent shear stress distribution is given by (see e.g., White 1991)

$$\tau_t = -\overline{\rho u'v'} = \mu_t \frac{\partial \bar{u}}{\partial y} \quad (5.2)$$

where  $\mu_t$  is the turbulent viscosity. Prandtl in 1925 (see Schlichting 1979) showed that the turbulent viscosity could be approximated by

$$\mu_t \propto \rho l^2 \left| \frac{\partial \bar{u}}{\partial y} \right| \quad (5.3)$$

where  $l$  is the mixing-length, which is a measure of the average distance a fluid element travels towards a reference height (in the RMS sense) due to turbulent mixing. Substituting (5.3) into (5.2) and rearranging for the mixing-length we have

$$l = \sqrt{-\overline{u'v'}} / (\partial \bar{u} / \partial y) \quad (5.4)$$

We can define a characteristic time-scale  $\tau_f$  based on this mixing-length and a local RMS streamwise velocity using

$$\tau_f = \frac{l}{\sqrt{\overline{u'^2}}} = \frac{\sqrt{-\overline{u'v'}}}{\sqrt{\overline{u'^2}} (\partial \bar{u} / \partial y)} \quad (5.5)$$

Comparing this to the time-response of the particles  $\tau_p$  through a shock wave (as outlined in chapter 3) we may write a *local Stokes number* within the boundary layer as

$$St(y) = \frac{\tau_p \sqrt{\overline{u'^2}} (\partial \bar{u} / \partial y)}{\sqrt{-\overline{u'v'}}} \quad (5.6)$$

Plotting  $St=St(y)$  reveals that in the outer part of the boundary layer (say  $y/\delta > 0.3$ ) then  $St \ll 1$ , and the particle slip criterion is effectively satisfied. The systematically lower values of Reynolds-averaged shear stress in this region are associated with the low-pass filtering effect of the PIV data. However, the onset of the rapid decrease in the Reynolds-averaged shear stress at about  $y/\delta = 0.15$  coincides with the rapid increase in  $St$ , which eventually exceeds unity in this region, indicating that  $\tau_p > \tau_f$ . One interpretation

therefore, is that the effects of particle slip become increasingly important as the wall is approached, and that the rapid and premature decrease in the Reynolds-averaged shear stress is due to the violation of the particle slip criterion.

The reader must be aware, however, of the limitations of the outline above, chiefly the crucial assumptions: (1) the characteristic length  $l$  in the approach  $u' \sim l \left| \frac{\partial \bar{u}}{\partial y} \right|$  is proportional to the distance from the wall, and (2) that  $u'$  and  $v'$  behave similarly, i.e.,  $u' \sim v'$ , in order to arrive at  $\overline{u'v'} \sim l^2 \left| \frac{\partial \bar{u}}{\partial y} \right| \frac{\partial \bar{u}}{\partial y}$ . The above mixing-length model merely serves as a starting point to develop a more comprehensive analysis, which may include for instance developing a nonisotropic eddy viscosity to make separate statements regarding the shear stress, and ones regarding  $u'$  and  $v'$ . The reader is referred to Obermeier (2006) for further details.

Moreover, since the Reynolds-averaged shear stress should in fact continue to increase until very close to the wall (typically  $y/\delta < 0.05$ , see e.g., Fernholz & Finley 1981; Pirozzoli & Grasso 2006), then under the present conditions, assuming our hypothesis to be correct, the particle response time  $\tau_p$  would have to be necessarily decreased in order to suppress the effects of particle slip. This may well constitute a fundamental limitation in obtaining accurate Reynolds-averaged shear stress measurements within compressible turbulent boundary layers using PIV, and further work is required in this area.

### 5.2.4 Space-Time Organization

To complement the discussion on the spatial characteristics of the undisturbed boundary layer, spatiotemporal information was obtained using HWA (see §3.3 for details). Data were acquired at 1000 kHz for a duration of 2 seconds under the same experimental conditions as the tomographic PIV experiment reported in §3.5, but without the presence of the shock wave generator. As noted by Spina *et al.* (1991), the hot-wire responds to the fluctuating streamwise mass-flux  $(\rho u)'$  and not simply the fluctuating streamwise velocity  $u'$ . The effects of the density on the measured momentum fluctuations  $(\rho u)'$  may be relieved, to first order, by dividing by the mean local density determined from the Crocco-Busemann relation, such that  $u' \sim (\rho u)' / \bar{\rho}$ . It must be noted, however, that in doing this the

fluctuating density  $\rho'$  is essentially ignored, since from Reynolds decomposition we have

$$(\rho u)' = \rho' \bar{u} + \bar{\rho} u' + \rho' u' - \overline{\rho' u'} \quad (5.7)$$

While the use of  $u' \sim (\rho u)' / \bar{\rho}$  is not strictly warranted, since  $\rho' \neq 0$  being proportional to  $(\gamma-1)M^2$ , the streamwise mass-flux fluctuations can still be considered proportional to the streamwise velocity fluctuations, at least approximately (see Spina *et al.* 1991), and will be considered as such here, in order to refer to flow regions in terms of speed and not momentum, in keeping with the PIV results. This does not affect the conclusions to be drawn.

The Fourier transform of the fluctuating streamwise mass-flux signal divided by mean local density is made using

$$\tilde{x}(\omega) = \frac{1}{\sqrt{2\pi}} \int_{-\infty}^{\infty} x(t) e^{2\pi i f t} dt \quad (5.8)$$

which for a finite, discrete time series becomes

$$\tilde{x}_n = \frac{1}{\sqrt{N}} \sum_{j=1}^N x_n e^{2\pi i n j / N} \quad (5.9)$$

The power spectrum is defined as the squared modulus of the Fourier transform

$$\Phi_{uu}(\omega) = |\tilde{x}_n|^2 \quad (5.10)$$

Ensembles of 75 records, each record containing approximately 26,600 samples, were used to estimate the power spectra  $\Phi_{uu}(\omega)$ , where  $\omega$  is the frequency, which yields a frequency resolution of  $\Delta f = 37$  Hz. Taylor's hypothesis was used to transform  $\omega$  into a wave number  $k$  (i.e.,  $k = 2\pi f / U_c$ , where  $U_c$  is the local convective velocity, taken as the mean local velocity in the present study).

The frequency spectrum  $\Phi_{uu}$  is shown in figure 5.5, taken at a height of  $y/\delta=0.1$  ( $y=2$  mm). The spectrum can be seen to exhibit a nearly flat distribution at wave numbers  $k_x\delta<0.6$ , and a  $k^{-1}$  power law behaviour over an intermediate wave number range  $0.6<k_x\delta<5$ . This is consistent with what has been observed by Kim & Adrian (1999), as well as Perry & Chong (1982), in their pipe and boundary layer flow, respectively. The cut-off frequency in the present data is taken to be  $f_c=20$  kHz, corresponding to a cut-off wave number of about  $k_x\delta=5$ , using Taylor's hypothesis, and is shown in the figure for comparison.

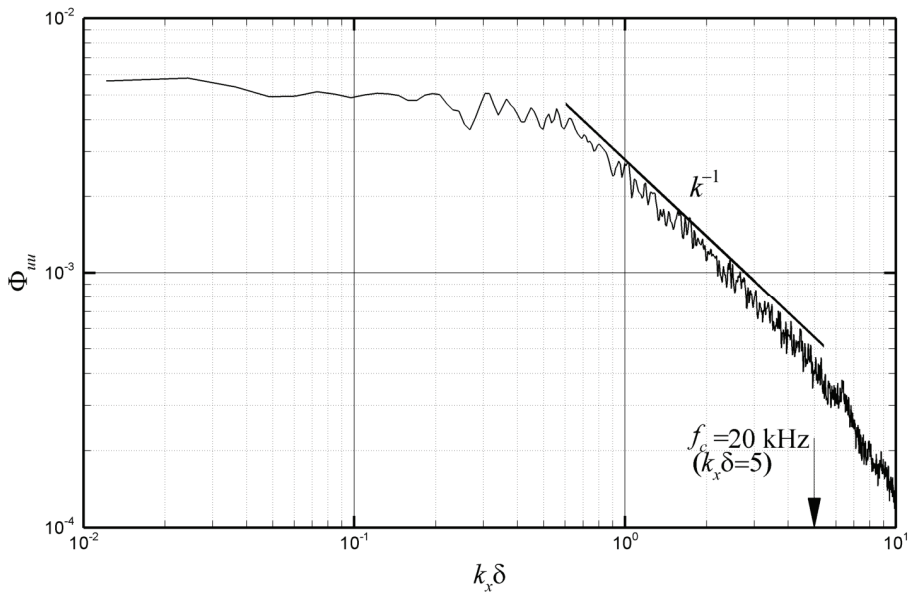


FIGURE 5.5: A typical wave number spectrum of the streamwise velocity component in log-log coordinates within the undisturbed boundary layer. Data is taken at  $y/\delta=0.1$  ( $y=2$  mm). Cut-off frequency  $f_c=20$  kHz ( $k_x\delta\approx 5$ , determined from Taylor's hypothesis) is shown for comparison.

The frequency spectrum  $\Phi_{uu}$  may be premultiplied by the wave number  $k_x$  in order to provide a different interpretation to the results (see Kim & Adrian 1999). This also ensures that equal areas under the graph correspond to equal energies. Figure 5.6 shows the premultiplied frequency spectrum  $k_x\Phi_{uu}$ , normalized by the total energy, against frequency  $f$  at a height of  $y/\delta=0.2$  ( $y=4$  mm). At this



level within the boundary layer, the most energetic frequencies occur in the kHz range, and no significant energy is present at the frequencies associated with the anticipated large-scale SWTBLI dynamics, which are typically in the range of a few hundred Hz to kHz (see e.g., Dolling 2001; Dupont 2006). The present results are also comparable with those of Dupont *et al.* (2006), who carried out HWA measurements within a Mach 2.3 boundary layer at the same height ( $y/\delta=0.2$ ), and also found maximal energy in this kHz range.

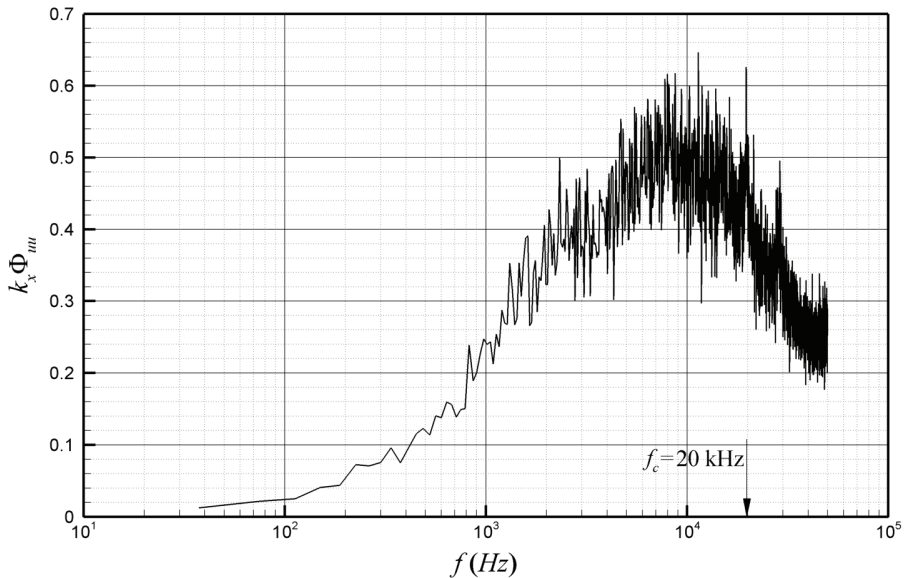


FIGURE 5.6: Premultiplied power spectrum  $k_x \Phi_{iii}$  within the undisturbed boundary layer against frequency  $f$ . Data taken at  $y/\delta=0.2$ . Spectrum is normalized by the total energy. Cut-off frequency  $f_c=20$  kHz is shown for comparison and data are not shown for  $f=50$  kHz.

To show the energy associated with the length-scales within the boundary layer, the premultiplied spectra is replotted in figure 5.7 at various heights, against the normalized wave-length  $\lambda_x/\delta$ , where  $\lambda_x=2\pi/k$ . To ease visualization, the data have been smoothed using a second-order least-squares regression with a 5-point kernel. This does not affect the trends shown. Within the range  $0.2 < y/\delta < 1.0$ , the spectra show a broad energetic peak in wave-lengths of around  $2\delta$ . This is consistent with the presence of  $\delta$ -scale bulges in this part of the

boundary layer, as demonstrated by the classical work of Kovaszny *et al.* (1970) for example. The energy contained at this length-scale increases appreciably towards the wall, but remains quite constant within the range  $0.1 < y/\delta < 0.8$ .

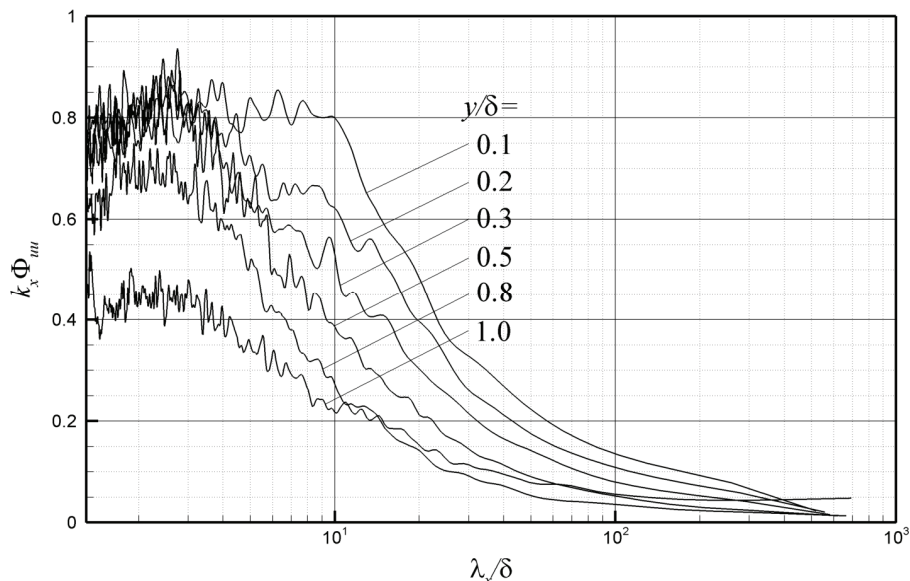


FIGURE 5.7: Premultiplied power spectra at various heights within the undisturbed boundary layer. Spectra are normalized by the total energy. Data are not shown below cut-off wave-length (estimated to be  $\lambda_x/\delta \approx 1.3$  using Taylor's hypothesis).

At  $y/\delta=0.1$ , however, the broad peak has shifted toward larger wave-lengths extending up to  $\lambda_x=10\delta$ , indicating the presence of very large-scale motions. This has also been observed by Kim & Adrian (1999), who formulated a conceptual model based on this observation, consisting of the coherent alignment of hairpins into groups to form so-called *hairpin packets*, and these packets then align to form the very large-scale streamwise-elongated regions of relatively low- and high-speed fluid near to the wall. Such long low- and high-speed regions have also been reported in numerous incompressible turbulent boundary layer studies, such as by Hutchins & Marusic (2007) using a spanwise array of hot-wires, as well as by Tomkins & Adrian (2003) and Ganapathisubramani *et al.* (2003) using planar PIV. Such regions have also been reported in supersonic turbulent

boundary layers by Ganapathisubramani *et al.* (2006) using planar PIV, as well as computationally using DNS by Ringuette *et al.* (2008).

In the present boundary layer, energy contained in these wave-lengths decreases significantly with distance from the wall, and by  $y/\delta=0.5$ , only half of the energy is present in wave-lengths of  $10\delta$  than at  $y/\delta=0.1$  for example. This suggests that such length-scales are confined mainly to the lower half of the boundary layer, as noted by Kim & Adrian (1999) and the references cited therein. The present results are also consistent with those of Elsinga (2008), who carried out HWA measurements in the undisturbed boundary layer of the same facility at a slightly lower Reynolds number. As remarked by Kim & Adrian (1999), it must be kept in mind that the wave-lengths reported here represent a lower bound on the actual wave-lengths, since they have been inferred from frequency spectra, which suffer from lost correlation due to convection velocity of the components in various values.

The reader should also consider the Reynolds number influence on the above discussion. As noted by Elsinga (2008), in low Reynolds number turbulent boundary layers, hairpins are found aligned in the streamwise direction into hairpin packets in the lower half of the boundary layer, which extend over a distance of about  $\delta$ . For high Reynolds number turbulent boundary layers, the packets themselves also seem to align in the streamwise direction, forming very long streamwise zones ( $>3\delta$ ) of low-velocity. Thus, we can anticipate that at high Reynolds numbers, the premultiplied spectrum reveals these very large-scale motions, as appears to be evidenced in figure 5.7. As further discussed by Adrian (2007), increasing the Reynolds number effectively makes more room for the packets to grow, so packets would contain more hairpins that may become more complex at higher Reynolds numbers, further noting that since the viscous length-scale is  $\delta_v = \nu/u_\tau$  ( $y^+ = y/\delta_v$ ) and that hairpins reach a mature shape when they are nominally 100 viscous wall units tall; then the ratio of the tallest to smallest hairpin becomes  $\delta/100\delta_v \approx Re_\tau/100$ .

Overall, the present incoming boundary layer clearly consists of very large-scale motions, and we will see in the forthcoming chapters the influential role that they play in the interaction's large-scale unsteadiness.



# CHAPTER 6 2D FLOW ORGANIZATION

---

## 6.1 Introductory Remarks

**W**E begin our discussion of the interaction by considering its two-dimensional flow organization using the planar PIV system. An assessment is first made of the possible spanwise nonuniformities that are often considered to be present in the type of interaction under investigation. Results from the planar PIV SWTBLI study are then presented, which describe the mean flow pattern and instantaneous flow organization of the interaction. Statistical flow properties are then presented, followed by a POD analysis of the data, which will begin to provide the context for a reduced-order description of the interaction's unsteady flow organization.

Before proceeding, it is worth mentioning that there are no surface pressure measurements reported in this thesis. Unfortunately, such measurements were not available within the present study. However, the mean static and total pressure distributions of the present interaction have been determined indirectly from the PIV data, via the momentum equations, in the recent article by van Oudheusden (2008).

## 6.2 Assessment of Spanwise Uniformity

### 6.2.1 Surface Flow Visualization

We first wish to assess possible spanwise nonuniformities that are often present in nominally two-dimensional SWTBLIs (Dolling 2001). Such an assessment is particularly important for the tomographic experiments, since the shock generator used only spans 65% of the test-section width. One of the simplest and most useful techniques for such an assessment is surface flow visualization. Here, we employ a dye dispersed in oil that is smeared onto the surface to visualize the near-wall velocity directional information. To improve the visibility of the flow pattern, a black adhesive tape was first applied to the surface, and then a mixture of titanium dioxide, kaoline, tween, and petroleum was applied.

As noted by Settles (1993), while this technique is effective, it suffers from several drawbacks that should be briefly addressed. For example, the oil remains wet throughout the wind-tunnel run and smears on wind-tunnel shut-down. Furthermore, there is a build-up of oil at the flow separation lines, which can produce anomalous patterns. Nevertheless, it is sufficient for our present purpose, which is to assess the global two-dimensionality of the interaction.

Figure 6.1 shows a surface flow visualization of the interaction. Experimental conditions are the same as for the tomographic PIV SWTBLI experiments. The flow direction is from top to bottom and is shown in a perspective view. The projection of the tomographic PIV measurement domain is indicated by the dashed box. Several runs were made, and this photograph may be considered as being representative of the results obtained. A separation line can be observed to extend across the measurement domain, as evidenced by the accumulation of oil into a thick white band.

Importantly, it can be seen that the interaction remains largely symmetrical about the centre-line within the spanwise region considered. For distances greater than  $\delta$  from the centre-line, however, then three-dimensional effects may be observed. In particular, there is an appreciable curvature of the oil flow pattern away from the centre-line. It is interesting to note that the region of spanwise uniformity ( $4\text{ cm}$ ,  $2\delta$ ) is much smaller than the width of the shock generator itself ( $18\text{ cm}$ ,  $9\delta$ ), and highlights the necessity of having a sufficiently large spanning shock generator in this type of experiment. Nevertheless, it can be concluded that the interaction remains two-dimensional within the measurement domain considered.

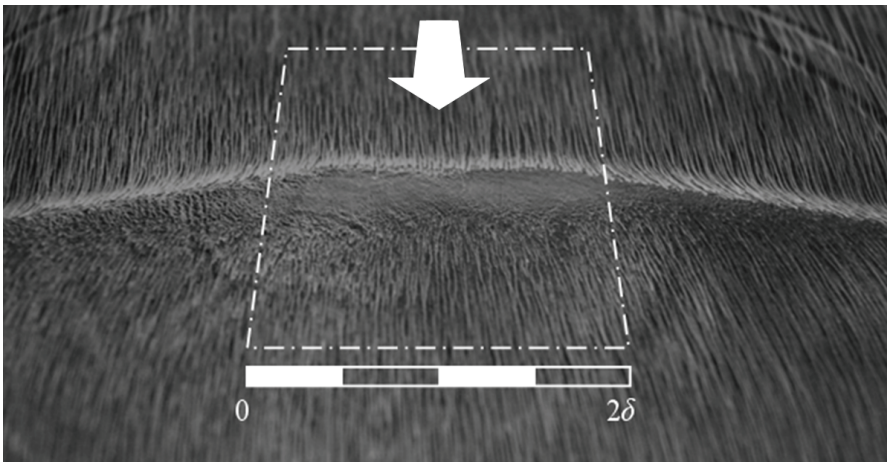


FIGURE 6.1: Surface flow visualization of the interaction. Flow is from top to bottom as indicated by the white arrow. Dashed box indicates tomographic PIV measurement domain. Note the skewed/perspective view. From Humble *et al.* (2008).

### 6.2.2 PIV Spanwise Survey

To examine the spanwise effects quantitatively, a multiplanar assessment of the interaction region was carried out using the planar PIV system but with the limited-span shock generator. Velocity fields were obtained in the streamwise–wall-normal plane within the spanwise range  $-2.5 \leq z/\delta \leq 2.5$ , in increments of  $z/\delta=0.5$  (i.e., 9 planes). This range was limited by the finite seeded flow volume

entering the test-section. A total of 50 images were acquired at each spanwise location. For illustrative purposes, figure 6.2 shows semitransparent isocontours of mean streamwise velocity. The slices in perpendicular planes have been linearly interpolated. The origin of the reference coordinate system is with  $x$  measured in the downstream flow direction from the extrapolated wall impingement point of the incident shock wave and  $y$  normal to the wall. From these results, the flow appears two-dimensional within the spanwise region investigated, consistent with the surface flow visualization.

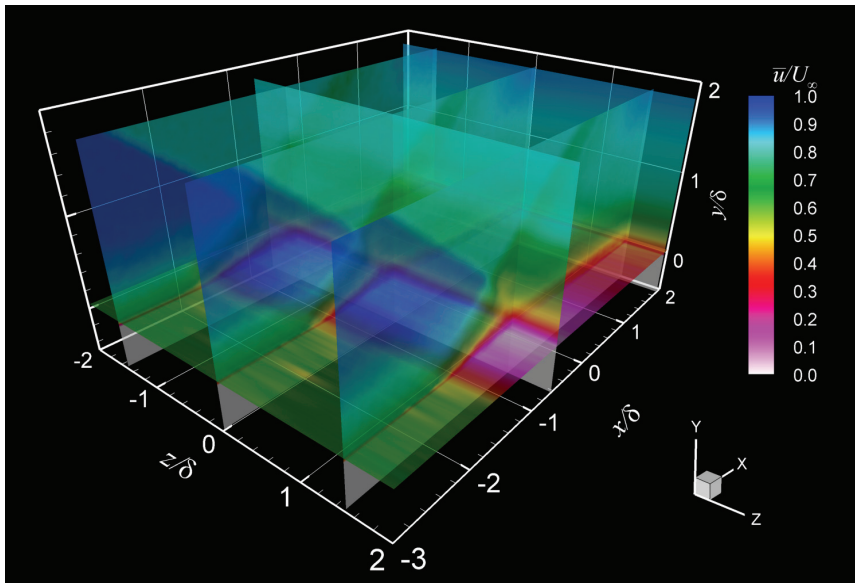


FIGURE 6.2: Spanwise survey of the interaction using planar PIV. Transparent slices show contours of mean streamwise velocity. The streamwise-spanwise plane is shown at  $y/\delta=0.05$ . The spanwise-wall-normal plane is shown at  $x/\delta=-1.0$ . Modified from Humble *et al.* (2007b).

In addition, figure 6.3 shows a rendered representation of the inner part of the interaction using the results shown in figure 6.2. Flooded contours of streamwise velocity are shown with mean two-dimensional streamtubes within the lower part of the boundary layer (beginning from the upstream edge of the measurement domain at  $y/\delta=0.15$ ). Unlike the surface flow visualization and mean streamwise velocity distributions, the variation of streamwise velocity around these tubes indicates that three-dimensional effects appear to



exist, albeit subtly, within the interaction. Overall, however, the interaction is considered to be sufficiently two-dimensional on the mean to proceed with conducting a planar PIV study along the centre-line of the interaction.

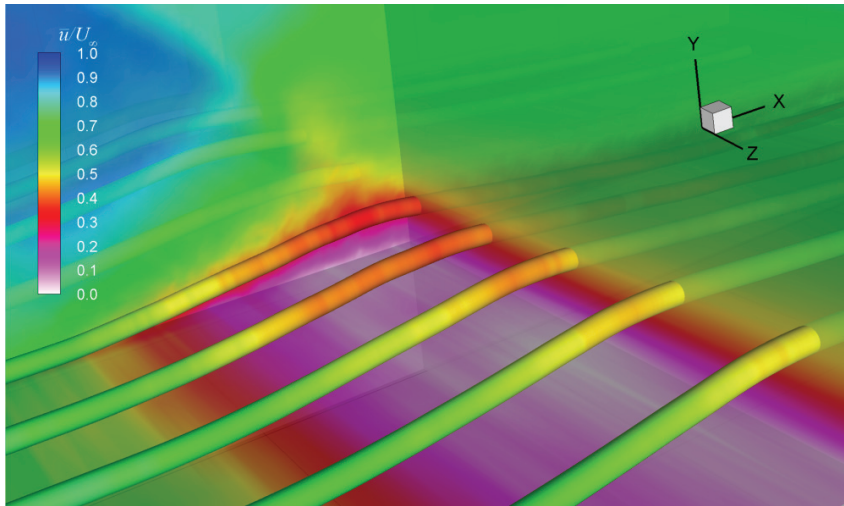


FIGURE 6.3: Rendering of the inner part of the interaction. Shown are mean streamtubes coloured by mean streamwise velocity. Streamtubes begin from the upstream edge of measurement domain at  $y/\delta=0.15$ . From Humble *et al.* (2007b).

## 6.3 Basic Flow Properties of the Interaction

### 6.3.1 Qualitative Features

To first provide an overview of the basic features of the interaction, figure 6.4 shows a series of uncorrelated short-exposure Schlieren visualizations. The aim with Schlieren photography is to make visible light ray deviations due to the refractive index heterogeneities. For an excellent introduction to Schlieren photography, the reader is referred to the book by Settles (2001). The first figure part highlights the incoming boundary layer, incident and reflected shock waves. The dashed line represents the extrapolation of the incident shock wave to the wall, and shows again the origin of the reference coordinate system used, with  $x$  measured in the downstream flow direction from the extrapolated wall impingement point of the incident shock wave and  $y$  normal to the wall.

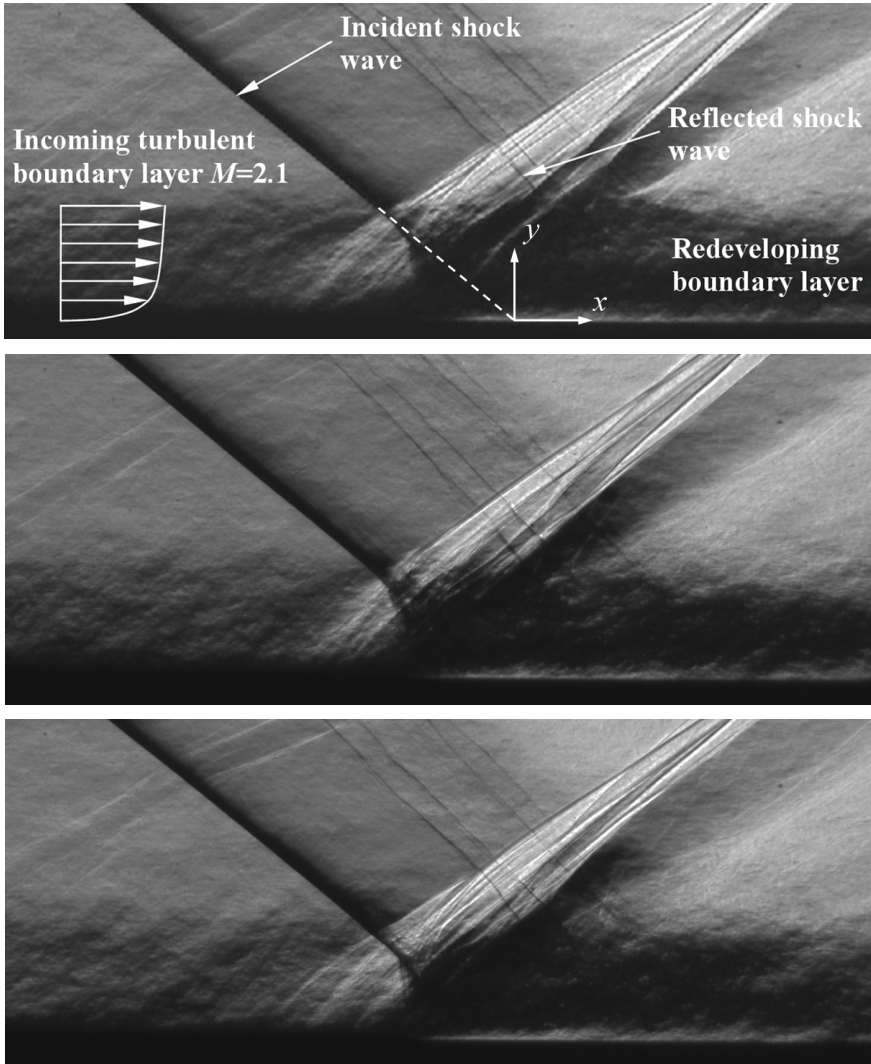


FIGURE 6.4: A series of uncorrelated short-exposure Schlieren visualizations of the interaction. (50 ns exposure time.) Origin of coordinate system is located at the extrapolated wall impingement point of the incident shock wave. Undisturbed boundary layer thickness is 20 mm. From Humble *et al.* (2008).

Because the Schlieren image represents a spanwise average of the density gradients, there is little indication of the turbulent structures present within the incoming boundary layer, consistent with the

Schlieren results of Dupont *et al.* (2006) in their incident SWTBLI at Mach 2.3 for example. The penetration of the incident shock wave into the boundary layer, however, can be readily observed, where it appears to fan out and break into a number of subsidiary shocks, as observed by Smits & Bogdonoff (1986) in their compression ramp interaction. Except for the part within the boundary layer, the incident shock wave appears quite uniform in the spanwise direction.

It is evident that compression waves form ahead of where the incident shock wave would impinge on the wall in the absence of the boundary layer. The comparatively high Reynolds number of the present experiments (c.f. Wu & Martin 2008; Pirozzoli & Grasso 2006) means that the waves emanate from deep within the boundary layer close to the wall. These waves coalesce to form the reflected shock wave. An appreciable spanwise distortion of the reflected shock wave can be observed in each frame. As reported by Smits and Bogdonoff (1986), Muck *et al.* (1985) showed that such a shock front was not split, but in fact wrinkled in the spanwise direction. The visualizations of Smith *et al.* (1991) also showed that the shock front can split. This will become a focal point of our discussion later on. Farther downstream, the redeveloping boundary layer undergoes a recovery process.

The planar PIV system can be used to provide a further characterization of the interaction's main phenomenological features. Figure 6.5 shows two-dimensional velocity streamlines complemented with mean wall-normal velocity contours. The spatial coordinates are normalized with the undisturbed boundary layer thickness  $\delta$ . The streamlines verify a uniform outer flow upstream, and illustrate the distortion of the flow-field, as a result of the interaction process. Regions of flow compression typically appear as densely-spaced wall-normal velocity contours, whereas sparsely-spaced wall-normal velocity contours typically indicate regions of flow expansion.

The incident shock wave can be seen to enter the boundary layer, where it begins to curve in response to the decreasing local Mach number (D elery & Bur 2000). It reflects from the sonic line as an expansion fan. Observe the compression waves generated within the incoming boundary layer approximately  $2\delta$  upstream of the origin. These compression waves coalesce as they leave the boundary layer

to form the reflected shock wave. Farther downstream, fluid close to the wall begins to contract, causing the outer fluid to move back towards the wall. Notice how close to the wall, the distance between adjacent streamlines *increases* throughout the interaction, whereas farther away from the wall the distance between adjacent streamlines *decreases* throughout the interaction. This highlights the contrasting behaviour between the subsonic and supersonic parts of the interaction, respectively, and gives us our first hint of a multistructured interaction. Although difficult to discern in the figure, a gradual recompression process takes place farther downstream, as fluid is slowly turned back parallel with the wall.

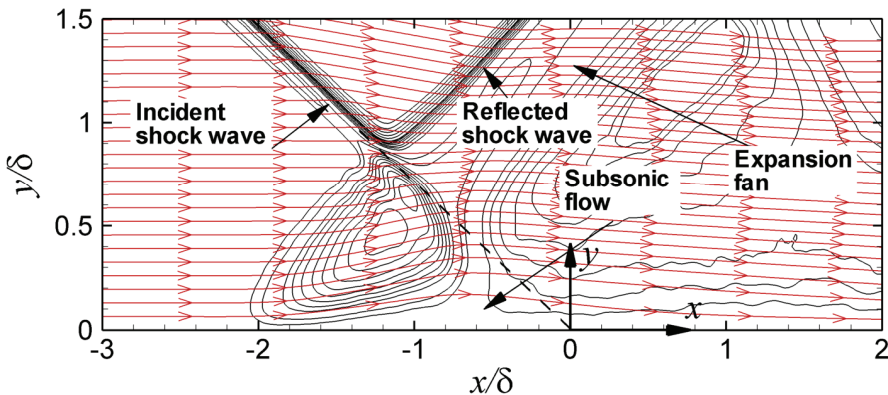


FIGURE 6.5: Mean flow organization of the interaction using planar PIV. Mean velocity streamlines are shown along with mean wall-normal velocity contours. Origin of coordinate system is located at the extrapolated wall impingement point of the incident shock wave. Modified from Humble *et al.* (2007b).

### 6.3.2 Mean Velocity Pattern

The mean velocity pattern of the interaction is quantitatively described by the ensemble-averaged streamwise and wall-normal velocity fields shown in figures 6.6 and 6.7, respectively. Mean velocity fields shown in figures 6.6 and 6.7, respectively. Mean velocity vectors are also shown, under-sampled showing 1 in 22 in the streamwise direction for clarity. The mean velocity fields again highlight the incident and reflected shock waves, as well as the overall distortion of the boundary layer. The mean velocity vectors within the incoming boundary layer are parallel with the wall, until about  $2\delta$  upstream of the origin, where they begin to deflect upwards. Fluid

then moves away from the wall in the first part of the interaction, with a maximal wall-normal velocity of about  $0.15 U_\infty$ .

The flow through the shock waves and expansion fan are also clearly described by the velocity components. The increased level of velocity along the incident and reflected shock waves in the free-stream is typically encountered in these experimental conditions, and is ascribed to the limitations of the PIV measurement technique, in particular due to particle inertia and finite spatial resolution (see Schrijer *et al.* 2006 for a further discussion). A weak feature immediately upstream of the incident shock wave (roughly parallel to it) can also be observed in figure 6.7. This is due to optical aberration effects introduced by the inhomogeneous index of refraction field of this compressible flow (see Elsinga *et al.* 2005).

Farther downstream in figure 6.6, there is a region in the lower 25% of the redeveloping boundary layer that has a significant streamwise velocity deficit compared with the incoming boundary layer. Such a deficit is associated with a series of inflected profiles, and represents the momentum loss extracted from the mean flow to the fluctuating flow-field. Figure 6.7 shows that in this same region, there is a large part of the redeveloping boundary layer that contains fluid returning towards the wall with a velocity magnitude within the range  $0\text{--}5\% U_\infty$ . Here, the boundary layer does not appear to attain the free-stream velocity value away from the wall, nor does its wall-normal velocity component become everywhere zero, except in the proximity of the wall due to the wall restraining effect.

Importantly, there are no reversed-flow velocity vectors detected within the interaction, indicating that the flow appears to remain fully-attached on average. Higher resolution experiments considering only the reversed-flow region (not shown here for brevity) revealed the same result. On the other hand, it is well-known that PIV has a limited resolution near the wall; averaging over a PIV interrogation window can mask small regions of reversed-flow. Furthermore, the separation bubble height can be very small (see e.g., Pirozzoli & Grasso 2006). Taken together with the surface flow visualization, which shows that flow separation occurs, the results are consistent with an interaction that exhibits incipient separation (see Simpson 1989).

A small reversed-flow region may therefore be present on average, even if it is not detected in the present results. Nevertheless, even if reversed-flow exists on the mean, it does not appear to significantly affect the overall mean flow-field structure. This conclusion will become a recurrent point throughout subsequent chapters.

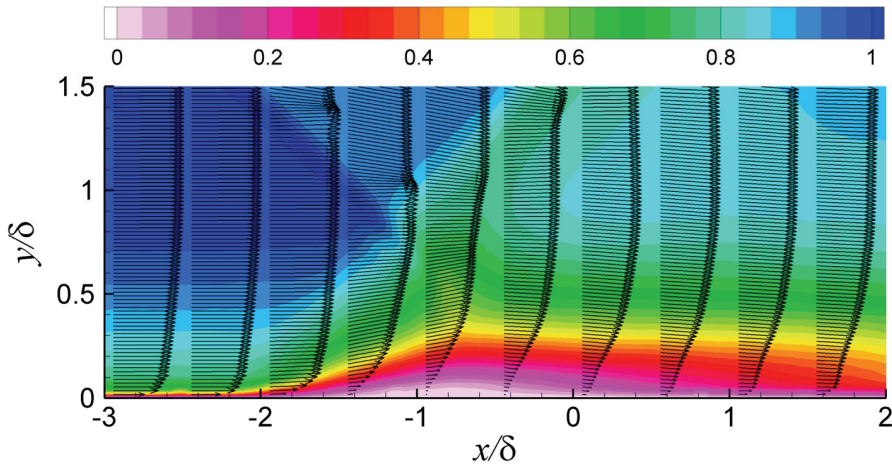


FIGURE 6.6: Mean streamwise velocity distribution  $\bar{u}/U_\infty$ . Mean velocity vectors show 1 in 22 in the streamwise direction. Modified from Humble *et al.* (2007b).

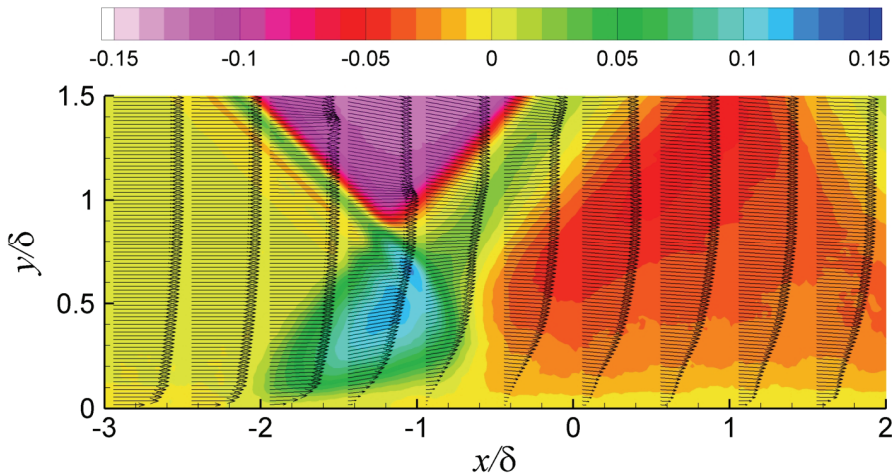


FIGURE 6.7: Mean wall-normal velocity distribution  $\bar{v}/U_\infty$ . Mean velocity vectors show 1 in 22 in the streamwise direction. Modified from Humble *et al.* (2007b).



### 6.3.3 Integral Parameters

To further characterize the mean flow organization of the interaction, mean streamwise velocity profiles are integrated at various streamwise locations to obtain incompressible values of the displacement thickness  $\delta_i^*$ , momentum thickness  $\theta_i$ , and shape parameter  $H_i$ , defined by

$$\delta_i^* = \int_0^\delta \left(1 - \frac{\bar{u}}{U_e}\right) dy, \quad \theta_i = \int_0^\delta \frac{\bar{u}}{U_e} \left(1 - \frac{\bar{u}}{U_e}\right) dy, \quad H_i = \delta_i^* / \theta_i, \quad (6.1)$$

respectively, where  $\bar{u}$  is the local mean streamwise velocity,  $\delta$  the undisturbed boundary layer thickness, and  $U_e$  is the boundary layer edge velocity. The evolution of these integral parameters is shown in figure 6.8 at various streamwise locations. It should be noted that integrating to infinity (in our case the height of the measurement domain) and using the undisturbed free-stream velocity  $U_\infty$  instead of  $U_e$  gives the same trends. Furthermore, it is anticipated that the evolution of the equivalent compressible versions of the integral parameters will be qualitatively similar, except perhaps, in the vicinity of the shock waves.

It can be seen that the integral parameters remain quite constant within the undisturbed boundary layer, but undergo different evolutions throughout the interaction. In particular, a rapid increase in the displacement thickness occurs in the first part of the interaction, reaching a maximum value of over 50% of the undisturbed boundary layer thickness. This is followed by a rapid decrease farther downstream. In contrast, the momentum thickness essentially increases throughout the interaction.

Following Délerly & Marvin (1986), this contrasting behaviour can be readily understood when one considers the von Kármán integral momentum equation, written for an incompressible flow for simplicity as

$$\frac{\partial \theta}{\partial x} = \frac{C_f}{2} - (2 + H) \frac{1}{U_e} \frac{\partial U_e}{\partial x} \theta \quad (6.2)$$

Since the pressure gradient remains positive throughout the first part of the interaction (i.e.,  $\partial U_e/\partial x < 0$ ), and the skin friction coefficient  $C_f$  remains a small (but positive) quantity, then  $\partial\theta/\partial x$  must also remain necessarily positive, and explains the increase in momentum thickness throughout most of the interaction. Note that in the compressible case, the integral momentum equation has the additional term  $-(\theta/\rho_e)\partial\rho_e/\partial x$  on the right-hand side. This term does not appear to significantly affect the results, however, since  $\partial\theta/\partial x$  remains positive throughout most of the interaction, even in the first part of the interaction, where we expect that  $\partial\rho_e/\partial x > 0$ .

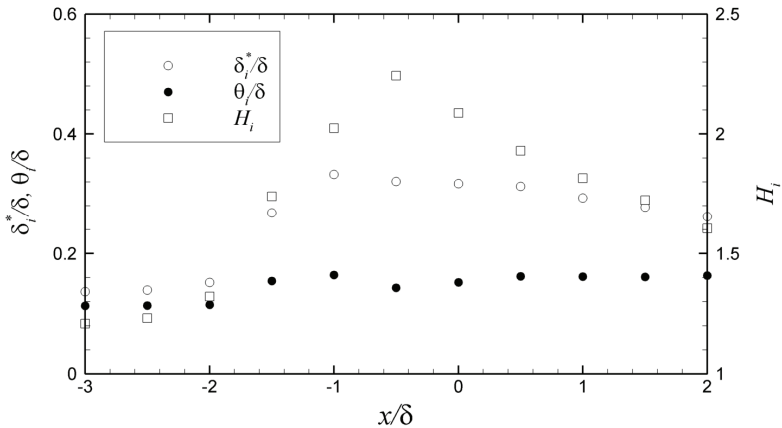


FIGURE 6.8: Streamwise evolution of the displacement thickness  $\delta_i^*$ , momentum thickness  $\theta_i$ , and shape parameter  $H_i$  throughout interaction.

These results suggest that the behaviour of the shape parameter is therefore primarily driven by the variation of the displacement thickness in this interaction, consistent with the observations of Déleroy & Marvin (1986) in their interactions involving transonic bumps. It is also interesting to note that the shape parameter attains a maximum incompressible value of approximately 2.3, appreciably less than the commonly admitted values associated with turbulent separation (about 2.8, see Déleroy & Marvin 1986). While this is consistent with a boundary layer that remains attached on the mean, it should also be remarked that an accurate determination of the shape parameter is difficult in regions of strong streamwise gradients and in the presence of shock waves.



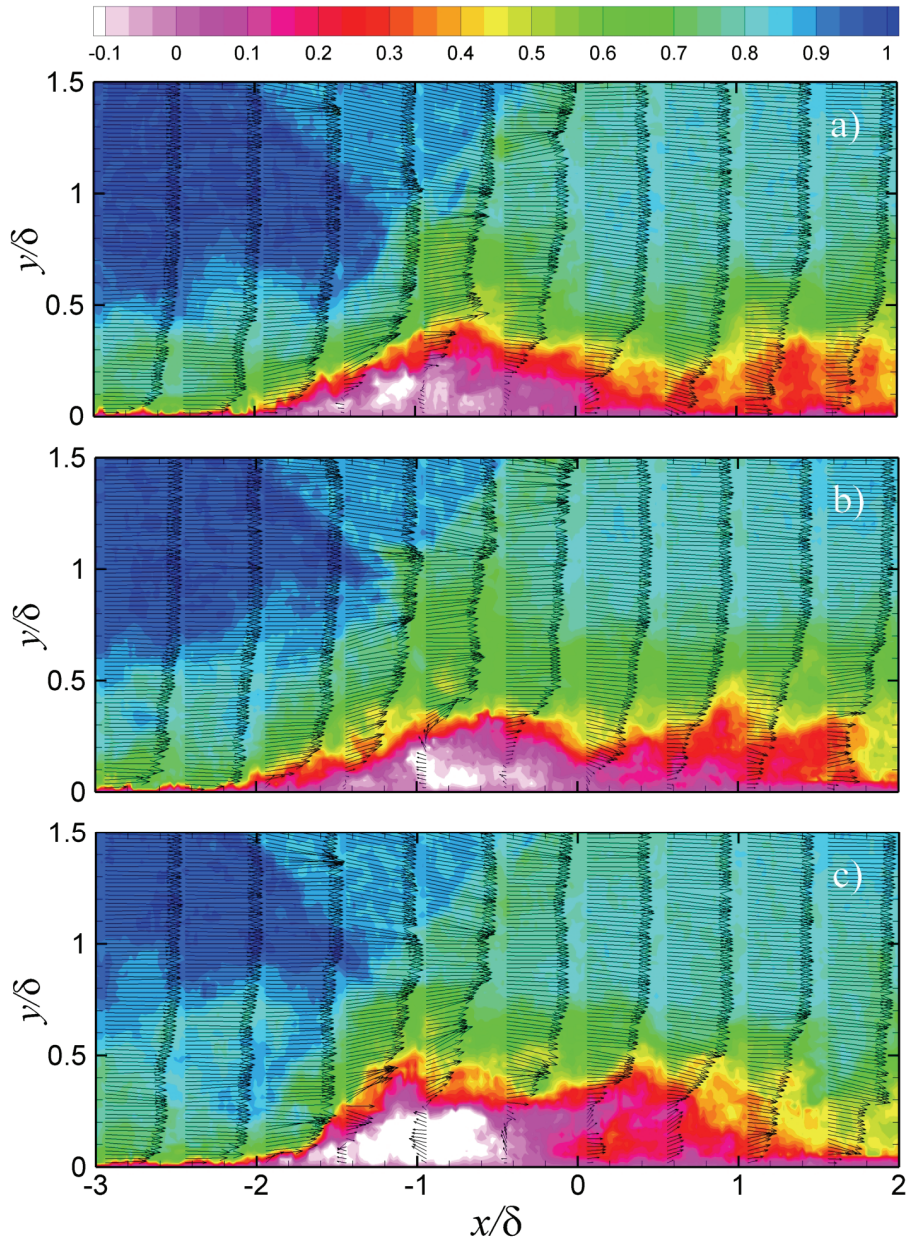
## 6.4 Unsteady Flow Properties

### 6.4.1 Instantaneous Velocity Patterns

Having outlined the basic features of the mean flow-field, the question naturally arises as to whether the above description is an accurate representation of the flow-field structure, since it is the result of time-averaging the flow-fields. A series of instantaneous streamwise velocity fields is shown in figure 6.9. These fields are chosen because they are representative of the complete dataset. Recall that the acquisition time between any two velocity fields (10 Hz recording rate) is much greater than any characteristic time-scale of interest, and so the velocity fields are uncorrelated in time. Velocity vectors are also shown, under-sampled with 1 in 22 in the streamwise direction for clarity. Note also the nonuniform axes.

The results portray an unsteady incoming boundary layer, with its instantaneous edge appearing as an intermittent interface with the outer free-stream flow. This is consistent with the observations of Smith & Smits (1995), who visualized the structure of supersonic boundary layers using Schlieren and Rayleigh scattering, and characterized the outer layer as consisting of an array of regularly-spaced uniform low-density bulges, separated from a uniform higher-density free-stream by a sharp, instantaneously ragged interface.

The global structure of the interaction can be seen to change significantly in time. Figures 6.9(a–c) show that, in contrast to the mean velocity distribution, fluid close to the wall is instantaneously redirected upstream as it approaches the interaction, leading to the formation of a separated flow region. At these instants, the flow structure is very different from the mean flow-field shown earlier, and the flow resembles the mean separated flow model, in the sense of a well-defined large-scale separation bubble (see Simpson 1989).



(see figure caption on next page.)

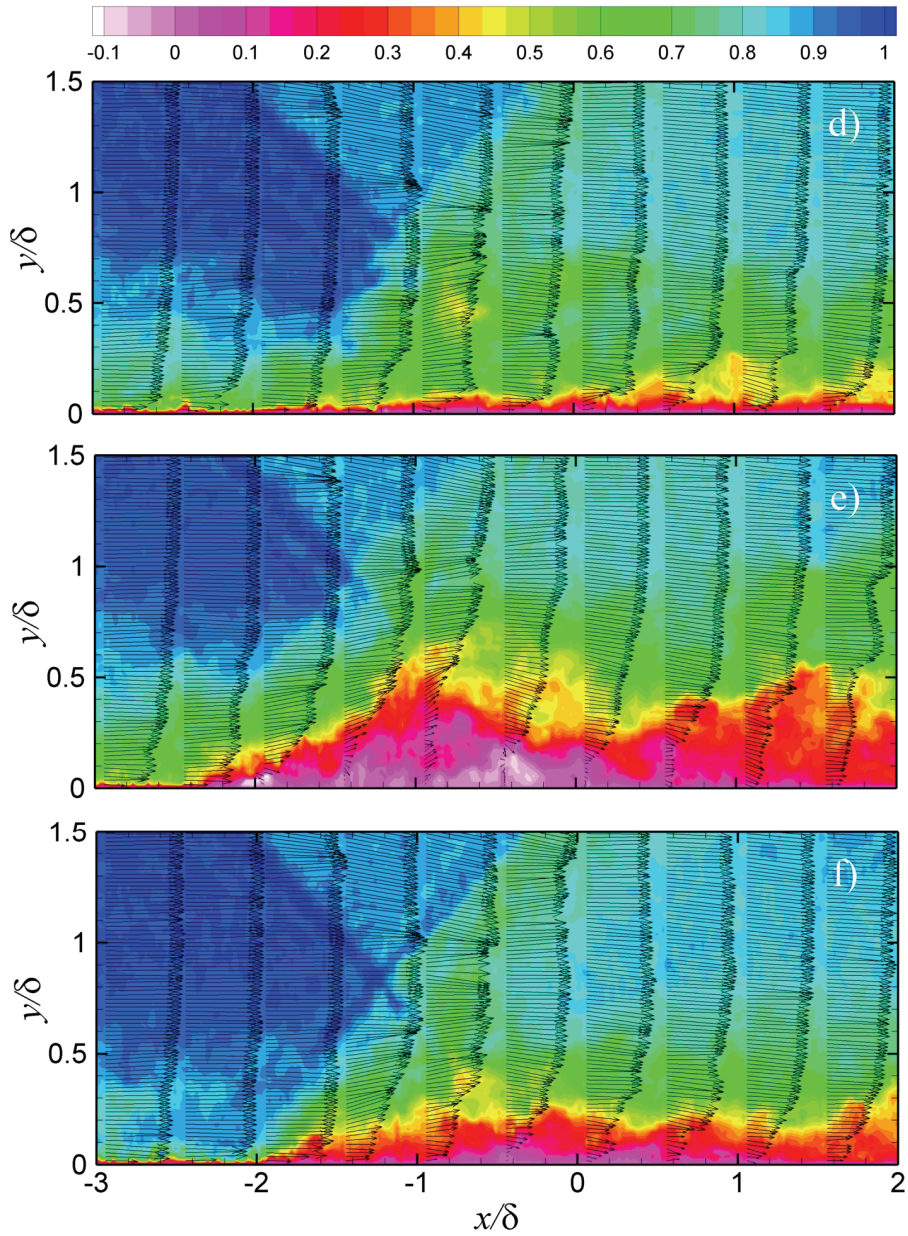


FIGURE 6.9: A series of uncorrelated instantaneous streamwise velocity distributions  $u/U_x$ . Velocity vectors show 1 in 22 in the streamwise direction. Note the nonuniform axes. Modified from Humble *et al.* (2007b).

The size of the separation bubble clearly varies in time. By visual inspection, it appears to have a streamwise length that varies in the range between  $0-2\delta$  (compare for instance figures 6.9(c, d)). The flow within the bubble cannot be characterized as a stagnant velocity zone; the maximum backflow velocity often exceeds  $-0.1U_\infty$ . This is consistent with the measurements made by Bookey *et al.* (2005) in their incident SWTBLI at Mach 2.9, who report a similar reversed-flow velocity. In contrast, figures 6.9(d, f) show instants in which the boundary layer remains fully attached throughout the interaction. Taken together with the mean velocity fields, it now becomes clear that the interaction may be conceived as an intermittently separated configuration.

It appears that the interaction instantaneously exhibits a multilayered structure, as first hinted in the time-averaged characterization. Figures 6.9(a-c, e) show that the interaction exhibits, on this instantaneous basis, a high-velocity outer layer (typically  $u/U_\infty > 0.5$  (shown in green-blue)), above a layer of low-velocity close to the wall (typically  $u/U_\infty < 0.5$  (shown in red-orange)). These layers are conceptually reminiscent of the zones of uniform momentum reported by Adrian *et al.* (2000) in their incompressible turbulent boundary layer. The term *layer* is used here to emphasize that while they are defined instantaneously, they typically extend in the streamwise direction across the measurement domain. The outer layer comprises most of the incoming boundary layer. The inner layer rapidly thickens as it enters the first part of the interaction, often reaching its maximum thickness beneath the incident shock wave. These layers loosely correspond to the supersonic and subsonic regions of the interaction, respectively. The reader should note, however, that the above is somewhat of a subjective characterization, given the complex nature of the interaction, and is done so for the purposes of simplifying the conceptual interpretation of the results.

Nevertheless, the two layers appear to be separated by a thin region of high shear, indicated by the yellow contour. Figures 6.9(b, c, e) show that this interface has an irregular and intermittent nature, with a typically downstream-sloping pattern within the redeveloping boundary layer. Figures 6.9(b, c) show that mixing occurs across these layers, with outer fluid injected deep into the low-velocity region. Overall, the flow in the detached shear layer appears to be

qualitatively similar to a plane mixing layer, as noted by Na & Moin (1998) in their DNS of an incompressible separated flow, for instance.

Moving downstream, figures 6.9(a–c) show that the separated shear layer locally reattaches. While this reattachment takes place within a streamwise extent  $0-2\delta$  after separation, the overall velocity deficit within the inner layer persists much farther downstream. In fact, it is clear that the boundary layer does not fully recover to its incoming conditions within the present measurement domain. Wu & Martin (2008) and Dupont *et al.* (2006) both report that the boundary layer relaxes to an equilibrium state downstream of the interaction that typically requires a length  $O(10)$  incoming boundary layer thicknesses.

### 6.4.2 Instantaneous Vorticity Patterns

To complement the discussion on the instantaneous velocity fields, out-of-plane vorticity and vortical (or coherent) structures within the interaction are visualized. This constitutes one of the more subtle aspects of interpreting the PIV velocity vector fields (see Adrian *et al.* 2000). The instantaneous velocity fields in figure 6.9 are reproduced in figure 6.10, now displaying flooded contours of instantaneous out-of-plane (spanwise) vorticity  $-\omega_z\delta/U_\infty$ . Note the nonuniform axes. To ease visualization, the spatial derivatives have been estimated by a second-order least-squares regression using a  $5\times 5$  kernel. This does not affect the conclusions to be drawn. Overlaid are white lines of instantaneous wall-normal velocity ( $v/U_\infty$ ) within the range  $-0.15 \leq v/U_\infty \leq 0.15$ , where dashed lines indicate negative values.

In addition, following the method proposed by Hunt *et al.* (1988), vortical structures are identified, as any contiguous region of flow where the second invariant  $Q$  of the velocity gradient tensor is greater than zero. In the present study, it is assumed that the criterion  $Q>0$  is valid in compressible flow, since the divergence of velocity field was found to be relatively small (typically an order of magnitude less than the rate-of-strain and rate-of-rotation tensors), except of course in the presence of shock waves, and more importantly, because results were obtained that were very similar to the use of other (incompressible) criterion, such as the  $\lambda_2$  criterion (see Jeong *et al.* 1997). The reader will note that in two-dimensional measurements there are also

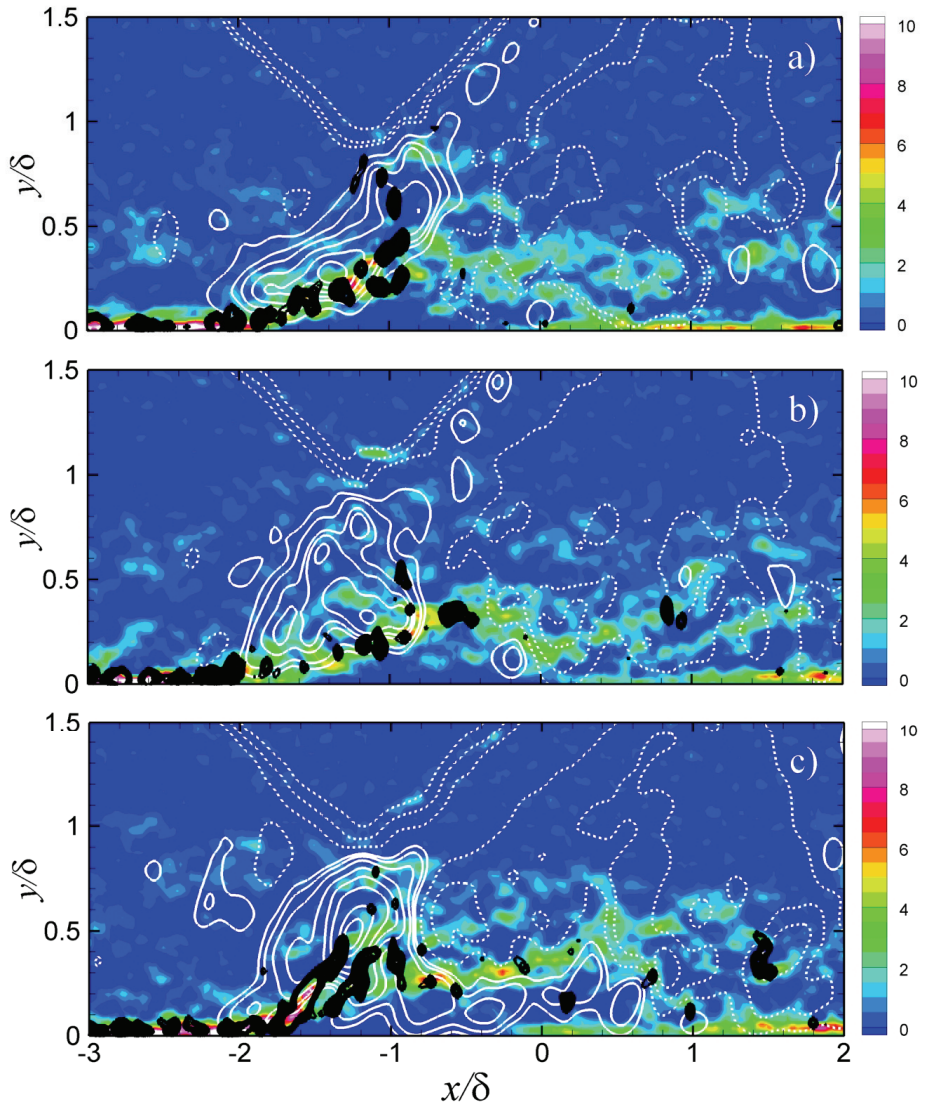
missing components of the velocity gradient tensor, and the following determined patterns must therefore be considered as only a section of the complete three-dimensional structure from the  $x$ - $y$  plane. Furthermore, since the present resolution cannot be used to accurately determine statistics of derived quantities such quantities as vorticity, the following results are used qualitatively to illustrate the interaction's global vorticity organization, and to provide a further characterization of the interaction unsteadiness.

Indeed, extending the measurement uncertainty analysis to the  $Q$  criterion, using its analytical expression for two-dimensional measurements (see Hunt *et al.* 1988), returns an RMS measurement uncertainty of 36% when normalized by the maximum  $(\partial u / \partial x)_{\text{RMS}}$  in the measurement domain, further justifying its qualitative discussion here. On the other hand, the reader is reminded that this value of uncertainty represents a 'worst case scenario' of uncorrelated data points, which when considered in the  $Q$  formulation leads to products of gradients that are separated by two standard deviations.

With these caveats in mind, figure 6.10 reveals some interesting features. It shows that within the incoming boundary layer, most of the vorticity tends to be concentrated close to the wall in the form of a vorticity layer. This is consistent with the work of Ringuette *et al.* (2008), who visualized instantaneous out-of-plane vorticity from the DNS of a supersonic boundary layer in the streamwise-wall-normal plane, and also observed regions of containing high levels of vorticity close to the wall. It was also shown by these authors when visualizing the same result in three-dimensions, that vortical structures are in fact connected out of the plane forming complicated hairpin packets. Our two-dimensional patterns must therefore be considered as only a cross-sectional view of the complete three-dimensional flow-field.

In the present results, flow structures revealed by the  $Q$  discriminant are also distinguished within the incoming boundary layer very close to the wall, although the reader must exercise caution in interpreting such structures. The present resolution is insufficient to properly resolve the swirling motions in this region, and many such motions are most likely numerical artefacts.





(see figure caption on next page.)

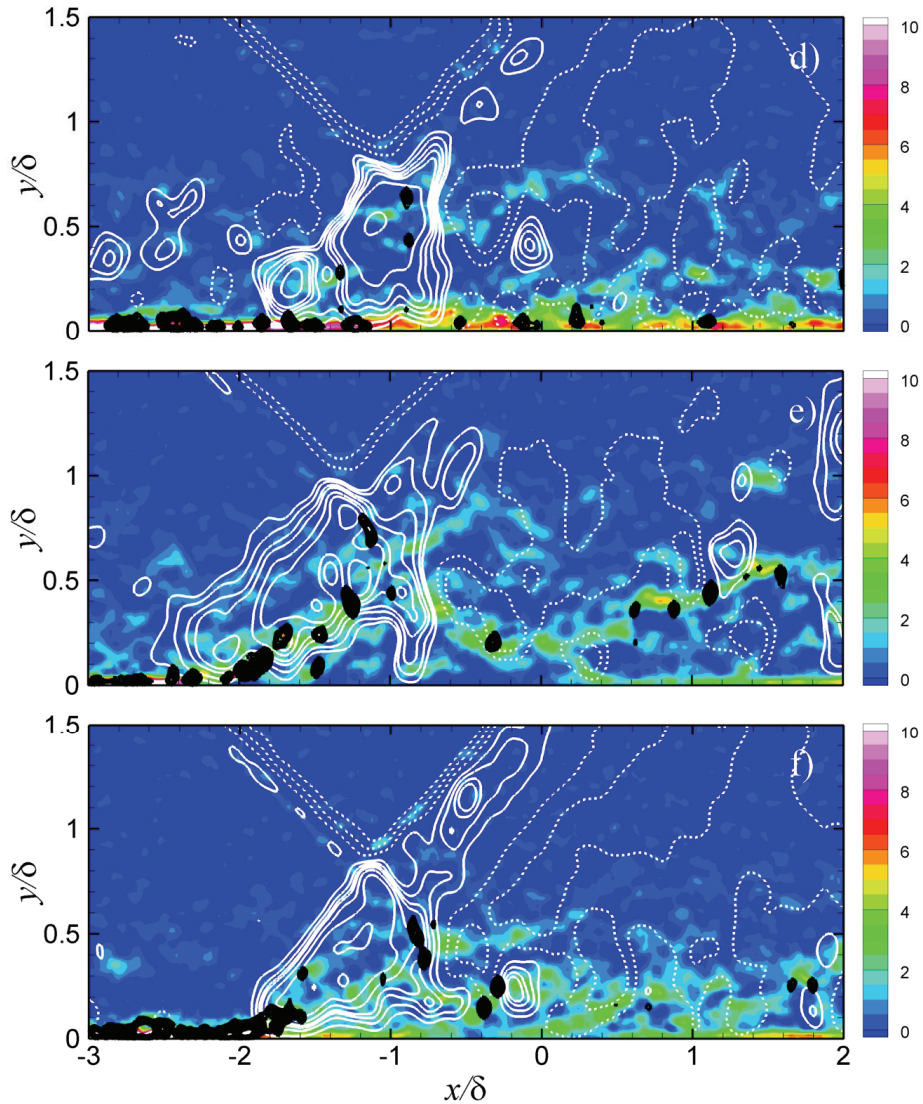


FIGURE 6.10: Instantaneous vorticity structure within the interaction. Discrete regions of  $Q > 0$  (determined using the  $Q$ -criterion) are shown in black along with flooded out-of-plane vorticity contours  $-\omega_z \delta / U_\infty$ . Wall-normal velocity contours are shown as white lines within 12 levels within the range  $-0.15 \leq v / U_\infty \leq 0.15$ . The dashed contours indicate negative values. Each figure part corresponds to the parts in figure 6.9.



As the interaction is approached, the flow-field structure can be seen to change dramatically. Figures 6.10(a–c) show that when flow separation occurs, the vorticity layer close to the wall and vortical structures are lifted up away from the wall into the shear layer within the detachment region. They appear to turn around the separation bubble, as revealed by a comparison of figures 6.9(b, c) and 6.10 (b, c) for instance. This is in agreement with the observations made by Na & Moin (1998) and Chong *et al.* (1998) in their DNS of incompressible separated flows, who observed that such structures would treat the separation bubble essentially like a streamlined obstacle, and would often impinge back onto the wall farther downstream.

The present vortical structures are lifted away from the wall and appear to propagate mainly through the incident shock wave's tip. This is consistent with the DNS of an incident SWTBLI by Pirozzoli & Grasso (2006), who found that the oscillatory motion of the incident shock wave occurs mainly at its tip. Farther downstream, the vortical structures indeed return to the proximity of the wall in the reattachment region. Notably, very few vortical structures can be observed within the separated flow region itself, and instead typically occur along the interface between our two layers.

It is interesting to observe that a similar lifting of the vorticity layer and vortical structures occurs even without a significant reversed-flow velocity region (c.f. figures 6.9(e) and 6.10(e)). It therefore appears that the vortical structures respond to a strongly retarded inner layer flow, in much the same way as they do to a recirculating bubble. Accordingly, when there is no significant inner layer velocity deficit, then there is no observed lifting of the vortical structures, as demonstrated in figure 6.10(d) for instance.

Farther downstream, regions of spanwise vorticity can be seen to spread more broadly over the spanwise height of the interaction with downstream development. Figures 6.10(a, b, e) show that they often appear as interconnected chains, in combination with isolated regions that are dispersed throughout the height of the boundary layer. Spatiotemporal studies of an incident SWTBLI by Dupont *et al.* (2006) have determined that energetic frequencies tend to decrease along the separated flow region, noting that in subsonic recirculating

flows, such frequency evolutions are associated with large-scale structures that are convected in a mixing layer that develops downstream of flow detachment. It therefore appears possible that vortical structures grow and develop within the separated shear layer, as part of a vortex shedding process associated with the separation bubble. This will become a focal point of the POD analysis later on.

The wall-normal velocity contours in the first part of the interaction indicate a zone of compression that is the reflected shock wave region. This zone changes significantly in time. It often appears as a diffuse feature, such as in figure 6.10(e), whereas in other instants it appears quite distinct, such as in figure 6.10(f). In addition, lines of wall-normal velocity often appear instantaneously warped. Figure 6.10(a) shows a concave compression region, whereas figure 6.10(b) shows a convex compression region. At other instants, the reflected shock wave region exhibits a combination of both these patterns, as shown in figure 6.10(c) for example. The behaviour of the reflected shock wave is therefore complex, and later on in chapter 8 we will use HWA to try and further characterize this behaviour in a temporal sense.

To investigate in more detail the role of the vortical structures in the separation process, figure 6.10(b) is repeated in figure 6.11(a), this time with velocity vectors in a convective frame of reference of  $0.8U_\infty$ . In this frame of reference, many of the velocity vectors can be seen to swirl around distinct regions of  $Q$  within the separated shear layer. It appears from these convective velocity vectors that a fluid exchange occurs between the inner and outer layers of the interaction. To better illustrate this, the instantaneous wall-normal velocity is extracted along the thick grey line  $S$ , which is judiciously chosen to be the locus of points through the vortical structures as they propagate throughout the interaction, and is shown in figure 6.11(b). The instantaneous separation  $x_s$  and reattachment  $x_r$  points (see §6.4.3 for further details), as well as the mean wall-normal velocity extracted along  $S$ , are also shown for comparison.

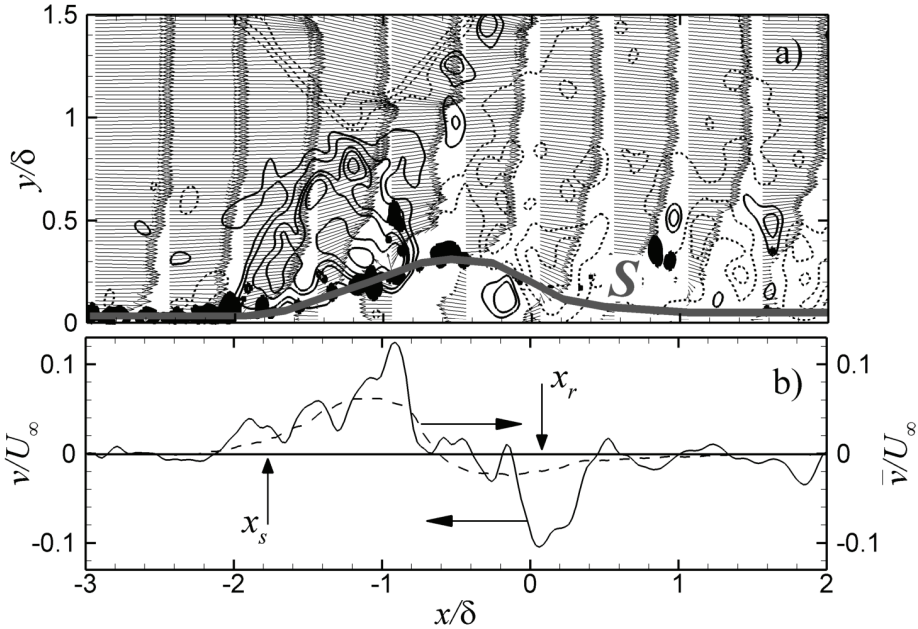


FIGURE 6.11: Instantaneous vortical structure distribution within the interaction. (a) Taken from figure 6.10(b) (see figure 6.10 caption) with velocity vectors shown in a convective frame of reference of  $0.8U_\infty$ , (b) Mean (dashed line) and instantaneous (solid line) wall-normal velocity profiles extracted along  $S$ . Arrows assign data with appropriate axis.

Both the mean and instantaneous wall-normal velocity remain approximately zero within the incoming boundary layer. Within the first part of the interaction, the instantaneous velocity profile begins to deviate from the mean profile, characterized by a sinuous alternation of positive and negative wall-normal fluctuations. Maximum instantaneous wall-normal velocities reach over 10% of  $U_\infty$ , which is comparable to the maximum (streamwise) reversed-flow velocity. A comparison of figure 6.11(a) with figure 6.9(a) suggests a physical mechanism, whereby high-velocity fluid is drawn in and ingested between the vortical structures as they ride over the inner flow, whereas low-velocity fluid from the separated flow is transported away from the wall. This description is not dissimilar to the scenario described by Simpson (1989) in low-speed incompressible separated flows, who discusses how movies of laser-illuminated smoke and turbulence energy results clearly reveal how

large-scale eddy structures supply most of the near-wall reversed-flow. The separation process of the present interaction therefore appears to share similarities with incompressible separated flows, and we will discuss later on how these structures may be reconciled with the large-scale unsteadiness.

### 6.4.3 Intermittency

It is clear that the structure of the interaction changes significantly in time. To characterize this behaviour statistically, figure 6.12 shows lines of constant value for the reversed-flow probability of the instantaneous streamwise velocity being less than zero  $p(u < 0)$ . These contours have been computed from histograms of the instantaneous streamwise velocity. For the sake of clarity, the inset shows a zoomed view of the interaction region, with the wall-normal coordinate greatly dilated.

The region of  $p(u < 0)$  appears as a relatively shallow region with respect to the boundary layer thickness, that is elongated in the streamwise direction and roughly symmetric about an axis in the wall-normal plane. This confirms the observation of an intermittent separated flow region with a streamwise extent that is within the range  $0-2\delta$ . Observe how  $p(u < 0)$  is never equal to unity anywhere in the flow, consistent with the observation that no reversed-flow flow occurs on average. On the other hand,  $p_{\max}(u < 0)$  within the interaction is about 0.5, indicating that flow reversal occurs in around half of the total number of realizations. Of course, this inference is a conservative estimate, since reversed-flow may occur in different regions. Note that because of the limited number of contour levels displayed, no reversed-flow is displayed within the incoming and redeveloping boundary layers.

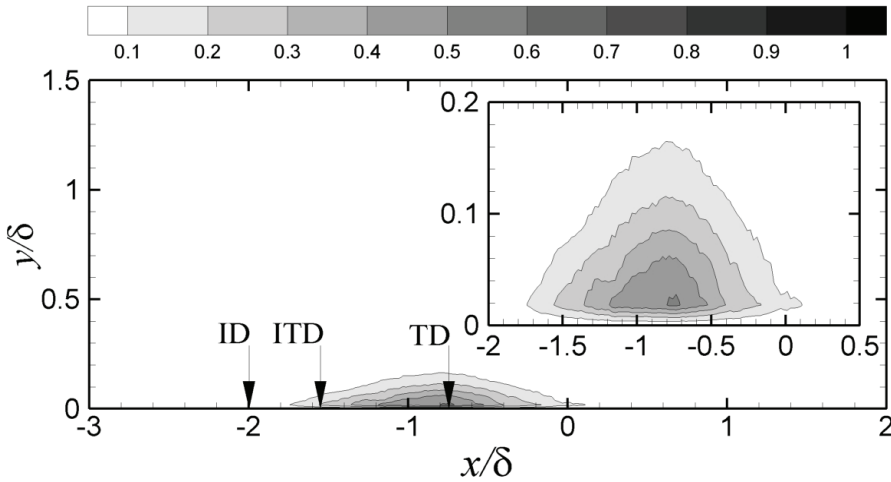


FIGURE 6.12: Regions of equiprobability of reversed-flow within the interaction  $p(u < 0)$ . The terms ID, ITD, and TD are defined in the text. Inset shows a zoomed view with the wall-normal coordinate dilated for clarity.

The existence of an intermittent backflow complicates the criterion used to define separation, and we need to distinguish between mean and instantaneous flow separation. For steady free-stream separating boundary layers, the following set of quantitative definitions on the separation state near the wall have therefore been proposed by Simpson (1989): *incipient detachment* (ID) occurs when the instantaneous backflow occurs 1% of the time; *intermittent transitory detachment* (ITD) occurs with instantaneous back flow 20% of the time; *transitory detachment* (TD) occurs with instantaneous backflow 50% of the time; and *detachment* (D) occurs where the time-averaged wall-shear stress  $\bar{\tau}_{wall} = 0$ . In the present study, the locations of ID, ITD, and TD occur at approximately  $(x/\delta)_{ID} = -2.0$ ,  $(x/\delta)_{ITD} = -1.6$ , and  $(x/\delta)_{TD} = -0.75$ , respectively, and are indicated in the figure, where ensemble-averages have been interpreted as time-averages. The location D does not exist in the present interaction, although its occurrence for a sufficiently stronger interaction is likely to be very close to TD (see Simpson 1989). Overall, it is clear that depending on the criterion used to define separation, there is quite some discrepancy in the spatial location of the separation point.

#### 6.4.4 Behaviour of Separation & Reattachment

As a result of the interaction's intermittency, the instantaneous separation and reattachment points wander back and forth along the wall in time. To characterize this behaviour, a statistical analysis of the instantaneous streamwise location of the separation  $x_s$  and reattachment points  $x_r$  was carried out. Following the approach of Kiya & Sasaki (1985), the reversed-flow region is defined as a contiguous region based on where the instantaneous streamwise velocity near the surface becomes negative, and we determine  $x_s$  and  $x_r$  as the zero-crossings of the instantaneous streamwise velocity. The velocity distribution at the height  $y/\delta=0.05$  ( $y=1.0$  mm) was selected for this purpose, and the data along this line were smoothed using a moving-average filter, with linear interpolation used to increase the number of data points (by a factor 2). It should be stressed that the overall trends of the results to be discussed were found to be rather insensitive to small changes in the height and filtering chosen, and the overall conclusions to be drawn remain unchanged.

Figure 6.13(a) shows  $x_s$  compared with  $x_r$ . The line  $x_s=x_r$  delimits the case when the separation and reattachment points coincide (i.e., when incipient separation occurs). The accumulation of many points along this line suggests that many small-scale separation regions occur, and inspection of the instantaneous realizations reveals that these regions are often present at several locations simultaneously along the wall. Given the present resolution, however, some of these small-scale separation regions should be considered as numerical artefacts.

Discrete joint PDFs are shown in figure 6.13(b), which indicate the relative probability of the separation and reattachment's  $i$ th streamwise position  $(x/\delta)_i$  falling within a range  $(x/\delta)_1 < (x/\delta)_i < (x/\delta)_1 + \Delta(x/\delta)$ , where  $\Delta(x/\delta)$  is the bin width of the PDF, taken as approximately 0.2 in the present study. These contours have been computed from histograms of the instantaneous streamwise velocity, and therefore  $p$  also includes the cases when the boundary layer remains fully attached. From these results, we may arbitrarily delineate the behaviour of the separated flow into the following regions, as indicated in the figure:

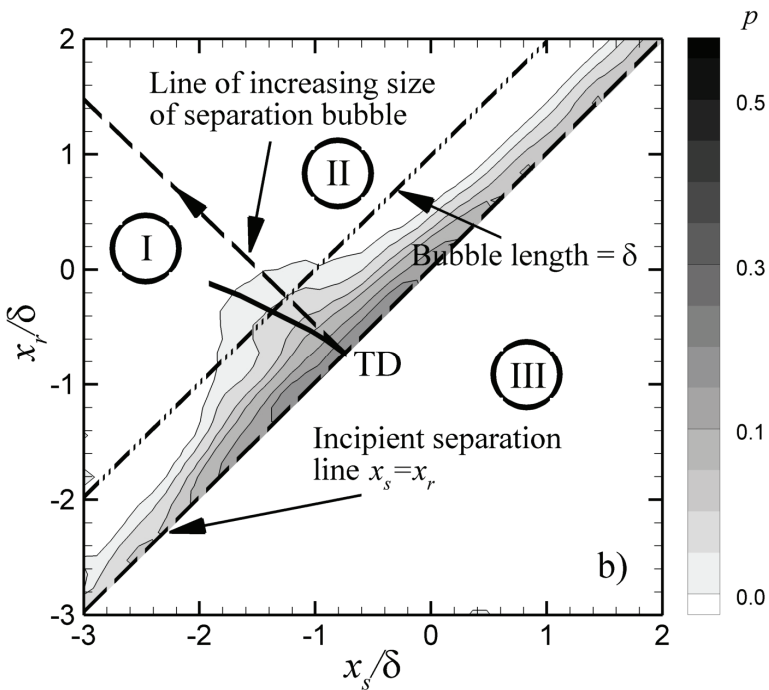
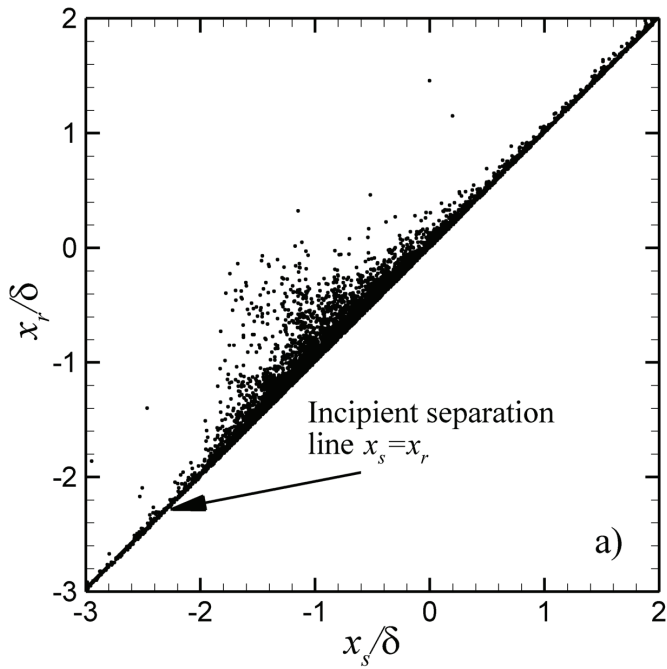
**Region I:** In this region  $x_s < x_r$ , and the separated flow region is relatively upstream of the interaction. That is, if the separation location is relatively upstream, then it is more likely to be accompanied by a relatively upstream reattachment location.

**Region II:** In this region  $x_s < x_r$ , and the separated flow region is relatively downstream of the interaction. That is, if the separation location is relatively downstream, then it is more likely to be accompanied by a relatively downstream reattachment location.

**Region III:** In this region  $x_s > x_r$ , which is a physically impossible case by convention, and so data points do not fall in this region.

The line perpendicular to the incipient separation line separates regions I and II, and marks the case of a separation bubble changing size symmetrically about a plane perpendicular to the wall. It emanates from TD at  $x/\delta = -0.75$ . Points along this line from TD represent separation zones of increasing streamwise extent. As expected,  $p$  rapidly decreases along this line, and no bubble size of larger than  $2\delta$  was found to occur in these data. Lines of equiprobability appear quasisymmetric about this line, indicating that for an increasing bubble size, it is more likely that  $x_s$  appears relatively upstream and  $x_r$  appears relatively downstream, and vice versa.

This is consistent with an expanding and contracting separation bubble, and is in line with the distribution of covariance coefficient of the separation and reattachment locations obtained by Pirozzoli & Grasso (2006), which indicate the occurrence of an expanding and contracting separation bubble. A trend line showing the locus of points of maximal probability is also shown in figure 6.13(b) for comparison, indicated by the solid line. This line can be seen to in fact deviate slightly into region I from the straight line emanating from TD, indicating the intriguing trend that for increasing bubble size, its centre appears slightly more upstream, in the time-averaged sense.



(see figure caption on next page.)



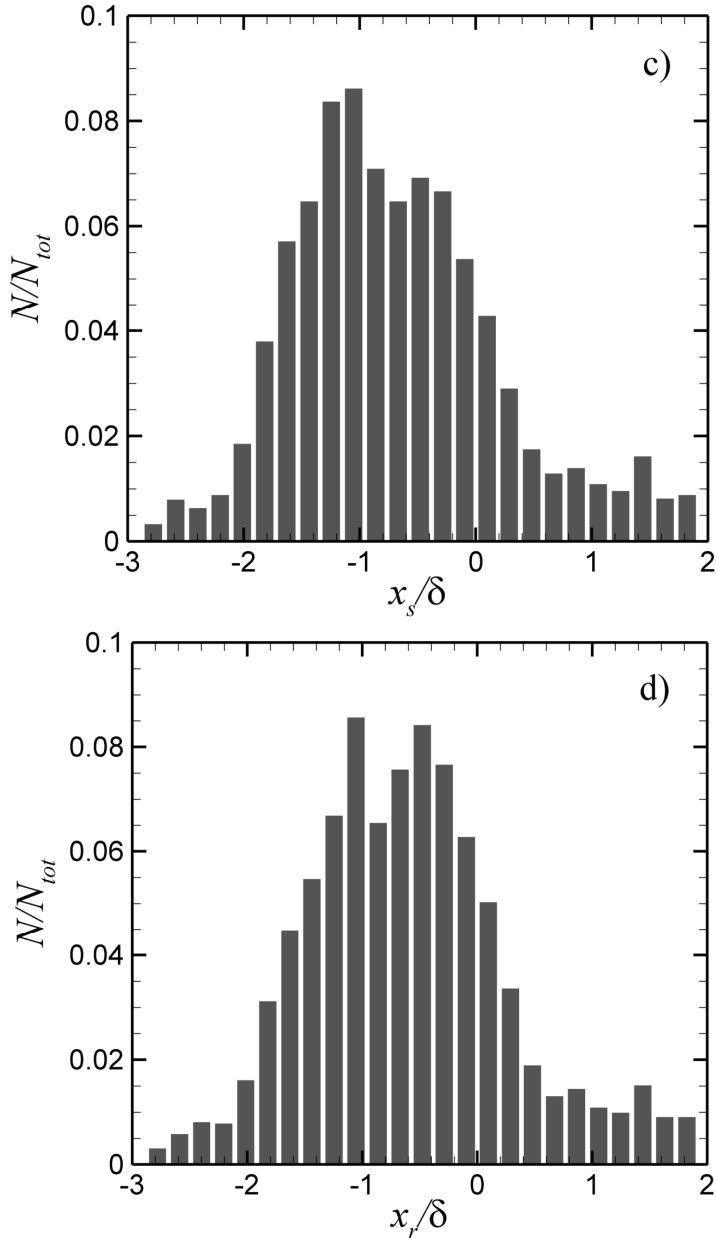


FIGURE 6.13: Statistical analysis of the instantaneous separation and reattachment points. (a) Separation point  $x_s/\delta$  compared with reattachment point  $x_r/\delta$ , (b) Joint PDFs of  $x_s/\delta$  and  $x_r/\delta$  showing the behaviour of the separated flow region. Solid line represents locus of maximal probability, (c) PDF of  $x_s/\delta$ , (d) PDF of  $x_r/\delta$ .

The discrete PDFs of  $x_s$  and  $x_r$  in figures 6.13(c, d), respectively, show that both locations occur along the complete streamwise extent of the measurement domain. The ID location at  $x/\delta = -2.0$  in particular, marks the onset of a significant fraction of separated flow cases, and roughly corresponds to the region where the boundary layer first encounters the upstream influence of the interaction. Observe how the PDF tails persist appreciably farther downstream of the interaction than upstream, indicating that reversed-flow regions occur more frequently within the redeveloping boundary layer than within the incoming boundary layer. The RMS values of  $x_s$  and  $x_r$  are approximately 0.3 and 0.29, respectively, indicating that the separation and reattachment points undergo somewhat similar degrees of spatial variation. This may be compared with the results of Pirozzoli & Grasso (2006), who found a more intermittent behaviour of the reattachment location, and Na & Moin (1998) who found a more intermittent behaviour of the separation location.

The size of the separated flow region is characterized by its streamwise extent  $\Delta = x_r - x_s$ , and is compared with the locations of  $x_s$  and  $x_r$  in figure 6.14. For illustration, linear regressions (arbitrarily chosen only for data points  $\Delta/\delta > 0.4$ ) are also shown. Note that these regressions do not meet precisely at TD, since their extrapolations are dependent on the threshold value of  $\Delta/\delta$  chosen. The results show the trend indicated in figure 6.13(b), that as the separation bubble increases, the separation and reattachment points move farther away from each other. The slope for the reattachment location appears slightly steeper than for the separation location, consistent with the deviating trend line of maximal probability shown in figure 6.13(b). The accumulation of  $x_s$  and  $x_r$  along the abscissa means that there exists momentarily small-scale flow reversal scattered both upstream and downstream of the interaction.

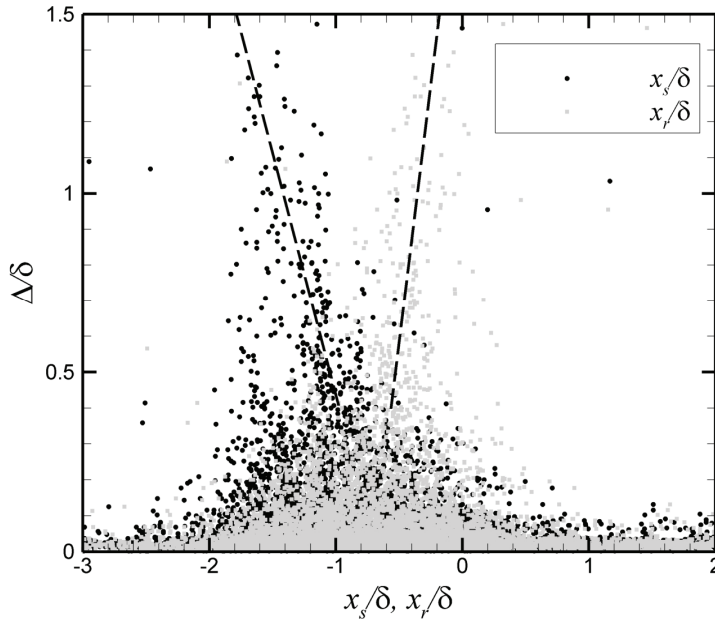


FIGURE 6.14: Streamwise extent of the separation bubble  $\Delta/\delta$ , compared with  $x_s/\delta$  and  $x_r/\delta$ . Linear regressions (for  $\Delta/\delta > 0.4$ ) are also shown for illustration.

### 6.4.5 Role of the Incoming Boundary Layer

Having outlined some physical and statistical properties of the interaction's unsteadiness, we now wish to shed some light on the possible mechanism(s) behind this behaviour. Of particular interest to the present study is the work by Beresh *et al.* (2002), who examined the role of the incoming boundary in a compression ramp interaction. Ensemble-average incoming boundary layer velocity profiles derived from PIV data were computed, conditioned on the instantaneous separation shock foot location derived from wall-pressure measurements. Ensemble-average velocity fluctuations conditioned on different types of shock motion revealed that positive fluctuations in streamwise velocity near to the wall corresponded to downstream shock motion, and vice versa. Since positive fluctuations within the boundary layer suggests that its profile is momentarily fuller than on average, and vice versa, then a suitable proposal would be that the shape parameter, which is a direct measure of the fullness of the

boundary layer's streamwise velocity profile, is first related to the size of the separated flow region.

To characterize the state of the incoming boundary layer in the present study, we use the *equilibrium shape parameter* defined as  $1-1/H_i$ , where  $H_i$  is the incompressible shape parameter. The use of  $1-1/H_i$  is particularly well-suited to SWTBLIs involving large-scale separated flows (see Délerly & Marvin 1986). The shape parameter  $H_i$  was determined by integrating the incoming streamwise velocity profiles at the upstream edge of the measurement domain  $x/\delta = -3.0$ . The trends to be discussed, however, were found to be rather insensitive to small variations in the streamwise location chosen, consistent with the long tails observed in streamwise velocity autocorrelation function (see e.g., Ganapathisubramani *et al.* 2006).

The size of the separated flow region is characterized by its streamwise extent  $\Delta = x_r - x_s$ . Since several reversed-flow regions often occur within a realization, only the largest value of  $\Delta$  in each realization (if reversed-flow occurs at all) is considered. Joint PDFs between  $1-1/H_i$  and  $\Delta$  are shown in figure 6.15(a), where  $1-1/H_i$  and  $\Delta$  have been normalized by their respective RMS values. The reader should exercise some caution when interpreting values of the shape parameter, due to the necessity of having to accurately resolve the velocity close to the wall. Based on a linear error propagation analysis of the shape factor (not reported in this thesis for brevity), taking into account the RMS measurement uncertainties of both the instantaneous streamwise velocity and PIV resolution, the estimated RMS measurement uncertainty on  $H_i$  is of the order of 5%. Indeed, figure 6.15(a) indicates that the median shape factor is  $1-1/H_i \approx 0.285$ , from which it can be deduced that  $H_i \approx 1.4$ , consistent with the value for a zero-pressure-gradient turbulent boundary layer (i.e.,  $H_i \approx 1.33$ , see Délerly & Marvin 1986). Note that  $\Delta$  is biased towards a median value that is slightly above zero, since the results are conditioned on only the largest reversed-flow region observed in each realization.

It can be seen that the contours of equiprobability appear elliptical, with the major-axis of the ellipse is slightly inclined with the vertical axis. Although this appearance depends somewhat on the scale chosen, the trend is clear: when  $1-1/H_i$  is greater than its median value (boundary layer less-full than on average), then the streamwise extent of the (largest) separated flow region is more likely to be larger

than its median size. Conversely, when  $1-1/H_i$  is less than its median value (boundary layer fuller than on average), then the streamwise extent of the (largest) separated flow region is more likely to be smaller than its median size. The correlation coefficient between these data is approximately  $-0.22$ , and so the relationship is considered weak although not negligible.

These results are qualitatively consistent with the model proposed by Beresh *et al.* (2002), in which a fuller incoming velocity profile entering the interaction provides an increased resistance to flow separation, which leads to a smaller separated flow region, and vice versa. It must be stressed, however, that given the limited correlation of the present data, this relationship may not be the most important mechanism present, and it furthermore represents a quasisteady view, in the sense that the incoming boundary layer profile and separated flow region are related, but no temporal delay is taken into account. In addition, integrating the velocity profile and comparing the shape parameter with shock wave position could give the appearance of a relatively weaker trend than conditionally-averaging the velocity profiles based on the shock wave location, since there will always be some scatter in the data, compounded by the difficulties of accurately resolving velocity fluctuations within the incoming boundary layer given the present resolution. The present results must therefore be viewed as a qualitative substantiation of the results of Beresh *et al.* (2001) rather than a new trend.

We also anticipate that  $1-1/H_i$  is related to the reflected shock wave position, since the latter has been shown to undergo a displacement due to the expansion and contraction of the separation bubble (see e.g., Dolling & Murphy 1983; Erengil & Dolling 1993). In the present study,  $1-1/H_i$  is compared with the instantaneous position of the reflected shock wave. The position was determined from the instantaneous wall-normal velocity distribution across the reflected shock wave in the free-stream and using the streamwise location where  $v/U_\infty=0$  as an indication for the shock wave's position. It should be stressed that the overall trends to be discussed were found to be rather insensitive to the velocity-based criterion chosen, including more exotic criterion, such as the flow-field (in-plane) divergence for instance.

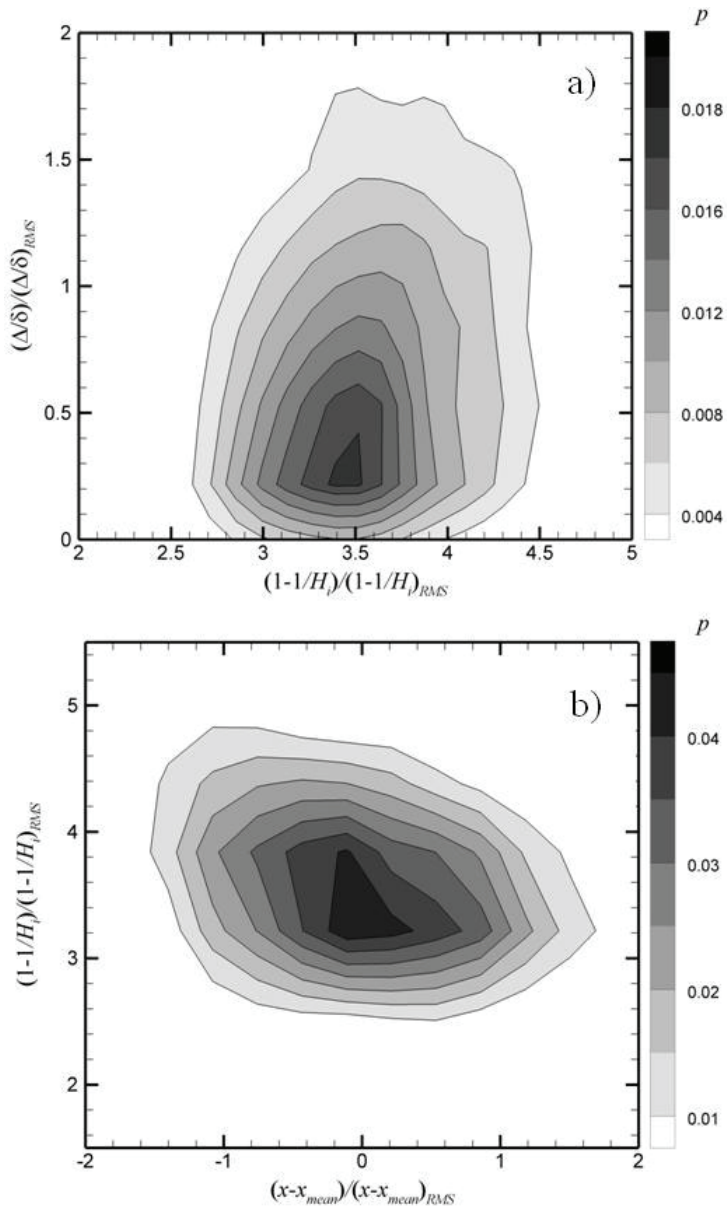


FIGURE 6.15: Relationship between incoming boundary layer and the interaction unsteadiness. (a) Joint PDF of equilibrium shape factor  $1-1/H_i$  and streamwise extent of separation bubble  $\Delta/\delta$ , (b) Joint PDF of  $1-1/H_i$  and streamwise location of reflected shock wave  $(x-x_{mean})/\delta$ . Shape factor computed at  $x/\delta = -3.0$  and only the largest value of  $\Delta$  in each realization is considered. Results are normalized by their respective RMS values.

Figure 6.15(b) shows joint PDFs of  $1-1/H_i$  and the position of the reflected shock wave relative to its mean position  $(x-x_{mean})/\delta$ . Note again, that these data have been normalized by their respective RMS values. The reflected shock wave undergoes a motion that has a streamwise extent of the order  $0.5\delta$  (shown as approximately four standard deviations in the figure), consistent with what is observed in the instantaneous realizations. The contours of equiprobability again appear elliptical, with the major-axis of the ellipse inclined with the abscissa. This suggests that when  $1-1/H_i$  is less than its median value (boundary layer fuller than on average), then the reflected shock wave is more likely to be located downstream of its mean position. Conversely, when  $1-1/H_i$  is greater than its median value (boundary layer less-full than on average), then the reflected shock wave is more likely to be located upstream of its mean position. The correlation coefficient of these data is approximately  $-0.3$ , indicating again that this relationship is weak although not negligible.

Dupont *et al.* (2008) have recently carried out PIV measurements of their shock reflection interaction, and also found a correlation between the instantaneous position of the shock wave and thickness of the recirculating zone. They proposed that when the recirculating zone dilates, the shock wave moves upstream, and when the bubble contracts, the shock wave moves downstream. It therefore appears that a statistical link exists in this type of interaction between the instantaneous size of the separation bubble and position of the reflected shock wave. Incidentally, the correlation coefficient in their study was  $-0.5$ , although it should be mentioned that only 200 realizations were used.

In the present study, the joint PDF shows a stronger correlation between the incoming boundary layer and reflected shock wave position, than the incoming boundary layer and separated flow extent. This seemingly contradictory result can be explained because only the largest value of  $\Delta$  was chosen within each realization, which exacerbates the correlation for small  $\Delta$ , since smaller values have been shown to have the largest spatial variation. We shall see later on how these results may be reconciled with the three-dimensional flow organization of the incoming boundary layer. (The curious reader may look ahead to the tomographic PIV statistical analysis given in §7.6 and/or the conceptual model presented in §9.)

On a final note, it may well be that the statistical link between the incoming boundary layer, separated flow region, and reflected shock wave is less strong here than in the other studies mentioned above, because the present interaction is only intermittently separated, and having only a small separation bubble on average (if any) may change the sensitivity of the shock wave to incoming disturbances (private communication, H. Babinsky 2008). Indeed, further differences between our intermittently separated interaction and interactions that have a large-scale separated flow region on average will also become apparent in the temporal analysis in §8.3 later on.

## 6.5 Turbulence Properties

### 6.5.1 RMS Velocity Distributions

Having discussed the instantaneous flow organization of the interaction, we now wish to investigate the statistical footprint of this unsteadiness on the turbulence properties. Figures 6.16(a, b) show the spatial distributions of the streamwise  $\langle u' \rangle$  and wall-normal  $\langle v' \rangle$  RMS velocity components, respectively. Note that  $\langle v' \rangle$  has been scaled about 2.5 times more sensitive than  $\langle u' \rangle$ . It can be seen that substantial increase in  $\langle u' \rangle$  occurs throughout the interaction, initiating itself within the reflected shock wave region within the boundary layer, and reaching a maximum value of approximately  $0.2U_\infty$  beneath the incident shock wave. Maximum levels of  $\langle u' \rangle$  are over 4 times greater than maximum levels of  $\langle v' \rangle$ , indicating that significant turbulence anisotropy is present.

These results are in general comparable to the laser velocimetry measurements of Rose and Johnson (1975), Moderass & Johnson (1976), and Meyer *et al.* (1997), as well as the LES computations of Garnier & Sagaut (2002), who have all considered an incident shock wave interacting with a flat plate turbulent boundary layer. In the present study, since the upstream flow is often lifted and turned around the bubble, whereas in other instances it remains fully attached, it is now clear that the locus of large  $\langle u' \rangle$  within the first part of the interaction is a result of the averaging of this intermittently separated flow. Note that an increased level of  $\langle u' \rangle$  can also be observed at the tip of the incident shock wave, indicating that the incident shock wave's tip undergoes an increased motion. This is in



agreement with the idea that vortical structures often propagate in this region, as shown earlier.

Farther downstream,  $\langle u' \rangle$  can be seen to rapidly decay. At the downstream edge of the measurement domain, the near-wall peak of  $\langle u' \rangle$  is now just beginning to reappear, indicating that the near wall boundary layer is starting to recover. As observed in the mean velocity fields, there is an increase in the level of velocity fluctuations along the incident and reflected shock waves in the free-stream (approximately 4% and 7%  $U_\infty$  respectively). The relative increase in velocity fluctuations across the reflected shock wave is attributed to its unsteady motion.

In the case of  $\langle v' \rangle$ , significant fluctuations appear across the entire extent of the reflected shock wave. This is consistent with the study of Dupont *et al.* (2006), who used both wall-pressure measurements at the reflected shock wave's median location, as well as HWA in the free-stream in the vicinity of the reflected shock wave, and characterized the reflected shock wave as a moving sheet, based on the coherence function of the two signals. Similarly, Souverein *et al.* (2008) have conducted dual-plane PIV of the present interaction at Mach 1.69, and characterized the reflected shock wave within the boundary layer as moving in harmony with the reflected shock wave in the outer free-stream flow.

Moving downstream, the redeveloping boundary layer portrays elevated levels of  $\langle v' \rangle$ , which are broadly distributed across the lower half of the boundary layer. While  $\langle u' \rangle$  rapidly decreases in this region, it can be seen that the elevated levels of  $\langle v' \rangle$  persist downstream, and spread more broadly over the vertical height of the interaction than the large values of  $\langle u' \rangle$ . This is thought to be the statistical footprint of the vortex shedding process, which occurs downstream of the interaction, as observed in the instantaneous realizations. This footprint extends over a streamwise distance of at least  $3\delta$  downstream, and shows no sign of recovery within the present measurement domain, unlike the  $\langle u' \rangle$  component.

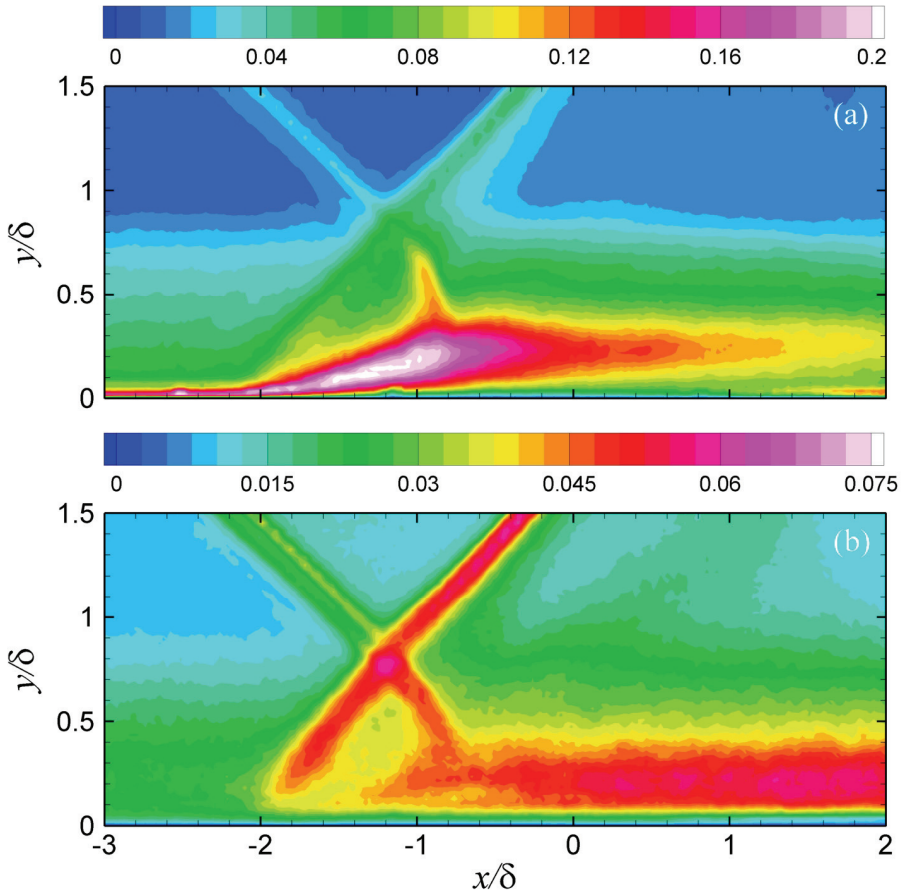


FIGURE 6.16: Distribution of RMS velocity fluctuations within the interaction. (a) Streamwise component  $\langle u' \rangle / U_\infty$ , (b) Wall-normal component  $\langle v' \rangle / U_\infty$ . Modified from Humble *et al.* (2007b).

The contrasting behaviour between the streamwise evolutions of  $\langle u' \rangle$  and  $\langle v' \rangle$  is illustrated in figure 6.17 by plotting the local maximum values  $\langle u' \rangle_{max}$  and  $\langle v' \rangle_{max}$  extracted at various streamwise locations.

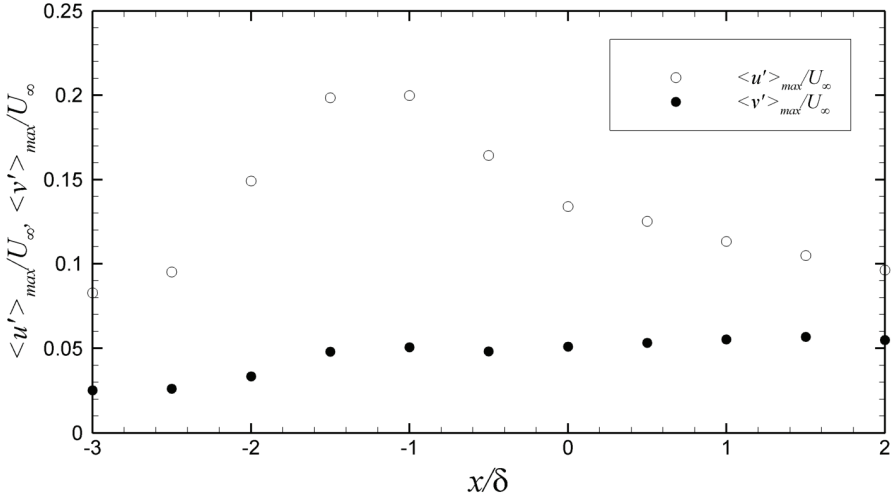


FIGURE 6.17: Evolution of  $\langle u' \rangle_{max}$  and  $\langle v' \rangle_{max}$  throughout the interaction.

The difference in these turbulence evolutions may be explained in more detail when one considers the production terms associated with each component. Following along the lines of the turbulence studies conducted in transonic SWTBLIs by Détery and Marvin (1986), consider first the production term of the streamwise component transport equation, written for an incompressible two-dimensional flow for simplicity as

$$P_u = -2\overline{u'v'} \frac{\partial \bar{u}}{\partial y} - 2\overline{u'^2} \frac{\partial \bar{u}}{\partial x} \quad (6.3)$$

It should be noted that there is an appreciable variation of mean density across the undisturbed boundary layer in the present study ( $\bar{\rho}_w / \bar{\rho}_e \approx 0.6$  at  $M_e = 2.1$ ) and so only a general discussion will be given. Qualitatively speaking, consider that in the first part of the interaction, the strain rate  $\partial \bar{u} / \partial y$  within the boundary layer is typically large (see Détery & Bur 2000). Furthermore, it is generally accepted that  $\overline{u'v'} < 0$  when  $\partial \bar{u} / \partial y > 0$ . (The reader may confirm this by looking ahead to figure 6.18.) With  $\partial \bar{u} / \partial x$  a necessarily negative value since the flow is decelerating, then the production term of the streamwise turbulence intensity is essentially the sum of two positive

terms. This explains the rapid increase in  $\langle u' \rangle$  the first part of the interaction. Consider now the production term for the wall-normal component given by

$$P_v = -2\overline{u'v'} \frac{\partial \bar{v}}{\partial x} - 2\overline{v'^2} \frac{\partial \bar{v}}{\partial y} \approx -2\overline{u'v'} \frac{\partial \bar{v}}{\partial x} + 2\overline{v'^2} \frac{\partial \bar{u}}{\partial x} \quad (6.4)$$

The reader will notice that the production term for the wall-normal component contains terms that are different than those occurring for the streamwise component. Following Détery and Marvin (1986),  $\partial \bar{v} / \partial y$  has been replaced with  $-\partial \bar{u} / \partial x$  since the incompressible continuity equation is essentially satisfied for weakly compressible flows at moderate Mach number. While the competing roles of each component are complicated in the first part of the interaction, the overall effect is a relatively slow increase in  $\langle v' \rangle$  with respect to  $\langle u' \rangle$ . Farther downstream, the flow begins to accelerate, and  $\partial \bar{u} / \partial x$  becomes positive. This leads to the continued slow increase in  $\langle v' \rangle$  with streamwise development.

### 6.5.2 Reynolds-Averaged Shear Stress Distribution

Consider now the Reynolds-averaged shear stress distribution. The measurement of this property has specific value to aid the modelling of turbulent effects by computational methods, and it is of particular importance in the validation of turbulence closure models, since theoretical efforts are generally hampered by the difficulties of representing the turbulence terms in the time-averaged equations. For compressible flows, the total (in-plane) Reynolds-averaged shear stress is more complicated than its incompressible counterpart, and is given by

$$\tau_{xy} = \mu(\partial \bar{u} / \partial y) - \overline{\rho u'v'} - \bar{v} \overline{\rho' u'} - \overline{\rho' u'v'} \quad (6.5)$$

The Reynolds-averaged shear stress is conventionally expressed by  $\overline{\rho u'v'}$ , when the density fluctuations are ignored. In the present study, the term  $\overline{u'v'}$  will be regarded as being representative of  $\overline{\rho u'v'}$ , and will hereafter be referred to simply as the Reynolds-averaged shear stress. In view of the difficulties in accurately measuring the Reynolds-

averaged shear stress with PIV, as demonstrated earlier in §5.2.3 within the undisturbed boundary layer, the Reynolds-averaged shear stress distribution presented here should be interpreted quantitatively with somewhat caution. The spatial distribution of  $\overline{u'v'}/U_\infty^2$  is shown in figure 6.18.

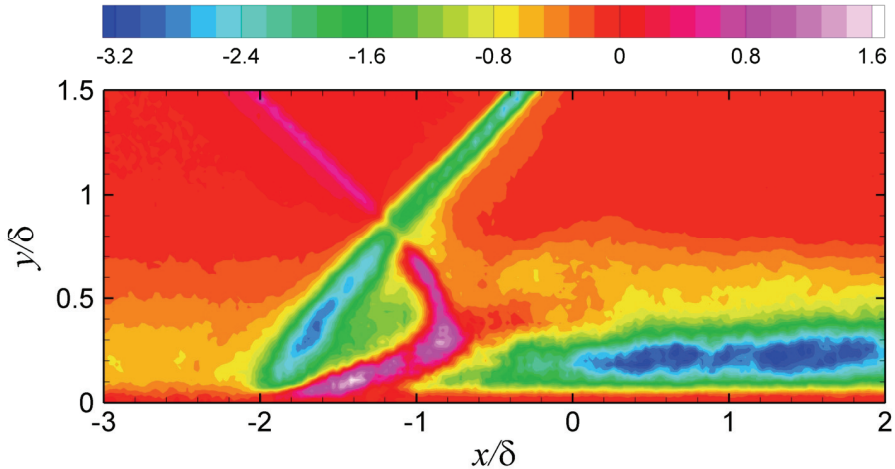


FIGURE 6.18: Reynolds-averaged shear stress distribution  $\overline{u'v'}/U_\infty^2 \times 10^3$ . Modified from Humble *et al.* (2007b).

It can be seen that initially moderate levels of  $-\overline{u'v'}$  are present within the undisturbed boundary layer. A substantial increase in Reynolds-averaged shear stress magnitude occurs within the incident and reflected shock wave regions within the boundary layer. This increase is expected, since it is known that supersonic flow that undergoes a compression is associated with turbulence augmentation (Spina *et al.* 1991). There appears to be a systematic change of Reynolds-averaged shear stress farther downstream. The redeveloping boundary layer can be characterized by the presence of a distinct streamwise-oriented region of large Reynolds-averaged shear stress magnitude in its lower part. Note the overwhelmingly negative values in this region, indicative of slower moving ( $u' < 0$ ), upward-oriented ( $v' > 0$ ) fluid, and/or faster moving ( $u' > 0$ ), downward-oriented ( $v' < 0$ ) fluid, relative to the mean flow.

As noted by Ardonceau (1983), among many others who have studied the structure of turbulence in SWTBLIs, these Reynolds-averaged shear stresses imply the existence of large-scale eddies, consistent with the instantaneous results shown earlier, and also indicated by the recovery of the boundary layer velocity profile with downstream development. The recovery of the turbulence properties, however, appears to be a gradual process, with the streamwise extent of the present measurement domain insufficient to observe the boundary layer returning to its initial conditions.

### 6.5.3 Equilibrium Phase Portraits

The entire history of interaction may be schematically characterized by plotting the streamwise evolution in ‘phase-space’ of some of the quantities discussed above. Following Délerly & Marvin (1986), we first define an *equilibrium boundary layer* as one that undergoes a transformation in which there is an instantaneous adjustment between the distributions of the mean velocity and shear stress. It is therefore a necessary condition that there is a unique relationship between the mean velocity and shear stress. Generally, only progressive and slow streamwise evolutions permit this equilibrium behaviour to actually occur. As reported by Délerly & Marvin (1986), East & Sawyer (1979) have introduced a function  $G$  defined by

$$G = (1 - 1/H_i) / \sqrt{0.5C_\tau} = 6.55 \quad (6.6)$$

where  $C_\tau$  is the shear stress coefficient given by

$$C_\tau = \frac{-\left(\overline{\rho u'v'}\right)_{\max}}{\frac{1}{2}\rho_e U_e^2} \quad (6.7)$$

According to East & Sawyer (1979), as reported by Délerly & Marvin (1986), the function  $G$  apparently remains constant for all equilibrium boundary layer flows, with the value of the constant corresponding to a zero-pressure-gradient boundary layer. On the other hand, the value of 6.55 may not be valid in general (private communication, H. Babinsky 2008), but we will use this value in the

present study, in order to make qualitative comparisons with the work reported by Délerly & Marvin (1986). Under these conditions then, the trend of an equilibrium boundary layer is a linear relationship between  $1-1/H_i$  and the (maximum) Reynolds-averaged shear stress. The equilibrium shape parameter  $1-1/H_i$  is plotted against the maximum Reynolds-averaged shear stress in figure 6.19, where we have used  $U_\infty$  instead of  $U_e$  and have omitted the density ratio for simplicity. The equilibrium line, as defined by equation (6.6), is also shown for comparison, although it should only be used as an indication of the present boundary layer equilibrium.

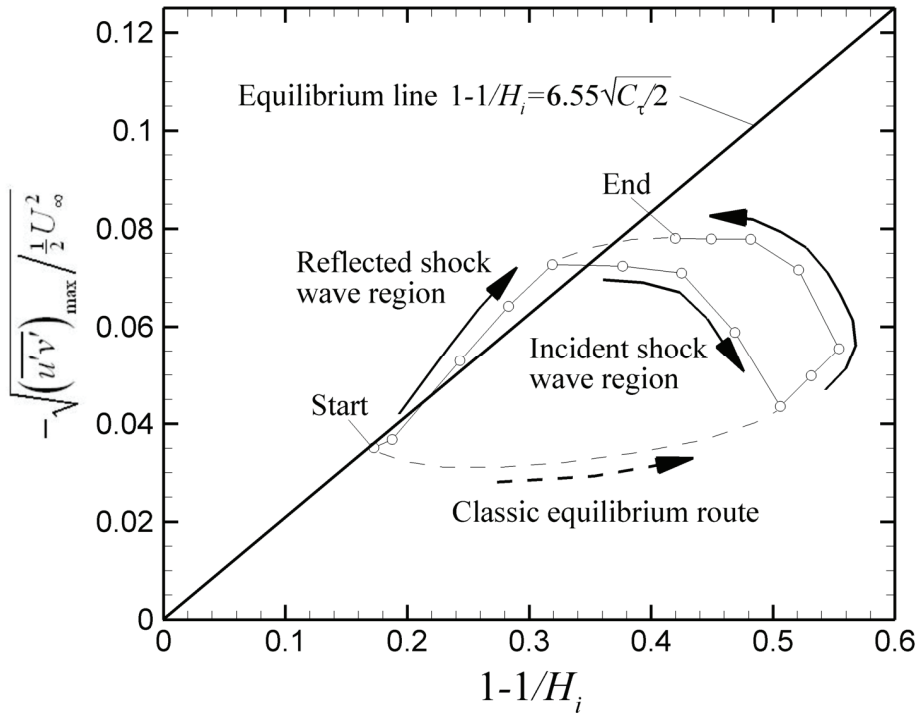


FIGURE 6.19: Evolution of  $1-1/H_i$  and maximum Reynolds-averaged shear stress throughout the interaction. The start and end points correspond to the upstream and downstream edges of the measurement domain, respectively. The classic equilibrium route refers to the external interaction of Délerly & Marvin (1986).

The results reveal that the incoming boundary layer is initially close to its equilibrium conditions.<sup>††</sup> As the boundary layer enters the interaction, there is a departure from its initial start conditions, where the start and end points correspond to the upstream and downstream edges of the measurement domain, respectively. In the classic interpretation of boundary layer nonequilibrium evolution in SWTBLIs (see Délerly & Marvin 1986), there is a rapid increase in  $1-1/H_i$ , followed by a lag of the maximum Reynolds-averaged shear stress, as the turbulence adjusts to the perturbation. This nonequilibrium route therefore follows a trajectory that is below the equilibrium line, highlighted in the figure by the dashed line.

In the present interaction, however, it can be seen that the opposite trend occurs: there is an increase in the maximum Reynolds-averaged shear stress magnitude followed by a lag in  $1-1/H_i$ . The present data points therefore follow a trajectory that is slightly above the equilibrium line, although the neglect of the density ratio may come into play here. This general difference in behaviour may be due to the different flow configurations considered. In the external interaction of Délerly & Marvin (1986), there is a single maximum in the Reynolds-averaged shear stress magnitude distribution followed by a decay farther downstream. In the present interaction, however, there are maxima due to the presence of the incident and reflected shock waves, with the amplification of the Reynolds-averaged shear stress magnitude within the reflected shock wave region within the boundary layer being responsible for the opposite trend observed in the first part of the interaction.

Farther downstream, the incident shock wave region is approached, and there is a decay of the maximum Reynolds-averaged shear stress magnitude. The boundary layer, however, continues to be retarded in this region, and this leads to the data points moving back towards the classic nonequilibrium route. Thereafter, values of  $1-1/H_i$  begin to culminate, accompanied by boundary layer recovery. The data points therefore bend around towards the equilibrium line. Both  $1-1/H_i$  and the maximum Reynolds-averaged shear stress magnitude begin to decrease as the trajectory heads back towards its

---

<sup>††</sup> We know in fact the density ratio for the start point since it is the undisturbed boundary layer. Incorporating the actual density ratio leads to the value of  $C_r$  shown decreasing by about 15%.



start position. It is evident, however, that the trajectory does not reach this start condition, demonstrating that the boundary layer does not fully recover within the present measurement domain. The expected trajectory with further streamwise development is illustrated by the dashed line from the end point, where it is anticipated that the boundary layer recovers back towards its initial equilibrium conditions, although it seems unlikely that it would follow the reverse trajectory within the reflected shock wave region.

The equilibrium shape parameter  $1-1/H_i$  is shown against the maximum streamwise RMS velocity fluctuations  $\langle u' \rangle_{max}/U_\infty$  in figure 6.20. As the boundary layer enters the interaction, both  $\langle u' \rangle_{max}/U_\infty$  and  $1-1/H_i$  increase together within the reflected shock wave region. In the mid-part of this phase,  $\langle u' \rangle_{max}/U_\infty$  increases more slowly than  $1-1/H_i$ , and the trajectory levels out. At some position farther downstream (at about  $x/\delta=-0.5$ ), the shape parameter culminates, and starts to decrease again. This indicates that the boundary layer profile is adjusting to its initial retardation through the reflected shock wave and is beginning to fill-out. This is accompanied by a rapid decrease in  $\langle u' \rangle_{max}/U_\infty$ , and the trajectory then heads back towards its start position. It is again evident that the trajectory does not reach this start condition. The expected trajectory with further streamwise development is illustrated by the dashed line.

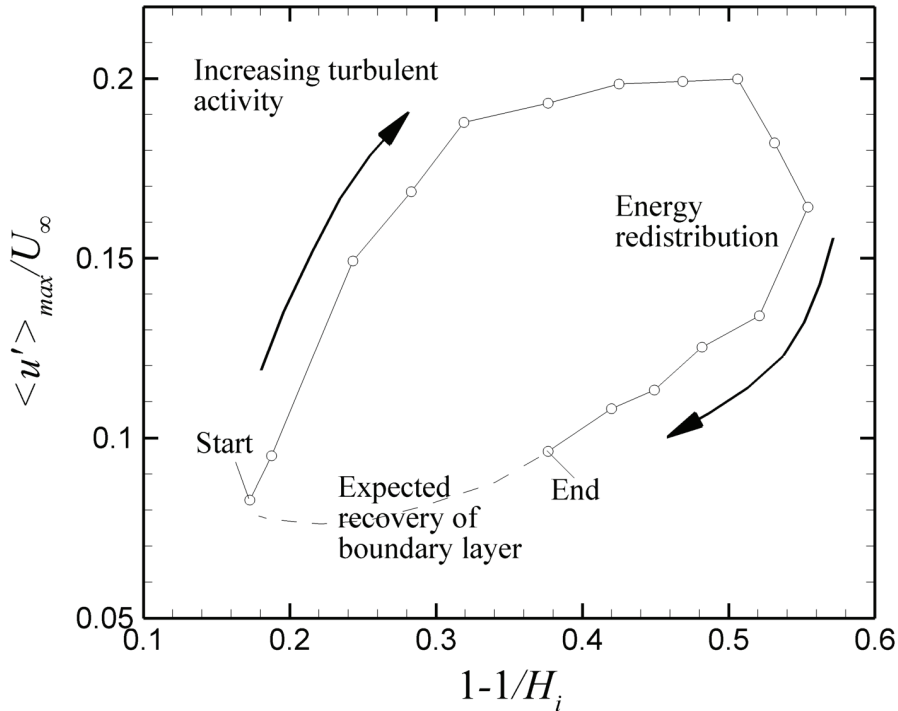


FIGURE 6.20: Evolution of  $\langle u' \rangle_{max}/U_\infty$  and  $1-1/H_i$  throughout the interaction. The start and end points correspond to the upstream and downstream edges of the measurement domain, respectively.

Plotting the evolution of  $\langle u' \rangle_{max}/U_\infty$  with the maximum Reynolds-averaged shear stress in figure 6.21 reveals a very different phase-space relationship to the ones above. The magnitude of both quantities can be seen to rapidly increase in the first part of the interaction, associated with the turbulence amplification within the reflected shock wave region. Farther downstream, however, as the incident shock wave region is approached, there is a rapid decrease in the Reynolds-averaged shear stress magnitude while  $\langle u' \rangle_{max}/U_\infty$  remains relatively high.

An interesting behaviour can be observed when the boundary layer starts to recover:  $\langle u' \rangle_{max}/U_\infty$  decays rapidly, but the Reynolds-averaged shear stress magnitude begins to increase again. This is associated with slower moving ( $u' < 0$ ), upward-oriented ( $v' > 0$ ) fluid, and/or faster moving ( $u' > 0$ ), downward-oriented ( $v' < 0$ ) fluid, relative

to the mean flow. Again, the boundary layer undergoes a recovery process back towards its initial conditions, but does not reach its start position. Notably, when the boundary layer reaches the end of the measurement domain,  $\langle u' \rangle_{max}/U_\infty$  has almost returned to its incoming value, whereas the Reynolds-averaged shear stress magnitude remains more than twice as high as its initial value.

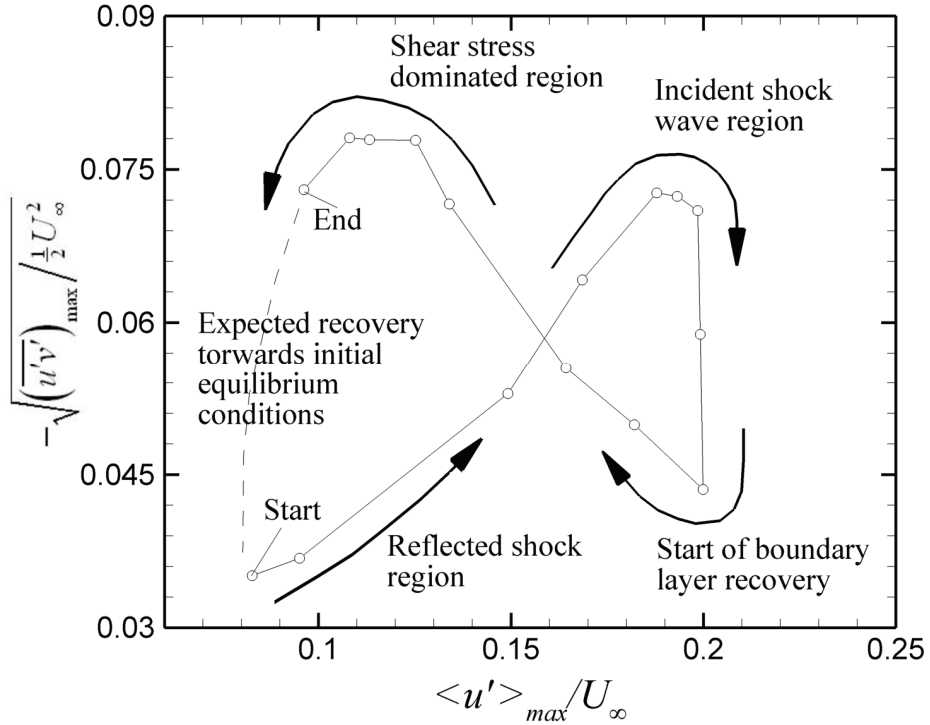


FIGURE 6.21: Evolution of  $\langle u' \rangle_{max}/U_\infty$  and maximum Reynolds-averaged shear stress throughout interaction. The start and end points correspond to the upstream and downstream edges of the measurement domain, respectively.

#### 6.5.4 Structural Parameters

Two parameters that can be used to further characterize the turbulence structure of the interaction, independent of the magnitude of the velocity fluctuations, are the correlation coefficient  $R_{uv}$  defined by

$$R_{uv} = \frac{\overline{u'v'}}{\langle u' \rangle^2 \langle v' \rangle^2} \quad (6.8)$$

and the anisotropy parameter  $A$  defined by

$$A = \frac{\langle v' \rangle^2}{\langle u' \rangle^2} \quad (6.9)$$

The variation of the correlation coefficient is shown in figure 6.22 at several streamwise locations. Upstream of the interaction,  $-R_{uv}$  remains at an approximate value of 0.45 throughout an appreciable portion of the boundary layer height ( $0.1 < y/\delta < 0.7$ ), and vanishes as the outer region is approached. Similar observations have also been made using LDV on a Mach 2.3 boundary layer by Eléna & Lacharme (1988), where it was found that  $-R_{uv}$  remained at an approximately constant value of 0.45 within the region  $0.1 < y/\delta < 0.8$ , as well as the DNS of Pirozzoli & Grasso (2006) in their Mach 2.25 boundary layer, which show a constant value of 0.45 within the region  $0.2 < y/\delta < 0.6$ . This is in fact, what is also observed in most subsonic flows (see for instance Klebanoff 1955). (The sharp reader may also compare the scatter in the present data with our 5% RMS measurement uncertainty for  $R_{uv}$  estimated earlier.)

Other studies of a Mach 2.9 boundary layer by Fernando & Smits (1990), however, have indicated that  $-R_{uv}$  decreases significantly with distance from the wall, and have suggested a compressibility effect as a possible cause. It should be noted, however, that such a decrease has also been speculated to be a Reynolds number effect (see Smits & Dussauge 2006 for a further discussion). It is therefore difficult to state precisely the effect of compressibility on the correlation coefficient, although these results collectively suggest that the behaviour of the correlation coefficient within moderately compressible supersonic turbulent boundary layers closely resembles incompressible flow behaviour.

Farther downstream, a rapid change in the turbulence structure occurs, with the correlation profiles becoming strongly distorted, particularly in the outer region of the boundary layer due to the presence of the incident and reflected shock waves. Observe also that

by  $x/\delta=1$ , the distribution of  $-R_{uv}$  has already begun recovering towards its undisturbed distribution, and by  $x/\delta=2$  it appears very similar to the distribution found upstream of the interaction.

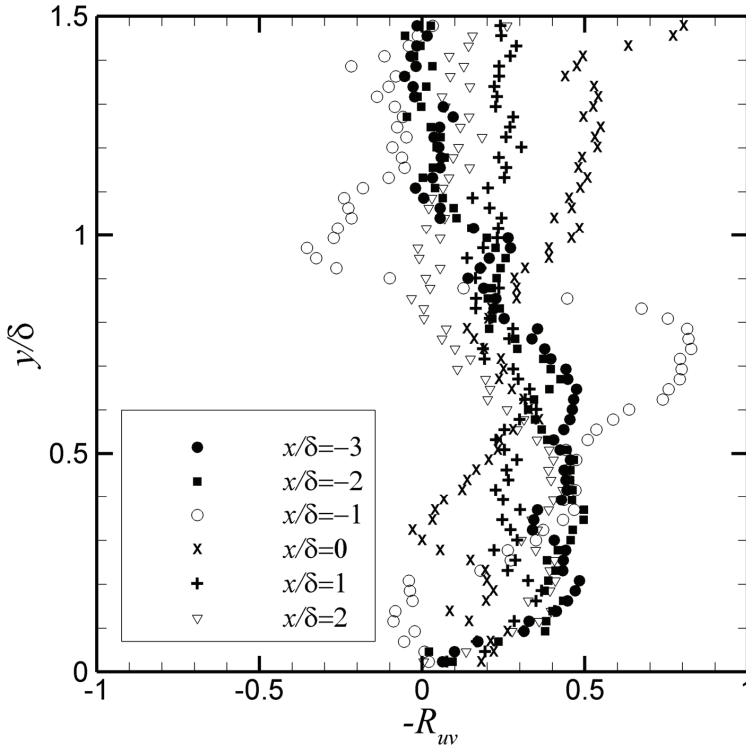


FIGURE 6.22: Variation of the correlation coefficient  $-R_{uv}$  throughout the interaction at various streamwise locations.

The variation of the anisotropy parameter is shown in figure 6.23. Consistent with the distribution of  $-R_{uv}$ , the anisotropy parameter indicates a constant turbulence structure upstream of the interaction, maintaining a reasonably constant value of 0.25 throughout most of the boundary layer. Outside of the boundary layer, however, changes in the anisotropy parameter become more noticeable with streamwise development, and values can be seen to systematically reach above unity for locations  $x/\delta > 1$ . This means that during and downstream of the interaction, contrary to the situation upstream, the wall-normal fluctuations now become greater than the streamwise fluctuations.

Similar observations have been also made in turbulence studies of a low-speed incompressible boundary layer by van Oudheusden (1999), where this behaviour was attributed to wall-normal velocity fluctuations occurring in the intermittent outer part of the boundary layer, which do not significantly affect the streamwise velocity fluctuations since the mean flow velocity defect is considered small. The presence of the shock waves clearly complicates this behaviour. It is interesting to observe, that the way in which the anisotropy parameter varies within the boundary layer and outer regions is distinctly different with streamwise development.

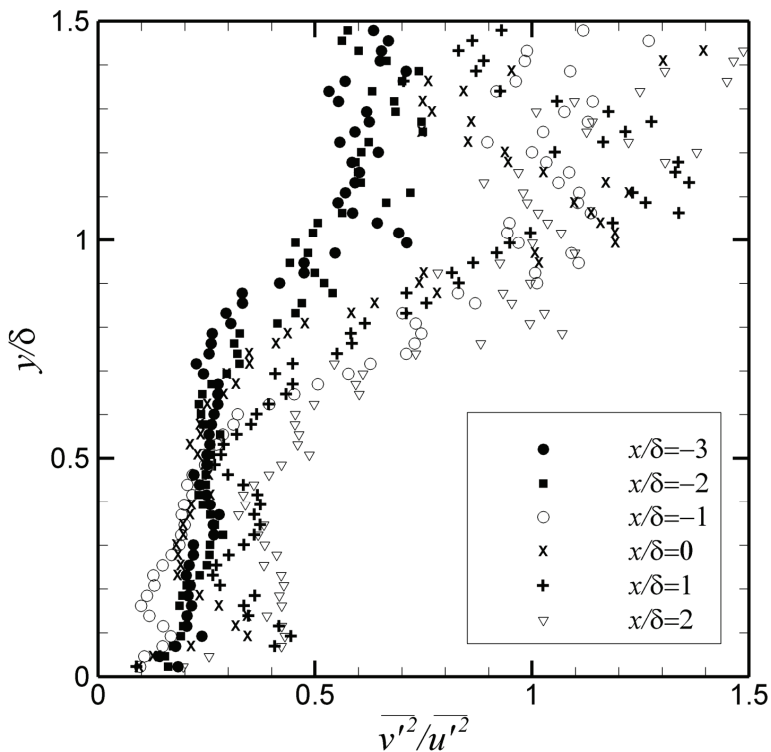


FIGURE 6.23: Variation of the anisotropy parameter  $\overline{v'^2}/\overline{u'^2}$  throughout the interaction at various streamwise locations.

## 6.6 POD Analysis

To complete our discussion on the two-dimensional flow organization of the interaction, we now decompose the fluctuating

part of the flow-field using the POD. Since the POD is based on ensemble-averaged correlations, the eigenmodes represent only statistical information about the flow features they represent. A conceptually appealing interpretation is to view the following eigenmodes as perturbations to the mean flow-field.

For the purposes of visualizing the two-dimensional eigenmodes, we first create a one-dimensional state-space  $\phi$  using the temporal coefficients from the analysis. Recall that one can arbitrarily choose a finite number  $K$  of the most energetic modes to form a subspace spanned by the first  $K$  eigenmodes. Similarly, subspaces can be formulated based on a single eigenmode, by first ordering the temporal coefficients of all  $M$  observations, such that  $\phi_n^k = \{a_k(t_n) \leq a_k(t_{n+1}) \leq \dots \leq a_k(t_M)\}$ . An eigenmode then yields  $M$  subspaces, the  $n$ th subspace of the  $k$ th eigenmode  $u_n^k(x, y)$  given by

$$u_n^k(x, y) = a_k(t_n) \psi_k(x, y), \quad n = 1, \dots, M \quad (6.10)$$

These subspaces provide a method to analyze the behaviour of the  $k$ th eigenmode. For notational convenience, we first arbitrarily define  $\phi$  as

$$\phi_n^k = \begin{cases} 0 & \text{when } a_k = (a_k)_{\min}; \quad n = 1 \\ \pi & \text{when } a_k = (a_k)_{\max}; \quad n = M \end{cases} \quad (6.11)$$

Using this procedure and considering the complete range of  $\phi_n^k$ , perspective renderings of the first four eigenmodes are presented in figures 6.24–6.27, sorted by decreasing fractional total energy. Streamwise and wall-normal velocity components of the modes are shown in figure parts (a) and (b), respectively, with their modal number and relative energy content shown inset. These figures may be conceptualized by considering the eigenmode in the  $x$ – $y$  plane and viewing it in the state-space  $\phi$  along the spanwise coordinate, created by weighting the eigenmode with the set of (ordered) temporal coefficients. Since the temporal coefficients associated with each eigenmode for a particular realization can be either positive or

negative, only the relative changes of sign within an eigenmode are important.

Recall that the first eigenmode is by far the most energetic. Figure 6.24(a) shows that this first mode contains large streamwise velocity fluctuations within the incoming boundary layer close to the wall and separated flow region, in combination with wall-normal velocity fluctuations across the reflected shock wave, as shown in figure 6.24(b). (The curious reader may look ahead to figure 6.28 to see how the projection of this eigenmode onto the mean flow-field contributes to the interaction unsteadiness.) Note also the lack of velocity fluctuations along the incident shock wave, indicating that it is a steady feature on this energetic basis.

Higher-order eigenmodes have an energy level that is significantly lower than the first eigenmode, and portray a more intricate structure. The streamwise component of modes 2 and 3 depicted in figures 6.25(a) and 6.26(a), respectively, show that qualitative changes take place within the separation bubble and farther downstream, leading to an increase in the number of spatially extended regions, in the form of smaller-scale coherent features of opposite sign. The term *subspace bifurcation* refers here to these qualitative changes. Such bifurcations are attributed to the higher-order harmonics required to properly represent the high-dimensional state-space of the data, and when used in combination with other modes, would separate the different temporal-scales within the flow-field.

For instance, Dussauge *et al.* (2006) have compared energetic frequencies within the reflected shock wave region and separation bubble using fluctuating wall-pressure measurements in their Mach 2.3 shock reflection experiments, and found that they are both different, with the separation bubble having energetic frequencies that are an order of magnitude larger than the one found in the reflected shock wave region. It is clear that the subspace bifurcations that occur within the separation bubble represent the higher-order harmonics required to properly represent this dynamical behaviour. The reader may note that no such bifurcations occur within the reflected shock wave region in the first two modes, which represent over 25% of the total energy.



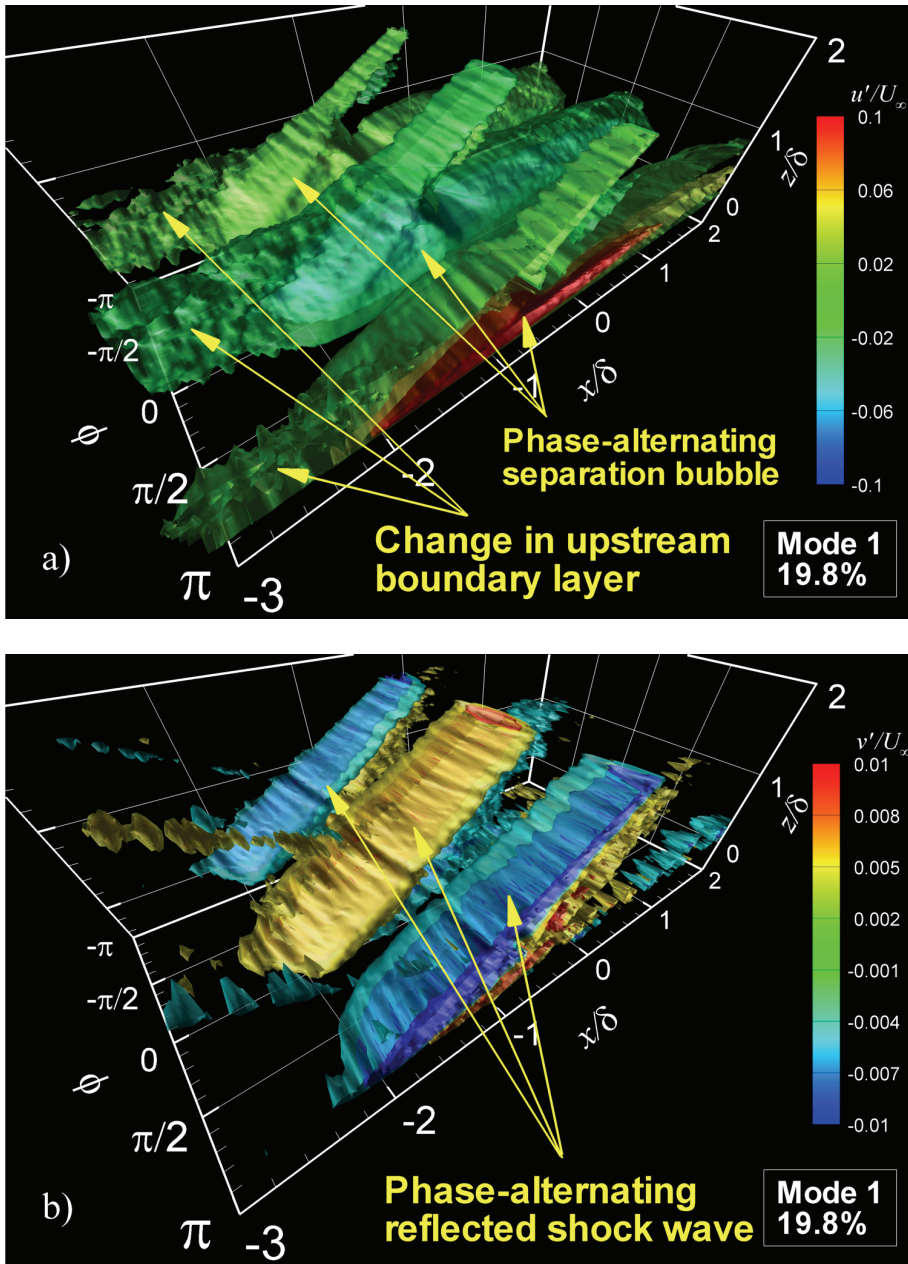


FIGURE 6.24. 1<sup>st</sup> POD eigenmode. (a)  $u'/U_\infty$ , (b)  $v'/U_\infty$ . (Note: modes  $\geq 2$  show  $2u'/U_\infty$ ).

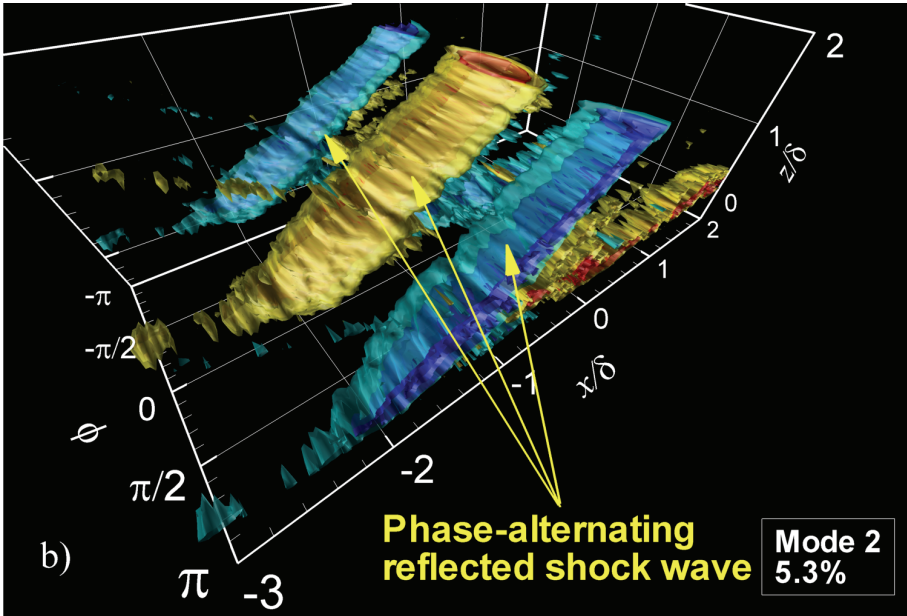
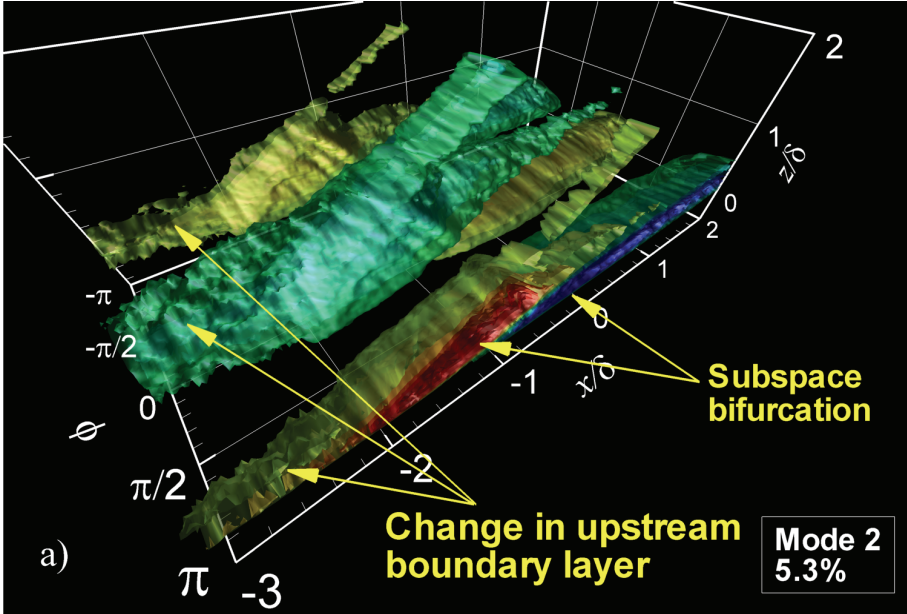


FIGURE 6.25. 2<sup>nd</sup> POD eigenmode. (a)  $u'/U_\infty$ , (b)  $v'/U_\infty$ . (Note: modes  $\geq 2$  show  $2u'/U_\infty$ ).

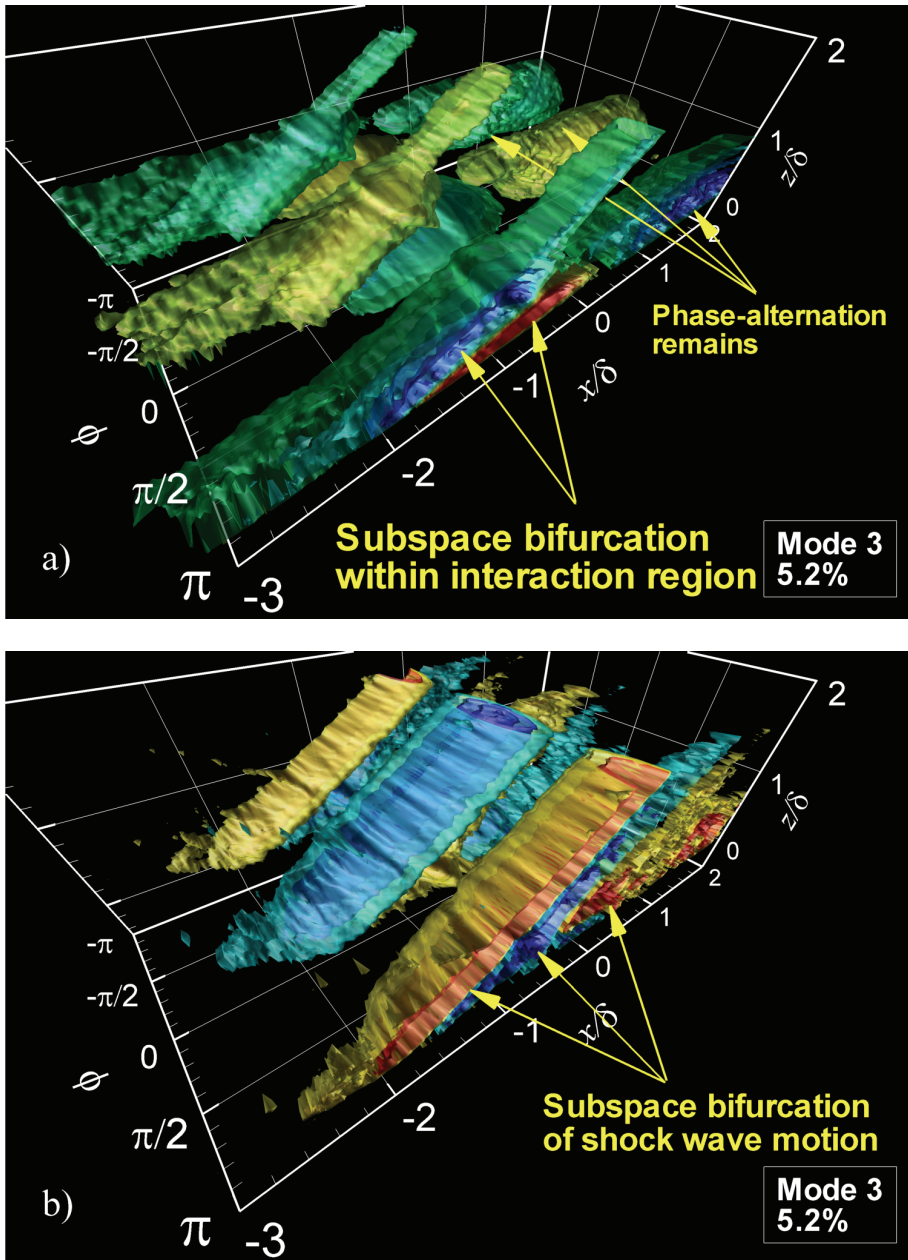


FIGURE 6.26. 3<sup>rd</sup> POD eigenmode. (a)  $u'/U_\infty$ , (b)  $v'/U_\infty$ . (Note: modes  $\geq 2$  show  $2u'/U_\infty$ ).

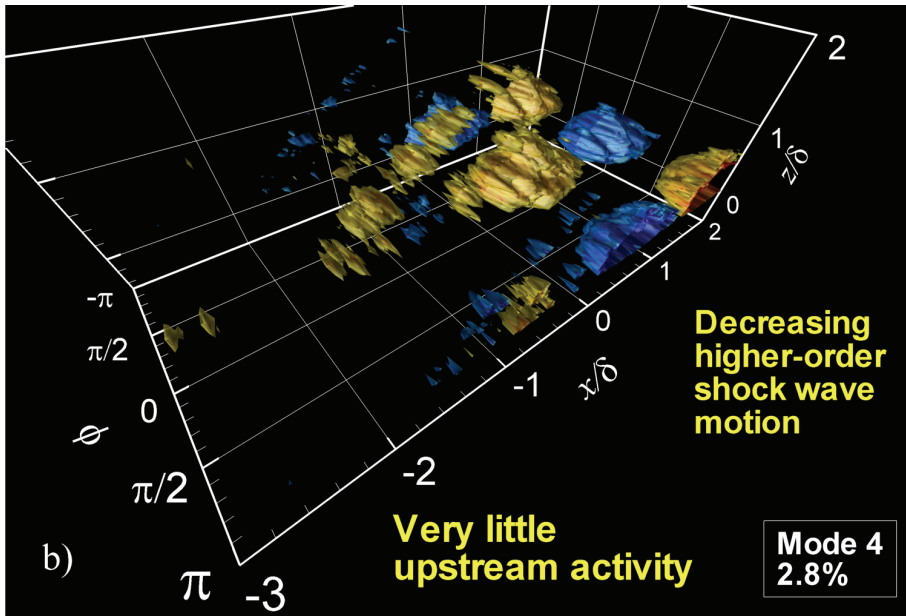
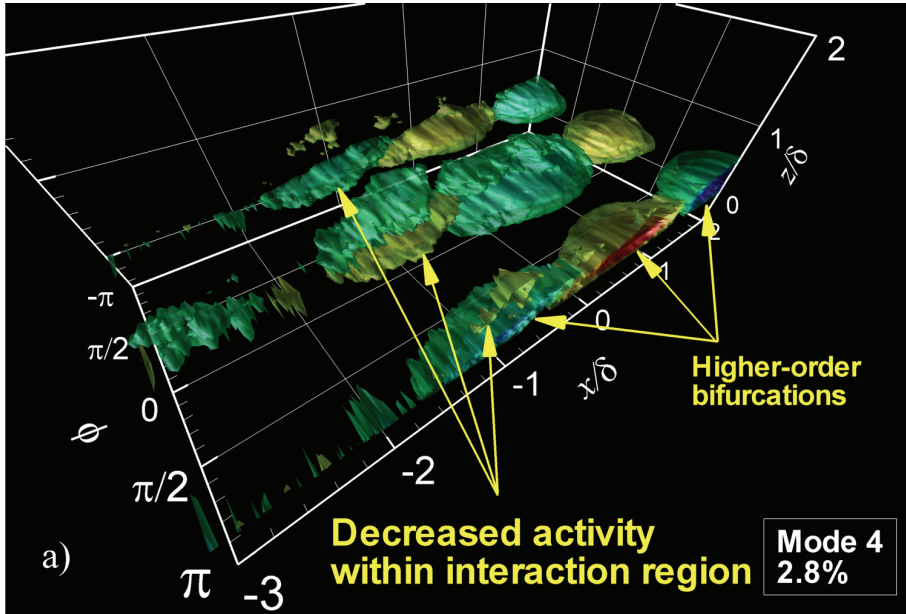


FIGURE 6.27. 4<sup>th</sup> POD eigenmode. (a)  $u'/U_\infty$ , (b)  $v'/U_\infty$ . (Note: modes  $\geq 2$  show  $2u'/U_\infty$ ).

In contrast, mode 4 in figures 6.27(a, b) shows energetic fluctuations exclusively within the redeveloping boundary layer, in the form of distinct regions of large streamwise and wall-normal velocity fluctuations of alternating sign. This pattern is consistent with the circular regions of wall-normal velocity often observed in the instantaneous realizations, and is indicative of a train of quasistreamwise vortices in the form of a convected vortex street. It therefore appears that the subspace features contained in the eigenmodes represent the phenomenology observed in the instantaneous realizations.

To better illustrate how an eigenmode contributes to the unsteadiness of the interaction, the first eigenmode is superimposed onto the mean flow and shown at three ‘phases’;  $\phi_1^1=0$ ,  $\phi^1=\pi/2$ , and  $\phi_M^1=\pi$  in figures 6.28(a–c), respectively. The subspaces at  $\phi_1^1=0$  and  $\phi_M^1=\pi$  represent the contribution of the first eigenmode to the mean flow-field when  $a_1(t_n)$  is at its minimum and maximum, respectively, therefore representing the two extrema of the eigenmode’s influence as a perturbation to the mean flow-field. The mean flow-field itself occurs at  $\phi^1=\pi/2$ , since here  $a_1(t_n)=0$ , and is shown as the intermediate case in figure 6.28(b). Wall-normal velocity contours are also displayed, with streamlines and incoming boundary layer velocity vectors. An indication of the mean position of the reflected shock wave is also shown by the dashed line. Zoomed incoming boundary layer profiles are displayed on the left for clarity.

It can be seen that at  $\phi_1^1=0$ , a separation bubble may be observed. The associated velocity vectors indicate that the incoming boundary layer is less-full than on the mean, and the reflected shock wave appears relatively farther upstream than its mean position. Conversely, at the other extreme when  $\phi_M^1=\pi$ , then the flow remains fully attached. The associated velocity vectors indicate that the incoming boundary layer is relatively fuller than on the mean, and the reflected shock wave appears relatively farther downstream than its mean position.

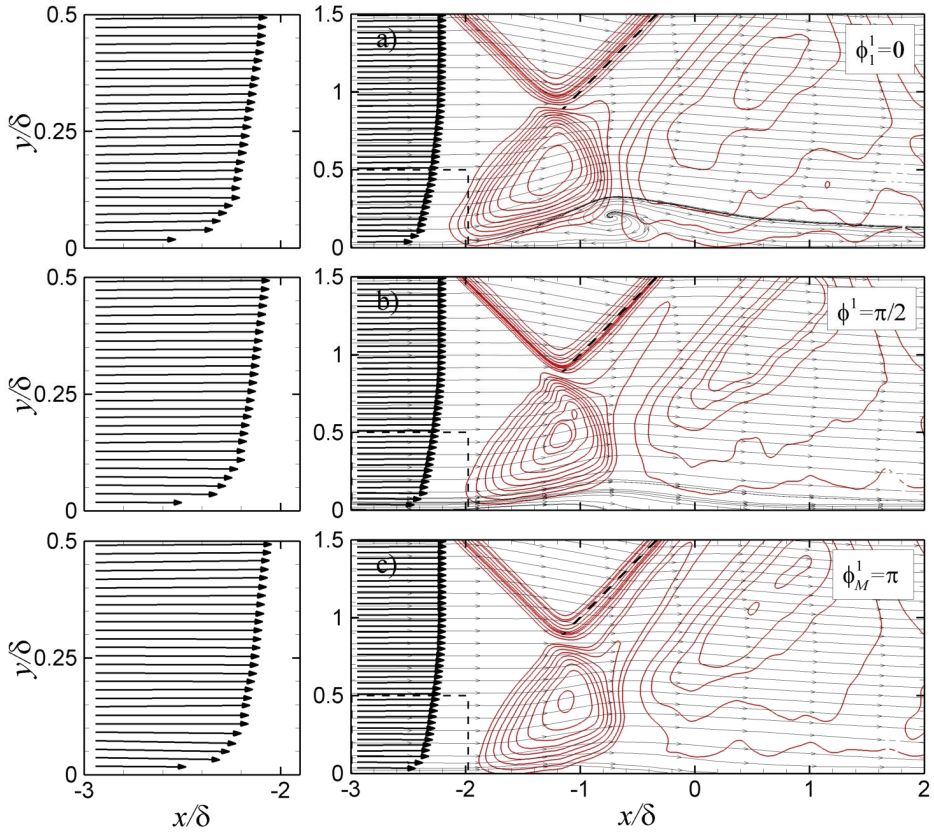


FIGURE 6.28. 1<sup>st</sup> POD eigenmode projected onto mean flow at three different phases. (a)  $\phi_i^1=0$ , (b)  $\phi^1=\pi/2$  (mean flow-field), (c)  $\phi_M^1=\pi$ . Wall-normal velocity contours are shown along with streamlines and incoming boundary layer velocity vectors. The mean position of the reflected shock wave is indicated by the dashed line. Shown on the left are the zoomed incoming velocity profiles of the incoming boundary layer.

These projections are consistent with the joint PDFs presented earlier, which show a correlation suggesting that when the incoming boundary layer is fuller than on the mean, then the streamwise extent of the (largest) separated flow region is more likely to be smaller than its median size, and the reflected shock wave is more likely to be located downstream of its mean position, and vice versa. On the other hand, we are courting difficulties if we wish to construct a model based on a single eigenmode, because a major limitation is the



loss of phase information, with velocity fluctuations within eigensubspace always in linear dependence with a temporal coefficient independent of time. Furthermore, attempts to rebuild the relationship between  $1-1/H_i$  and  $(x-x_{mean})/\delta$  using only the first eigenmode, revealed that variations of  $1-1/H_i$  and  $(x-x_{mean})/\delta$  were less than 3% and 13% of the variations found in the original data, respectively. Thus, the use of the first eigenmode alone cannot be used to accurately describe the interaction's unsteadiness in any decisive way, and this necessitates the utility of additional eigenmodes to properly represent the interaction's unsteadiness. However, attempts at determining state-space relationships between the various temporal coefficients were unsuccessful. This is yet further evidence that the interaction's unsteadiness may be characterized as a complex dynamical process.





# CHAPTER 7 3D FLOW ORGANIZATION

---

## 7.1 Introductory Remarks

**W**E now extend our discussion of the interaction's unsteady flow organization to a three-dimensional characterization using tomographic PIV. Two-dimensional cross-sectional velocity distributions in the wall-parallel plane are first shown, in order to highlight the basic features of the interaction in terms of all three velocity components. The three-dimensional volumetric representations are then presented. The results are discussed in terms of the interaction's instantaneous velocity distribution and vorticity organization. This is followed by a statistical analysis of the results, including a POD analysis, which will help set the scene for the construction of a physical model.

## 7.2 Cross-Sectional Representations

As the motivating prelude to the volumetric results, cross-sectional representations of the interaction are extracted from the tomographic PIV measurement volumes close to the wall at  $z/\delta=0.12$ . Figures 7.1–7.3 each present two uncorrelated instantaneous velocity distributions, representing the colour-coded instantaneous streamwise ( $u/U_\infty$ ), spanwise ( $v/U_\infty$ ), and wall-normal velocity ( $w/U_\infty$ ) components, respectively. Each field is over-laid with the in-plane instantaneous velocity vectors shown in a convective frame of reference  $0.8U_\infty$  in the streamwise direction. These results have been chosen because they exemplify the typical flow features observed.

The results capture the incoming boundary, as well as the reflected shock wave region, the latter initiating at approximately  $x/\delta=-1.5$  (see e.g., figure 7.1(a)). The redeveloping boundary layer is observed farther downstream. Even in this cross-sectional representation, it is clear that the interaction is highly unsteady and complex. The instantaneous streamwise velocity distribution shown in figure 7.1(a) portrays distinct, large-scale regions containing low- and high-speed fluid within the incoming boundary layer, which appear parallel to the wall, and elongated in the streamwise direction. Large velocity differences of up to  $100 \text{ m s}^{-1}$  ( $0.2U_\infty$ ) can occur between these low- and high-speed regions, consistent with the observations made by Ganapathisubramani *et al.* (2006) who carried out planar PIV measurements in a supersonic turbulent boundary layer at Mach 2 and  $z/\delta=0.16$ .

Because of the limited size of the present measurement domain and number of measurement volumes, it is not possible to accurately determine their characteristic geometry (in particular, their streamwise length). However, they appear to have a streamwise extent of at least  $2\delta$  based upon the present measurement domain. Ganapathisubramani *et al.* (2007) reported lengths of up to  $40\delta$  using planar laser scattering and Taylor's hypothesis in their Mach 2 boundary layer. Such long low- and high-speed regions have been reported by numerous researchers in compressible boundary layers, such as Samimy *et al.* (1994), Elsinga *et al.* (2007), Ringuette *et al.* (2008) for instance, as well as in incompressible boundary layers by Kim & Adrian (1999), Tomkins & Adrian (2003), Ganapathisubramani *et al.* (2003), and Hutchins & Marusic (2007) to

name a few. On the other hand, the streamwise-elongated regions are not ubiquitous in the present data. For instance, figure 7.1(b) shows a relatively high-speed region that appears to span almost the measurement domain.

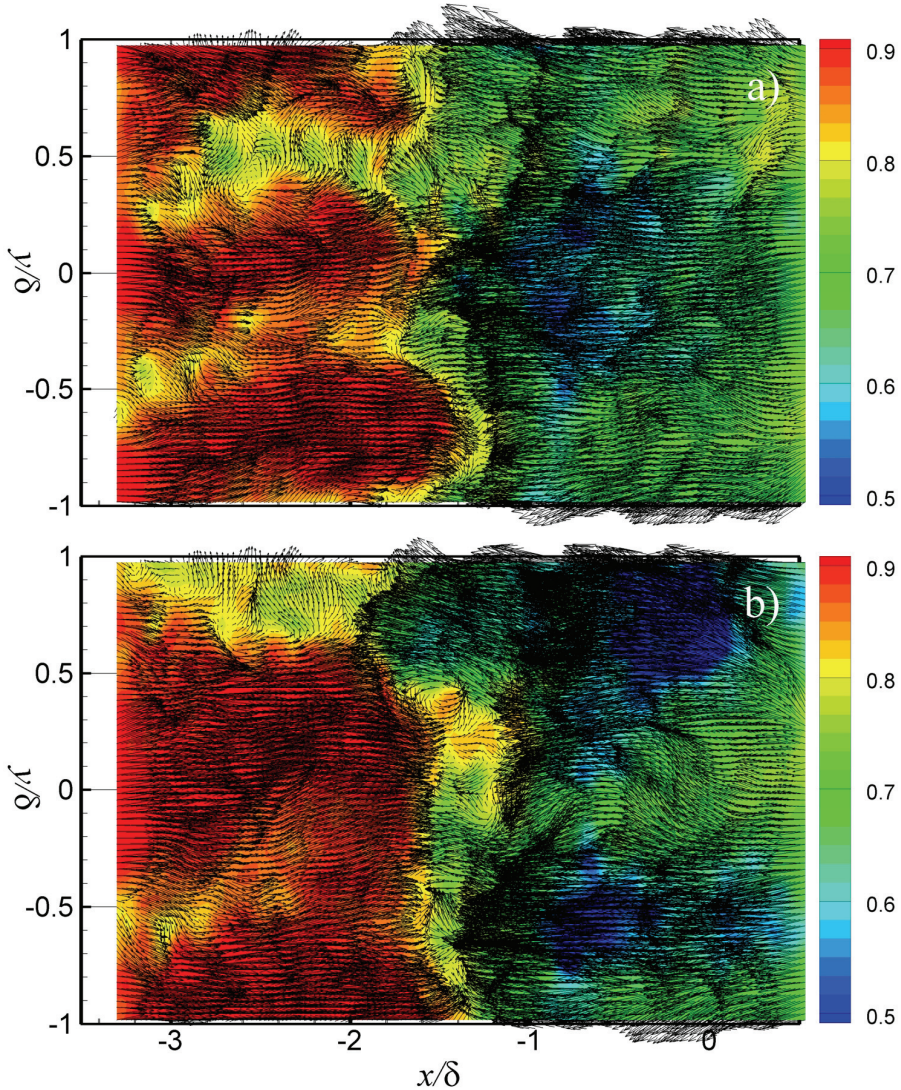


FIGURE 7.1: Two uncorrelated instantaneous streamwise velocity distributions  $u/U_\infty$  at  $z/\delta=0.12$ . Over-laid are in-plane instantaneous velocity vectors shown in a convective reference frame of  $0.8U_\infty$  in the streamwise direction. Modified from Humble *et al.* (2008).

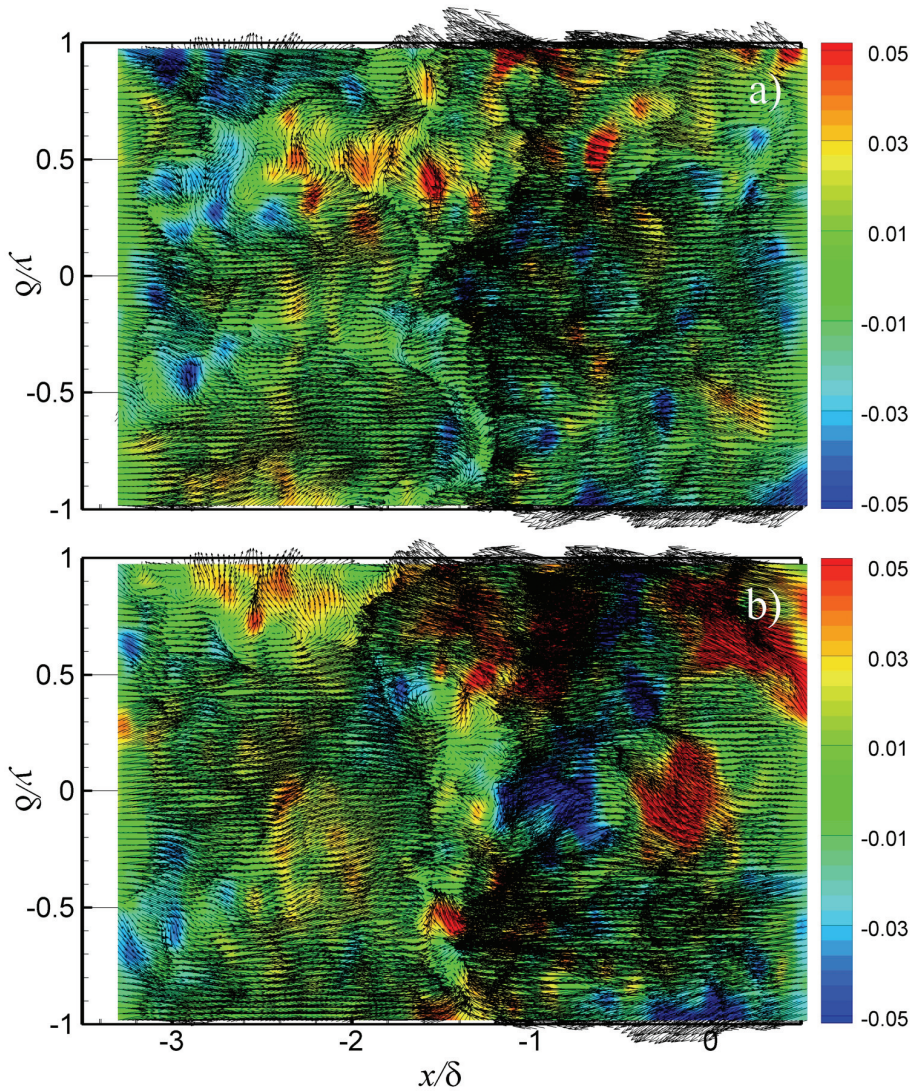


FIGURE 7.2: Two uncorrelated instantaneous spanwise velocity distributions  $v/U_\infty$  at  $z/\delta=0.12$ . Over-laid are in-plane instantaneous velocity vectors shown in a convective reference frame of  $0.8U_\infty$  in the streamwise direction. Modified from Humble *et al.* (2008).



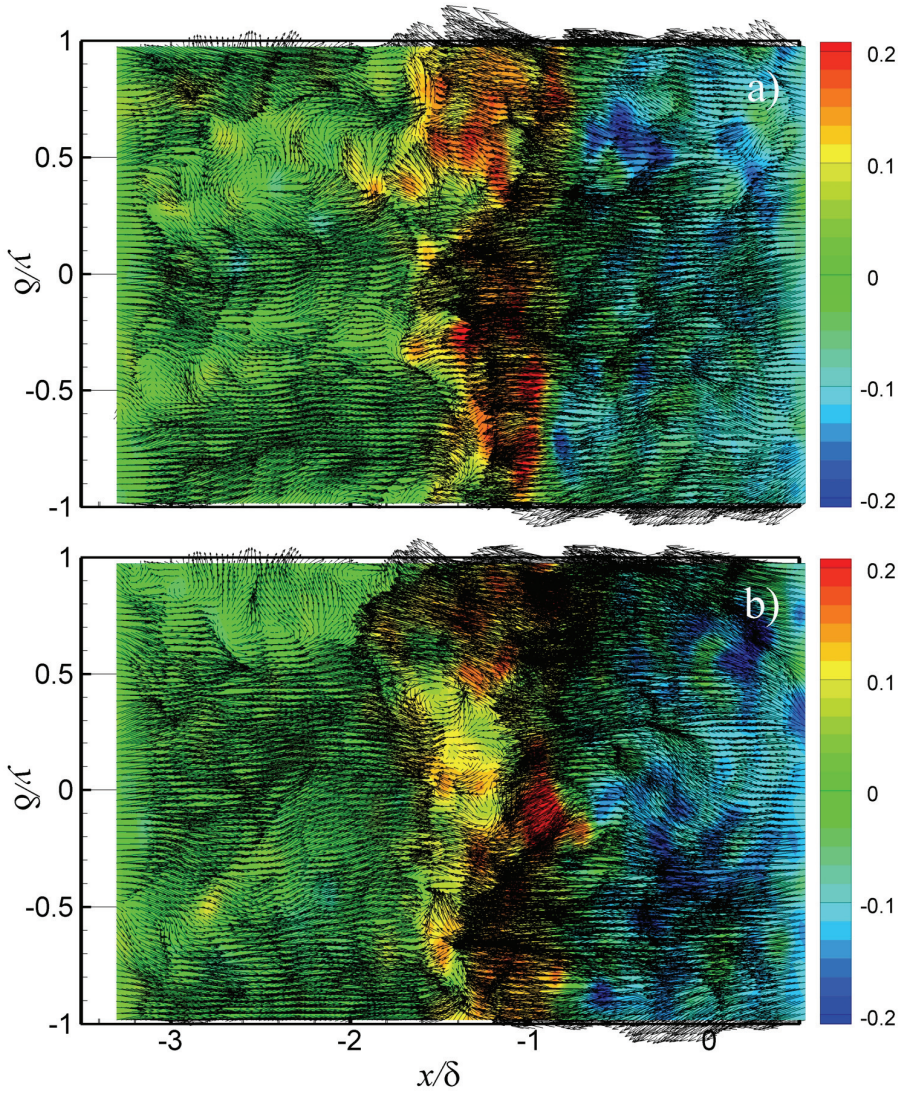


FIGURE 7.3: Two uncorrelated instantaneous wall-normal velocity distributions  $w/U_\infty$  at  $z/\delta=0.12$ . Over-laid are in-plane instantaneous velocity vectors shown in a convective reference frame of  $0.8U_\infty$  in the streamwise direction. Modified from Humble *et al.* (2008).

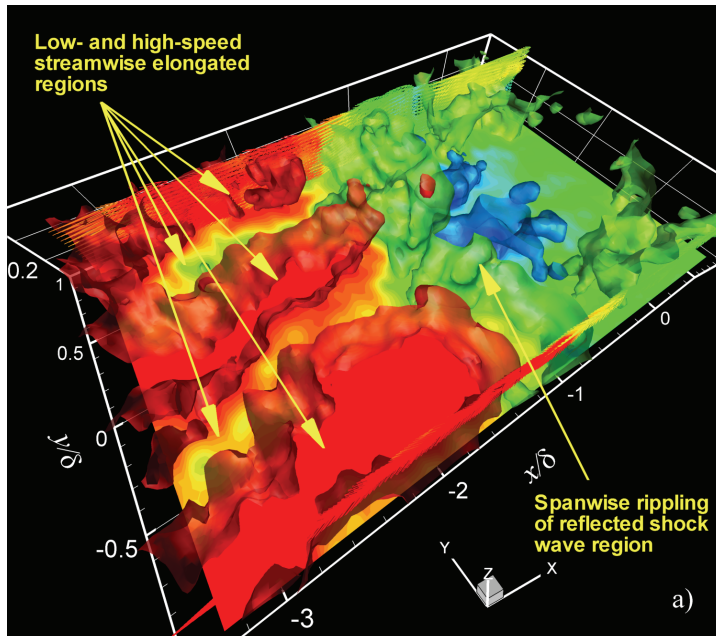
The streamwise-elongated regions appear to have a limited spanwise extent. Figure 7.1(a) suggests that the spanwise dimensions of the low-speed regions are typically within the range  $\Delta y=4\text{--}10$  mm ( $0.2\text{--}0.5\delta$ ), as confirmed by the statistical analysis performed by Elsinga *et al.* (2007) in the undisturbed boundary layer of the present study. These results are also consistent with what has been reported in other supersonic boundary layers, such as the range  $0.25\text{--}0.5\delta$  reported by Ganapathisubramani *et al.* (2006) at  $z/\delta=0.16$ , the range  $0.4\text{--}0.5\delta$  reported by Spina *et al.* (1991) using two-point correlations, as well as the DNS computations of Ringuette *et al.* (2008) who report about  $0.5\delta$ . It is important to remark that the spatial organization of these regions disappears after data averaging, indicating that they are not stationary features.

The corresponding instantaneous spanwise velocity distributions are shown in figures 7.2(a, b). Note that the spanwise velocity range is smaller than for the other velocity components. The spanwise velocity appears less coherent along both the streamwise and spanwise directions in comparison to the streamwise component, consistent with the two-point correlations made by Ganapathisubramani *et al.* (2005). A comparison between figures 7.1(a) and 7.2(a) indicates that the spatially compact regions of spanwise velocity are typically observed within the streamwise-elongated low-speed regions. Figure 7.2(a) shows that these spanwise velocity regions persist throughout the interaction, whereas figure 7.2(b) shows an increase in both their magnitude and spatial extent. It is therefore often difficult to determine the compression region from the spanwise velocity distributions alone.

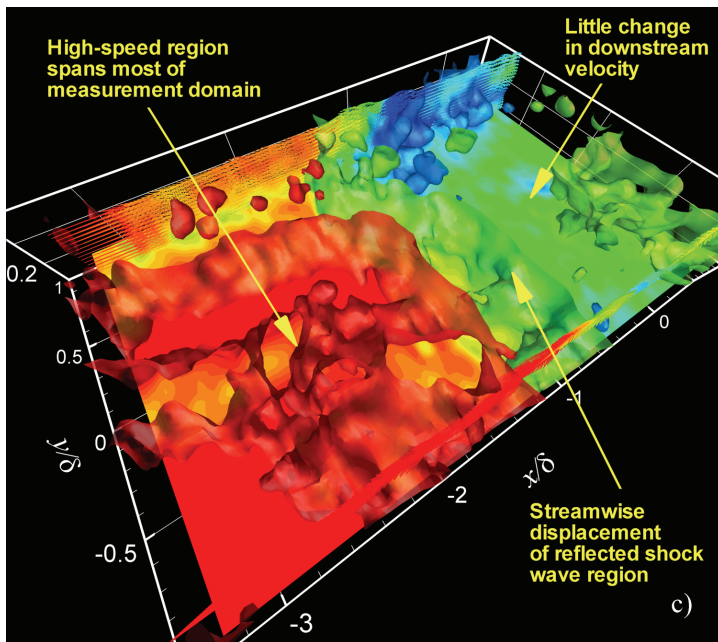
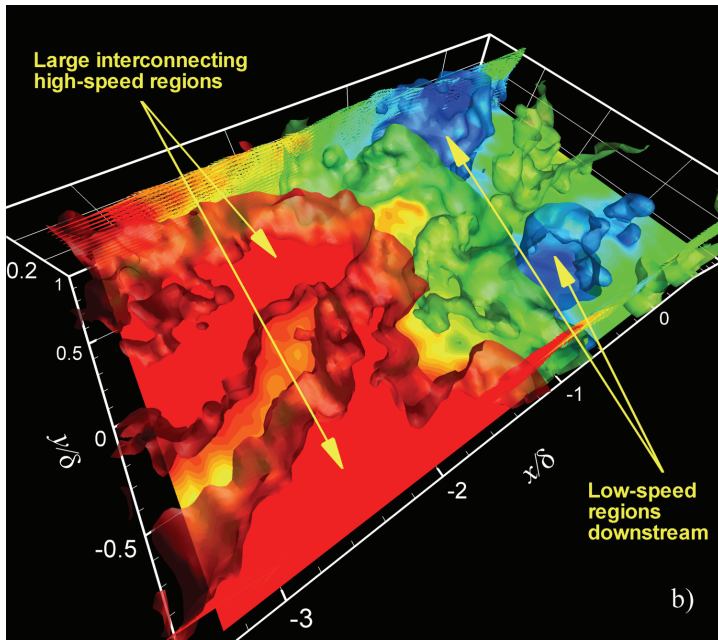
The corresponding wall-normal velocity distributions are shown in figures 7.3(a, b). Small velocity fluctuations are present within the incoming boundary layer. In contrast, larger positive fluctuations of the order of  $100\text{ m s}^{-1}$  ( $0.2U_\infty$ ) can be observed in the compression region, associated with the dilatation of the subsonic flow in this part of the interaction. Farther downstream, the redeveloping boundary layer becomes populated with spatially compact regions of negative wall-normal velocity, consistent with the formation of a mixing-type layer, as observed by Pirozzoli & Grasso (2006) in their DNS of an incident SWTBLI.

### 7.3 3D Instantaneous Flow Organization: Lower Region

The main results are now presented. Figure 7.4 shows a series of uncorrelated volumetric representations of the lower region of the interaction ( $z/\delta=0.1-0.6$ ) containing instantaneous streamwise velocity isosurfaces. Note that figures 7.1(a, b) correspond to figures 7.4(a, b), respectively. For the purposes of illustration, three values of streamwise velocity isosurface are displayed: high-speed in red ( $0.9U_\infty$ ), intermediate velocity in green ( $0.75U_\infty$ ), and low-speed in blue ( $0.55U_\infty$ ). Velocity vectors in the streamwise-wall-normal plane are shown coloured with streamwise velocity. Figure 7.4(a) shows that the relatively low- and high-speed regions observed in the cross-sectional results are in fact three-dimensional, with widths that can vary in the wall-normal direction. This phenomenology is consistent with the results of Ringuette *et al.* (2008), who also visualized such features using an isosurface of velocity, and found them to be highly three-dimensional, interpreting them as chains of bulges.



(see figure caption on next page.)



(see figure caption on next page.)



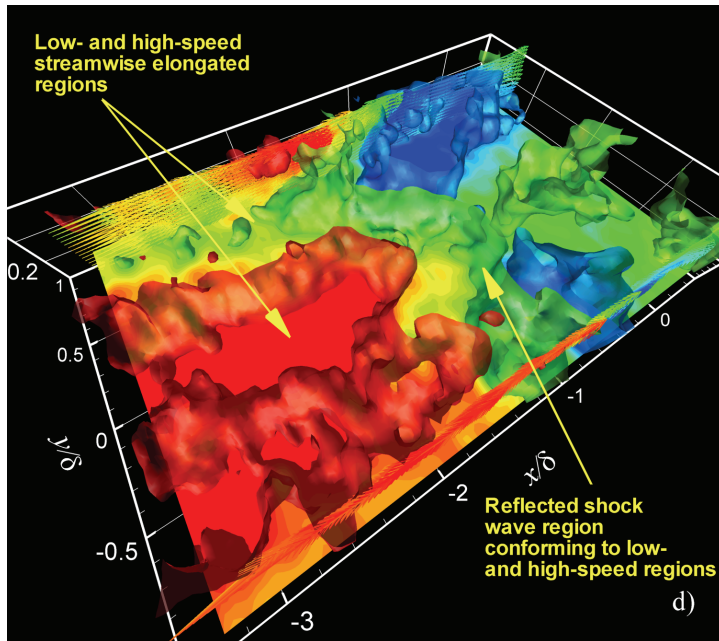


FIGURE 7.4: Volumetric representations of the instantaneous structure of the interaction: lower region ( $z/\delta=0.1-0.6$ ). Isosurfaces of streamwise velocity are shown: high-speed in red ( $0.9U_\infty$ ), intermediate velocity in green ( $0.75U_\infty$ ), and low-speed in blue ( $0.55U_\infty$ ). Velocity vectors are shown flooded with instantaneous streamwise velocity. Modified from Humble *et al.* (2008).

Figure 7.4(b) shows that the widths of the high-speed regions also vary in the streamwise direction. In this particular case, they appear to be interconnected, although this is more likely to be associated with the termination of the low-speed region between. The closing pattern of the isosurface around this feature suggests that it does not extend much farther than the edge of the measurement domain ( $z/\delta=0.6$ ), and is therefore embedded within the lower part of the incoming boundary layer. A volumetric representation of this feature therefore reduces the complexity and ambiguity of the cross-sectional results by providing a volumetric synthesis of such an observation, as discussed by Delo *et al.* (2004).

Instantaneous velocity isosurfaces are used to make inferential statements regarding the overall reflected shock wave pattern within the boundary layer, similar to the approach carried out by

Ganapathisubramani *et al.* (2007), who computed a surrogate for the instantaneous separation point using a velocity threshold criterion. Figures 7.4(a, b) show that the reflected shock wave region undergoes spanwise undulations of the order of  $0.5\delta$ , whereas figure 7.4(c) shows a quite uniform reflected shock wave region that is displaced in the streamwise direction. Wu & Martin (2008) carried out a DNS of a compression ramp interaction, and using contours of the pressure gradient magnitude in streamwise–spanwise planes, observed that the streamwise movement of the shock wave was about  $\delta$ , with a wrinkling in the spanwise direction of about  $0.5\delta$ . The instantaneous spatial organization of the reflected shock wave region may therefore be considered as being a superposition of streamwise translation and spanwise rippling patterns, as first proposed by Wu & Martin (2008).

To further illustrate some of the internal structure of the interaction, figure 7.5 shows a rendering of an instantaneous separation bubble captured within one of the measurement volumes. The bubble is defined by a semitransparent isosurface of  $u=0$  m s<sup>-1</sup> shown in dark blue, along with the instantaneous subsonic bubble, defined by a semitransparent isosurface of  $M=1$  ( $u=213$  m s<sup>-1</sup>) shown in light-green, determined using the adiabatic flow assumption. Reversed-flow occurs in less than 10% of the dataset (c.f. figure 6.12) at this region within the interaction, but typically occurs in distinct, isolated regions, like that shown in the figure. The results also show velocity vectors in a convective frame of reference of  $0.1U_\infty$ , along with streamlines computed within this convective reference frame, coloured by instantaneous streamwise velocity.

The separation bubble appears as a distinct, isolated region, with a size of approximately  $0.3\delta \times 0.3\delta \times 0.3\delta$ . It exhibits an irregular shape, which can be characterized by two large elongations both upstream and downstream of its main body, as well as appearance of a protruding head. Note also the fragmented regions of reversed-flow farther downstream of the main bubble, which may be due to measurement noise and therefore may be considered as being numerical artefacts.

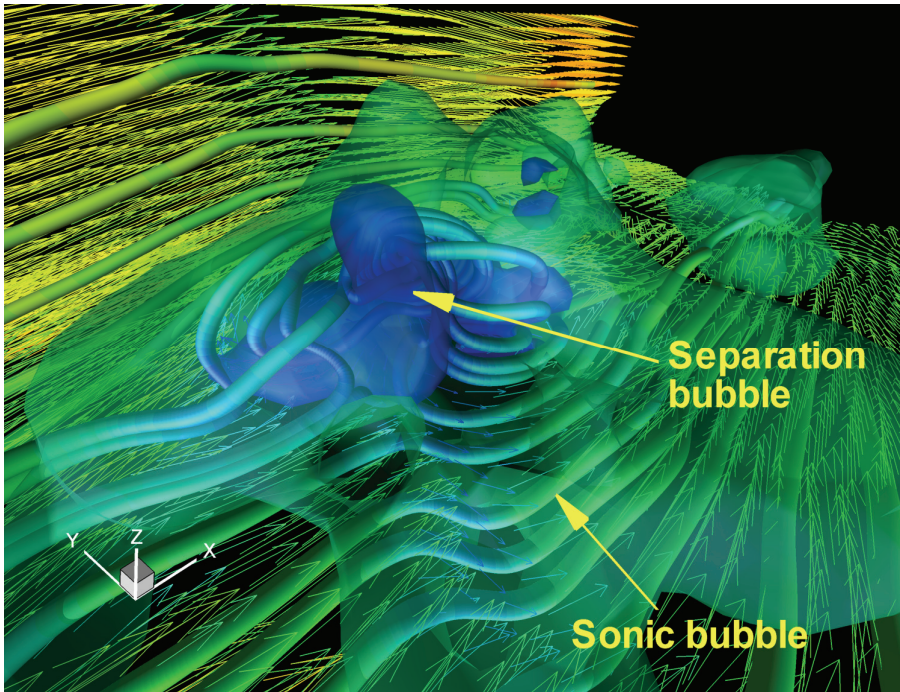


FIGURE 7.5. Instantaneous internal flow structure of the interaction: lower region ( $z/\delta=0.1-0.6$ ). Results show a rendering of an instantaneous separation bubble (defined by a semitransparent isosurface of  $u=0 \text{ m s}^{-1}$  in dark blue) and the sonic bubble (defined by a semitransparent isosurface of  $M=1$  ( $u=213 \text{ m s}^{-1}$ ) in light-green, determined using the adiabatic flow assumption). Velocity vectors with a convective velocity of  $0.1U_\infty$  are shown in two planes: at  $y/\delta=0.1$  and  $z/\delta=0.6$ , both flooded with streamwise velocity contours. Streamlines are computed within this convective reference frame.

The tomographic data enable streamlines to be traced out through a three-dimensional measurement domain. The streamline pattern around the separation bubble shows a large-scale swirling, which entangles the separation bubble around its elongations. In this convective frame of reference, observe how the velocity vectors turn around the bubble's body, treating it as if it were an obstacle. This is consistent with the planar PIV SWTBLI results presented earlier, which show that fluid is lifted up and rides over the separated flow region (an observation that is also hinted at by the velocity vectors in the streamwise-wall-normal plane shown in the present figure). In

this three-dimensional representation, however, it is also clear that a similar behaviour occurs in the streamwise-spanwise plane.

The separation bubble is clearly engulfed by a much larger subsonic region. The latter is bounded by a sonic surface that has a three-dimensional corrugated appearance, with undulations in all directions. Both the separation and subsonic bubbles reach their maximum thickness in approximately the same region of the interaction; quite an ubiquitous observation in the dataset. It is clear from this type of representation, that such a configuration, as portrayed in the planar results, is in fact much more complicated in three-dimensional space, although the reader should always keep in mind the difficulty in interpreting such visualizations.

## 7.4 Vorticity Characterization

To further characterize the interaction's three-dimensional flow organization, regions of vorticity magnitude are visualized. Although the present resolution is insufficient to permit a quantitative study of the vorticity characteristics, the results may be used qualitatively to highlight the overall vortex organization. An artistic overview of the main phenomenological features is presented in figure 7.6. Isosurfaces of vorticity magnitude  $|\boldsymbol{\omega}| = \sqrt{(\omega_x^2 + \omega_y^2 + \omega_z^2)}$  showing  $|\boldsymbol{\omega}|\delta/U_\infty = 1$  are displayed, determined using central-differencing. The measurement volume of figure 7.4(a) was chosen because it contains several key elements that are characteristic of the ensemble of data.

The results portray an incoming boundary layer with a rich, instantaneous structure, populated with numerous regions of concentrated vorticity of various shapes and sizes. While in the planar PIV measurements, discrete, disconnected regions of vorticity have been identified (see e.g., Adrian *et al.* 2000; Tomkins & Adrian, 2003; Ganapathisubramani *et al.* 2006), it is now clear that these regions are in fact connected out of the plane of the laser sheet in three-dimensional space, forming a complicated flow structure. They often appear to form interconnected agglomerations, consistent with the observations of Delo *et al.* (2004) in their three-dimensional visualizations of an incompressible boundary layer, and are most likely the remnants of the inclined vortex loops, horseshoes, or hairpin structures, as described by Head & Bandyopadhyay (1981) and Adrian *et al.* (2000).

The structures typically appear in a quasistreamwise alignment, in agreement with the observations made by Elsinga *et al.* (2007) and Ringuette *et al.* (2008), who visualized three-dimensional hairpin-type structures. It is evident that the present regions of vorticity typically occur within the low-speed regions and at the interface between the low- and high-speed regions. This is also consistent with the observations made by Elsinga *et al.* (2007) and Ringuette *et al.* (2008), who found that groups of hairpin packets were frequently located above long low-momentum regions, thereby supporting the hairpin packet model reported by Kim & Adrian (1999), Adrian *et al.* (2000), Tomkins & Adrian (2003), and Ganapathisubramani *et al.* (2003) among many others, which explains the existence of the streamwise-elongated regions of uniform velocity extending to distances greater than  $2\delta$ , by asserting that the induced motion of several hairpins in streamwise alignment perpetuates the low- and high-speed regions. The tomographic PIV results also provide visual evidence for the large wave-lengths found within the incoming boundary layer using HWA (see chapter 5).

In addition, it can be seen that very few structures occur within the high-speed regions, as shown in figure 7.6(bottom-left). Instead, the high-speed regions exhibit a three-dimensional spanwise sinuous or undulating motion, and appear to meander between the surrounding vortical structures. Such a scenario would be consistent with a number of vortical structures that are in a spanwise-staggered array, an intriguing observation that has been reported by Elsinga *et al.* (2007) using autocorrelations of wall-normal swirl strength in a plane parallel to the wall. Although not as widely documented as some of their other characteristic features, such diagonal inclinations of the vortical structures have also been reported in the three-dimensional visualization study of an incompressible boundary layer by Delo *et al.* (2004).



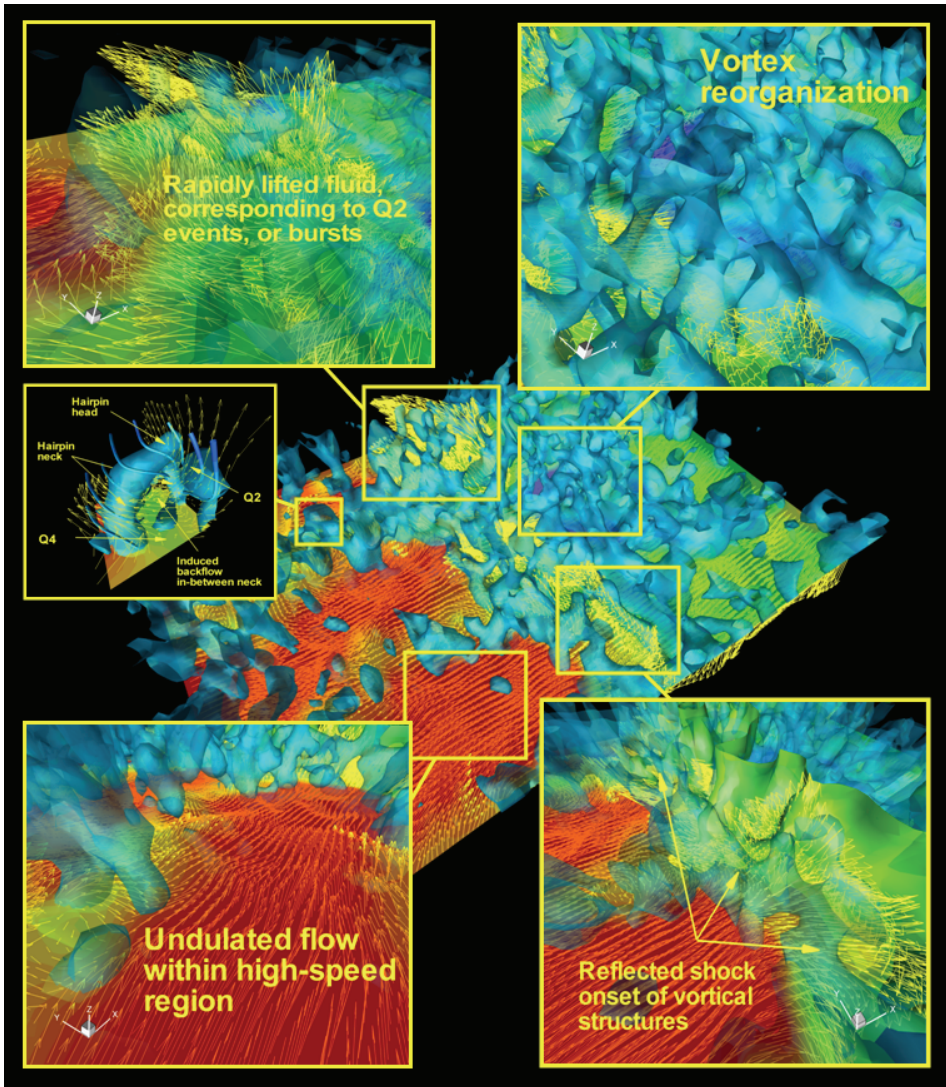


FIGURE 7.6: Overview of interaction phenomenology: lower region ( $z/\delta=0.1-0.6$ ). Semitransparent vorticity isosurfaces for  $|\omega|\delta/U_\infty=1$  are shown. Velocity vectors with a convective velocity of  $0.8U_\infty$  are shown at  $z/\delta=0.26$  along with flooded streamwise velocity contours. From Humble *et al.* (2008).

Considered individually, there are many structures in the dataset that form arch, cane, and hairpin-type structures, as discussed by Robinson (1991) and Adrian *et al.* (2000) among many others. For the purposes of illustration, one such structure is displayed in greater

detail in figure 7.6(middle-left). This type of structure was in fact first introduced by Theodorsen (1952) as a horse-shoe type structure, with an attendant swirling motion, as shown in figure 7.7(left), from Theodorsen (1952). The various parts of the structure have been labelled as shown in figure 7.7(right), from Robinson (1991). The present structure is approximately  $0.3\delta$  wide and  $0.4\delta$  high, and is convecting at around 80% of  $U_\infty$ . Elsinga *et al.* (2007) and Ringuette *et al.* (2008) have visualized a packet of such structures of similar geometric dimensions in their compressible boundary layers.

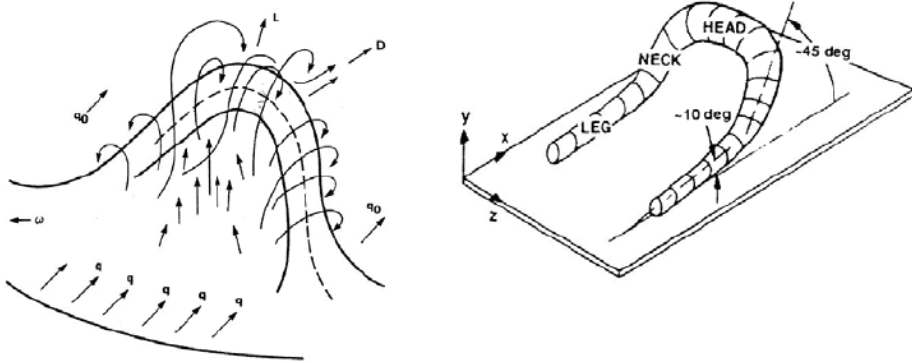


FIGURE 7.7: Theodorsen's horse-shoe model (left). From Theodorsen (1952). Hairpin nomenclature (right). From Robinson (1991).

The illustrated structure in figure 7.6(middle-left), however, is neither symmetric nor identical to the other structures observed. While it is embedded within the surrounding turbulent environment, its imprint on the velocity field is clear: a spanwise vortex core can be seen located at its head, rotating in the same direction as the mean circulation. A region of backflow located below and slightly downstream of the head can be seen to be induced between its neck. Faster moving fluid can be seen to be induced on the outboard portions of the hairpin's neck. Below and downstream of its head, there is a region of Q2 ( $u' < 0$ ,  $w' > 0$ ) events opposed by a region of Q4 ( $u' > 0$ ,  $w' < 0$ ) events, although no stagnation point can be unambiguously identified.

Ejected fluid extends from near to the wall ( $z/\delta \approx 0.1$ ), into the outer portion of the boundary layer ( $z/\delta > 0.6$ ). This represents a

significant fluid exchange, and the fact it takes place within the upstream boundary layer suggests that it is already quite active as it approaches the interaction. Streamlines of locally induced flow show a swirling pattern around the necks and head, indicating an overall circulation around the hairpin. The correspondence between this swirling motion and the isosurfaces justifies the use of vorticity magnitude as an appropriate quantity for the visualization of vortical structures in this flow.

Figure 7.6(top-left) shows a large region containing Q2 events develops within the reflected shock wave region. While the planar PIV results have shown that in the first part of the interaction ejected fluid can penetrate a significant distance into the outer part of the boundary layer (often up to  $z/\delta=0.6$ ), it can now be seen that this process is highly three-dimensional, with the ejection of fluid varying significantly across the span of the interaction.

One can only speculate about the interaction between the Q2 events produced by the hairpin structures and those produced by the displacement of supersonic fluid. The complex, three-dimensional nature of the flow makes even the unambiguous detection of such a process extremely difficult. Nevertheless, we expect this type of behaviour to be a significant source of kinematic Reynolds-averaged shear stress, since any element of fluid with a less than average  $u$  and positive  $w$  contributes to this quantity. Turbulence statistics of the interaction that show the reflected shock wave to be a region of explosive increase in Reynolds-averaged shear stress is a testament to this.

Figure 7.6(bottom-right) shows that the reflected shock wave region is also the nucleation site for the onset of vorticity across the span of the interaction. This is in agreement with the vorticity results obtained by Ganapathisubramani *et al.* (2007) in their compression ramp interaction, who report that the interaction acts like a vorticity amplifier. As the vortical structures propagate through the interaction, it appears that they undergo a significant spatial reorganization. Figure 7.6(top-right) shows that the structures typically lose their identity downstream, and develop approximately parallel, nonparallel, and orthogonal alignments, which occur in close proximity. They appear to concatenate with each other to form more complicated arrangements, whereas in other cases, they appear



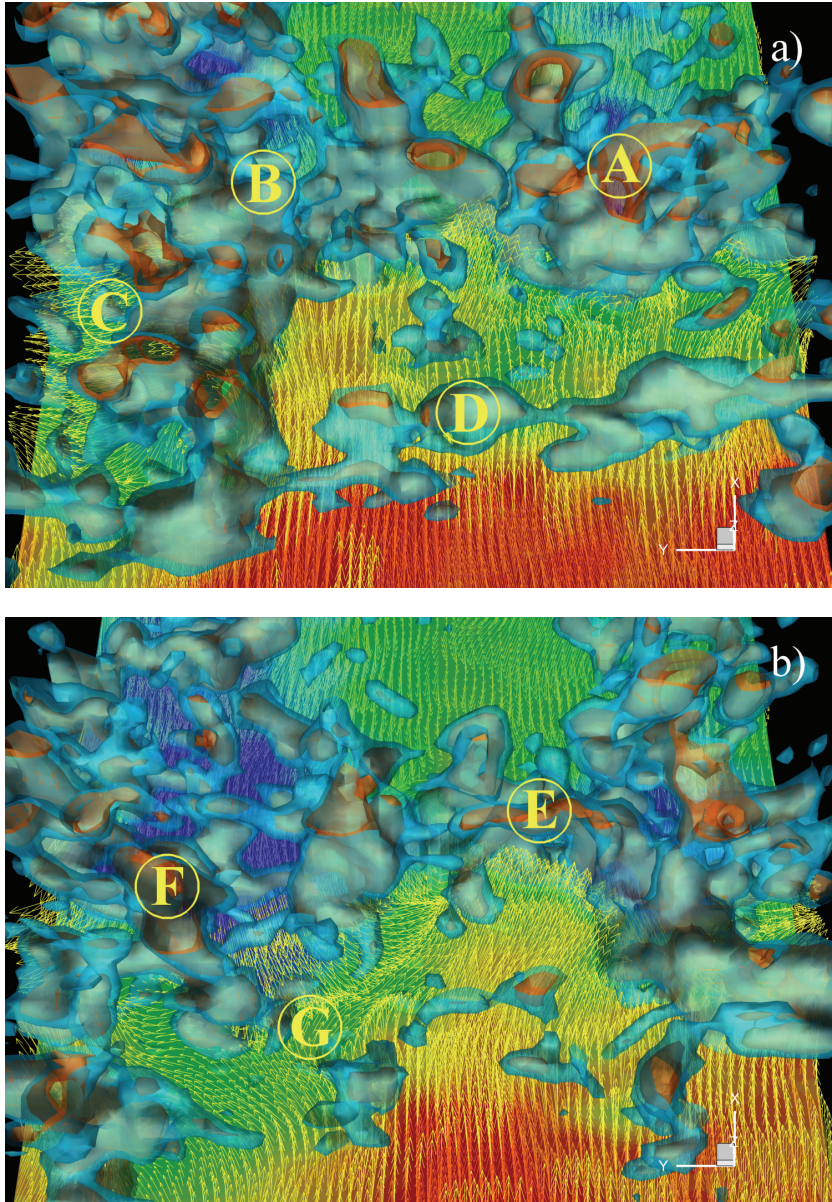
isolated and disconnected. Wu & Martin (2007) also visualized vortical structures within their compression ramp interaction, and found that the structures became more chaotic and of smaller extent as a result of the interaction, attributing the latter observation to either the chopping of the structures by the shock wave, or due to their compression through the shock wave.

The interaction region is examined in more detail in figure 7.8, which shows a series of uncorrelated snapshots of its instantaneous vorticity organization. Visualization details are the same as those used in figure 7.6, except the isosurfaces have now been nucleated for clarity (i.e., two levels of isosurface are shown in close proximity, one inside the other). It can be seen that there is quite some difference in the global vorticity organization from instant to instant. For example, figure 7.8(d) shows regions of vorticity that persist throughout the interaction into the redeveloping boundary layer. In contrast, figure 7.8(c) shows that the redeveloping boundary layer is absent of the same levels of vorticity (see downstream and to the left of region (I)).

These results substantiate the notion that the reflected shock wave region is the nucleation site for the onset of vorticity across the span of the interaction. Figures 7.8(a, c) in particular, show that regions of vorticity spread broadly over the span of the interaction, beginning at the inception of the reflected shock wave region within the boundary layer. Figures 7.8(a, c) illustrate the common observation that these regions often appear as interconnecting chains, as shown in regions (D) and (H) for instance. These interconnecting chains may well be the remnants of spanwise roller-type structures, as observed in the DNS of Pirozzoli & Grasso (2006), who mention that they become important in the interaction zone.

Although difficult to discern from this representation, it appears that very few vortical structures are in contact with the wall, as the flow passes through the interaction. This is consistent with the planar results shown earlier, as well as with the results of Pirozzoli & Grasso (2006), who have attributed the onset of such structures to the formation of a mixing layer and their subsequent evolution, eventually leading to new structures farther downstream. The present results are also reminiscent of the DNS of incompressible separated flows by Na & Moin (1998) and Chong *et al.* (1998), which showed

that vortical structures and the vorticity layer are lifted away from the wall in the first part of the separation process.



(see figure caption on next page.)

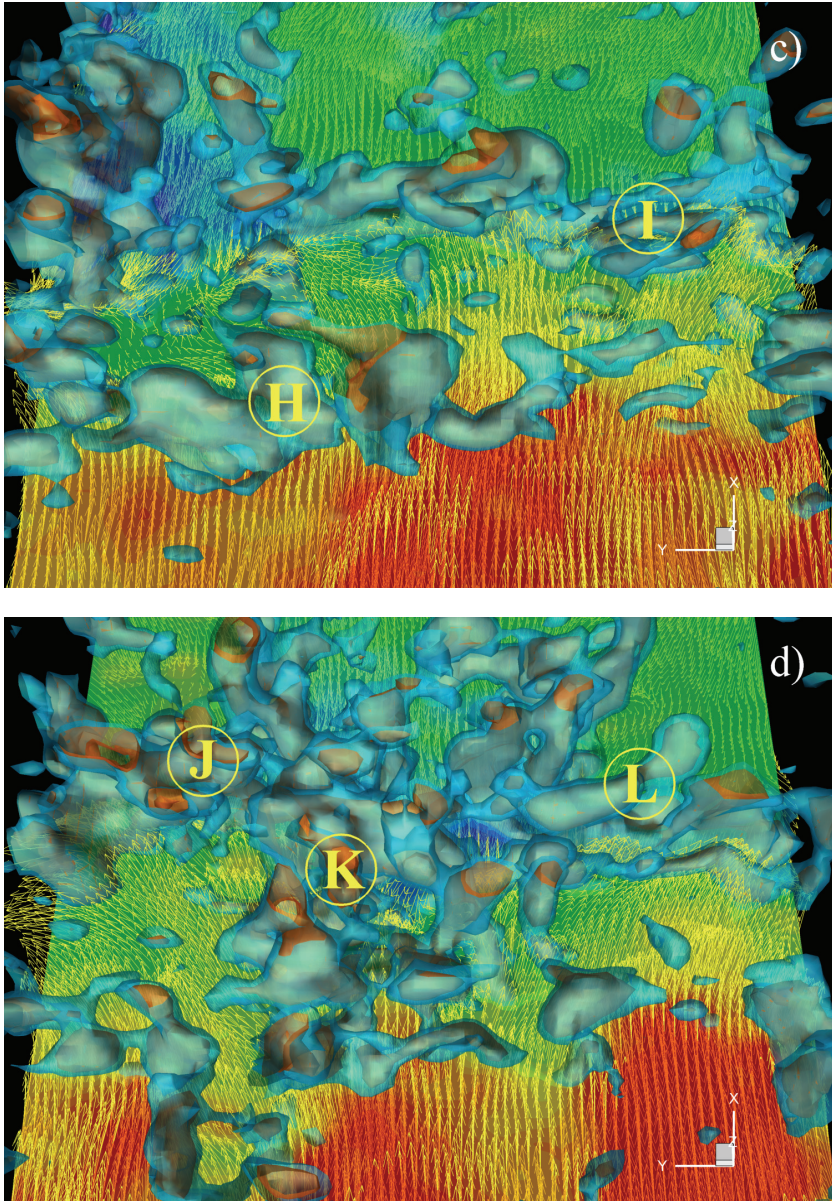


FIGURE 7.8: A series of uncorrelated visualizations of the instantaneous flow structure of the interaction: lower region ( $z/\delta=0.1-0.6$ ). See figure 7.6 for visualization details. Flow is from bottom to top. Labelled regions are discussed in the text. Modified from Humble *et al.* (2008).



Notice that many of the present structures, particularly those predominantly oriented normal to the wall, are cut in the streamwise–spanwise plane due to the limited height of the measurement volume. This occurs particularly within the redeveloping boundary layer, as shown in regions (A), (F), and (J) for instance, and is consistent with the idea that there is an increase in vorticity throughout the interaction zone. This in agreement with the vorticity results obtained by Ganapathisubramani (2007), who report that the interaction acts like a vorticity amplifier.

The spatial organization of the incoming boundary layer appears to affect the spanwise vorticity distribution. Regions (B), (F), and (K) show a train of vortical structures persisting throughout the interaction, extending from a relatively low-speed region within the incoming boundary layer well into the redeveloping boundary layer. In contrast, region (E) shows that a relatively high-speed region entering the interaction leads to a significant downstream displacement and distortion of a vorticity region in the streamwise direction. It therefore appears that the instantaneous vorticity distribution in this region is affected by the incoming boundary layer in much the same way as for the velocity isosurfaces.

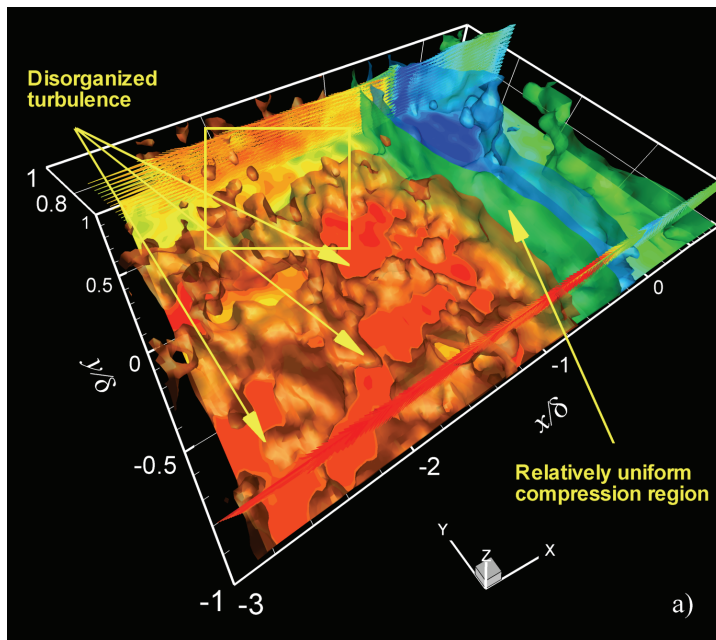
Interestingly, observe also how a significant spanwise flow tends to precede the low-speed region within the incoming boundary layer, such as in regions (C) and (G) for instance. This is in contrast to what typically precedes the high-speed regions (see to the left of (D) and upstream of (E)), where flow appears to penetrate into the reflected shock wave region with little spanwise motion. Furthermore, velocity contours in figure 7.8 indicate that a larger retardation typically occurs downstream of a relatively low-speed region than downstream of a relatively high-speed region (compare regions (E) and (F), respectively for example). Thus, slower moving fluid is decelerated more than faster moving fluid.

This behaviour can be understood following the argument of Luker *et al.* (2000): as fluid elements travel through the reflected shock wave region they receive an impulse  $\int F dt$ , where  $F$  is the forced applied to the fluid element over time. Since the time-scale of the fluid element's transit through the deceleration region is much smaller than the time-scale of the reflected shock wave region's motion (i.e.,  $\tau_f \ll \tau_{\text{shock}}$ , since  $\tau_f \sim \delta/U_\infty$  (typically  $O(10^{-4})$ ) and  $\tau_{\text{shock}} \sim$

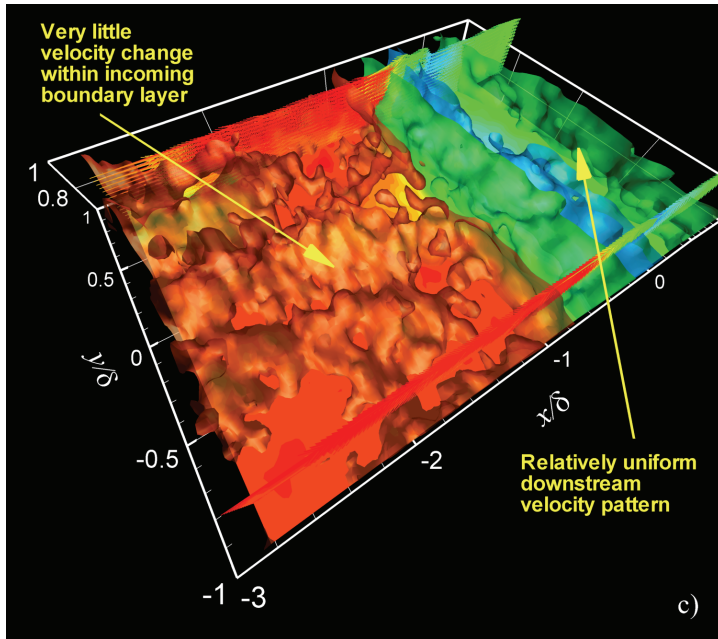
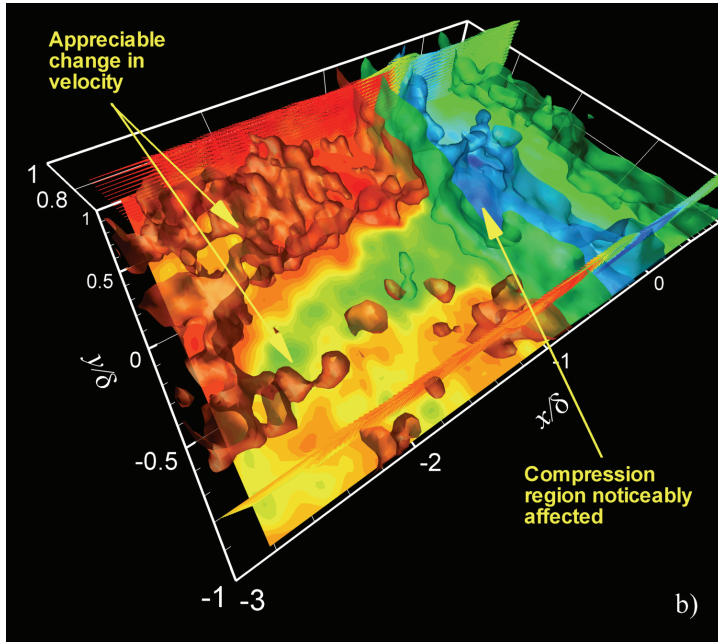
$O(10^{-3})$ , see Dolling 2001), then the force applied is a function of space only i.e.,  $F=F(x, y, z)$ . Thus,  $I = -\int (F/V) ds$ , where  $V$  represents the fluid element's velocity magnitude,  $ds$  is the distance travelled by the fluid element, and the negative sign indicates that the fluid element decelerates. Therefore, for a given trajectory, slower moving fluid elements receive a larger (negative) impulse, and therefore decelerate more than faster fluid elements.

## 7.5 3D Instantaneous Flow Organization: Upper Region

Moving farther away from the wall, a series of uncorrelated measurement volumes in the upper region of the interaction are presented in figure 7.9. Three values of streamwise velocity isosurface are displayed: high-speed in red ( $0.99U_\infty$ ), intermediate velocity in green ( $0.85U_\infty$ ), and low-speed in blue ( $0.75U_\infty$ ).



(see figure caption on next page.)



(see figure caption on next page.)

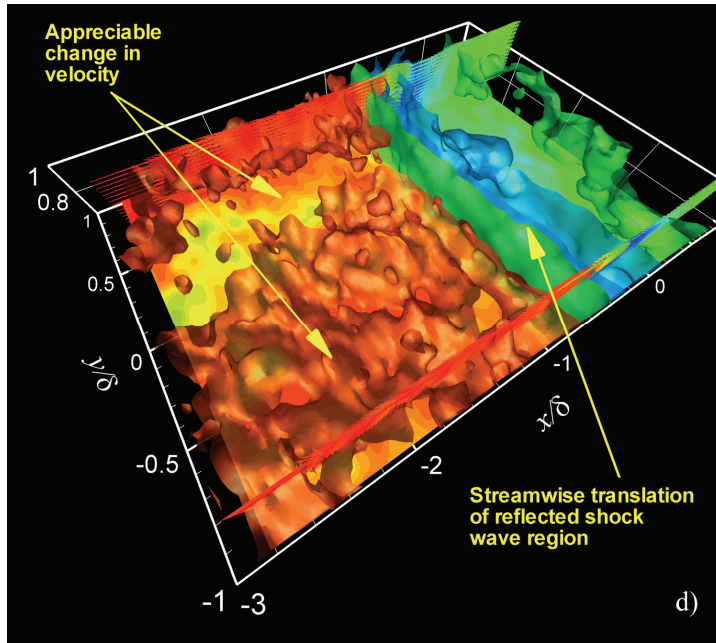


FIGURE 7.9. Volumetric representations of the instantaneous structure of the interaction: upper region ( $z/\delta=0.6-1.0$ ). Isosurfaces of streamwise velocity are shown: high-speed in red ( $0.99U_\infty$ ), intermediate velocity in green ( $0.85U_\infty$ ), and low-speed in blue ( $0.75U_\infty$ ). Velocity vectors are shown flooded with instantaneous streamwise velocity. The subvolume indicated in figure 7.9(a) by the yellow box is rendered in greater detail in figure 7.10. Modified from Humble *et al.* (2008).

The results at this level portray a rather different type of flow organization than observed closer to the wall. Although streamwise-elongated regions of relatively low-speed fluid can still be observed within the boundary layer at this height (e.g., figure 7.9(b)), such observations are not as common in this dataset. This is in agreement with the observations made by Ganapathisubramani (2007), who obtained sequences of images of their compression ramp interaction using PLS at  $z/\delta=0.7$ , and also found that the strips of uniform momentum in the upstream boundary layer were not as prevalent compared with measurements closer to the wall. These authors still observed, however, occasional long structures extending several boundary layer thicknesses in the streamwise direction.

In the present results, there is also evidence of a significant fluid exchange that takes place between the outer part of the boundary layer and free-stream flow. Based on the high-speed isosurface ( $0.99U_\infty$ ), it appears that at the boundary layer edge, the turbulent/nonturbulent interface may be characterized as a highly corrugated surface. This is consistent with the observations of Smith & Smits (1995), who visualized the structure of supersonic boundary layers using Schlieren and Rayleigh scattering, and characterized the outer layer as consisting of an array of regularly-spaced uniform low-density bulges separated from a uniform higher-density free-stream by a sharp, instantaneously ragged interface. The average velocity inside the high-vorticity regions in figure 7.9 is close to the free-stream ( $\sim 0.9U_\infty$ ), consistent with observations of Smith & Smits (1995), who report that large-scale structures in the outer region convect at around  $0.9U_\infty$ .

To illustrate more clearly some typical instantaneous flow structure in the outer part of the boundary layer, the subvolume indicated by the yellow box in figure 7.9(a) is rendered in greater detail in figure 7.10. The results show semitransparent vorticity magnitude isosurfaces for  $|\omega|\delta/U_\infty=0.5$ , half the value for the appropriate visualization of vortical structures closer to the wall, along with velocity vectors in a convective frame of reference of  $0.8U_\infty$ . Flooded streamwise velocity contours are also shown in the streamwise–spanwise plane. A large-scale rotating bulge can be observed in the centre-left of the figure, as indicated by tangent vectors in the streamwise–wall-normal plane. This swirling pattern is approximately  $0.5\delta$  in length and has a convection velocity of around  $0.8U_\infty$ . The major vorticity component is parallel with the wall and normal to the free-stream direction.

The tomographic data also enable streamlines to be traced out throughout the complete three-dimensional measurement domain. These streamlines are computed within the convective reference frame  $0.8U_\infty$  and are also shown in figure 7.10, coloured by instantaneous streamwise velocity. The instantaneous streamline pattern depicts a large-scale swirling, in the form of a distorted helicoidal bundle of streamlines, which can be seen to pass through the large-scale rotating bulge, and quickly degenerate outside the vector plane. Although the appearance of such a representation is



obviously sensitive to the way in which it is visualized, the results are consistent with an active boundary layer, which exhibits a large-scale organized structure as it enters the interaction.

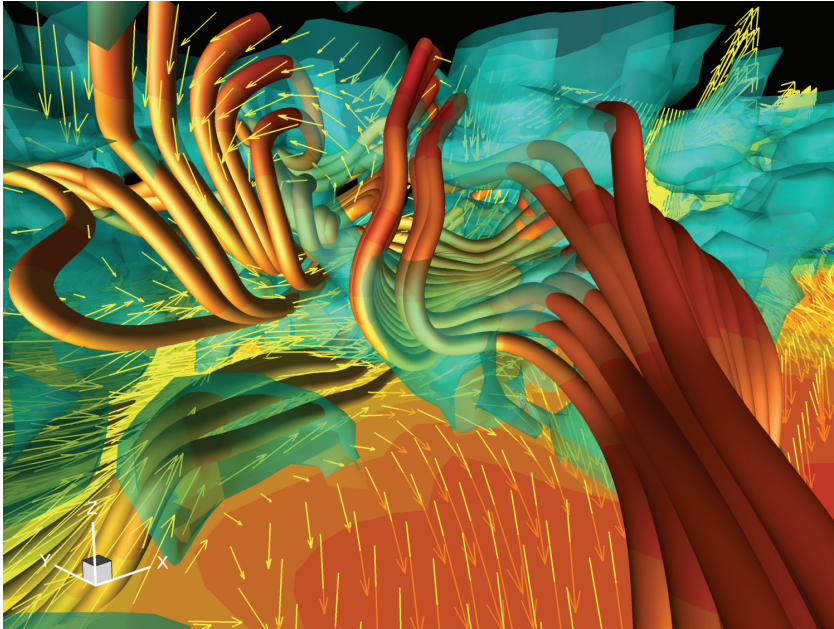


FIGURE 7.10. Instantaneous flow structure of the interaction: upper region ( $z/\delta=0.6-1.0$ ). Semitransparent vorticity magnitude isosurfaces of  $|\omega|\delta/U_\infty=0.5$  are shown. Velocity vectors with a convective velocity of  $0.8U_\infty$  are shown in two planes; at  $y/\delta=0.5$  and  $z/\delta=0.6$ , the latter is flooded with streamwise velocity contours. Streamlines are computed within this convective reference frame. From Humble *et al.* (2008).

Such a large-scale feature has been illustrated by Smith & Smits (1995) in the outer layer of their supersonic boundary layer, which they refer to as a ‘large-scale bulge’, and is reproduced for comparison in figure 7.11, from Smith & Smits (1995). These authors discuss how such bulges may support Reynolds shear stress by acting as a pump, drawing high-momentum fluid down into the boundary layer. Indeed, ingested fluid can be seen both upstream and downstream of the structure in figure 7.10, extending from the undisturbed boundary layer edge ( $z/\delta = 1.0$ ) deep into the boundary layer ( $z/\delta = 0.6$ ), as part of the intermittency process.

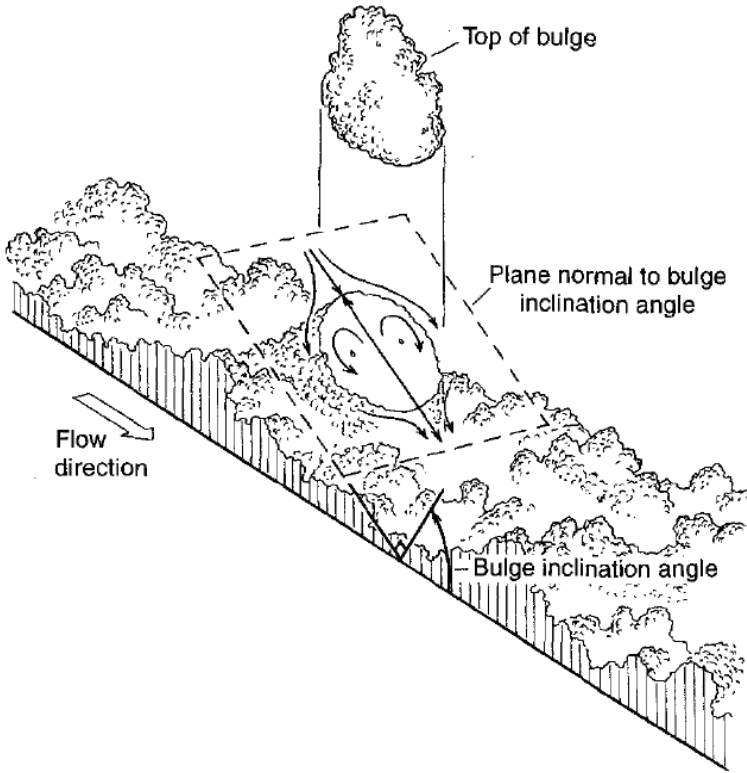


FIGURE 7.11. Suggested structure of a turbulent bulge in a supersonic boundary layer. From Smith & Smits (1995).

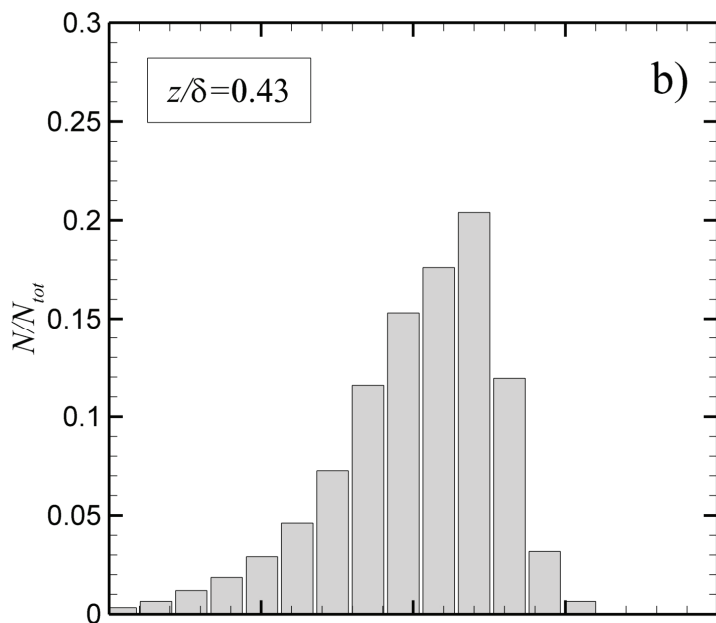
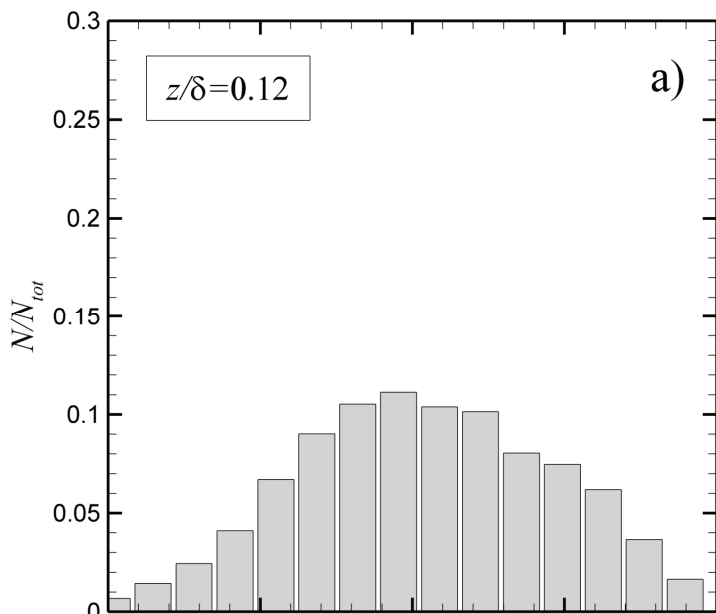
The effect of these motions on the spatial organization of the reflected shock wave region is important. All figure parts of figure 7.9 show that the reflected shock wave pattern is more uniform in the spanwise direction, and appears to undergo a relatively smaller streamwise motion than observed closer to the wall. However, streamwise-elongated regions of relatively low-speed fluid can still occasionally be observed at this height, which noticeably affect the reflected shock wave region. Overall, these results are consistent with the observations made by Dupont *et al.* (2006) in their incident SWTBLI, who recorded hot-wire signals and wall-pressure fluctuations simultaneously at the reflected shock wave's mean position, and were able to deduce that the reflected shock wave's length of excursion decreases with distance from the wall.

## 7.6 Statistical Analysis

In order to substantiate some of the observations made above, a statistical analysis is carried out. To first characterize the reflected shock wave's behaviour with distance from the wall, the streamwise position of velocity isosurfaces  $(x-x_{mean})/\delta$  (where  $x_{mean}$  is the mean position) is used as a surrogate for the streamwise position of the reflected shock wave. This is similar to the approach of Ganapathisubramani *et al.* (2007) who computed the instantaneous separation point using a velocity threshold criterion. Velocity thresholds of  $0.75U_\infty$ ,  $0.8U_\infty$ , and  $0.85U_\infty$  are used to characterize the shock wave position at  $z/\delta=0.12$ ,  $0.43$ , and  $0.82$ , respectively. The qualitative trends of the results to be discussed do not change with small variations in the threshold values chosen.

At each spatial location where a velocity vector is obtained, an ensemble of order 200 isosurface positions is determined. From this ensemble, discrete PDFs are generated, which indicate the relative probability of the isosurface's  $i$ th streamwise position  $(x/\delta)_i$  falling within a range  $(x/\delta)_i < (x/\delta)_{i+1} < (x/\delta)_i + \Delta(x/\delta)$ , where  $\Delta(x/\delta)$  is the bin width of the PDF, taken as approximately 0.05 in the present study. A series of PDFs are shown in figure 7.12 computed for all spanwise locations at the various distances from the wall.

Figure 7.12(a) suggests that close to the wall at  $z/\delta=0.12$ , the reflected shock wave region undergoes a streamwise motion that is of the order of the boundary layer thickness. In contrast, the PDFs in figures 7.12(b, c) appear much narrower, consistent with the streamwise extent of the reflected shock wave's motion decreasing with distance from the wall. Note also that the mean and median positions do not precisely coincide with each other.



(see figure caption on next page.)

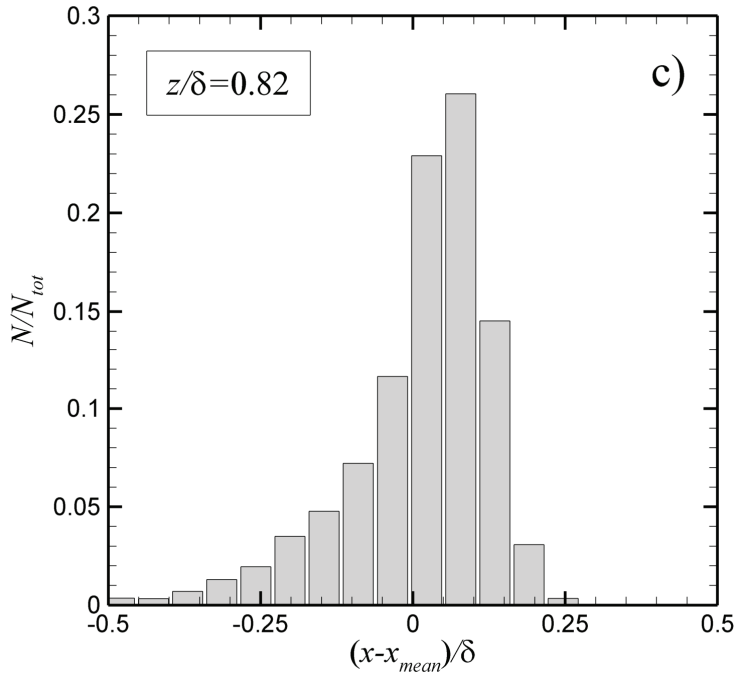


FIGURE 7.12. Discrete PDFs of the reflected shock wave surrogate  $(x-x_{mean})/\delta$ . (a)  $z/\delta=0.12$ , (b)  $z/\delta=0.43$ , (c)  $z/\delta=0.82$ . Modified from Humble *et al.* (2008).

To establish a statistical link between the reflected shock wave and incoming boundary layer, streamwise velocity fluctuations within the incoming boundary layer  $u'/U_\infty$  are compared with the reflected shock wave surrogate's streamwise position, as carried out by Ganapathisubramani *et al.* (2007). The streamwise location  $x/\delta=-2.7$  was chosen to obtain the velocity data for each spanwise location, although the results to be discussed were found to be insensitive to small variations in the streamwise location chosen. This is consistent with the long tails found in the streamwise velocity autocorrelation function (see e.g., Ringuette *et al.* 2008; Hutchins & Marusic 2007; Ganapathisubramani *et al.* 2006).

Figure 7.13 shows joint PDFs of  $u'/U_\infty$  and  $(x-x_{mean})/\delta$ , at the various distances from the wall. Figure 7.13(a) indicates that close to the wall at  $z/\delta=0.12$ , the streamwise velocity fluctuation range within the incoming boundary layer is approximately  $-0.1 < u'/U_\infty < 0.1$ , corresponding to a net velocity fluctuation range of  $0.2U_\infty$  ( $100 \text{ ms}^{-1}$ ),

in agreement with the range reported by Ganapathisubramani *et al.* (2007). It is evident that the contours of equiprobability appear elliptical, with the major-axis of the ellipse inclined with the abscissa, again consistent with the observations made by Ganapathisubramani *et al.* (2007). The reader should note that the same trends were found when the data were normalized by their RMS values. This suggests that when negative streamwise velocity fluctuations are present within the incoming boundary layer ( $u' < 0$ ), then the reflected shock wave is more likely to be upstream of its median position, and when positive streamwise velocity fluctuations are present within the incoming boundary layer ( $u' > 0$ ), then the reflected shock wave is more likely to be downstream of its median position.

The correlation coefficient between  $u'/U_\infty$  and  $(x-x_{mean})/\delta$  at this distance from the wall ( $z/\delta=0.12$ ) is about 0.5, in agreement with the value of 0.4 reported by Ganapathisubramani *et al.* (2007) (taken at  $z/\delta=0.16$ ), as well as the value of about 0.5 reported by Wu & Martin (2008), who carried out the same type of analysis in their DNS study of a compression ramp interaction. Such a trend is qualitatively consistent with the results obtained by Beresh *et al.* (2002) in their compression ramp interaction, who carried out a conditional analysis on planar PIV data in the streamwise-wall-normal plane and found that positive fluctuations within the incoming boundary layer corresponded with a downstream shock position, and vice versa.

Figures 7.13(b, c) show that the streamwise velocity fluctuation range decreases with distance from the wall to about  $-0.1 < u'/U_\infty < 0.05$  by  $z/\delta=0.82$ , corresponding to a net fluctuating velocity range of  $0.15U_\infty$  ( $75 \text{ m s}^{-1}$ ). The contours of equiprobability now appear much more circular and compact, and this is accompanied by a decrease in the correlation coefficient to below 0.4. However, lobes of probability within the  $u' < 0$  and  $x < x_{mean}$  region still persist at this distance from the wall, associated with the occasional passage of relatively low-speed regions throughout the interaction, as can be seen in figure 7.9(b) for instance. Observe how the distance between adjacent lines of equiprobability rapidly decreases for  $u' > 0$  and  $x > x_{mean}$ , indicating that the probability of observing a relatively high-speed region and downstream reflected shock wave position decreases with distance from the wall.

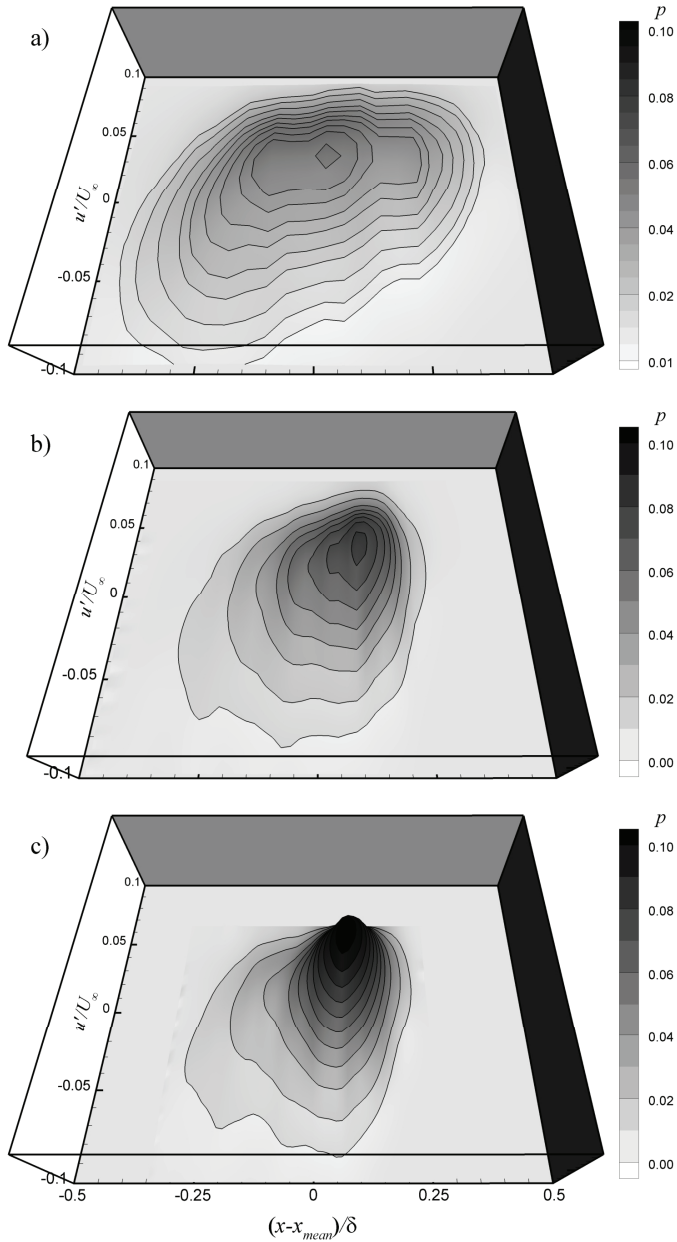


FIGURE 7.13. Relationship between incoming boundary layer velocity fluctuations  $u'/U_\infty$  and streamwise position of the reflected shock wave surrogate  $(x-x_{mean})/\delta$ . Data taken at  $x/\delta=-2.7$  for each spanwise location. Joint PDFs of  $u'/U_\infty$  and  $(x-x_{mean})/\delta$ . (a)  $z/\delta=0.12$ , (b)  $z/\delta=0.43$ , (c)  $z/\delta=0.82$ . Modified from Humble *et al.* (2008).

## 7.7 POD Analysis

Following a similar analysis as for the planar results, the tomographic PIV volumes are decomposed using the POD. Figure 7.14 presents the streamwise component of the first four global eigenmodes. Their modal number and relative energy content are shown inset. Recall that since the temporal coefficients associated with each eigenmode for a particular realization can be either positive or negative, only the relative changes of sign within an eigenmode are important.

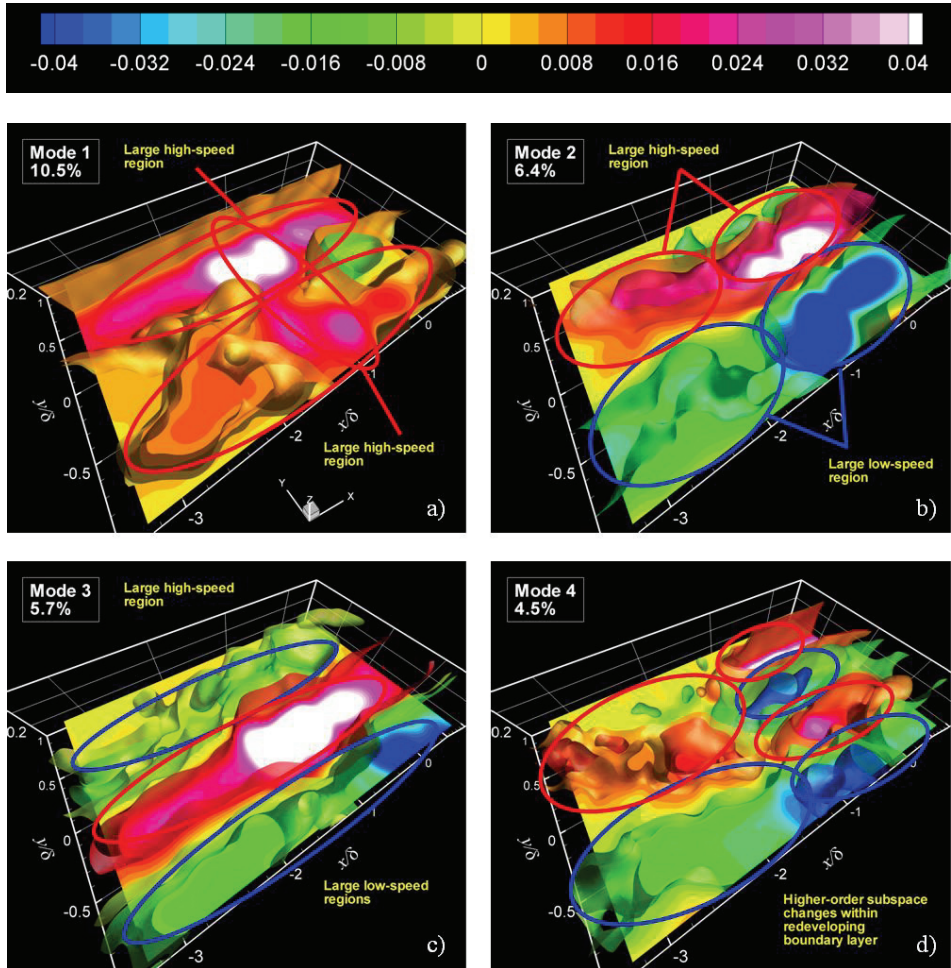


FIGURE 7.14. Tomographic POD eigenmodes for  $u'/U_\infty$ . Modal energy is shown inset. (Note: modes  $\geq 2$  show  $2u'/U_\infty$ ).



The first eigenmode in figure 7.14(a) portrays a broad spanwise zone of velocity fluctuations within the reflected shock wave region that is energetically correlated with velocity fluctuations within the incoming boundary layer. The superposition of these fluctuations onto the mean flow returns a streamwise displacement of the reflected shock wave region; a behaviour that can be observed in the tomographic instantaneous realizations. The translation component is therefore the pattern that contains the largest fraction of the total energy, consistent with the observations of Wu & Martin (2008), who found that the amplitude of the shock motion in the streamwise direction was twice that of the spanwise wrinkling.

The second eigenmode in figure 7.14(b) shows two large-scale regions of uniform opposed velocity, oriented parallel to the wall, and elongated in the streamwise direction. The width of these regions is approximately  $\delta$ , and they extend the streamwise length of the measurement domain. Note the increase in fluctuation magnitude throughout the interaction, consistent with the observation that the interaction acts like an amplifier for the turbulent fluctuations. The superposition of these fluctuations onto the mean flow returns an undulating pattern of the reflected shock wave region; a behaviour that can be observed in the instantaneous realizations. This eigenmode therefore captures the spanwise rippling component of the reflected shock wave patterns.

The third eigenmode in figure 7.14(c) shows three large-scale regions, each approximately  $0.6\delta$  wide, extending the streamwise length of the measurement domain. This eigenmode therefore appears to represent the higher-order harmonics of the spanwise rippling component. Wu & Martin (2008) also reported a superposition of wave-lengths associated with the spanwise rippling component of their shock wave in a compression ramp interaction. The notion of a supposition of streamwise translation and spanwise rippling motions may well be a general result of the large-scale shock wave unsteadiness.

In contrast, the fourth eigenmode in figure 7.14(d) shows distinct velocity regions of alternating sign within the redeveloping boundary layer, demonstrating that qualitative changes may take place locally within an eigenmode. Such features are also observed in the planar

POD eigenmodes and are thought to be associated with a vortex shedding process that is observed to take place downstream of the separation bubble (see also Dupont *et al.* 2006). Taken together, the eigenmodes may be viewed as a family of modes, each containing subspace representations of the phenomenology observed in the instantaneous realizations.

On a final note, it is worth mentioning that in general, although POD is well-known to be the best in the energy norm, it may not be the best in the dynamical sense. For instance, Gibson *et al.* (2008) insist that the solutions considered should be exact solutions of the Navier-Stokes equations because low-order models reproduce some qualitative features, but their quantitative accuracy is often uncertain. This posed problems for instance, in the truncation specification in the models formulated by Aubry *et al.* (1988), who wished to capture the major aspects of the ejection and bursting events associated with the streamwise vortex pairs, experimentally observed in the classical experiments of Kline *et al.* (1967), but who had to specify which modes were to be used in the analysis.

In the present study, clearly the first POD eigenmode, or indeed any other mode considered individually, is not an exact solution of the Navier-Stokes equations, even though they satisfy the boundary conditions, and it is not obvious how these modes are inter-related given the complicated state-space relationship between the temporal coefficients. On the other hand, the present eigenmodes do appear to be qualitatively consistent with what is observed in the instantaneous realizations, and with what has been reported elsewhere in literature. The reader should therefore not take the eigenmodes presented in this thesis uncritically and at face value, but rather view them as statistical representations of what is observed within the instantaneous and statistical results, keeping in mind their definition and interpretation.

# CHAPTER


# 8

# TEMPORAL

# ORGANIZATION

---

## 8.1 Introductory Remarks

O far the discussion has focused exclusively on the spatial characterization of the interaction's unsteady flow organization, of which the reflected shock wave region and incoming boundary layer have been shown to play important roles. Information is still lacking, however, on the temporal characteristics, such as time-scales and characteristic frequencies etc. Furthermore, given the fact that the interaction is only intermittently separated, and we wish to make references and statements of a large-scale relatively low-frequency shock wave unsteadiness with literature, it is crucial to have an idea of the time-scales of the shock unsteadiness to check if these low-frequencies are effectively developed in the present interaction.

To shed some light on these aspects, HWA measurements are carried out within the reflected shock wave region. A characterization of the associated mass-flux time signal is first made in a spectral sense. We then analyze the signal using tools from nonlinear dynamical systems theory to make further statements regarding the temporal organization of the data. Before proceeding, it is worth mentioning that clearly we are courting difficulties by assuming that a time series signal within the reflected shock wave region represents the overall large-scale dynamics of the interaction. Furthermore, the lack of simultaneous multiple-point measurements, such as provided by an array of surface pressure transducers for instance, precludes the often-used box-car representations and conditional sampling techniques typically employed in shock wave analyses (see e.g., Erengil & Dolling 1993). We merely state that the focus of the large-scale unsteadiness is on the reflected shock wave, and that this is in some sense portrayed by our time series signal, recognizing that we are observing only one aspect of a complex dynamical process.

## 8.2 Time Series History

As the motivating prelude, a sample time series history of the normalized streamwise fluctuating mass-flux signal within the reflected shock wave region at  $x/\delta=-1.8$  and  $y/\delta=0.2$  ( $y=4$  mm) is shown in figure 8.1. This location was chosen because the flow here is supersonic, which avoids the complexities of HWA in transonic flow, but is sufficiently close to the wall to make comparisons with other results from literature. Details of the hot-wire experiments are provided in §5.2.4. Naturally, other measurements within the undisturbed boundary layer at the same distance from the wall and farther away from the wall were also made, but no evidence of the low-dimensional behaviour reported in what follows was observed (see discussion in §8.4.1 for further details). We therefore restrict our attention to discussing this time series.

Returning to figure 8.1, only the first 12,000 data points are shown for clarity. The mass-flux here, and in what follows, has again been normalized by the local mean density  $\bar{\rho}$  and free-stream velocity  $U_\infty$ , such that  $(\rho u)' / \bar{\rho} U_\infty \sim u' / U_\infty$ , recognizing that  $\rho' = 0$  may not be strictly valid in the presence of shock waves. The mean density within the

reflected shock wave region was estimated from the study of van Oudheusden (2008), who has extracted the mean static pressure and temperature fields from the present interaction. The present procedure is only made for the interpretation of what follows, in keeping with the PIV results; it does not affect the conclusions to be drawn. It can be seen that the fluctuating velocity signal within the interaction exhibits a broad range of frequencies and appears at first glance to have a random-looking behaviour (c.f. figure 1.10). It is the underlying structure of this signal that will form the principal basis of this chapter.

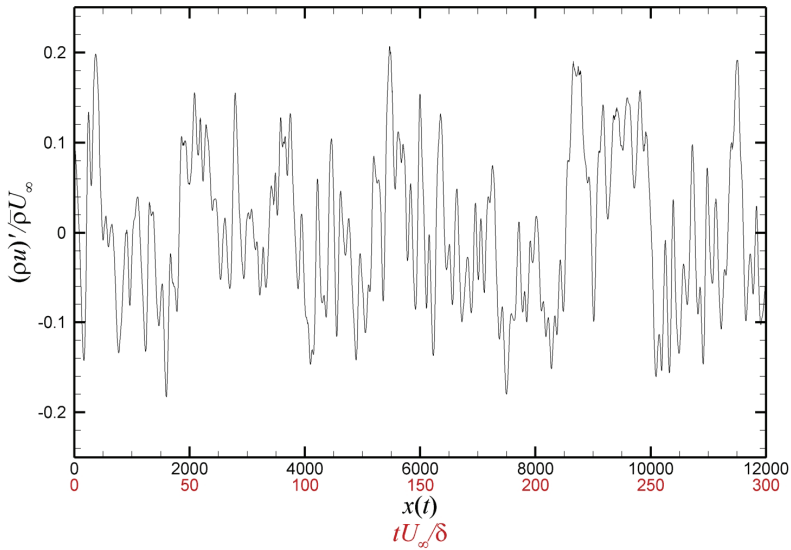


FIGURE 8.1: Sample time series history of the normalized streamwise mass-flux signal within the interaction. Data taken at  $y/\delta=0.2$ . The first 12,000 data points are shown for clarity.

### 8.3 PSD Distributions

Figure 8.2 presents the premultiplied power spectra  $k_x \Phi_{uu}$  against frequency  $f$ . Results are also shown within the undisturbed boundary layer for comparison. The PSDs confirm that both signals exhibit a broad range of frequencies. The most energetic frequencies within the undisturbed boundary layer and reflected shock wave region occur in the kHz range, but the trend within the reflected shock wave region is

clear: the most energetic frequencies have shifted, relative to the undisturbed boundary layer spectrum, towards significantly lower values and there is an attendant increase in amplitude, although this latter observation is dependent on the total energy used to normalize the spectra (c.f. figure 1.14). Peak energetic frequencies occur within the undisturbed boundary layer and reflected shock wave region of around 10 kHz and 1–3 kHz, respectively, or in nondimensional terms, about  $0.4U_\infty/\delta$  and  $0.04\text{--}0.12U_\infty/\delta$ , respectively.

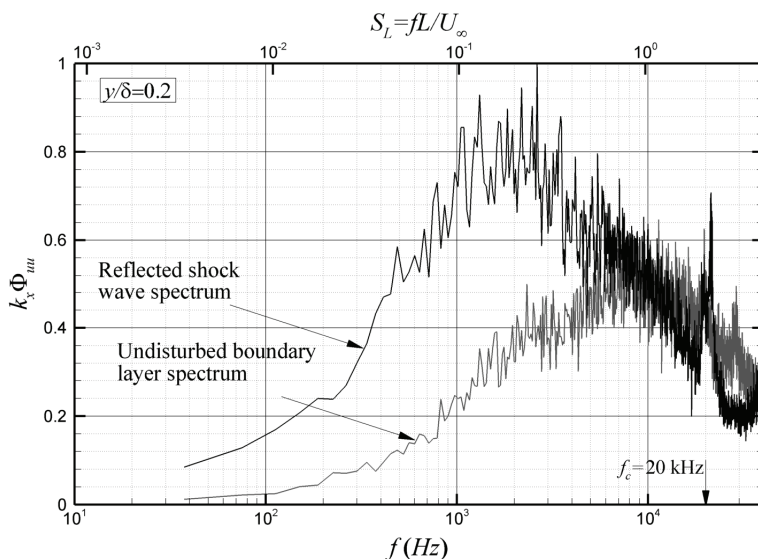


FIGURE 8.2: Premultiplied power spectra  $k_x \Phi_{iii}$  against frequency  $f$ . Undisturbed boundary layer spectrum (*grey*), and reflected shock wave region spectrum (*black*). Data taken at  $y/\delta=0.2$ . Spectra are normalized by the total energy. Cut-off frequency  $f_c=20$  kHz is shown for comparison.

This substantiates the well-known experimental observation that frequencies within the reflected shock wave region are at least an order of magnitude lower than the characteristic boundary layer frequency  $U_\infty/\delta$  (see also e.g., Dussauge *et al.* 2006 for a further discussion and compilation of the data available in literature). Interestingly, the 1–3 kHz range within the reflected shock wave region corresponds to about the  $10\delta$  wave-lengths in the power spectrum closer to the wall at  $y/\delta=0.1$  (c.f. figure 5.7). It may therefore be that such structures are lifted up in the reflected shock wave region.

The values of the most energetic frequencies within the reflected shock wave region compare favourably with the dual-PIV results of Souverein *et al.* (2008), who considered the present interaction at Mach 1.69, and determined dominant frequencies of around 1–1.5 kHz within the reflected shock wave region, based on the spatial distribution of the correlation coefficient of the streamwise velocity fluctuations. Erengil & Dolling (1993) also report energetic frequencies within the separation shock wave of their compression ramp interaction within the range 0.3–1 kHz, and Thomas *et al.* (1994) report about 1 kHz in their compression ramp interaction.

To make fair comparisons with literature, however, the frequencies must be normalized. Shown also in the figure for comparison is therefore the Strouhal number  $S_L = fL/U_\infty$ , where  $L$  is the length of the interaction zone, as used by Erengil & Dolling (1991) in their compression ramp interaction at Mach 5 based on subsonic scaling. Following the approach of Dupont *et al.* (2006),  $L$  is defined in the present interaction as the distance between the extrapolated wall impingement points of the reflected and incident shock waves, which gives  $L/\delta = 2.27$  ( $L = 45$  mm). This may be compared with the results of Dupont *et al.* (2006), who obtain  $L/\delta = 4.18$  for their  $\theta = 8^\circ$  shock reflection case at Mach 2.3 and  $Re_\theta = 6.9 \times 10^3$ . In addition, Dussauge *et al.* (2006) define the shock oscillation amplitude as  $L_{ex}$ , and have summarized its value for various types and strengths of interactions. The present reflected shock oscillation amplitude inferred from the PIV and Schlieren results is loosely estimated to be  $L_{ex}/\delta = 0.5$ – $1.0$ , which returns  $L_{ex}/L = 0.22$ – $0.44$ . This is consistent with the results reported by Dussauge *et al.* (2006), who state the range  $0.26 < L_{ex}/L < 0.34$  for shock reflection experiments at Mach 2.3.

Although the present values of the most energetic frequencies within the reflected shock wave region are similar to other studies, the corresponding Strouhal number is within the range  $S_L = 0.1$ – $0.27$ , about three to ten times larger than the energetic Strouhal numbers reported elsewhere. For example, Dussauge *et al.* (2006) have compared values of  $S_L$  for several configurations in literature where experimental data is available, including compression ramp and blunt fin interactions, as well as over-expanded nozzles. A compilation of the data revealed that for a wide range of experimental conditions,  $S_L$

grouped the experiments together for Strouhal numbers between about 0.02 and 0.05. The present value of  $S_L$  is therefore unexpected.

The reader is reminded, however, that the present interaction is only *intermittently* separated, perhaps remaining fully attached on average, and so this could be a possible explanation for the higher values of  $S_L$  reported here. Indeed, Dussauge *et al.* (2006) note that in their particular case,  $L$  is a reasonable approximation of the separation length, and that the situation is similar for the other configurations considered. In the present interaction, however, the mean separation length does not exist, and the use of  $L$  as the appropriate length-scale for the Strouhal number may not therefore be appropriate.

As a possible alternative, we introduce the length-scale  $L_{RMS}$  in the present study, as the RMS of the (largest) instantaneous separation bubble length, which includes the cases when no bubble occurs. The bubble lengths were estimated from the planar PIV SWTBLI snapshots. This returns  $L_{RMS}/\delta=0.28$ , and results in a new Strouhal number range of  $S_L=0.01-0.03$ . This is in much better agreement with the results reported in literature. The use of the length of the interaction  $L$  as an appropriate length-scale for the Strouhal number may not therefore be appropriate for intermittently separated flows that are attached on the mean. The reader may note, however, that  $L_{ex}$  no longer scales with our new length-scale  $L_{RMS}$ . In the absence of further results the data therefore remain provocative.

Nevertheless, the fact remains that the reflected shock wave region is dominated by energetic frequencies that are an order of magnitude lower than those within the undisturbed boundary layer at the same distance from the wall, consistent with what has been reported in literature. However, as noted by Guckenheimer (1986), the power spectrum is limited as a tool for distinguishing between different *types* of dynamics, since it only provides information on the spectral content. In seeking tools that provide additional insight into the interaction's dynamics, we turn to nonlinear time series analysis.



## 8.4 Nonlinear Time Series Analysis

### 8.4.1 Attractor Reconstruction

With the necessary mathematical background established in chapter 4, we first begin by representing the signal as an attractor in state-space to show the signal's asymptotic (long-term) behaviour, and because this will greatly facilitate the techniques that follow. Recall that the hot-wire signal is denoted by  $x(t)$ ,  $t=1, \dots, N$  and that it can be viewed as an attractor in state-space using  $\mathbf{x}(t)=\{x(t), x(t+\tau), \dots, x(t+n\tau)\}$ . Since we are interested in length-scales of several  $\delta$ , and since the data are affected by the frequency response of the wire up to  $1.3\delta$ ,  $x(t)$  is low-pass filtered using a second-order regression. As noted by Elsinga (2008), because the regression is a nonlinear filter, the modulation transfer function depends on the input signal, of which there is no established filter-length. We therefore estimate the filter wave-length as  $2\delta$ , a reasonable approach at  $\gamma/\delta=0.2$ , where we are interested in wave-lengths of typically  $2-10\delta$  (see premultiplied spectra within the undisturbed boundary layer §5.2.4). It must be stressed that the results do not change significantly for filter-length changes  $O(\delta)$ , and the filtering does not affect the overall conclusions to be drawn. The main motivation for its implementation was to ease the visualization of the attractors that follow.

To specify a suitable value of time-delay  $\tau$ , we compute the averaged mutual information  $I(\tau)$  distribution. Figure 8.3 shows the distribution of  $I(\tau)$  for various time-delays  $\tau$ . Based on this distribution, we obtain an optimum time-delay  $\tau_{opt}=37$ , as the first minimum, where  $\tau$  is shown in the number of sample points. This optimum time-delay corresponds to a frequency of 27 kHz, or a length-scale of about  $\delta$ , when a local convective velocity of  $U_c \sim 400 \text{ m s}^{-1}$  is used. This value may be compared with the time required for the autocorrelation to reach  $1/e$  for instance, which returns  $\tau_{opt}=66$ . This discrepancy is attributed to the general (nonlinear) dependence of mutual information, in contrast to the linear dependence of the autocorrelation, and such a difference is qualitatively consistent with the comparisons between mutual information and autocorrelation made by Martinerie *et al.* (1992) among others, considering various dynamical systems.

Although it appears that statistical convergence is not completely reached in the present results, the optimum time-delay was found to always remain within the range 30–50 data points when varying the number of data points considered in the dataset, even by orders of magnitude. We can therefore assure ourselves that the same structure of the optimum attractor (to be shown shortly) is always observed.

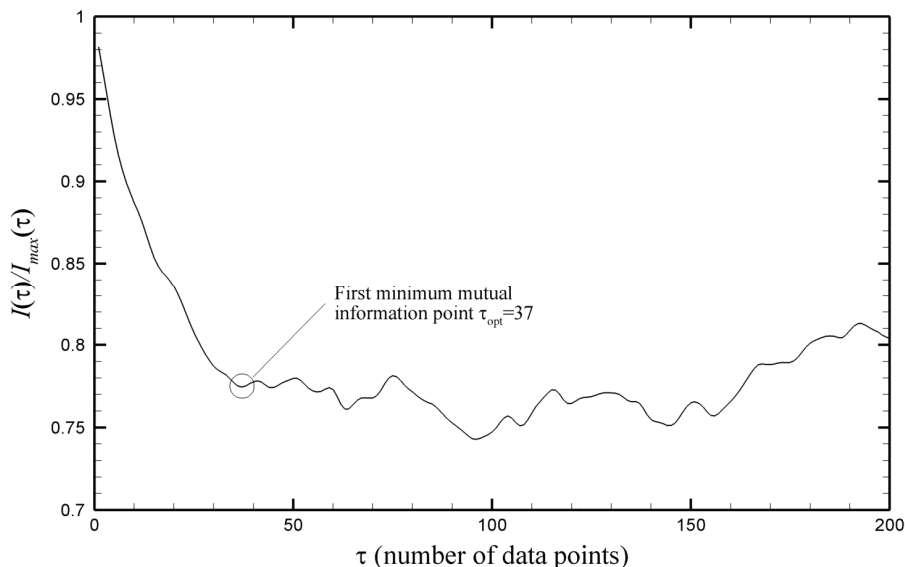
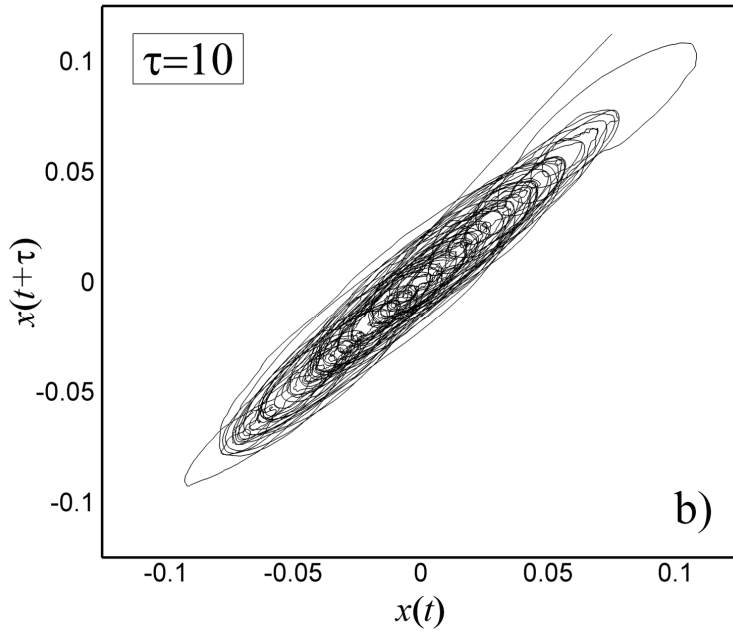
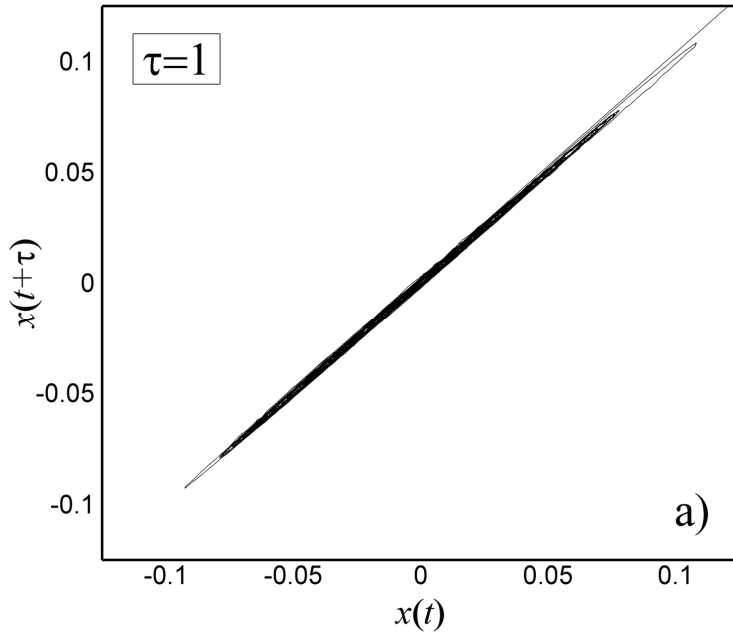
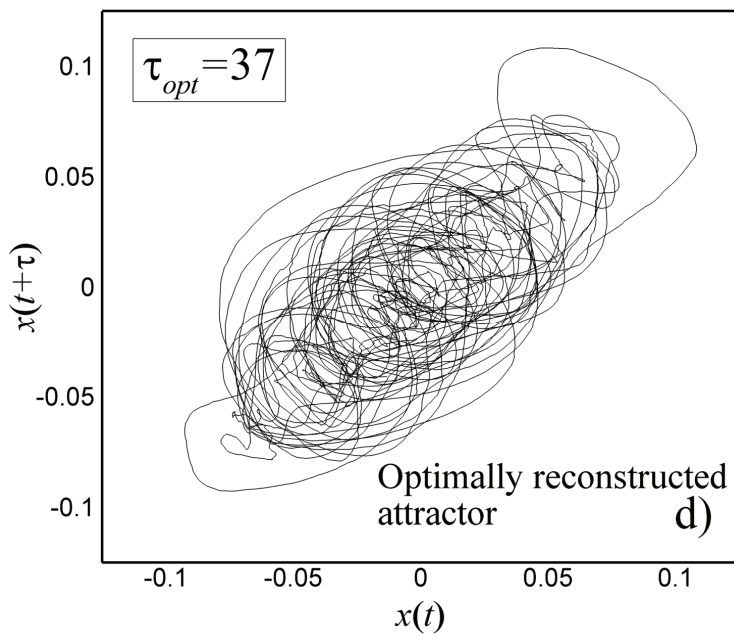
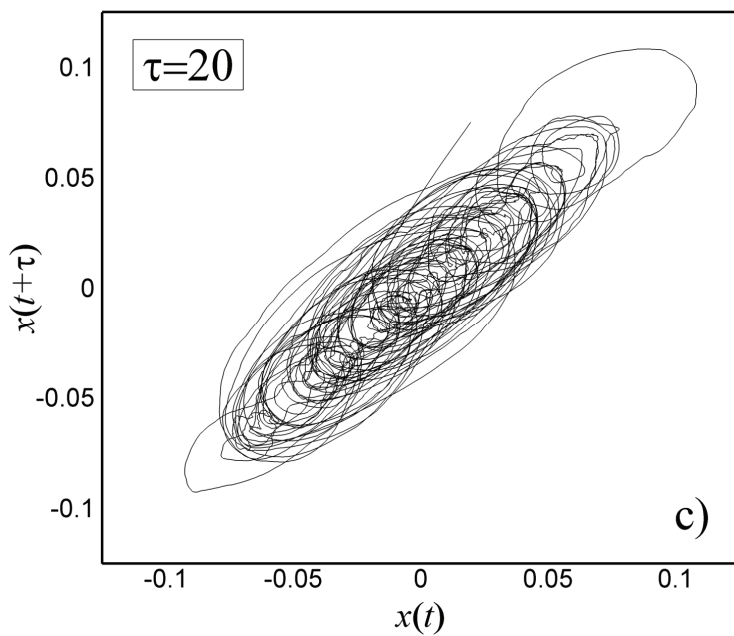


FIGURE 8.3: Distribution of the mutual information  $I(\tau)$ . The first minimum is used to specify the optimum time-delay  $\tau_{opt}$ , i.e., the time-delay that gives the best estimate of the topological properties of the reconstructed attractor.

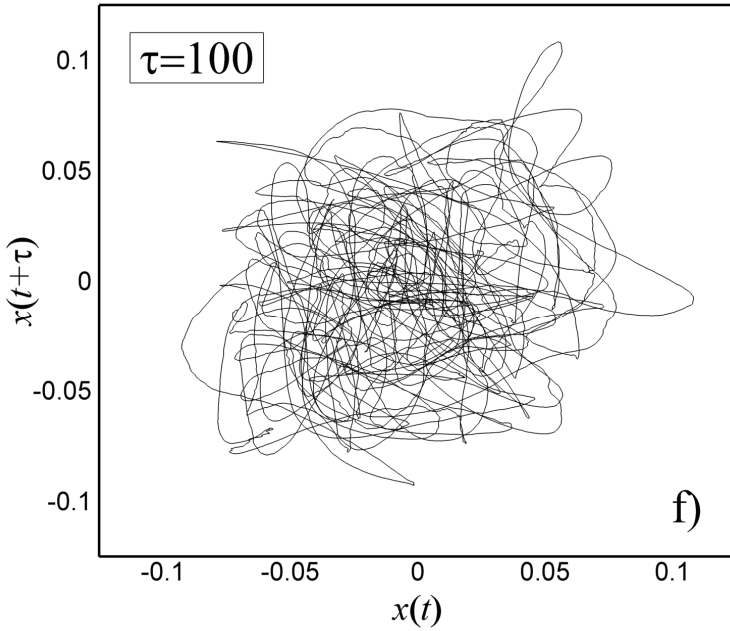
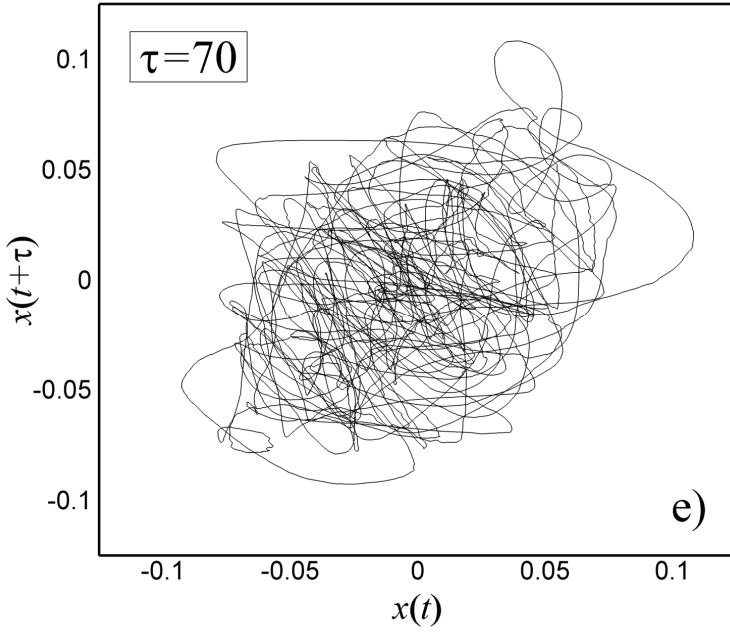
Using  $\tau_{opt}$ , we can construct the vector  $\mathbf{x}(t)$  from  $x(t)$  to reconstruct the attractor. The results for the first 12,000 points are shown in figure 8.4, where the original signal  $(\rho u)'$  is divided by  $\bar{\rho} U_\infty$ , such that  $(\rho u)' / \bar{\rho} U_\infty \sim u' / U_\infty$ . For the purposes of illustration, other arbitrary values of time-delay are shown to reveal how the attractor unfolds within its embedding space.



(see figure caption on next page.)



(see figure caption on next page.)



(see figure caption on next page.)

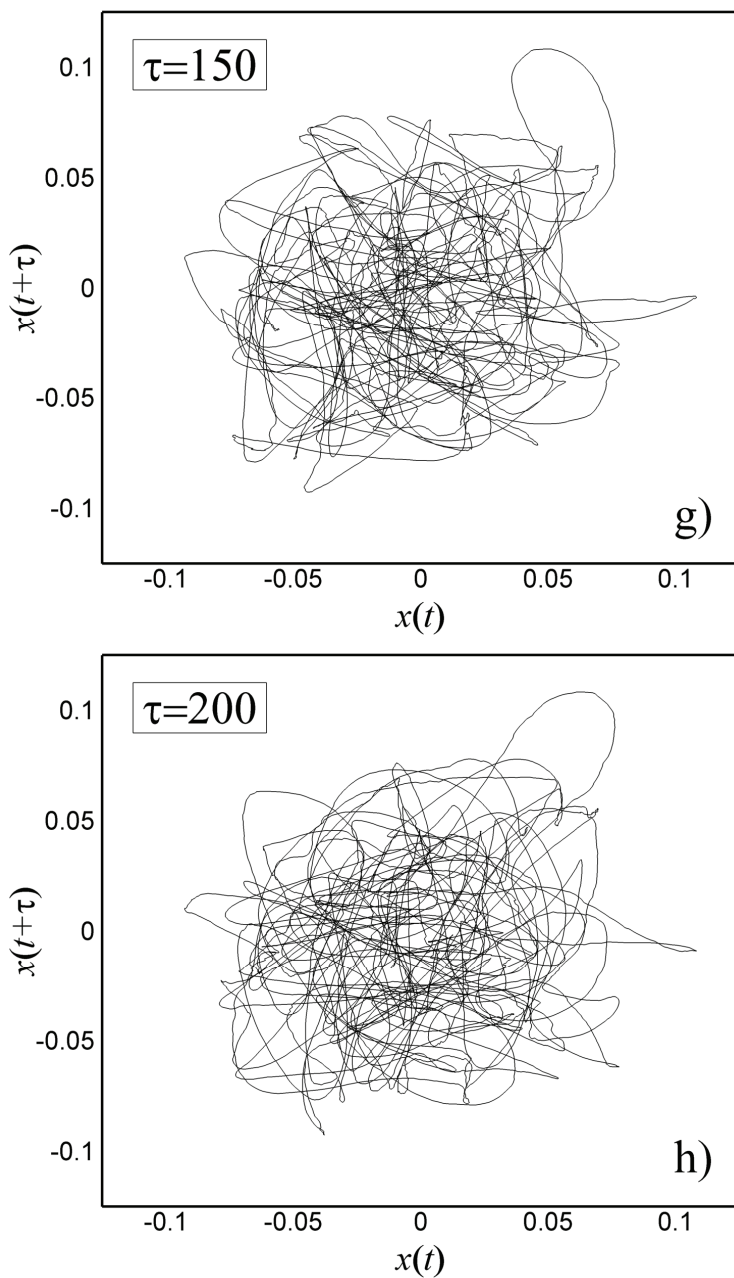


FIGURE 8.4: A series of reconstructed attractors from the signal  $x(t)$ . Note the attractor at the optimum time-delay  $\tau_{opt}$  is the best representation of the topological properties of the reconstructed attractor. The first 12,000 data points are shown for clarity.

It can be seen that for the smallest time-delay considered ( $\tau=1$ ), state-space points form near-linear reconstructions. There is a very high correlation between consecutive state-space points and it is clear that the time-delay is too small to reveal any noticeable structure. For larger time delays, however, we see that the structure of the attractor begins to unfold in embedding space. Specifically, for our optimum time-delay  $\tau_{opt}=37$ , trajectories form a series of circular motions aligned with the  $x(t)=x(t+\tau)$  axis. These motions exhibit a wide range of radii and eccentricities, forming a rich coherent structure. When the trajectories are animated in time, they exhibit an irregular oscillation, but they do not repeat their previous behaviour exactly. Trajectories pass arbitrarily close to one another an arbitrary number of times. Locally nearby trajectories can be observed to separate, but the dynamics remain confined to a finite portion of embedded state-space.

For much larger time-delays ( $\tau>100$ ), the attractor's structure quickly degenerates, becoming obscure for the highest time-delay considered (i.e.,  $\tau=200$ ). This is because this delay has led to vectors whose components are (almost) uncorrelated, and thus the data appear to be randomly distributed within the embedding space. It now becomes clear why we used a prescriptive measure to specify the optimum time-delay. The sharp reader may also note the attenuation of the signal amplitude in state-space due to the filtering (c.f. figure 8.1).

Having established  $\tau_{opt}$ , we can also reconstruct a three-dimensional optimal attractor using the sequenced triplet  $\mathbf{x}(t)=\{x(t), x(t+\tau_{opt}), x(t+2\tau_{opt})\}$ . The results for the first 15,000 points are shown in figure 8.5 for clarity. It can be seen that in three-dimensional embedding space, the attractor retains its structure as observed above. Although difficult to discern in the figure, trajectories in fact tend to spiral around the  $x(t)=x(t+\tau)=x(t+2\tau)$  axis; a behaviour that cannot be easily seen in the two-dimensional representation. The main features of the attractor, however, remain complex, and as will be shown shortly, the complete structure is not adequately unravelled even in three-dimensions.

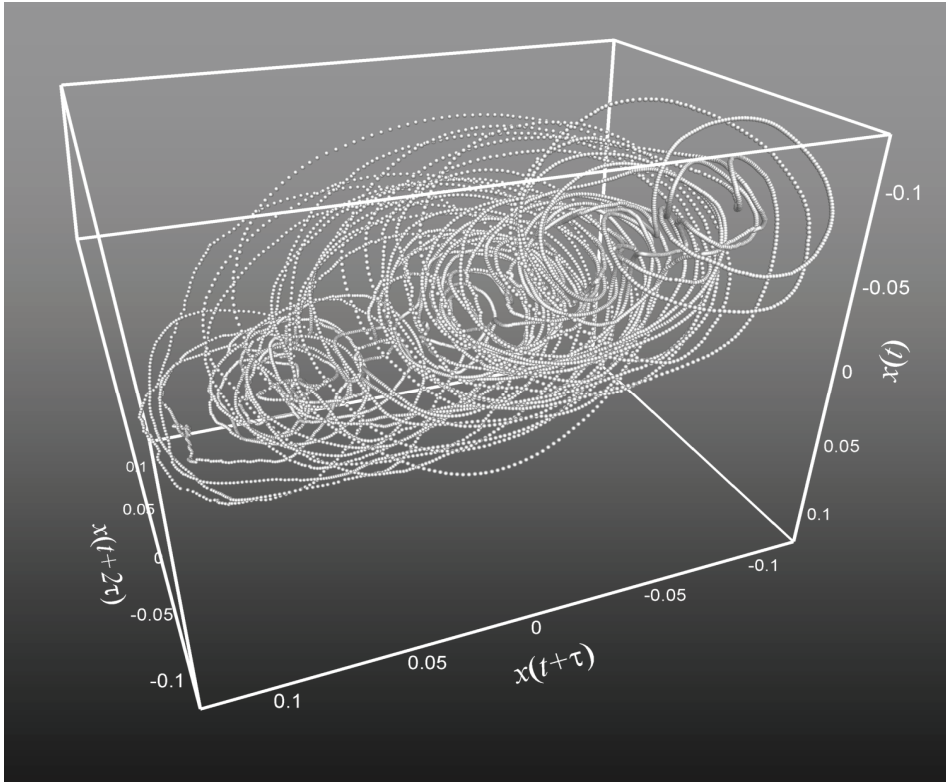


FIGURE 8.5: A three-dimensional view of the optimally reconstructed attractor based on  $\tau_{opt}$ . Results show the sequenced triplet  $\{x(t), x(t+\tau_{opt}), x(t+2\tau_{opt})\}$ . The first 15,000 data points are shown for clarity.

Although the time series history shown earlier has an apparently random-looking behaviour, as well as a broad-band power spectrum; the state-space investigation appears to show an underlying order, which collapses onto a structured attractor that unfolds in an optimum embedding space. Thus, while the PIV results have shown that the reflected shock wave region within the boundary layer has a spatial organization, consisting of a streamwise translation and spanwise rippling, we now see that it also appears to have an asymptotic temporal organization, embodied by the genesis of a (what will later be shown to be chaotic) attractor.



However, given all the approximations made in the analysis (i.e., one-dimensional, filtering, specification of optimal time-delay etc.), the reader must exercise some degree of caution. We therefore keep in mind the interpretations and limitations of the methods used; the representation of the signal as an attractor in state-space merely opens up some interesting possibilities regarding the further characterization of the data. On the other hand, it is important to stress again, that repeating such an attractor reconstruction procedure at the same height within the undisturbed boundary layer, and also farther away from the wall, did not appear to give rise to an attractor with a well-defined structure, whether the data were filtered or not. Only data obtained with the undisturbed boundary layer closer to the wall at  $y/\delta=0.1$  could be said to give rise to a similar attractor structure, which consistent with what is observed in their premultiplied power spectra, and the notion that the very large-scale structures are lifted up into the reflected shock wave region.

To make further statements regarding the dynamical structure of the present signal, we compute the acceleration by differentiating the fluctuating velocity signal using finite differencing. Premultiplying the acceleration with the fluctuating velocity gives us a measure of the work done per unit time on a fluid element, or equivalently its power. Although we are courting difficulties in differentiating filtered experimental data, the overall trends to be discussed are in fact the same for the original signal, and justify the qualitative discussion here.

The phase relationship between the velocity fluctuations and the normalized power within the reflected shock wave region is shown in figure 8.6. Several interesting observations can be made. The phase portrait is characterized by two lobes quasisymmetrical oriented about the vertical axis, which are connected precisely at the origin. (Note that the data within the high-speed regions are particularly sensitive to the filtering.) This portrait can be seen to encompass four distinct regions; namely, region (I) in which a relatively low-speed region decelerates, (II) a relatively high-speed region accelerates, (III) a relatively high-speed region decelerates, and (IV) a relatively low-speed region accelerates. The entire dynamics of the signal may be characterized as being a transition through these four regions in time.

Although difficult to interpret in this ‘static’ representation, animating the data in time was much more instructive. The results reveal that trajectories wander erratically within the phase portrait, swinging back and forth from lobe to lobe, within the four regions shown, and crossing through the origin an arbitrary number of times. A trajectory passes arbitrarily close to its previous path an arbitrary number of times, but never repeats its previous path exactly. Since the magnitude of the power developed within a low- or high-speed region is expected to increase with the magnitude of the velocity fluctuations within the region, any large deviations from the mean velocity typically necessitate larger orbits that appear more inclined when they pass through the origin. This helps explain why no exceptionally elongated orbits along the abscissa are observed.

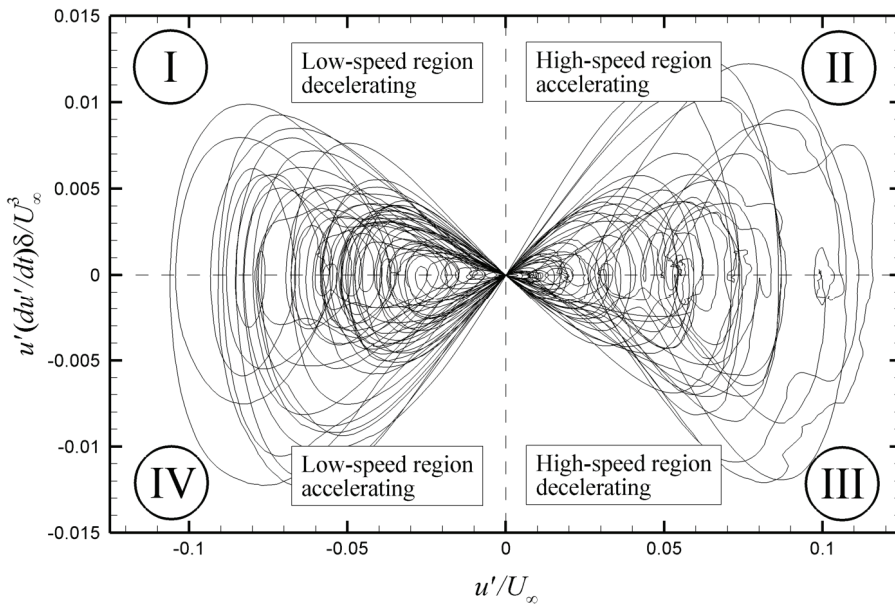


FIGURE 8.6: Phase portrait between the streamwise velocity fluctuations and work done per unit time (i.e., power). The first 12,000 data points are shown for clarity.

Occasionally, several orbits within a lobe will occur, before the trajectory crosses over to the opposite side. This behaviour occurs when a local acceleration, deceleration, and then acceleration takes place (and vice versa), all within a relatively low- or high-speed

region. We speculate that within a relatively low-speed region, this behaviour may well be the footprint of the streamwise alignment of vortical structures, whereas within a relatively high-speed region, this behaviour could be the footprint of the spanwise meandering that has been observed in the tomographic PIV results. Regardless, the fact is that while much of our discussion has implicitly considered the low- and high-speed regions as contiguous features, the reality is more complex, with important local changes velocity taking place within a low- or high-speed region.

Thus, the global dynamics of the signal manifests itself a series of nested lobes on each side of the portrait, which are reminiscent of the nested spirals observed on the optimally reconstructed attractor. Indeed, it is interesting to observe in the present phase representation, that segments of trajectories often exhibit a recurrent passage, as observed on the optimally reconstructed attractor, without use of the embedding procedures described above. It is worth mentioning that the phase portrait here can in fact be qualitatively reproduced using a series of simple sinusoidal signals, which is consistent with the idea that the original signal can be conceived as being a superposition of sinusoids of different frequencies.

Overall, this type of plot is instructive from the point of view that it distinguishes the dynamical behaviour within the low- and high-speed regions. Judging from the symmetry of the portrait shown, it appears that the dynamical structure within the low- and high-speed regions, as presently understood in these data, are actually quite similar, although this should be taken as a rather tentative conclusion given the above approximations. At the very least, the above representation demonstrates another way of characterizing the data to make further statements regarding its temporal organization.

## 8.4.2 Correlation Dimension

As well as quantifying the signal's unsteadiness, we would also like to quantify its complexity. Now whenever one wishes to discuss complexity, then matters generally become more complicated, and one must necessarily resort to more abstract methods. The quantification of the signal's complexity is accomplished by computing the correlation dimension  $\nu$  of the optimally reconstructed

attractor. The results are shown in figure 8.7 for various embedding dimensions  $d$ . The visual recurrence analysis toolbox 5.01 by Eugene Kononov (2007) was used in the calculations, and has been validated against a variety of well-known attractors, such as the Lorenz attractor and Rössler attractor for example. As mentioned earlier, for a completely random signal, the correlation dimension would scale linearly with the embedding dimension, because no matter how the noise was embedded, it would eventually fill the embedding space. This distribution for noise is shown by the thick black line. The signal obtained within the reflected shock wave region, however, saturates as the embedding dimension increases, suggesting that it comes from a finite-dimensional attractor (Grassberger & Procaccia 1983). Importantly, this behaviour was always observed, independent of the time series length considered. This means that points that are neighbours in  $d-1$  dimensions are also neighbours in the next higher embedding dimension  $d$ , indicating that the unfolding of the attractor is complete. This condition appears to be met only for  $d \geq 7$ .

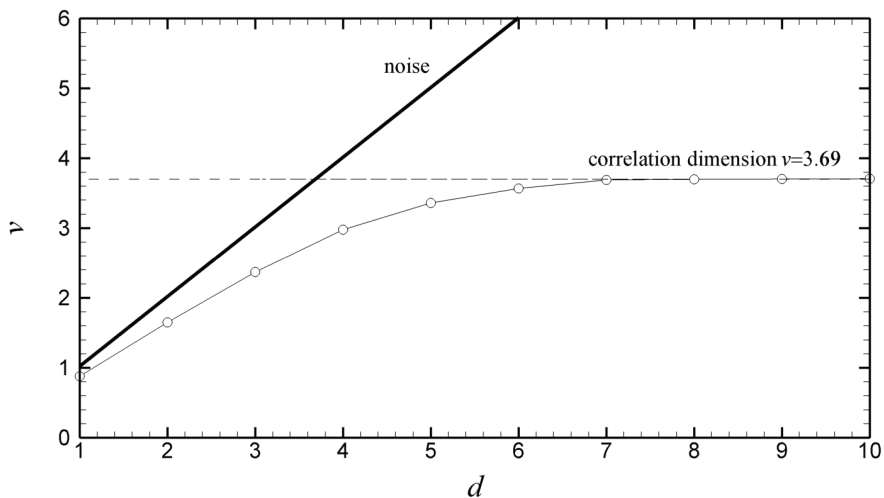


FIGURE 8.7: Plot of the correlation dimension against embedding dimension  $d$  for the optimally reconstructed attractor. Results show that the minimum embedding dimension is  $d=7$ , and the correlation dimension of the attractor is about  $\nu=3.69$ . The thick solid black line shows the trend for noise. Calculations are based on 100,000 data points.

Thus, the correlation dimension distribution shows that the minimum embedding dimension for which the signal can be completely unfolded is  $d=7$ . This means that the signal's dynamics are best represented by an attractor within a seven-dimensional embedding space. This value is in the spirit of the POD analyses shown earlier, where a limited number of about the first 10 eigenmodes capture an appreciable fraction of the total kinetic energy of the flow (say  $> 2\%$ ). However, as noted by Berkooz *et al.* (1993), a finite dimensional attractor does not always guarantee that there are also a finite number of energy-containing POD eigenmodes.

Nevertheless, while the reflected shock wave dynamics are clearly complex, there appears to be a limited number of underlying degrees of freedom present. As noted by Abarbanel & Kennel (1993), the minimum appropriate embedding dimension represents the number of degrees of freedom that are active on the attractor; namely, the number which one must model in order to produce an accurate representation of the orbits of the system for prediction or possible control purposes. This will become important in our forecasting strategy later on.

Furthermore, the minimum appropriate embedding dimension corresponds to a correlation dimension of approximately  $\nu=3.69$ . Although no real comparisons of this value could be made with those reported elsewhere, to give the reader a flavour of some values found in literature, the correlation dimension of some classical attractors include the Lorenz attractor in our illustrative example earlier ( $\nu=2.05$ ), the Rössler attractor ( $\nu=1.99$ ), and the Ueda attractor ( $\nu=2.68$ ) (see Sprott & Rowlands 2001 for a further list of the correlation dimensions of various attractors).

Correlation dimensions obtained from experimental data also vary widely. For example, Sivakumar (2000) reports on a series of chaos studies made on rainfall records by Rodriguez-Iturbe *et al.* (1989) who reported about  $\nu=3.78$ , Sharifi *et al.* (1990) who reported  $\nu=3.35-3.60$ , Tsonis *et al.* (1993) who reported about  $\nu=2.4$ , as well as Islam *et al.* (1993) who reported values as low as  $\nu=1.5$ . Given the well-known difficulty of determining the correlation dimension from experimental data, the reader should not take the present value uncritically and at

face value, but rather view it as an estimate, keeping in mind its probabilistic definition and interpretation.

Nevertheless, the present attractor clearly has a fractal correlation dimension (a noninteger value), meaning the way in which the attractor fills its space is not continuous, unlike in Euclidean or plane geometry for instance, where objects are solid and continuous. It is hypothesized that such a fractal nature is associated with the hierarchically structured series of nested loops that occur in state-space, which makes the attractor appear to have a similar structure at smaller scales—a hall-mark of fractal objects. Without a thorough comparison of  $\nu$  with other definitions of the fractal dimension, however, it would be speculation to draw further conclusions from the noninteger value of  $\nu$  (see also Pincus 1991), although the existence of fractals and multifractals in turbulence is well-known (see Sreenivasan 1991).

### 8.4.3 Recurrence Plot

To provide an overview of the temporal correlation of the points in state-space and reveal recurrence in the data, a recurrence plot of the optimally reconstructed attractor is shown in figure 8.8, where  $n$  is the number of points. Instead of using a predefined threshold  $\varepsilon$ , which would lead to a binary recurrence plot often seen in literature (see Marwan 2003), we consider all values of  $\varepsilon$  to give the variable colour plot shown. Thus, we consider that

$$\mathbf{R}_{i,j} = \|\mathbf{x}_i - \mathbf{x}_j\|, \quad i, j = 1, \dots, N \quad (8.1)$$

and therefore essentially have a *distance plot* (see Marwan 2003). Although difficult to discern at first sight, there is in fact a wealth of information present in the recurrence plot. The plot shows a rich texture, consisting of numerous horizontal and vertical lines, rectangular blocks, as well as diagonal lines. (Note that the figure is diagonally-symmetric, and the diagonal line running from bottom-left to top-right is the trivial case in the matrix  $\mathbf{R}_{i,j}$  when  $i=j$ .) If the signal was completely random, then there would be no such features, and the plot would be homogeneously distributed with single points

(Marwan 2003). It is therefore clear that the signal portraying the reflected shock wave's dynamics has a recurrent structure.

Specifically, many horizontal and vertical lines can be observed, as highlighted in region (C) for example. These mark the length of time in which a state does not change appreciably (Marwan 2003). Such lines are therefore associated with segments of the trajectory that remain trapped within a certain part of the attractor for a limited amount of time. Physically, this may be interpreted as the sustained passage of a low- or a high-speed region entering the interaction, since the velocity fluctuations remain (crudely) constant within such regions, in comparison to when an alternating passage of regions occur. In the example region (C) shown, the length of the line equates to a length of about  $20\delta$ , assuming a local convective velocity  $U_c \sim 400$  m s<sup>-1</sup>, therefore representing a very long large-scale structure.

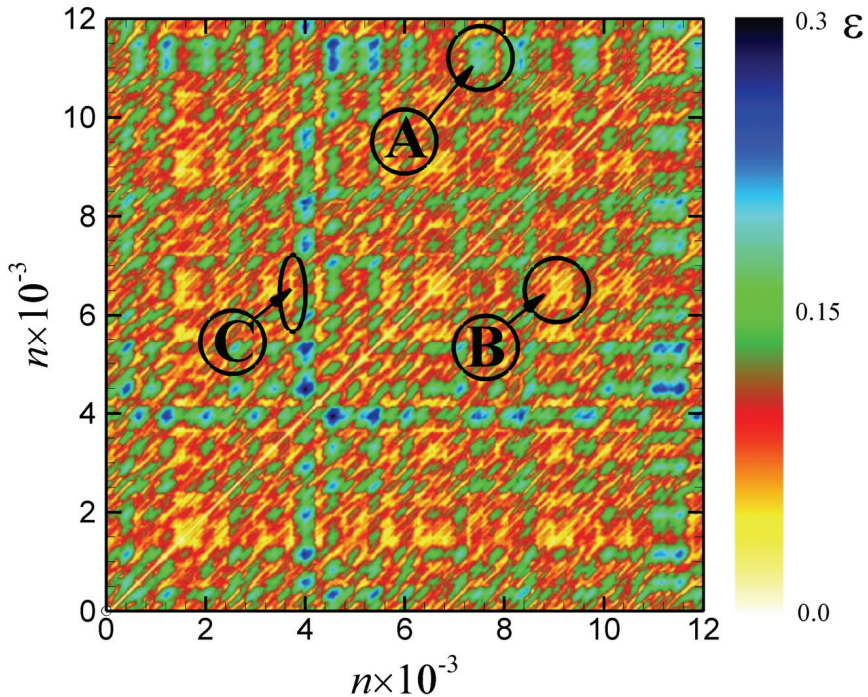


FIGURE 8.8: Recurrence plot of the optimally reconstructed attractor. The first 12,000 data points are shown for clarity. Highlighted regions (A), (B), and (C) are discussed in the text.

The horizontal and vertical lines of relatively low values of  $\varepsilon$  can be seen to be interdispersed with numerous rectangular blocks shown in blue, such as the one highlighted in region (A) for example. These regions contain a density of points of relatively large values of  $\varepsilon$ , which can be of the order of the attractor diameter. Inspection of the attractor reveals that these values of  $\varepsilon$  are associated with the largest orbits that occur in state-space. Since, for a fixed time-delay (i.e.,  $\tau_{opt}=37$ ), the change in signal amplitude essentially translates into an increase in the relative difference between  $x(t)$ ,  $x(t+\tau)$ , ...,  $x(t+n\tau)$ , and hence a departure from the  $x(t)=x(t+\tau)=x(t+2\tau)$  axis, then these large orbits represent the transition that occurs between a low- and a high-speed region, as sensed by the stationary probe.

In addition, a series of diagonal lines may also be observed, as shown in region (B) for example. Diagonal lines occur when a segment of the trajectory runs parallel with another trajectory, meaning that the attractor trajectory visits roughly the same region of state-space, but at different times (Marwan 2003). This means that there is a sustained recurrence (in time) of the signal, when it is mapped into the optimum embedding space. Importantly, this behaviour cannot be discerned from reconstructed attractors using much higher (and indeed lower) time-delays, where the attractor structure becomes obscure, nor is such behaviour obvious in the premultiplied power spectra. It is evident that much of the recurrence plot contains the presence of such diagonal lines, consistent with an incoming boundary layer that is populated with numerous low- and high-speed regions. As a matter of fact, the time evolution of these very similar trajectories is the foundation on which our forecasting capability will be based.

#### 8.4.4 Lyapunov Exponent

As the first step in establishing a forecasting capability, we estimate the long-term predictability of the time series signal by determining the Lyapunov exponent of the optimally reconstructed attractor. Following the approach of Rosenstein *et al.* (1993), who have developed an algorithm for determining the (largest) Lyapunov exponent, we estimate it to be  $\lambda_1 \sim 8000 \text{ bits s}^{-1}$ . This estimate was found to be relatively insensitive to the number of data points considered, which was systematically varied from 10,000–100,000.



The exponent can be thought of in information theoretic terms, as representing the rate at which information is destroyed (Wolf *et al.* 1985). Like the correlation dimension estimate above, given the well-known difficulty of determining the Lyapunov exponent from experimental data, it should be viewed as an estimate.

We can use the Lyapunov exponent to give a rather rough estimate of our prediction horizon—a Lyapunov time  $t_{lyap}$ , beyond which we can no longer say anything useful about the future behaviour of the signal. Beyond  $t_{lyap}$  not even qualitative predictions can be made. We estimate  $t_{lyap}$  for the optimally reconstructed attractor in the following way. Let  $\varepsilon$  be a measure of our tolerance, (i.e., if the prediction is within  $\varepsilon$  of the true state then we consider it to be acceptable). Our prediction therefore becomes intolerable when  $\delta x(t) \geq \varepsilon$ . From the definition of the Lyapunov exponent,  $t_{lyap}$  can be estimated as

$$t_{lyap} \sim O\left(\frac{1}{\lambda} \ln \frac{\varepsilon}{|\delta x(0)|}\right) \quad (8.2)$$

As an instructive example, let the initial error between any two trajectories be  $\delta x(0) = 2 \times 10^{-3}$  (0.2% of  $U_\infty$ , or about  $u = 1 \text{ m s}^{-1}$ ), and specify the threshold of tolerance to be  $\varepsilon = 1 \times 10^{-1}$  (10% of  $U_\infty$ , or about  $u = 50 \text{ m s}^{-1}$ ), then with  $\lambda_1 \sim 8000 \text{ bits s}^{-1}$ , the time horizon becomes  $t_{lyap} \sim 5 \times 10^{-4} \text{ s}$ , corresponding to a Lyapunov frequency of  $f_{lyap} \sim 2 \text{ kHz}$ . Assuming a convective velocity of  $U_c \sim 400 \text{ m s}^{-1}$ , we obtain a wave-length of about  $\lambda_x = 10\delta$ . Returning to the premultiplied power spectra in §5.2.4, this corresponds to the most energetic large-scale motions within the incoming boundary layer closer to the wall at  $y/\delta = 0.1$ . This means our (average) long-term predictive capability in the example above is associated with a wave-length of the order of the most energetic large-scale motions found within the undisturbed boundary layer.

Although the above example is somewhat arbitrary, compounded by the additional approximations that have been made, the agreement between the above frequencies is not a coincidence: the logarithmic dependence ensures that our prediction horizon is rather insensitive to sensible thresholds chosen. This suggests that the prediction of the

time series signal portraying the reflected shock wave's dynamics is associated with wave-lengths of the most energetic low- and high-speed regions within the incoming boundary layer. This will be discussed further in the next section.

More fundamentally, it should now be clear that an arbitrarily long-term prediction of the time series signal (and the interaction dynamics in general) is impossible, since *any* uncertainty in the initial state  $\delta x(0)$  grows exponentially in time within state-space (i.e., a positive Lyapunov exponent); this is the essence of chaos (Wolf *et al.* 1985). Yet the present data have also been shown to be deterministic (i.e., there exists an attractor with a recurrent structure), and even though there is a fundamental limit on our long-term prediction capability (i.e., a positive Lyapunov exponent), there is the possibility of short-term prediction, since the signal has been shown to be characterized by an attractor involving only a limited number of degrees of freedom (i.e., seven). The application of a forecasting model in the short-term is therefore considered to be well-posed.

### 8.4.5 Short-Term Forecasting

The ability to successfully forecast the signal portraying the reflected shock wave's dynamics from an available time history may be the strongest test of whether or not low-dimensional chaos is really present, and has tremendous implications within the context of understanding and characterizing the underlying processes. The forecasting methodology outlined earlier clearly has many empirical elements, most notably the specification of the optimum time-delay  $\tau$ , the embedding dimension  $d$ , as well as the number of closest  $k$  neighbours to be chosen. In what follows, we use the optimal parameters  $\tau_{opt}=37$  and  $d=7$ , as described earlier, and investigate the effects of varying the number of neighbourhood trajectories considered  $k$ , since this is considered to be the most important parameter in the nearest neighbour approach (see e.g., Yankov *et al.* 2006).

For the purposes of illustration, the first 12,000 points of  $x(t)$  are considered in the forecasting model (i.e.,  $N=12,000$ ). The model was trained using the first 10,000 points (i.e.,  $N'=10,000$ , or about 20  $\delta$ -scale orbits), and is evaluated over the last 2,000 points. Although these numbers are chosen somewhat arbitrarily, it will be shown that

enough orbits must be present to be included in the search, and clearly it is not wise to predict arbitrarily into the future due to the finite Lyapunov exponent ( $\lambda \sim 8000$  bits  $s^{-1}$ , which equates to  $O(500)$  points of (average) long-term predictive capability). Although the results obviously change with varying such parameters, numerous combinations were explored, and the overall conclusions to be drawn remain unchanged. It is worth emphasizing again, that we wish to distil some underlying aspects about the temporal nature of the interaction, rather than conduct a systematic quantitative study.

Figure 8.9 shows the time series of the original signal  $(\rho u)'$  divided by the mean local mass-flux to give  $(\rho u)' / \bar{\rho} U_\infty \sim u' / U_\infty$  in blue, along with the predicted signal in red, against the number of points  $n$  and nondimensional time  $tU_\infty / \delta$  for various values of  $k$ . In all cases presented here, both the original and predicted signals are coincident up to  $n=10,000$ , where the training phase ends and the prediction phase begins. Thereafter, an appreciable departure of the predicted signals from the originals can be observed, with the predictive model sensitive to the number of neighbours  $k$  included in the search.

Specifically, for relatively small values of  $k$  considered (i.e.,  $k=10$ ), the predictive model performs poorly and there is only modest qualitative agreement with the original signal. This is because the local predictor is essentially interpolating between points on the current trajectory (i.e.,  $k$  is numerically similar to  $d+1$ ) and so produces a large bias. Results therefore quickly diverge after an initial period.

The agreement between the predicted and original signals, however, is much better for  $k=14$ , where it can be seen that the predicted signal follows the general trend of the original. In this particular case, the two signals match qualitatively up to about  $n=1700$  (or  $O(30\delta)$  assuming a convective velocity  $U_c \sim 400$  m  $s^{-1}$ ). The most energetic wave-lengths within the undisturbed boundary layer extend up to  $10\delta$ , and so it appears that we can predict, at least in this case, over a length-scale of several of these most energetic wave-lengths. Several other instances of this level of prediction were also found. In comparison, for relatively large values of  $k$  considered (i.e.,  $k \geq 18$ ), the predictive model again performs poorly. This is because the local predictor is now becoming a global predictor, since many

neighbouring orbits are being used in the reconstruction (i.e., we are moving towards the condition  $k \gg d+1$ ). This has the effect of low-pass filtering the predicted signal, as most clearly seen in figure 8.9(d).

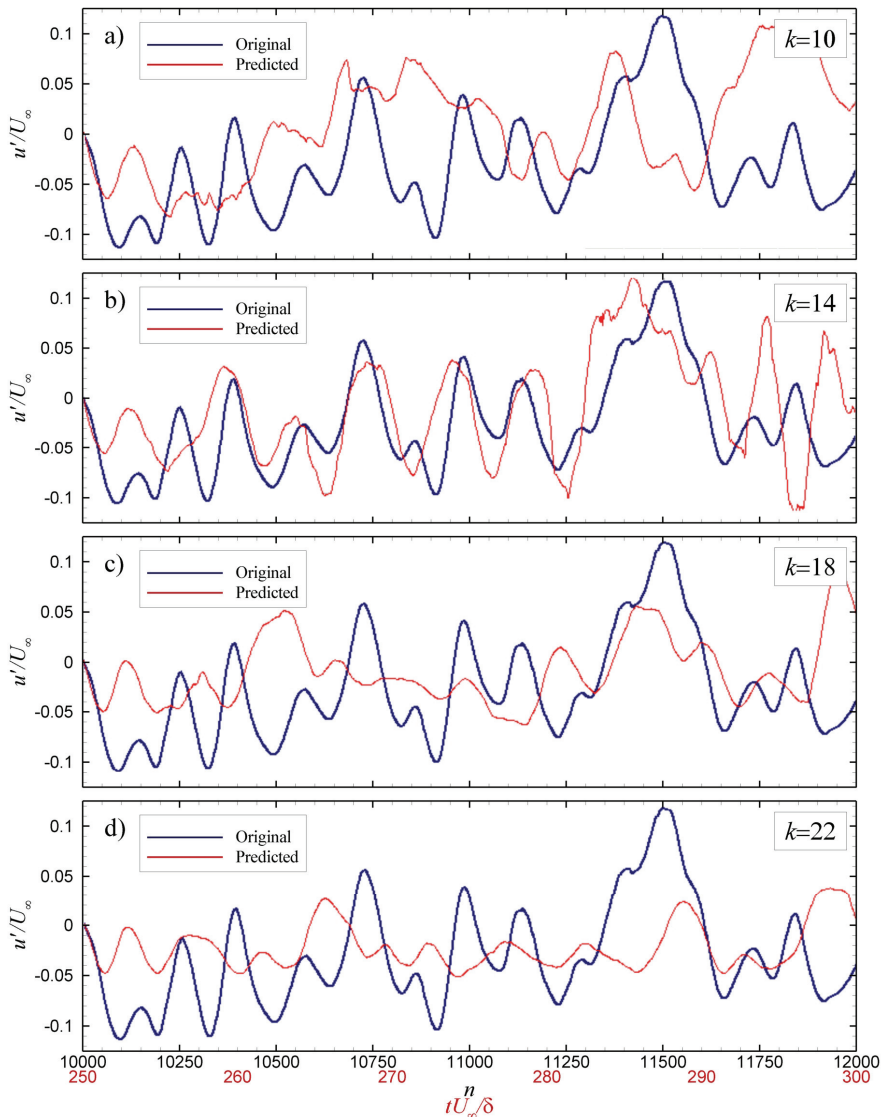


FIGURE 8.9: Comparison between original signal (*blue*) and predicted signals (*red*) for various nearest neighbours  $k$ . (a)  $k=10$ , (b)  $k=14$ , (c)  $k=18$ , (d)  $k=22$ . A total of 12,000 points are used. Training phase is based on the first 10,000 data points. Prediction phase is for the last 2,000 data points (as shown).

It now becomes clear that the (optimum) choice of  $k$  is problematic in this model because of the complicated structure of the attractor, whereby it is not obvious which neighbouring trajectories should be included in the prediction, since not all neighbours will be relevant for a given attractor segment. Furthermore, it is also difficult to separate the effects of  $k$  and the effects of the distances in state-space of the  $k$  neighbours. As noted by Yankov *et al.* (2006), the impact of the number of neighbours is especially interesting, as the results of the model have intrinsically different characteristics. In essence, a forecast combining too many neighbours often turns out to be biased, whereas one that uses too few often has a large variance. This is known as the *bias-variance dilemma*, and has been noted within the context of the present approach by several authors (see e.g., Sauer *et al.* 1994). It must be stressed that although only a very small sample of time series predictions are shown, the same general conclusions above could be drawn for many other cases, and justify not repeating the results here.

The prediction beyond the average Lyapunov horizon is especially interesting. It suggests that there appears to be some regions on the attractor for which adjacent points diverge more slowly than for other regions. This is evidenced for the case when  $k=14$ , where we can predict beyond our average Lyapunov time horizon by at least a factor of three. An improvement to the strategy may therefore be to optimize  $k$  for a given segment of the attractor, although it is not immediately clear how this should be done (see Yankov *et al.* 2006 for a further discussion and some perspective possibilities).

More fundamentally, one of the most interesting points to be drawn is that some parts of the signal appear to be *more predictable* than others, and from the recurrence plot shown earlier, it seems that this predictability could be associated with the low- and high-speed regions that enter the interaction. Given that the optimum time-delay is associated with a length-scale  $O(\delta)$ , one can tentatively imagine that the length of prediction (in time) is determined by, or at least associated with, the degree of streamwise alignment of such structures when an appropriate value of  $k$  is chosen. This is consistent with the notion that our (average) Lyapunov predictability is associated with the most energetic wave-lengths found within the

boundary layer of  $\sim 10\delta$ , and that it is possible to predict beyond this when exceptionally long large-scale structures are present. The ultimate level of prediction may well therefore be associated with the largest structures within the boundary layer.

The concept of variable prediction has been addressed by May (1995), who advocates the use of *local* Lyapunov exponents instead of a global Lyapunov average. This obviously has consequences for the characterization of the signal and determinism of the interaction in general. It may be that in regions on the attractor where there is a slow divergence of nearby trajectories, corresponding to the passage of a very long structure, then the globally-averaged Lyapunov exponent is less useful than a more fine-grained approach (May 1995). Future work may aim to explore these aspects in further detail. The success of such a short-term forecasting strategy may also open up a new approach to SWTBLI control.

# CHAPTER 9 TOWARD A CONCEPTUAL MODEL

---

## 9.1 Introductory Remarks

**T**HE stage is now set for a description of a physical model of the interaction's unsteady flow organization. In what follows, we consolidate the major observations made in this thesis into a plausible description that is consistent with the present results and with what has been reported in literature. We first give an outline of the key phenomenology of the observed interaction unsteadiness in both two- and three-dimensions. The POD eigenmodes and temporal analysis are then used to elaborate on the model. A unification of some of the physical mechanisms associated with the interaction unsteadiness reported in this thesis and in literature is made.

## 9.2 Outline of a Physical Model

In the proposed model, the undisturbed boundary layer first encounters the interaction. As the boundary layer enters the interaction, it undergoes a significant transformation. Based on the work carried out in this thesis, the following (inter-related) interpretations of the interaction's unsteady flow organization are offered:

### 9.2.1 Two-Dimensional Characterization

As the boundary layer encounters the reflected shock wave region, the first regions of flow separation occur. The probability of observing flow-reversal increases downstream, towards a maximal probability of about 50%. It is therefore an intermittently separated configuration. On average, the interacting boundary layer appears to be fully-attached, although this is by no means definitive, and the interaction is most likely close to incipient separation.

On an instantaneous basis, the interaction appears quite different from its time-averaged counterpart. It may be characterized by a high-velocity outer layer and a low-velocity inner layer. These two layers are separated by a thin region of high shear, in which discrete vortical structures are present. These vortical structures are initially located close to the wall. Investigation of the interaction's three-dimensional instantaneous structure using tomographic PIV shows that these structures are often in streamwise alignment, giving rise to streamwise-elongated regions of relatively low- and high-speed fluid. Measurements made in the streamwise-wall-normal cross-sectional plane would detect such regions as a sustained deformation of the instantaneous velocity profile, leading to a change in its fullness. One can now see how such small-scale structures could be associated with the large-scale unsteadiness of the incoming boundary layer.

Statistically speaking, when the incoming boundary layer velocity profile is fuller than on the mean, then the flow has a greater resistance to flow separation, and the streamwise extent of the (largest) separated flow region is more likely to be smaller than its median size. The reflected shock wave is therefore more likely to be located downstream of its mean position, and vice versa. This relationship is somewhat weak (correlation coefficient of about  $-0.3$ ), although it is not negligible, and is qualitatively consistent with other



models that have been reported in literature considering compression ramp interactions in particular.

As the vorticity layer and vortical structures proceed into the reflected shock wave region they are lifted away from the wall when flow separation is present, (or when there is a significant inner velocity deficit). The structures ride over the separation bubble, creating a fluid exchange between the outer and inner layers of the interaction. Outer high-velocity fluid is drawn in and ingested between the vortical structures, whereas low-velocity from the separated flow region is transported away from the wall. As a result, the instantaneous reversed-flow is intermittently supplied with fluid by the vortical structures as they propagate through the interaction, and not from downstream, as in the traditional (steady) view of separation, consistent with what is observed instantaneously in incompressible separated flows.

Fluid along the dividing streamline must necessarily reach the wall again in order to bound the separation bubble. This reattachment determines the size of the separation bubble, and depends critically upon the ability of fluid along the streamline to overcome the adverse pressure gradient at reattachment, which is a function of momentum available. (The reader is referred to the work of Good & Joubert 1968 for work in this area within the context of bluff plates.) In this respect, the vortical structures may be reconciled with the large-scale unsteadiness in the following way. Wu & Martin (2008) have recently hypothesized that one of the mechanisms of the large-scale low-frequency motion of the shock wave involves a feed-back loop between the separation bubble, separated shear layer, and shock system. This mechanism involves a large-scale enlarging and shrinking of the bubble that is associated with an instantaneous imbalance between shear layer entrainment from the separation bubble and fluid injection near reattachment, and draws upon the earlier work of Eaton & Johnston (1982), who carried out experiments in incompressible separated flows involving backward-facing steps. Kiya & Sasaki (1985) further inferred from Eaton & Johnston's (1982) model, that this imbalance is associated with the spatial organization of vortical structures, which play an important role in the instantaneous reattachment length by influencing the level of entrainment through a change in spanwise coherency.

Within the context of the present study, one can envisage the passage of the vortical structures, as they ride over the separation bubble, being associated with this spanwise coherency, with the resulting fluctuating level of momentum playing a role in the imbalance between shear layer entrainment from the separation bubble and fluid injection near reattachment, and therefore the instantaneous bubble size. It is unclear at this point, however, how this mechanism may be reconciled with the influence of the vortical structures within the incoming boundary layer, but it is not inconceivable to believe that several mechanisms associated with the large-scale unsteadiness coexist. The number of divergent theories that attempt to explain the cause(s) of the large-scale unsteadiness seems to suggest that this is the case.

Farther downstream, after turning around the separation bubble, the vortical structures often return to the proximity of the wall, whereas in other cases become more broadly distributed normal to the wall than in the first part of the interaction. This behaviour is associated with the separation bubble's vortex shedding process. While boundary layer recovery initiates downstream, complete recovery is not observed within the present measurement domain. A schematic of the model portraying the main phenomenological features discussed is shown in figure 9.1.

The reader may compare this figure with the mean unseparated and separated interaction representations reported in figures 1.8 and 1.9, respectively. While both the mean and unsteady representations share some important similarities, such as the overall shock wave and expansion fan patterns, there are also some important differences; most notably an intermittent, highly irregular boundary layer edge, the existence of an interacting inner and outer layer, the presence of the vortical structures, strongly inflected velocity profiles, a vortex shedding process within the redeveloping boundary layer, as well as the statistical link between the incoming boundary layer velocity profile, size of the separated flow region, and position of the reflected shock wave.

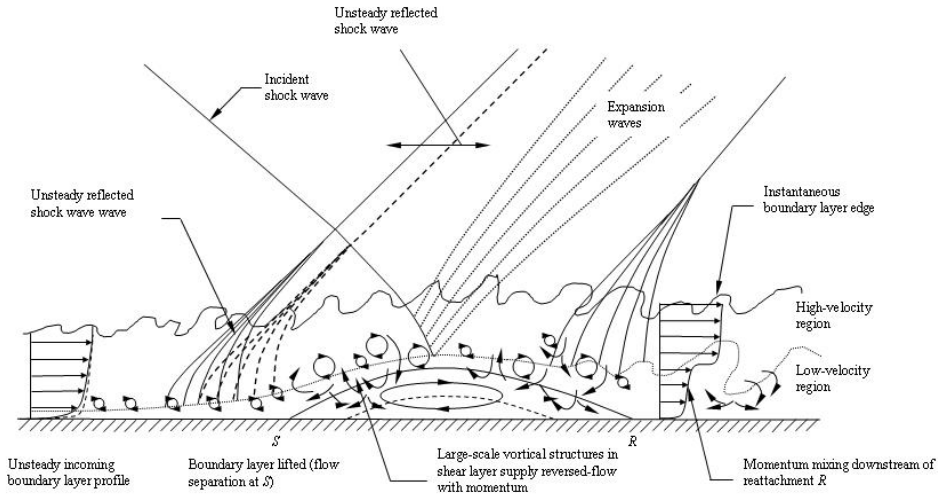


FIGURE 9.1. Two-dimensional conceptual model of the interaction's unsteady flow organization. Shown is the unsteady incoming boundary layer velocity profile and its association with the size of the separated flow region and reflected shock wave position. Also shown is the distinction between the inner and outer layers of the interaction, with discrete vortical structures along their interface.

The POD provides a complementary analysis to the results. Projections of the first eigenmode onto the mean flow are consistent with the statistical results that show when the incoming boundary layer velocity profile is fuller than on the mean, then the streamwise extent of the (largest) separated flow region is more likely to be smaller than its median size, and the reflected shock wave is more likely to be located downstream of its mean position, and vice versa. On the other hand, however, the failure to rebuild the relationship between  $1-1/H_i$  and  $(x-x_{mean})/\delta$  using only the first eigenmode, suggests that the first eigenmode alone cannot be used to accurately describe the interaction's unsteadiness in any decisive way, and this necessitates the utility of additional eigenmodes to properly represent the interaction's unsteadiness. These higher-order modes represent higher-order harmonics required to properly represent the complex dynamics of the interaction.

### 9.2.2 Three-Dimensional Characterization

Extending the description to include the spanwise dimension, the interaction exhibits a complex, three-dimensional instantaneous structure, but which can still be reconciled with its planar representation. The three-dimensional instantaneous flow organization of the incoming boundary layer may be explained by the hairpin vortex packet model, by asserting that the backflow created by several vortical structures in quasistreamwise alignment perpetuates the regions of low-speed fluid within the incoming boundary layer. This gives rise to the formation of very long alternating low- and high-speed regions. The high-speed regions typically contain no vortical structures, and exhibit a three-dimensional spanwise sinuous or undulating motion, and meander between the surrounding vortical structures.

These coherent motions affect the organization of the reflected shock wave pattern. As the low- and high-speed regions enter the interaction, the reflected shock wave pattern responds to the local incoming conditions that it experiences. High-speed fluid is able to negotiate the adverse pressure gradient better than low-speed fluid, and thus, when a relatively high-speed region enters the interaction, it displaces the reflected shock wave region downstream of its median position. Conversely, when a relatively low-speed region enters the interaction, the reflected shock wave region moves upstream of its median position. The spatial organization of the low- and high-speed regions therefore gives rise to the streamwise translation and spanwise rippling patterns, and one can see how this behaviour, when viewed in the lower-dimensional representation of a streamwise-wall-normal cross-sectional plane, could give rise to the appearance of the more or less random shock motion behaviour reported in numerous experiments (see e.g., Dolling 2001; Dolling & Murphy 1983; Ünalmsis & Dolling 1998; Beresh *et al.* 2002).

Farther from the wall, changes in the incoming boundary layer's flow organization take place, which have important consequences for the reflected shock wave pattern. Flow features become more spatially disorganized and uncorrelated with the flow phenomenology closer to the wall, as well as the appearance of boundary layer intermittency. The velocity range decreases, with the velocity fluctuations and gradients becoming weaker. As a result, the

shock wave pattern becomes more uniform in the spanwise direction, and undergoes a smaller streamwise motion with distance from the wall. Large-scale organized motions are still occasionally observed, however, in the form of streamwise-elongated regions of relatively low-speed fluid, as well as rotating bulges near the boundary layer edge. The latter in particular, seems associated with fluid being ingested into the boundary layer, where it can penetrate deep into the boundary layer. A schematic of the three-dimensional model showing the main phenomenological features is shown in figure 9.2.

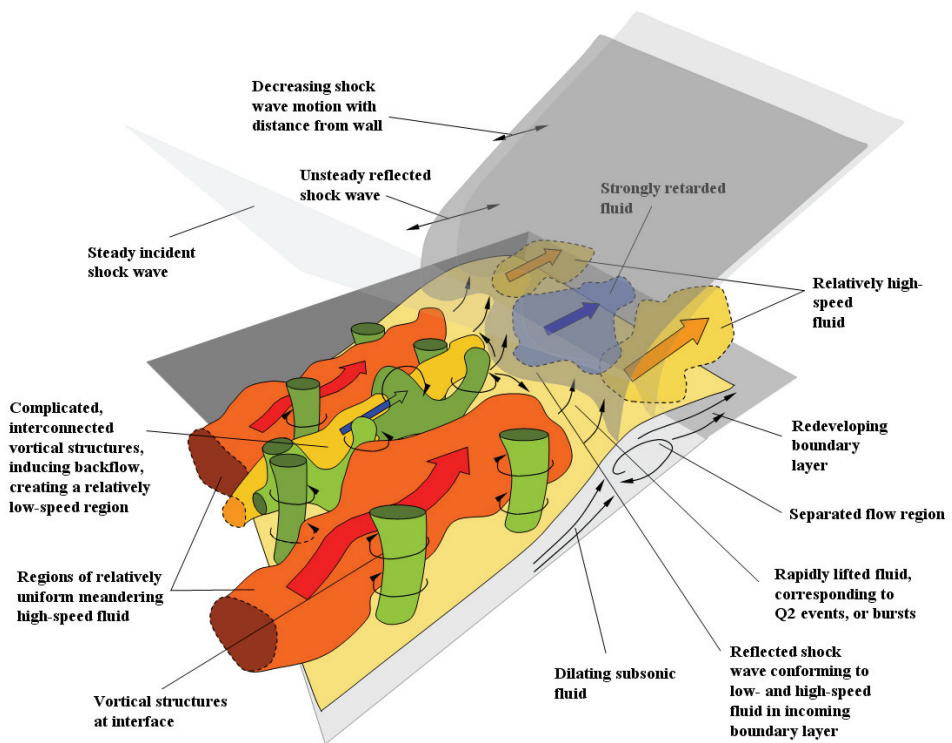


FIGURE 9.2. Three-dimensional conceptual model of the interaction's unsteady flow organization. Shown are the low- and high-speed regions within the incoming boundary layer. Low-speed regions are associated with vortical structures, whereas high-speed regions fill-in the separation between these structures. The corresponding streamwise translation and spanwise rippling patterns of the reflected shock wave are also indicated. From Humble *et al.* (2008).

The POD eigenmodes provide a synthesis to these observations, in much the same way as they do for the planar results. The translation component of the reflected shock wave is the pattern that contains the largest fraction of total energy of the POD eigenmodes, and is consistent with the first eigenmode of the planar results. Higher-order eigenmodes depict the spanwise rippling component of the reflected shock wave region and its harmonics.

### 9.2.3 Temporal Characterization

While the above picture consolidates observations of the interaction's spatial organization, the interaction has also been shown to exhibit a temporal organization that may be reconciled with the above description. The fluid dynamical behaviour of the mass-flux time signal within the reflected shock wave region may be characterized as a chaotic attractor in an optimum embedding space of limited dimension. This attractor has a rich, recurrent structure, which contains the signatures of the low- and high-speed regions as they enter the interaction.

In the model, the sustained passage of a low- or a high-speed region entering the interaction leads to state-space trajectories remaining trapped within a certain part of the attractor for a limited time. Within a low-speed region, the relatively small-scale spiralling may well be the footprint of the streamwise alignment of vortical structures, whereas within a high-speed region it may well be the footprint of the spanwise meandering. This behaviour is interdispersed with larger orbits, which correspond to the alternating passage of the low- and high-speed regions. Since the asymptotic structure of such trajectories is bounded within a finite region of state-space, then trajectories visit roughly the same regions of state-space but at different times, consistent with an incoming boundary layer that is populated with numerous recurring low- and high-speed regions.

Since velocity fluctuations within a relatively low-speed region give rise to orbits spiralling lower down the  $x(t)=x(t+\tau)=x(t+2\tau)$  axis, whereas velocity fluctuations within a relatively high-speed region gives rise to orbits spiralling higher up the  $x(t)=x(t+\tau)=x(t+2\tau)$  axis, then the passage of numerous low- and high-speed regions of various wave-lengths, as depicted in the premultiplied power spectra, gives rise to an attractor structure that may be conceptualized as a series of

nested spirals wrapping up and down the  $x(t)=x(t+\tau)=x(t+2\tau)$  axis in time. This description is schematically depicted in figure 9.3. The reader is reminded that the attractor is not completely unfolded in this three-dimensional representation, but is shown this way for illustrating the model. The attractor is completely unfolded only in a seven (or higher) dimensional embedding space. This is in the spirit of the POD analyses, in the sense that the large-scale dynamics seem to be represented by a limited number of degrees of freedom.

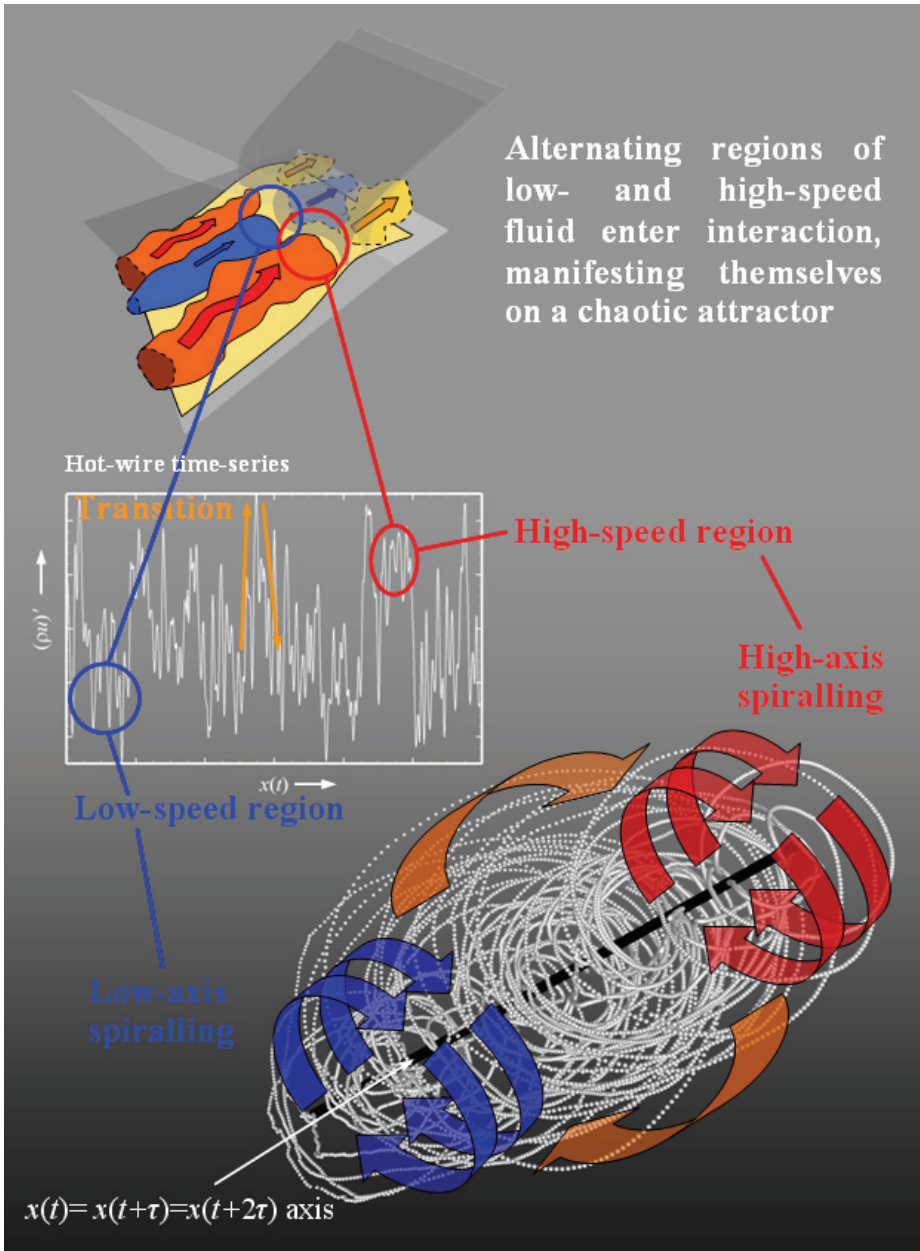


FIGURE 9.3: Schematic of the relationship between the structure of the optimally reconstructed attractor and dynamics of the reflected shock wave region. Shown inset is a sample time series of the mass-flux fluctuations within the reflected shock wave region. This translates into a *high-axis spiralling* (red) and a *low-axis spiralling* (blue) respectively. Transitions between the two are shown in orange.



### 9.3 Final Remarks

Thus, while at first glance the dynamics of the interaction appear hopelessly complex, it seems that there are some underlying features of its unsteady organization, involving large-scale motions within the incoming boundary layer, the separation bubble, and the reflected shock wave pattern that suggest that this may not be the case. Based on the present results, we may tentatively conceive the dynamics of the interaction as being a transition through a finite alphabet of admissible flow organizations, whose spatial organization is represented here by the POD eigenmodes, and whose temporal organization is represented by a chaotic attractor in a limited dimensional state-space. As the interaction dynamics evolve, every so often we catch a glimpse of a recurrent flow pattern, with the prevalence of any given flow pattern associated with the eigenmode's fraction of the total energy of the flow.

This interpretation is in the spirit of Hopf's (1948) vision of the function space of Navier-Stokes velocity fields, as being an infinite-dimensional state-space, parameterized by viscosity and boundary conditions, in which each three-dimensional velocity field is represented as a single point (see Gibson *et al.* 2008). Turbulent velocity fields are represented by chaotic state-space trajectories, with the long-term solutions of the Navier-Stokes equations lying on finite-dimensional manifolds embedded within the infinite-dimensional state-space of allowed velocity fields. The conceptual gap that separates low-dimensional dynamical systems and the challenges we face in understanding the complex dynamics of SWTBLIs may well therefore be narrowed (Gibson *et al.* 2008).



# CHAPTER 10 CONCLUSIONS & OUTLOOK

---

## 10.1 Conclusions

**M**EASUREMENTS of the two- and three-dimensional spatial organization of an incident SWTBLI at Mach 2.1 have been made using planar and tomographic PIV, respectively, complemented with a temporal characterization using HWA. As a result, several main conclusions may be drawn from the work carried out in this thesis:

PIV is a well-suited flow diagnostic technique to investigate the spatial organization of SWTBLIs. Tomographic PIV in particular, is well-suited to the investigation of the interaction's three-dimensional instantaneous structure, and reduces the complexity and ambiguity of cross-sectional representations by providing a volumetric synthesis of the results.

The global structure of the interaction region varies considerably in time. Reversed-flow is measured instantaneously, and is observed in about 50% of the realizations. The interaction is therefore an intermittently separated configuration. On average, no reversed-flow is observed, and the interaction is thought to be close to incipient separation.

On an instantaneous basis, the interaction exhibits a multilayered structure, consisting of a high-velocity outer region, and a low-velocity inner region, separated by an interface where discrete vortical structures are present. The mean flow-field is therefore a simplified representation of the interaction's instantaneous flow structure.

The turbulence properties evolve very differently throughout the interaction. The normal stress components are highly anisotropic, with the streamwise component dominating over the wall-normal component. The highest streamwise turbulence intensity occurs in the region beneath the impingement of the incident shock wave, reaching 20% of the free-stream velocity, and rapidly decays farther downstream. In contrast, the wall-normal component persists well into the redeveloping boundary layer. Such anisotropic turbulence evolution is observed within SWTBLIs in general.

An inter-relationship appears to exist between the incoming boundary layer, separated flow region, and reflected shock wave. Specifically, when the boundary layer velocity profile is less-full than on the mean, then the streamwise extent of the separated flow region is more likely to be larger than its median size, and the reflected shock wave appears upstream of its mean position, and vice versa. The correlation coefficient between these data is about  $-0.3$  indicating that this statistical link is weak although not negligible.

The PIV data are also well-suited for POD analyses of the interaction, with the global eigenmodes providing a way to further characterize the interaction's unsteady flow organization. The first planar POD eigenmode is consistent with the statistical relationship described above concerning the incoming boundary layer velocity profile, size of separated flow region, and position of the reflected shock wave.

Extending the representation of the interaction to include the spanwise dimension reveals a complex instantaneous three-dimensional flow organization. The incoming boundary layer

contains large-scale coherent motions, in the form of three-dimensional streamwise-elongated regions of relatively low- and high-speed fluid, similar to what has been observed in other subsonic and supersonic boundary layers.

The reflected shock wave pattern is affected by these flow organizations. The reflected shock wave region conforms to the streamwise-elongated low- and high-speed regions within the incoming boundary layer as they enter the interaction, and can be qualitatively decomposed into an overall streamwise translation and a spanwise rippling pattern. Farther from the wall, the streamwise motion of the reflected shock wave region decreases and appears more uniform in the spanwise direction.

The temporal analysis reveals that the reflected shock wave region is dominated by energetic frequencies that are an order of magnitude lower than those found in the undisturbed boundary layer at the same distance from the wall. The mass-flux time signal within the reflected shock wave region has an underlying structure that can be represented as a chaotic attractor in a limited dimensional state-space of seven. This attractor has a rich, recurrent structure, which contains the signatures of the low- and high-speed regions as they enter the interaction.

When considered in greater detail, attractor segments at earlier times resemble segments at later times, which lends itself to the application of a predictive strategy of the interaction's future dynamics. The signal's behaviour can be predicted over a length-scale that is several times greater than the most energetic wave-lengths found within the undisturbed boundary layer.

## 10.2 Outlook

As a result of the present work, several perspectives concerning future related studies may be offered:

The PIV technique has demonstrated its potential in the characterization of the interaction's spatial flow organization. Whole-field information is still lacking, however, on its temporal characteristics, such as time-scales, characteristic frequencies, and flow acceleration. Time-resolved PIV, consisting of both dual-plane PIV (see Souverein *et al.* 2008), as well as fully time-resolved PIV,

would shed light on the whole-field spatiotemporal characteristics of the interaction, and therefore be instructive in the further investigation of the interaction's large-scale unsteadiness.

A major contribution of the present research has been to experimentally investigate for the first time the instantaneous three-dimensional structure of a SWTBLI using tomographic PIV. Although the technique has been successful in the characterization of the interaction's global organization, the spatial resolution, however, must be improved if quantitative statements are to be made regarding derived quantities, such as velocity gradients and vorticity. Accurate estimates of these quantities are desirable in general, given the value of accurately measuring the three-dimensional velocity field at the (high) Reynolds numbers reported in this thesis.

Furthermore, as noted by Elsinga (2008), one of the current limitations of tomographic PIV is the large processing time associated with the reconstruction and volume interrogation (approximately one hour for  $10^8$  voxels on a Pentium 4 PC) and it is worth emphasizing this point again here. It is anticipated by Elsinga (2008) that advanced algorithms will exploit the sparseness of the reconstructed volumes (i.e., many of the voxel intensities are equal to zero), in order to significantly reduce the computation time, and further efforts should be directed in this area, especially in view of the value of accurately estimating turbulence statistics, but which typically require large datasets (e.g.,  $O(1000)$  velocity fields for statistically converged Reynolds-averaged shear stresses).

An important contribution of the present research has been to highlight the difficulty in obtaining accurate Reynolds-averaged shear stress values within the compressible turbulent boundary layer close to the wall (i.e.,  $y/\delta < 0.1$ ) using PIV. The effect of particle slip have been hypothesized to account for the discrepancies between the present measured Reynolds-averaged shear-stress values and those reported in literature, and further work should be conducted in this area to assess the effects of particle response time on the turbulence properties close to the wall.

Within a broader context, the manipulation of the velocity data has recently allowed the extraction, under certain restrictions, of the mean static and total pressure fields within the interaction (see van Oudheusden & Souverein 2007). For high-speed aeronautical

applications, maximum mean and fluctuating pressure loads often occur in regions of SWTBLIs, and there is a great interest in being able to characterize them, particularly in view of the difficulties of obtaining accurate pressure loads with the most promising CFD models (see Dolling 2001). Although extension to the determination of the instantaneous pressure field remains a significant experimental challenge in view of the difficulties in obtaining reliable acceleration data under high-speed flow conditions, attention should also be focused in this area, especially since velocity alone is somewhat less well-suited to the identification of shock waves than pressure for example.

The desire to control the interaction between a shock wave and a boundary layer is a problem that has been continuously addressed in recent decades. Although the subject of SWTBLI control is a broad field, with numerous control methods with varying degrees of success, the present research suggests that manipulating the large-scale organized motions within the incoming boundary layer may be an effective strategy in modifying the structure of the interaction. One can imagine for instance control devices, such as jets or passive vortex generators etc., being spatially distributed according to the large-scale motions within the incoming boundary layer.

In a related area, another important and novel contribution of the present research has been the successful application of nonlinear dynamical systems theory to the SWTBLI problem, by characterizing the temporal organization of a mass-flux time signal within the interaction as a chaotic attractor in a limited dimensional state-space. The nonlinear time series analysis has also demonstrated its potential as a short-term forecasting strategy, which could possibly be combined with the control methods mentioned above. One can envisage for instance, using forecasting information within the framework of a pre-emptive SWTBLI control strategy, using knowledge of the low- and high-speed regions before they enter the interaction.

With respect to the relevance of the present research to a real flow problem, the present experiments are considered representative of the processes that typically takes place within high-speed air intakes for example (see e.g., Dupont *et al.* 2006; Dussauge *et al.* 2006). This is perhaps best exemplified by the participation and interest of the

present research within the context of the UFAST network; a European initiative that has been recently created to foster experimental and theoretical work in the area of unsteady SWTBLIs to provide benchmark test cases for the most promising computational models using RANS and LES (see Doerffer 2007). Nevertheless, efforts should be directed towards the investigation of other incoming flow conditions, by varying the free-stream Mach number, interaction strength, and characteristics of the incoming boundary layer, in order to characterize the mean and statistical properties of the interaction within a broader context to aid computational modelling efforts, as well as to gain knowledge of the interaction's phenomenology at engine 'off-design' operations for instance.

On a final note, we modify the analogy offered by Witten (1998), and liken SWTBLI research to a vast mountain range, much of which is still covered in fog. Only the loftiest peaks, which reach high above the clouds, are readily observed in experiments and numerical simulations. These peaks have historically been studied in relative isolation, however, because above the clouds they are isolated from one another. Lost in the mist of the mountain range below remains the myriad of phenomenological treasures. But questions as to the underlying inter-relationships between these features are now being asked, although the answers still lie mainly ahead. And so there is one obvious, though seemingly provocative, prediction about SWTBLI research: that it will remain one of the main themes in high-speed fluid dynamics research in the decades to come.



# REFERENCES

---

Abarbanel, H. D. I. & Kennel, M. B. (1993) Local false nearest neighbors and dynamical dimensions from observed chaotic data. *Phys. Rev. E* **47**, pp. 3057–3068.

Adamson, T. C. Jr. & Messiter, A. F. (1980) Analysis of two-dimensional interactions between shock waves and boundary layers. *Annu. Rev. Fluid Mech.* **12**, pp. 103–138.

Adrian, R. J. (1986) Multipoint measurements of simultaneous vectors in unsteady flows – a review. *Int. J. Heat and Fluid Flow* **7**, pp. 127–145.

Adrian, R. J. (1991) Particle image techniques for experimental fluid mechanics. *Annu. Rev. Fluid Mech.* **23**, pp. 261–304.

Adrian, R. J., Meinhart, C. D. & Tomkins, C. D. (2000) Vortex organization in the outer region of the turbulent boundary layer. *J. Fluid Mech.* **442**, pp. 1–54.

Adrian, R. J. & Moin, P. (1988) Stochastic estimation of organized turbulent structure: homogeneous shear flow. *J. Fluid Mech.* **190**, pp. 531–559.

Akeret, J., Feldmann, F. & Rott, N. (1947) Investigations of compression shocks and boundary layers moving in gases moving at high speed. NACA TM 1113.

Allen, J. H., Heaslet, M. A. & Nitzberg, G. E. (1947) The interaction of boundary layer and compression shock and its effect upon airfoil pressure distributions. NACA RM A7A02.

Anderson, J. D. (1991) Fundamentals of aerodynamics. 2<sup>nd</sup> Ed. McGraw-Hill, New York, USA.

Anderson, J. D. (1990) Modern compressible flow: with historical perspective. 2<sup>nd</sup> Ed. McGraw-Hill, New York, USA.

Andreopoulos, Y., Agui, J. H. & Briassulis, G. (2000). Shock wave & turbulence interactions. *Annu. Rev. Fluid Mech.* **32**, pp. 309–345.

Andreopoulos, Y. & Muck, K. C. (1987) Some new aspects of the shock-wave/boundary-layer interaction in compression ramp flows. *J. Fluid Mech.* **180**, pp. 405–428.

Antonia, R. A. (1981) Conditional sampling in turbulence measurement. *Annu. Rev. Fluid Mech.* **13**, pp. 131–156.

Ardonceanu, P. L. (1983) The structure of turbulence in a supersonic shock wave/boundary layer interaction. *AIAA J.* **22**, pp. 1254–1262.

Atkeson, C., Moore, A. & Schaal, S. (1996) Locally weighted learning. *Artificial Intelligence Review* **11**, pp. 75–113.

Aubry, N., Holmes, P., Lumley, J.P. & Stone, E. (1988) The dynamics of coherent structures in the wall region of the turbulent boundary layer. *J. Fluid Mech.* **192**, pp. 115–173.

Baals, D. D. & Corliss, W. R. (1981) Wind-tunnels of NASA. NASA SP-440.

Bajo-Rubio, O., Sosvilla-Rivero, S. & Fernández-Rodríguez, F. (2002) Non-linear forecasting methods: some applications to the analysis of financial series. FEDEA.

Bar-Meir, G. (2008) Fundamentals of compressible flow. Online version at <http://www.potto.org>.

Benedict, L. H. & Gould, R. D. (1996) Towards better uncertainty estimates for turbulence statistics. *Exps. Fluids* **22**, pp. 129–136.

- Beresh, S. J., Clemens, N. T. & Dolling, D. S. (2002) Relationship between upstream turbulent boundary-layer velocity fluctuations and separation shock unsteadiness. *AIAA J.* **40**, pp. 2412–2422.
- Beresh, S. J., Clemens, N. T., Dolling, D. S. & Comninou, M. (1997) Investigation of the causes of large-scale unsteadiness of shock-induced separated flow using planar laser imaging. AIAA Paper 97-0064.
- Berkooz, G., Holmes, P. & Lumley, J. L. (1993) The proper orthogonal decomposition in the analysis of turbulent flows. *Annu. Rev. Fluid Mech.* **25**, pp. 539–575.
- Bernero, S. & Fiedler, H. E. (2000) Application of particle image velocimetry and proper orthogonal decomposition to the study of a jet in counterflow. *Exps. Fluids* **29**, pp. 274–281.
- Blinowska, K.J. & Malinowski, M. (1991) Non-linear and linear forecasting of the EEG time series. *Biol. Cybern.* **66**, pp. 159–165.
- Bollerslev, T., Chou, R. Y. & Kroner, K. F. (1992) ARCH modelling in finance: a review of the theory and empirical evidence. *Journal of Econometrics* **52**, pp. 5–59.
- Bookey, P., Wyckham, C. & Smits, A. J. (2005) Experimental investigations of Mach 3 shock-wave turbulent boundary layer interactions. AIAA Paper 2005-4899.
- Brucker, C. (1996) 3-D Scanning particle image velocimetry: technique and application to a spherical cap wake flow. *Appl. Sci. Res.* **56**, pp. 157–179.
- Bueno, P. C. (2006) The effects of upstream mass injection by vortex generator jets on shock-induced turbulent boundary layer separation. PhD Thesis, Department of Aerospace Engineering and Engineering Mechanics, The University of Texas at Austin, Texas, USA.

Caiani, L., Casetti, L., Clementi, C. & Pettini, M. (1997) Geometry of dynamics, Lyapunov exponents, and phase transitions. *Phys. Rev. Lett.* **79**, pp. 4361–4363.

Cambell, A., Pham, B. & Tian, Y. –C. (2005) A delay-embedding approach to multi-agent construction and calibration. In *MODSIM 2005 International Congress on Modelling and Simulation*. (Eds. A. Zerger & R. M. Argent), *Modelling and Simulation Society of Australia and New Zealand*, pp. 170–176.

Cantwell, B. J. (1981) Organized motion in turbulent flow. *Annu. Rev. Fluid Mech.* **13**, pp. 457–515.

Cebeci, T. & Cousteix, J. (1999) Modeling and computation of boundary-layer flows. Springer-Verlag, Berlin, Germany.

Cecen, A., Agirdas, C, Ugur, A. & Tuzcu, V. (2004) From market crashes to heart attacks: On the empirics of nonlinear dynamics in nature and society. *Journal of Econometric and Social Research* **6**, pp. 1–32

Challis, J. (1848) On the velocity of sound. *Philos. Mag.* **XXXII**, pp. 494–499.

Chapman, D. R., Kuehn, D. M. & Larson, H. K. (1958) Investigations of separated flows in supersonic and subsonic streams with emphasis on transition. NACA Rep. 1356.

Chong, M. S., Soria, J., Perry, A. E., Chacin, J., Cantwell, B. J. & Na, Y. (1998) Turbulence structures of wall-bounded shear flows using DNS data. *J. Fluid Mech.* **357**, pp. 225–247.

Coles, D. (1956) The law of the wake in the turbulent boundary layer. *J. Fluid Mech.* **1**, pp. 191–226.

Comte-Bellot, G. (1976) Hot-wire anemometry. *Annu. Rev. Fluid Mech.* **8**, pp. 209–231.

- Dangelmayr, G., Gadaleta, S., Hundley, D. & Kirby, M. (1999) Time series prediction by estimating Markov probabilities through topology preserving maps. In *Applications and Science of Neural Networks, Fuzzy Sets and Evolutionary Computation II*. (Eds. B. Bosacchi, D. B. Vogel and J. C. Bezdek), *Proceedings of SPIE 44<sup>th</sup> Annual Meeting, SPIE Proceedings Series* **3812**.
- Davidson, P. A. (2004) *Turbulence: an introduction for scientists and engineers*. Oxford University Press. United Kingdom.
- Délery, J. M. (1983) Experimental investigation of turbulence properties in transonic shock-wave/boundary-layer interactions. *AIAA J.* **21**, pp. 180–185.
- Délery, J. M. (1985) Shock wave/turbulent boundary layer interaction and its control. *Prog. Aerospace Sci.* **22**, pp. 209–280.
- Délery, J. M. & Bur, R. (2000) The physics of shock wave/boundary layer interaction control: last lessons learned. ECCOMAS 2000, Barcelona, Spain.
- Délery, J. M. & Marvin J. G. (1986) Shock-wave boundary layer interactions. AGARDograph 280.
- Delo, C. J., Kelso, R. M. & Smits, A. J. (2004) Three-dimensional structure of a low Reynolds-number turbulent boundary layer. *J. Fluid Mech.* **512**, pp. 47–83.
- Doerffer, P. (2007) European research on unsteady effects of shock wave induced separation UFAST – project. In *Proc. 8<sup>th</sup> Int. Symp. on Experimental and Computational Aerothermodynamics of Internal Flows*. Lyon, France.
- Dolling, D. S. (1993) Fluctuating loads in shock wave/turbulent boundary layer interaction: tutorial and update. AIAA Paper 93-0284.

Dolling, D. S. (2001) Fifty years of shock wave/turbulent boundary layer interaction research: what next? *AIAA J.*, **39**, pp. 1517–1531.

Dolling, D. S. & Murphy, M. T. (1983) Unsteadiness of the separation shock wave structure in a supersonic compression ramp flow-field. *AIAA J.* **21**, pp. 1628–1634.

Donaldson, C. Dup. (1944) Effects of interaction between normal shock and boundary layer. NACA CB 4A27.

Donaldson, C. Dup. & Lange, R. H. (1952) Study of the pressure rise across shock waves required to separate laminar and turbulent boundary layers. NACA TN 2770.

Dupont, P., Haddad, C. & Debiève, J. F. (2006) Space and time organization in a shock-induced separated boundary layer. *J. Fluid Mech.* **559**, pp. 255–277.

Dupont, P., Piponniau, S., Sidorenko, A. & Debiève, J. F. (2008) Investigation by particle image velocimetry measurements of oblique shock reflection with separation. *AIAA J.* **46**, pp. 1365–1370.

Dussauge, J. -P., Dupont, P. & Debiève, J. F. (2006) Unsteadiness in shock wave boundary layer interactions with separation. *Aero. Sci. Technol.* **10**, pp. 85–91.

East, L. F. & Sawyer, W. G. (1979) An investigation of the structure of equilibrium turbulent boundary layers. AGARD CP-271.

Eaton, J. K. & Johnston, J. P. (1982) Low-frequency unsteadiness of a reattaching turbulent shear layer. In *Turbulent Shear Flows 3*. (Eds. L. J. S. Bradbury, F. Durst, B. E. Launder, F. W. Schmidt & J. H. Whitelaw), Springer, pp. 162–170.

Eckmann, J. P., Kamphorst, S. O. & Ruelle, D. (1987) Recurrence plots of dynamical systems. *Europhysics Lett.* **5**, pp. 973–977.

- Eckmann, J. P. & Ruelle, D. (1992) Fundamental limitations for estimating dimensions and Lyapunov exponents in dynamical systems. *Physica D* **56**, pp. 185–187.
- Elena, M. & Lacharme, J. P. (1988) Experimental study of a supersonic turbulent boundary layer using a laser Doppler anemometer. *J. Theor. Appl. Mech.* **7**, pp. 175–190.
- Elsinga, G. E. (2008) Tomographic particle image velocimetry: and its application to turbulent boundary layers. PhD Thesis, Faculty of Aerospace Engineering, Delft University of Technology, Delft, The Netherlands.
- Elsinga, G. E., Adrian, R. J., van Oudheusden, B. W. & Scarano, F. (2007) Tomographic-PIV investigation of a high Reynolds number turbulent boundary layer. In *Proc. 7<sup>th</sup> Int. Symp. on Particle Image Velocimetry*, Rome, Italy, Sep. 11–14.
- Elsinga, G. E., Kuik, D. J., van Oudheusden, B. W. & Scarano, F. (2007*b*) Investigation of the three-dimensional coherent structures in a turbulent boundary layer with tomographic-PIV. In *Proc. 45<sup>th</sup> AIAA Aerospace Sciences Meeting & Exhibit*, Reno, NV, Jan. 8–11.
- Elsinga, G. E., Scarano, F., Wieneke, B. & van Oudheusden, B. W. (2006) Tomographic particle image velocimetry. *Exps. Fluids* **41**, pp. 933–947.
- Elsinga, G. E., van Oudheusden, B. W. & Scarano, F. (2005) Evaluation of aero-optical distortion effects in PIV. *Exps. Fluids* **39**, pp. 246–256.
- Erengil, M. E. & Dolling, D. S. (1991) Unsteady wave structure near separation in a Mach 5 compression ramp. *AIAA J.* **29**, pp. 728–735.
- Erengil, M. E. & Dolling, D. S. (1993) Physical causes of separation shock unsteadiness in shock wave/turbulent boundary layer interactions. AIAA Paper 93-3134.

Fage, A. & Sargent, R. F. (1947) Shock-wave and boundary-layer phenomena near a flat surface. *Proc. Roy. Soc. London* **190**, pp. 1–20.

Farmer, J. D. & Sidorowich, J. J. (1987) Predicting chaotic time series. *Phys. Rev. Lett.* **59**, pp. 845–848.

Fernholz, H. H. & Finley, P. J. (1981) A further compilation of compressible turbulent boundary layer data with a survey of turbulence data. AGARDograph AG-263, AGARD.

Ferri, A. (1939) Experimental results with aerofoils tested in the high speed tunnel at Guidonia. NACA 946 (translation 1940).

Fraser, A. & Swinney, H. (1986) Independent coordinates for strange attractors from mutual information. *Phys. Rev. A* **33**, pp. 1134–1140.

Ganapathisubramani, B., Clemens, N. T. & Dolling, D. S. (2006) Large-scale motions in a supersonic turbulent boundary layer. *J. Fluid Mech.* **556**, pp. 71–282.

Ganapathisubramani, B., Clemens, N. T. & Dolling, D. S. (2007) Effects of upstream boundary layer on the unsteadiness of shock-induced separation. *J. Fluid Mech.* **585**, pp. 369–394.

Ganapathisubramani, B., Hutchins, N., Hambleton, W. T., Longmire, E. K. & Marusic, I. (2005) Investigation in a turbulent boundary layer using two-point correlations. *J. Fluid Mech.* **524**, pp. 57–80.

Ganapathisubramani, B., Longmire, E. K. & Marusic, I. (2003) Characteristics of vortex packets in turbulent boundary layers. *J. Fluid Mech.* **478**, pp. 35–46.

Garnier, E. & Sagaut, P. (2002) Large eddy simulation of shock/boundary-layer interaction. *AIAA J.* **40**, pp. 1935–1944.

Gibson, J. F., Halcrow, J. & Cvitanović, P. (2008) Visualizing the geometry of state-space in plane Couette flow. *J. Fluid Mech.* **611**, pp.



107–130.

Gleick, J. (1987) *Chaos: making a new science*. Sphere Books Ltd., London, United Kingdom.

Good, M. C. & Joubert, P. N. (1968) The form drag of two-dimensional bluff-plates immersed in turbulent boundary layers. *J. Fluid Mech.* **31**, pp. 547–582.

Gori, F., Ludovisi, D. & Cerritelli, P. F. (2006) Forecast of oil price and consumption in the short term under three scenarios: Parabolic, linear and chaotic behaviour. *Energy* **32**, pp. 1291–1296.

Grant, I. (1997) Particle image velocimetry: a review. *Proc. Instn. Mech. Engrs.* **211**, part C, pp. 55–76.

Grassberger, P. & Procaccia, I. (1983) Measuring the strangeness of strange attractors. *Physica D* **9**, pp. 189–208.

Grassberger, P., Schreiber, T. & Schaffrath, C. (1991) Non-linear time sequence analysis. *Int. J. Bifurcation & Chaos* **1**, pp. 521–547.

Green, J. E. (1970) Interactions between shock waves and turbulent boundary layers. *Prog. Aero. Sci.* **11**, pp. 253–340.

Guckenheimer, J. (1986) Strange attractors in fluids: another view. *Ann. Rev. Fluid Mech.* **18**, pp. 15–31.

Haller, G. (2005) An objective definition of a vortex. *J. Fluid Mech.* **525**, pp. 1–26.

Hankey, W. L. Jr. & Holden, M. S. (1975) Two-dimensional shock-wave boundary layer interactions in high-speed flows, AGARDograph 203.

Head, M. R. & Bandyopadhyay, P. (1981) New aspects of turbulent boundary-layer structure. *J. Fluid Mech.* **107**, pp. 297–338.

Herman, G. T. & Lent, A. (1976) Iterative reconstruction algorithms. *Comput. Biol. Med.* **6**, pp. 273–294.

Herzog, S. (1986) The large-scale structure in the near-wall region of a turbulent pipe flow. PhD Thesis, Cornell University, Ithaca, New York, USA.

Hinsch, K. D. (2002) Holographic particle image velocimetry. *Meas. Sci. Technol.* **13**, R61–R72.

Holder, D. W., Pearcy, H. H. & Gadd, G. E. (1955) The interaction between shock waves and boundary layers. British ARC Tech. Rep. C.P. No. 180.

Hopf, E. (1948) A mathematical example displaying features of turbulence. *Commun. Appl. Maths* **1**, pp. 303–322.

Hou, Y. X. (2003) Particle image velocimetry study of shock-induced turbulent boundary layer separation. PhD Thesis, Department of Aerospace Engineering and Engineering Mechanics, The University of Texas at Austin, Texas, USA.

Houwing, A. F. P., Smith, D. R., Fox, J. S., Danehy, P. M. & Mudford N. R. (2001) Laminar boundary layer separation at a fin-body junction in a hypersonic flow. *Shock Waves* **11**, pp. 31–42.

Howarth, L. (1948) The propagation of steady disturbances in a supersonic stream bounded on one side by a parallel subsonic stream. *Proc. Camb. Philos. Soc.* **44**, pp. 380–390.

Hugoniot, P. H. (1887) Memoire sur la propagation du mouvement dans les corps et plus spécialement dans les gaz parfaits, 1e Partie, *J. Ecole Polytech. Paris* **57**, pp. 3–97.

Hugoniot, P. H., (1889) Memoire sur la propagation du mouvement dans les corps et plus spécialement dans les gaz parfaits, 2e Partie, *J. Ecole Polytech. Paris* **58**, pp. 1–125.

- Humble, R. A., Elsinga, G. E., Scarano, F. & van Oudheusden, B. W. (2007*a*) Investigation of the instantaneous 3D flow organization of a shock wave/turbulent boundary layer interaction using tomographic PIV. AIAA Paper 2007-4112.
- Humble, R. A., Elsinga, G. E., Scarano, F. & van Oudheusden, B. W. (2008) Instantaneous three-dimensional structure of a shock wave/turbulent boundary layer interaction. *J. Fluid Mech.* (accepted.)
- Humble, R. A., Scarano, F. & van Oudheusden, B. W. (2006) Experimental study of an incident shock wave/turbulent boundary layer interaction using PIV. In *Proc. 36<sup>th</sup> AIAA Fluid Dynamics Conference*, San Francisco, CA, USA.
- Humble, R. A., Scarano, F. & van Oudheusden. (2007*b*) Particle image velocimetry measurements of a shock wave/turbulent boundary layer interaction. *Exps. Fluids* **43**, pp. 173–183.
- Humble, R. A., Scarano, F. & van Oudheusden. (2007*c*) Unsteady flow organization of compressible planar base flows. *Phys. Fluids* **19**, pp. 1–17.
- Hunt, D. & Nixon, D. (1995) Very large eddy simulation of an unsteady shock-wave/turbulent boundary-layer. AIAA Paper 95-2212.
- Hunt, J. C. R., Wray, A. A. & Moin, P. (1988) Eddies, streams, and convergence zones in turbulent flows. Center for turbulence research report CTR-S88, 193.
- Hutchins, N. & Marusic, I. (2007) Evidence of very long meandering features in the logarithmic region of turbulent boundary layers. *J. Fluid Mech.* **579**, pp. 1–28.
- Islam, S., Bras, R. L. & Rodriguez-Iturbe, I. (1993) A possible explanation for low correlation dimension estimates for the atmosphere. *J. Appl. Meteor.* **32**, pp. 203–208.

Jeong, J., Hussain, F., Schoppa, W. & Kim, J. (1997) Coherent structures near the wall in a turbulent channel flow. *J. Fluid Mech.* **332**, pp. 353–396.

Kim, K. C. & Adrian, R. J. (1999) Very large-scale motion in the outer layer. *Phys. Fluids* **11**, pp. 417–422.

Kistler, A. L. (1964) Fluctuating wall-pressure under a separated supersonic flow. NASA-CR-56564.

Kiya, M. & Sasaki, K. (1985) Structure of large-scale vortices and unsteady reverse flow in the reattaching zone of a turbulent separation bubble. *J. Fluid Mech.* **154**, pp. 463–491.

Klebanoff, P. (1955) Characteristics of turbulence in a boundary layer with zero pressure gradient. NACA Rept. 1247.

Kline, S. J. & McClintock, F. A. (1953) Describing uncertainties in single-sample experiments. *Mech. Eng.* **75**, pp. 3–8.

Kline, S. J., Reynolds, W. C., Schraub, F. A. & Rundstadler, P. W. (1967) The structure of turbulent boundary layers. *J. Fluid Mech.* **30**, pp. 741–773.

Knight, D. D. & Degrez, G. (1998) Shock wave boundary layer interactions in high speed flows: a critical survey of current numerical prediction capabilities. Advisory Rept. 319, AGARD 2:1. 1–1.35.

Ko, C. L., McLaughlin, D. K. & Troutt, T. R. (1978) Supersonic hot-wire fluctuation data analysis with a conduction end-loss correction. *J. Phys. E: Sci. Instrum.* **11**, pp. 488–494.

Kononov, E. (2007) Visual recurrence toolbox 5.01. <http://www.myserver.com/~nonlinear/vra/download.html>.

Kostas, J., Soria, J. & Chong, M. S. (2005) A comparison between snapshot POD analysis of PIV velocity and vorticity data. *Exps. Fluids* **38**, pp. 146–160.

- Kovaszny, L. S. G., Kibens, V. & Blackwelder, R. F. (1970) Large-scale motion in the intermittent region of a turbulent boundary layer. *J. Fluid Mech.* **41**, pp. 283–325.
- Krischer, K., Rico-Martinez, R., Kevrekidis, I. G. Rotermund, H. H., Ertl, G. & Hudson, J. L. (1993) Model identification of a spatially varying catalytic reaction. *A. I. Ch. E. J.* **39**, pp. 89–98.
- Kuik, D. J. (2007) Tomographic PIV investigation of a turbulent boundary layer. Masters Thesis, Faculty of Aerospace Engineering, Delft University of Technology, Delft, The Netherlands.
- Kuntz, D. W., Amatucci, V. A. & Addy, A. L. (1987) Turbulent boundary-layer properties downstream of the shock-wave/turbulent boundary-layer interaction. *AIAA J.* **25**, pp. 668–675.
- Kuo, Y. -H. (1953) Reflection of weak shock wave from a boundary layer along a flat plate II: interaction of oblique shock wave with a laminar boundary layer analyzed by differential-equation method. NACA TN 2869.
- Lanford, O. E. (1982) The strange attractor theory of turbulence. *Ann. Rev. Fluid Mech.* **14**, pp. 347–364.
- Liberzon A., Gurka, R., Tiselj, I. & Hetsroni, G. (2005) Spatial characterization of the numerically simulated vorticity fields of a flow in a flume. *Theoret. Comp. Fluid Dyn.* **19**, pp. 115–125.
- Liepmann, H. W., Roshko, A. & Dhawan, S. (1952) On reflection of shock waves from boundary layers. NACA TN 1100.
- Lighthill, M. J. (1953) On boundary layers and upstream influence. Part II: Supersonic flows without separation. *Proc. Roy. Soc. London A* **217**, pp. 478–507.

Ligrani, P. M., Westphal, R. V. & Lemos, F. R. (1989) Fabrication and testing of subminiature multi-sensor hot-wire probes. *J. Phys. E: Sci. Instrum.* **22**, pp. 262–268.

Logan, P. (1989) Improved method of analyzing hot-wire measurements in supersonic turbulence. *AIAA J.* **27**, pp. 115–117.

Lorenz, E. N. (1956) Empirical orthogonal functions and statistical weather prediction. Sci. Rep. No. 1, Statistical Forecasting Project, M.I.T., Cambridge, MA, pp. 48.

Lorenz, E. N. (1963) Deterministic nonperiodic flow. *J. Atmos. Sci.* **20**, pp. 130–141.

Luker, J. J., Bowersox, R. D. W. & Buter, T. A. (2000) Influence of curvature-driven favorable pressure gradient on supersonic turbulent boundary layer. *AIAA J.* **38**, pp. 1351–1359.

Lumley, J. L. (1967) The structure of inhomogeneous turbulence. In *Atmospheric Turbulence and Wave Propagation* (Eds. A. M. Yaglom, V. I.) Tatarski, Moskow, Nauka, pp. 166–178.

Mandelbrot, B. (1982) The fractal geometry of nature. W. H. Freeman & Co., New York, USA.

Martinerie, J. M., Albano, A. M., Mees, A. I. & Rapp, P. E. (1992) Mutual information, strange attractors, and the optimal estimation of dimension. *Phys. Rev. A* **45**, pp. 7058–7064.

Marwan, N. (2003) Encounters with neighbours: current developments of concepts based on recurrence plots and their applications. PhD Thesis, University of Potsdam, Germany.

May, R. M. (1995) Necessity and chance: deterministic chaos in ecology and evolution. *American Mathematical Society* **32**, pp. 291–308.

McClure, W. B. (1992) An experimental study of the driving mechanism and control on shock induced turbulent separation in a

- Mach 5 compression corner flow. PhD Thesis, Department of Aerospace Engineering and Engineering Mechanics, The University of Texas at Austin, Texas, USA.
- Melling, A. (1986) Seeding gas flows for laser anemometry. Proceedings on the Conference of Advanced Instrumentation for Aero Engine Components. AGARD CP-399, 8.1.
- Meyer, M. J., Butler, T. A. & Bowersox, R. D. W. (1997) Compressible turbulence measurements in a supersonic boundary layer with impinging shock wave interactions. AIAA Paper 97-0427.
- Miller, I. S., Shah, D. A. & Antonia, R. A. (1987) A constant temperature hot-wire anemometer. *J. Phys. E: Sci. Instrum.* **20**, pp. 311–314.
- Moderass, D. & Johnson, D. A. (1976) Investigation of shock-induced separation of a turbulent boundary layer using laser velocimetry. AIAA Paper 76-374.
- Moeckel, W. E. (1951) Flow separation ahead of a blunt axially symmetric body at Mach numbers 1.76 to 2.10. NACA RM E51125.
- Moin, P. & Moser, R. D. (1989) Characteristic-eddy decomposition of turbulence in a channel. *J. Fluid Mech.* **200**, pp. 471–509.
- Moore, J. D. & Stenning, K. (2001) Proceedings of the twenty-third annual conference of the Cognitive Science Society. Human Communication Research Centre, University of Edinburgh, Edinburgh, Scotland.
- Moreno, D., Krothapalli, A., Alkisar, M. B. & Lourenco, L. M. (2004) Low-dimensional model of a supersonic rectangular jet. *Phys. Rev. E* **69**, 026304.
- Morkovin, M. (1960) Effects of compressibility on turbulent flows. In *Mecanique de la Turbulence*. (Eds. A. Favre, Gordon & Breach), New York. pp. 367–380.

Muck, K. C., Dussauge, J. -P. & Bogdonoff, S. M. (1985) Structure of the wall-pressure fluctuations in a shock-induced separated turbulent flow. AIAA Paper 85-0179.

Na, Y. & Moin, P. (1998) Direct numerical simulation of a separated turbulent boundary layer. *J. Fluid Mech.* **374**, pp. 379–405.

Neiland, V. Y. (1969) On the theory of laminar separation in supersonic flow. *Izv. Akad. Nauk. SSSR, Mech. Zhidk. Gaza* **4**, pp. 53–57 (in Russian.)

Obermeier, F. (2006) Prandtl's mixing-length model – revisited. *Proc. Appl. Math. Mech.* **6**, pp. 577–578.

Packard, N., Crutchfield, J. P., Farmer, J. & Shaw, R. (1980) Geometry from a time series. *Phys. Rev.* **45**, pp. 712–716.

Patte-Rouland, B., Lalizel, G., Moreau, J. & Rouland, E. (2001) Flow analysis of an annular jet by particle image velocimetry and proper orthogonal decomposition. *Meas. Sci. Technol.* **12**, pp. 1404–1412.

Pereira, F. & Gharib, M. (2002) Defocusing digital particle image velocimetry and the three-dimensional characterization of two-phase flows. *Meas. Sci. Technol.* **13**, pp. 683–694.

Perry, A. E. & Chong, M. S. (1982) On the mechanism of wall turbulence. *J. Fluid Mech.* **119**, pp. 173–217.

Pincus, S. M. (1991) Approximate entropy as a measure of system complexity. *Proc. Natl. Acad. Sci. USA* **88**, pp. 2297–2301.

Pirozzoli, S. & Grasso, F. (2006) Direct numerical simulation of impinging shock wave/turbulent boundary layer interaction at  $M=2.25$ . *Phys. Fluids* **18**, 065113.



- Plotkin, K. J. (1975) Shock wave oscillation driven by turbulent boundary-layer fluctuations. *AIAA J.* **13**, pp. 1036–1040.
- Poggie, J. & Smits, A. J. (2001) Shock unsteadiness in a reattaching shear layer. *J. Fluid Mech.* **429**, pp. 155–185.
- Poisson, S. D. (1808) M'emoire sur la th'eorie du son. *J. Ecole. Polytech.* **14**, pp. 319–392.
- Prandtl, L. (1904) Uber Flussigkeits bewegung bei sehr kleiner Reibung. *Verhaldlg III Int. Math. Kong.* (Heidelberg: Teubner) pp 484–491; Also available in translation as: Motion of fluids with very little viscosity. NACA TM 452 (March 1928).
- Preisendorfer, R. W. (1988) Principal component analysis in meteorology and oceanography. Elsevier, Amsterdam, The Netherlands.
- Raffel, M. Willert, C. & Kompenhans, J. (2007) Particle image velocimetry: a practical guide. 2<sup>nd</sup> Ed. Springer-Verlag, Berlin, Germany.
- Rangarajan, G., Habib, S., & Ryne, R. D. (1998) Lyapunov exponents without rescaling and reorthogonalization. *Phys. Rev. Lett.* **80**, pp. 3747–3750.
- Rankine, W. J. M. (1870a) On the thermodynamic theory of waves of finite longitudinal disturbance, *Phil. Trans. Roy. Soc. London.* **160**, pp. 277–286.
- Rankine, W. J. M. (1870b) Supplement to a paper, On the thermodynamic theory of waves of finite longitudinal disturbance, *Phil. Trans. Roy. Soc. London* **160**, pp. 287–288.
- Ringuette, M. J., Wu, M. & Martin, M. P. (2008) Coherent structures in direct numerical simulation of turbulent boundary layers at Mach 3. *J. Fluid Mech.* **594**, pp. 59–69.

Ritter, A. & Kuo, Y-H. (1953) Reflection of a weak shock wave from a boundary layer along a flat plate I: interaction of weak shock waves with laminar and turbulent boundary layers analyzed by momentum-integral method. NACA TN-2868.

Robinson, J. C. (2008) A topological time-delay embedding theorem for infinite dimensional cocycle dynamical systems. *Discrete and Continuous Dynamical Systems Series B* **9**, pp. 734–741.

Robinson, S. K. (1991) Coherent motions in the turbulent boundary layer. *Annu. Rev. Fluid Mech.* **23**, pp. 601–639.

Rodriguez-Iturbe, I., De Power, F. B., Sharifi, M. B. & Georgakakos, K. P. (1989) Chaos in rainfall. *Water Resour. Res.* **25**, pp.1667–1675.

Rose, W. C. & Johnson, D. A. (1975) Turbulence in a shock-wave boundary-layer interaction. *AIAA J.* **13**, pp. 884–889.

Rosenstein, M. T., Collins, J. J. & De Luca, C. J. (1993) A practical method for calculating the largest Lyapunov exponents from small data sets. *Physica D* **65**, pp. 117–134.

Rowley, C. W., Colonius, T. & Murray, R. M. (2004) Model reduction for compressible flows using POD and Galerkin projection. *Physica D* **189**, pp. 115–129.

Ruelle, D. & Takens, F. (1971) On the nature of turbulence. *Communs. Math. Phys.* **42**, pp. 137–151.

Rummelhart, D. E., Hinton, G. E. & Williams, R. J. (1986) Learning internal representations by error propagation. In *Parallel Distributed Processing*. (Eds. D. E. Rummelhart & J. E. McClelland), **1**, pp. 318–362. MIT-Press, Cambridge, MA, USA.

Samimy, M., Arnette, S. A. & Elliot, G. S. (1994) Streamwise structures in a turbulent supersonic boundary layer. *Phys. Fluids* **6**, pp. 1081–1083.

- Samimy, M. & Lele, S. K. (1991) Motion of particles with inertia in a compressible free shear layer. *Phys. Fluids A* **3**, pp. 1915–1923.
- Sauer, T. (1994) Time series prediction by using delay coordinate embedding. *Time series Prediction. Forecasting the Future and Understanding the Past* **59**, pp. 175–193.
- Scarano, F. (2003) Theory of non-isotropic spatial resolution in PIV. *Exps. Fluids* **35**, pp. 268–277.
- Scarano, F. (2006) Quantitative visualization in the high-speed flow regime: heritage, current trends and perspectives. In *Proc. 12<sup>th</sup> Int. Symposium on Flow Visualization*, Göttingen, Germany.
- Scarano, F., Elsinga, G. E., Bocci, E. & van Oudheusden, B. W. (2006) Investigation of the 3-D coherent structures in the turbulent cylinder wake using tomo-PIV. In *Proc. 13<sup>th</sup> Int. Symposium on Applications of Laser Techniques to Fluid Mechanics*, Lisbon, Portugal.
- Scarano F, & Riethmuller, M. L. (2000) Advances in iterative multi-grid PIV image processing. *Exps. Fluids* **29**, S051–S060.
- Scarano F. & van Oudheusden B. W. (2003) Planar velocity measurements of a two-dimensional compressible wake flow. *Exps. Fluids* **34**, pp. 430–441.
- Schaaf, S. A. & Chambre, P. L. (1958) Fundamentals of gas dynamics. Princeton University Press, Princeton, New Jersey, USA.
- Schlichting, H. (1979) Boundary layer theory. 7<sup>th</sup> Ed. McGraw-Hill, New York.
- Schrijer, F. F. J. & Scarano, F. (2007) Particle slip compensation in steady compressible flows. In *Proc. 7<sup>th</sup> International Symposium on Particle Image Velocimetry*, Rome, Italy, Sept. 11–14.

Schrijer, F. F. J. & Scarano, F. (2008) Effect of predictor-corrector filtering on the stability and spatial resolution of iterative PIV interrogation. DOI: 10.1007/s00348-008-0511-7.

Schrijer, F. F. J., Scarano, F. & van Oudheusden, B. W. (2006) Application of PIV in a Mach 7 double-ramp flow. *Exps. Fluids* **41**, pp. 353–363.

Schröder, A., Geisler, R., Elsinga, G. E., Scarano, F. & Dierksheide, U. (2007) Investigation of a turbulent spot and a tripped turbulent boundary layer flow using time-resolved tomographic PIV. *Exps. Fluids* **44**, pp. 305–316.

Selig, M. S., Andreopoulos, Y., Muck, K. C., Dussauge, J. -P. & Smits, A. J. (1989) Turbulence structure in a shock wave/turbulent boundary-layer interaction. *AIAA J.* **27**, pp. 862–869.

Sello, S. (2001) Solar cycle forecasting: a nonlinear dynamics approach. *A&A* **377**, pp. 312–320.

Settles, G. S. (1993) Swept shock/boundary-layer interaction - Scaling laws, flow-field structure, and experimental methods. AGARD-R-792, Paper No. 1.

Settles, G. S. (2001) Schlieren and shadowgraphy techniques: visualizing phenomena in transparent media. Springer-Verlag, Heidelberg, Germany.

Settles, G. S. & Dolling, D. S. (1990) Swept shock/boundary layer interactions - Tutorial and update. AIAA Paper 90-0375.

Sharifi, M. B., Georgakakos, K. P. & Rodriguez-Iturbe, I. (1990) Evidence of deterministic chaos in the pulse of storm rainfall. *J. Atmos. Sci.* **47**, pp. 888–893.

Simpson, R. L. (1989) Turbulent boundary-layer separation. *Annu. Rev. Fluid Mech.* **21**, pp. 205–234.

- Sirovich, L. (1987) Turbulence and the dynamics of coherent structures. *Q. Appl. Math.* **XLV**, pp. 561–571.
- Sivakumar, B. (2000) Chaos theory in hydrology: important issues and interpretations. *J. Hydrology* **227**, pp. 1–120.
- Smith, D. R., Poggie, J., Konrad, W. & Smits, A. J. (1991) Visualization of shock wave turbulent boundary layer interactions using Rayleigh scattering. AIAA Paper 91-0651.
- Smith, M. W. & Smits, A. J. (1995) Visualization of the structure of supersonic turbulent boundary layers. *Exps. Fluids* **18**, pp. 288–302.
- Smits, A. J. & Bogdonoff, S. M. (1986) A “preview” of three-dimensional shock-wave/turbulent boundary-layer interaction. In *Turbulent Shear Layer/Shock Wave Interactions*. (Ed. J. Détery), *IUTAM Symposium Palaiseau*, 1985. Springer, Berlin Heidelberg, Germany.
- Smits, A. J. & Dussauge, J. -P. (2006) Turbulent shear layers in supersonic flow. 2<sup>nd</sup> Ed. American Institute of Physics, New York, USA.
- Smits, A. J., Hayakawa, K. & Muck, K. C. (1983) Constant temperature hot-wire anemometer practice in supersonic flows. Part I: the normal wire. *Exps. Fluids* **1**, pp. 83–92.
- Soloff, S. M., Adrian, R. J. & Liu, Z-C. (1997) Distortion compensation for generalized stereoscopic particle image velocimetry. *Meas. Sci. Technol.* **8**, pp. 1441–1454.
- Sommerer, J. C., Ott, E. & Tél, T. (1997) Modeling two-dimensional fluid flows with chaos theory. John Hopkins APL Technical Digest, **18**, pp. 193–203.
- Souverein, L. J., van Oudheusden, B. W., Scarano, F. & Dupont, P. (2008) Unsteadiness characterization in a shock wave turbulent boundary layer interaction through dual-PIV. AIAA Paper 2008-4169.

Spalding, D. B. (1961) A single formula for the law of the wall. *J. Appl. Mech.* **28**, pp. 455–457.

Spina, E. F., Donovan, J. F. & Smits, A. J. (1991) On the structure of high Reynolds-number supersonic turbulent boundary layers. *J. Fluid Mech.* **222**, pp. 293–327.

Spina, E. F., Smits, A. J. & Robinson, S. K. (1994) The physics of supersonic turbulent boundary layers. *Annu. Rev. Fluid Mech.* **26**, pp. 287–319.

Sprott, J. C. (2003) Chaos and time series analysis. Oxford University Press, Great Britain.

Sprott, J. C. & Rowlands, G. (2001) Improved correlation dimension calculation. *Int. J. Bifurcation & Chaos* **11**, pp. 1865–1880.

Sreenivasan, K. R. (1991) Fractals and multifractals in turbulence. *Ann. Rev. Fluid Mech.* **23**, pp. 539–600.

Stack, J. (1934) Effects of compressibility on high speed flight. *J. Aero. Sci.* **1**, pp. 40–43.

Stanewsky, E. (1973) Shock-boundary layer interaction in transonic and supersonic flow. In *Transonic Flows in Turbomachinery*. Lecture Series 59, Von Kármán Institute, Rhodes-Saint-Genève, Belgium.

Stern, F., Muste, M., Beninati, M. –L. & Eichinger, W. E. (1999) A summary of experimental uncertainty assessment methodology with example. IIHR Technical Rept. 406, Iowa Institute of Hydraulic Research, College of Engineering, The University of Iowa, Iowa City, Iowa 52242, USA.

Stewartson, K. & Williams, P. G. (1969) Self-induced separation. *Proc. Roy. Soc. London A* **312**, pp. 181–206.

- Takens, F. (1981) Detecting strange attractors in turbulence. In *Lecture notes in mathematics* **898**. *Dynamical systems and turbulence*, pp. 366, Springer, Berlin, Germany.
- Theodorsen, T. (1952) Mechanisms of turbulence. In *Proc. Midwestern Conference on Fluid Mechanics*. Ohio State University, Columbus, OH.
- Theunissen, R., Scarano, F. & Riethmuller, M. L. (2007). An adaptive sampling and windowing interrogation method in PIV. *Meas. Sci. Tech.*, **18**, pp. 275–287.
- Thomas, F. O., Putman, C. M. & Chu, H. C. (1994) On the mechanism of unsteady shock oscillation in shock wave/turbulent boundary layer interaction. *Exps. Fluids* **18**, pp. 69–81.
- Thompson, J. M. T. & Stewart, H. B. (1986) *Nonlinear dynamics and chaos*. Wiley.
- Tomkins, C. D. & Adrian, R. J. (2003) Spanwise structure and scale growth in turbulent boundary layers. *J. Fluid Mech.* **490**, pp. 37–74.
- Touber, E. & Sandham, N. D. (2008) Oblique shock impinging on a turbulent boundary layer: low-frequency mechanisms. AIAA Paper 2008-4170.
- Townsend, A. A. (1956) *The structure of turbulent shear flow*. 1<sup>st</sup> Ed. Cambridge University Press, Cambridge, United Kingdom.
- Tsien, H. S. & Finston, M. (1949) Interaction between two parallel streams of subsonic and supersonic velocities. *J. Aeronaut. Sci.* **15**, pp. 515–528.
- Tuinstra, M. (2005) A PIV investigation on shock wave boundary layer interaction: an oblique shock impinging on a flat plate turbulent boundary layer. Masters Thesis, Faculty of Aerospace Engineering, Delft University of Technology, Delft, The Netherlands.

Tsonis, A. A., Elsner, J. B. & Georgakakos, K. P. (1993) Estimating the dimension of weather and climate attractors: important issues about the procedure and interpretation. *J. Atmos. Sci.* **50**, pp. 2549–2555.

Ünalms, Ö.H. & Dolling, D.S. (1998) Experimental study of causes of unsteadiness of shock-induced turbulent separation. *AIAA J.* **36**, pp. 371–378.

Van Driest, E. R. (1951) Turbulent boundary layer in compressible fluids. *J. Aero. Sci.* **18**, pp. 145–160.

Van Oudheusden, B.W. (1999) An experimental study of transition and the development of turbulence in a linearly retarded boundary-layer flow. *The Aeronautical Journal* **103**, pp. 497–509.

Van Oudheusden, B. W. (2008) Principles and application of velocimetry-based planar pressure imaging in compressible flows with shocks. *Exps. Fluids*, **45**, pp. 657–674.

Wang, Z. S., He, Z. & Chen, J. D. Z. (2004) Chaotic behavior of gastric migrating myoelectrical complex. *IEEE Trans. Bio. Eng.* **51**, pp. 1401–1406.

Weiss, J. & Chokani, N. (2007) Effects of free-stream noise on shock-wave/turbulent-boundary-layer interaction. *AIAA J.* **45**, pp. 2352–2355.

Westerweel, J. (1997) Fundamentals of digital particle image velocimetry. *Meas. Sci. Technol.* **8**, pp. 1379–1392.

Westerweel, J. & Scarano, F. (2005) Universal outlier detection for PIV data. *Exps. Fluids* **39**, pp. 1096–1100.

White, F. M. (1991) Viscous fluid flow. 2<sup>nd</sup> Ed. McGraw-Hill, New York, USA.



- Wieneke, B. (2007) Volume self-calibration for stereo-PIV and tomographic-PIV. In *Proc. 7<sup>th</sup> Int. Symp. on Particle Image Velocimetry*, Rome, Italy, Sep. 11–14.
- Wisse, M. E. N. (2005) An asymptotic analysis of compressible base flow and the implementation into linear plug nozzles. PhD Thesis, Faculty of Aerospace Engineering, Delft University of Technology, Delft, The Netherlands.
- Witten, E. (1998) Magic, mystery, and matrix. **45**, pp. 1124–1129.
- Wolf, A., Swift, J., Swinney, H. & Vastano, J. (1985). Determining Lyapunov exponents from a time series. *Physica D* **16**, pp. 285–317.
- Wu, M. & Martin, M. P. (2007) Direct numerical simulation of supersonic turbulent boundary layer over a compression ramp. *AIAA J.* **45**, pp. 879–889.
- Wu, M. & Martin, M. P. (2008) Analysis of shock motion in shockwave and turbulent boundary layer interaction using direct numerical simulation data. *J. Fluid Mech.* **594**, pp. 71–83.
- Yankov, D., DeCoste, D. & Keogh, E. (2006) Ensembles of nearest neighbors forecasts. In *Proc. 17<sup>th</sup> European Conference on Machine Learning (ECML 2006). Lecture Notes in Computer Science.* pp. 545–556.
- Young, A. D. (1989) Boundary layers. AIAA Education series.
- Zhou, J., Adrian, R. J., Balachandar, S. & Kendall, T. M. (1999) Mechanisms for generating coherent packets of hairpin vortices in channel flow. *J. Fluid Mech.* **387**, pp. 353–396.



# LIST OF PUBLICATIONS

---

## BOOK CHAPTERS

Humble, R. A., Scarano, F. & van Oudheusden, B. W. (2008) Unsteady flow organization of a shock wave/turbulent boundary layer interaction. In *Unsteady Separated Flows and their Control*. (Ed. Marianna Braza), *IUTAM Symposium*. Springer, Germany (to appear).

Scarano, F., Humble, R. A. & van Oudheusden, B. W. (2007) PIV measurements of a shock wave/turbulent boundary layer. In *Particle Image Velocimetry: A Practical Guide*. By Raffel, M., Willert, C. E., Wereley, S. T. & Kompenhans, J. 2<sup>nd</sup> Ed. Springer, Germany. ISBN: 978-3-540-72307-3.

## JOURNAL ARTICLES

Blinde, P. L., Humble, R. A., van Oudheusden, B. W. & Scarano, F. (2008) Effects of micro-ramps on a shock wave/turbulent boundary layer interaction using PIV. *Shock Waves* (accepted).

Humble, R. A., Elsinga, G. E., Scarano, F. & van Oudheusden, B. W. (2008) Three-dimensional instantaneous structure of a shock wave/turbulent boundary layer interaction. *J. Fluid Mech.* (accepted).

Humble, R. A., Scarano, F. & van Oudheusden, B. W. (2008) Unsteady effects in an incident shock wave/turbulent boundary layer interaction. *J. Fluid Mech.* (under review).

Humble, R. A., Elsinga, G. E. & van Oudheusden, B. W. (2008) Time series analysis of a shock wave/turbulent boundary layer interaction using chaos theory. (in preparation.)

Humble, R. A., Scarano, F. & van Oudheusden, B. W. (2007) Unsteady flow organization of planar compressible base flows. *Phys. Fluids* **19**, pp. 1–17.

Humble, R. A., Scarano, F. & van Oudheusden, B. W. (2007) Particle image velocimetry measurements of a shock wave/turbulent boundary layer interaction. *Exps. Fluids* **43**, pp.173–183.

## CONFERENCE PROCEEDINGS

Humble, R. A., Elsinga, G. E. & van Oudheusden, B. W. (2009) Time series analysis of a shock wave/turbulent boundary layer interaction using chaos theory. In *Proc. 39<sup>th</sup> AIAA Fluid Dynamics Conference*, San Antonio, TX, USA.

Blinde, P. L., Humble, R. A., van Oudheusden, B. W. & Scarano, F. (2009) Effects of micro-ramps on a shock wave/turbulent boundary layer interaction using PIV. In *Proc. 39<sup>th</sup> AIAA Fluid Dynamics Conference*, San Antonio, TX, USA.

Van Oudheusden, B. W., Scarano, F., Elsinga, G. E., Humble, R. A. & Souverein, L. J. (2008) Advanced techniques for the temporal and spatial characterization of turbulent structures in high-speed flows. In *Proc. International Workshop on Compressible Turbulent Flow Research for the Next Generation of Air Vehicles*, Marseille, France.

Humble, R. A., Elsinga, G. E., Scarano, F. & van Oudheusden, B. W. (2008) Experimental investigation of the instantaneous spatial flow organization of high-speed turbulent boundary layers. In *Proc. EWA International Workshop on Advanced Techniques in Experimental Aerodynamics*, Delft, The Netherlands.

Van Oudheusden, B. W., Humble, R. A., Souverein, L. J., Scarano, F., Beer, A., Pirozzoli, S. & Grasso, F. (2007) Experimental and numerical flow field study of a reflecting shock interaction with a high Reynolds number turbulent boundary layer. (Eds. P. Doerffer, J. Drbohlav & K. Sjors.) In *Proc. Joint EWA and UFAST Workshop on Validation of Numerical Methods by Experiments in Aerodynamics*, Prague, Czech Republic.

Humble, R. A., Elsinga, G. E., Scarano, F. & van Oudheusden, B. W. (2007) Experimental investigation of the three-dimensional structure of a shock wave/turbulent boundary layer interaction. In *Proc. 16<sup>th</sup> Australasian Fluid Mechanics Conference*, Gold Coast, Australia.

Humble, R. A., Scarano, F. & van Oudheusden, B. W. (2007) Unsteady flow organization of a shock wave/turbulent boundary layer interaction. In *Proc. IUTAM Symposium on Unsteady Separated Flows and Their Control*, Corfu, Greece.

Humble, R. A. (2007) Deterministic chaos within a forced boundary layer. In *Proc. 37<sup>th</sup> AIAA Fluid Dynamics Conference*, Miami, FL, USA.

Humble, R. A., Elsinga, G.E., Scarano, F. & van Oudheusden, B. W. (2007) Instantaneous 3D flow organization of a SWTBLI using tomographic PIV. In *Proc. 37<sup>th</sup> AIAA Fluid Dynamics Conference*, Miami, FL, USA.

Humble, R. A., Scarano, F. & van Oudheusden, B. W. (2006) Experimental study of an incident shock wave/turbulent boundary layer interaction using PIV. In *Proc. 36<sup>th</sup> AIAA Fluid Dynamics Conference*, San Francisco, CA, USA.

Humble, R. A., Scarano, F., van Oudheusden, B. W. & Tuinstra, M. (2006) PIV measurements of a shock wave/turbulent boundary layer interaction. In *Proc. 13<sup>th</sup> Int. Symp. On Applications of Laser Techniques to Fluid Mechanics*, Lisbon, Portugal.

Humble, R. A., Scarano, F. & van Oudheusden, B. W. (2006) Unsteady Planar Base Flow Investigation using PIV and POD. In *Proc. 44<sup>th</sup> AIAA Aerospace Sciences Meeting*, Reno, NV, USA.

Humble, R. A., Scarano, F. & van Oudheusden, B. W. (2005) Application of PIV and POD to unsteady planar base flows. In *Proc. PIVNET II International Workshop on the Application of PIV in Compressible Flows*, Delft, The Netherlands.

## **MAGAZINES**

Elsinga, G. E., Humble, R. A., van Oudheusden, B. W. & Scarano, F. (2007) A new frontier in velocity measurements. *Leonardo Times* **3**, pp. 36–37.